# NANO-SCALED AMINO ACID BASED POLY(ESTER AMIDE)S AS THE DELIVERY VEHICLES FOR THERAPEUTICS AGAINST TUMOR

A Dissertation

Presented to the Faculty of the Graduate School

of Cornell University

In Partial Fulfillment of the Requirements for the Degree of

Doctor of Philosophy

by

Ying Ji

January 2017

© 2017 Ying Ji

# NANO-SCALED POLY(ESTER AMIDE)S AS THE DELIVERY VEHICLES FOR THERAPEUTICS AGAINST TUMOR

Ying Ji, Ph. D.

Cornell University 2017

Amino acid based poly(ester amide)s are a family of biodegradable polymers which have been designed and synthesized for various biomedical applications including tissue engineering scaffold, hydrogels, coating for cardiovascular stents, nanofibrous membrane and sutures etc. The aim for this study is to investigate the potential of poly(ester amide)s materials as nano-carriers for the delivery of multiple therapeutics including chemotherapeutics, photosensitizers and proteins, in the treatment of cancer. The amino acid based poly(ester amide)s provided the physical encapsulation of the payloads, and further impact the interactions and communication with cancer cells, comparing to the direct administration of free therapeutics. In addition, by adjusting different amino acids on poly(ester amide)s, or froming hybrid nanomaterials with other biodegradable polymers, functionalities can be introduced into the delivery systems so that “smart” delivery can be achieved. The therapeutic potency of poly(ester amide)s based delivery systems, are closely related to a series of stimuli, which includes biological cues such as enzymatic degradation, or physical cues such as light. The thesis demonstrated the potency of poly(ester amide) nano-carriers from both in vitro and in vivo characterization, and further validated their application potential to be developed as spatio-temporally controllable delivery systems.

# BIOGRAPHICAL SKETCH

Ying Ji was born in Taiyuan, China on August 8th, 1987. She began her undergraduate studies at Zhejiang University in Hangzhou, China, where she completed her bachelor's degree in Department of Polymer Science and Engineering in 2009. In September of the same year, Ying began her graduate studies at Zhejiang University. She received her Master of Science degree in Department of Polymer Science and Engineering in 2012. She started her Ph.D. studies at Cornell University in the fall of 2012. At Cornell University, she specialized in the study of polymeric biomaterials, especially synthesis and preparation of biodegradable polymeric delivery systems for various therapeutics against tumor.

ACKNOWLEDGMENTS

I would like to express my gratitude to my major advisor, Dr. Chu, for his guidance throughout the research. I would also like to express my sincere appreciation to Dr. Jonathan Butcher, Dr. Minglin Ma, Dr. Margret Frey and Dr. Jintu Fan as my graduate committee members. Their comments and suggestions have greatly improved the quality of this research. Also with heartfelt thanks, I would like to acknowledge Alice Woo who generously funded my graduate study for two years. Her financial support made me able to concentrate on my research.

I am grateful to Carol Bayles from Biotechnology Resource Center, the Imaging Facilities, for her help in flow cytometry and confocal microscopy. I'm grateful to Dr. Jihui Zhao, Dr. Mingyu He, Dr. Dequn Wu, Dr. Alicia Potuck and Shuo Shan for their collaboration and valuable advice. Finally, I owe much to my parents for always believing in me and encouraging me to achieve my goals. All the support they have provided me over the years was the greatest gift anyone has ever given me

TABLE OF CONTENTS

LIST OF FIGURES

LIST OF TABLES

# CHAPTER 1

# SUMMARY OF POLYMERIC NANOMEDICINE AS TREATMENT OF CANCER

### *1.1 Nanomedicine in the treatment of cancer*

Cancer is a leading cause of death worldwide and rapid growth in nanotechnology towards the development of nanomedicine products holds great promise to improve therapeutic efficiency against cancer. As suggested in Figure 1.1, different nanomedicine products such as drug conjugates, lipid-based nanocarriers, polymer-based nanocarriers, inorganic nanoparticles, and viral nanoparticles are used in clinical cancer care [1].

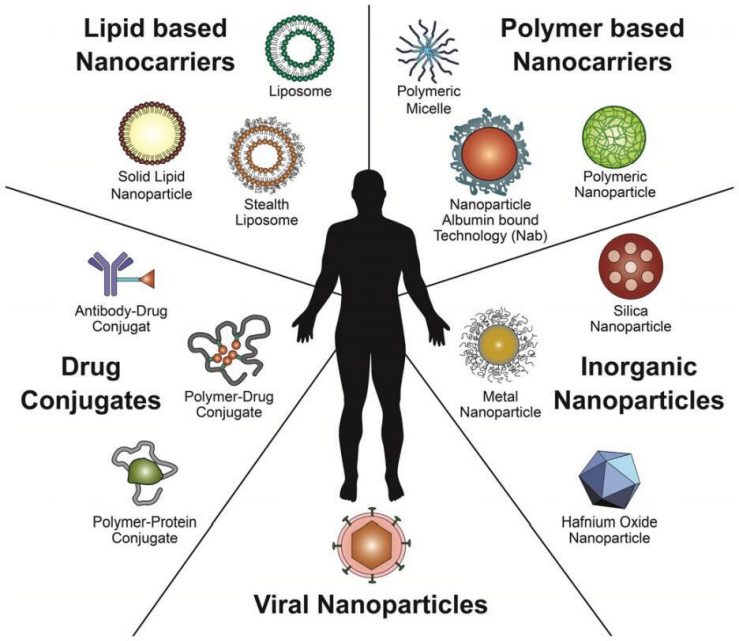


**Figure 1.1**. Schematic illustration of most extensively studied nanotherapeutic platforms [1].

These Nanocarriers can improve the solubility and chemical stability of anti-cancer drugs; protect anti-cancer compounds from degradation or excretion and influence their pharmacokinetic profile; improve the distribution and targeting of anti-tumor medication; and stimuli-sensitive release of payloads can be achieved in

response to a series of biological, chemical or physical triggers [2]. All the advantages mentioned here helped to improve the therapeutic efficiency of anticancer medication, compared to the direct administration of free drug. Table 1.1 summarized the drug-conjugates or nanocarrier based anticancer drug delivery systems that have been approved by FDA for cancer therapy. To date, the majority of the approval nanomedicine are polymer based or lipid based.

**Table 1.1**. Approved drug conjugates and nanocarriers for cancer therapy [1].

| Product [company] | Material | Drug | Indication | Approval |
|---|---|---|---|---|
| Abraxane® (ABI-007) [Abraxis/Celgene] | Nanoparticle albumin-bound | Paclitaxel | Breast cancer, pancreatic cancer, non-small-cell lung cancer | 2005 |
| DaunoXome® [Galen] | Liposome | Daunorubicin | Kaposi's sarcoma | 1996 |
| DepoCyt® [Pacira] | Liposome | Cytosine Arabinoside (cytarabine) | Neoplastic meningitis | 1999 |
| Doxil®/Caelyx® [Johnson & Johnson] | Liposome | Doxorubicin | Kaposi's sarcoma<br>Ovarian cancer<br>Breast cancer<br>Multiple myeloma | 1995<br>1999<br>2003<br>2007 (Europe, Canada) |
| Genexol-PM® (IG-001) [Samyang Biopharm] | PEG-PLA polymeric micelle | Paclitaxel | Breast cancer<br>Lung cancer<br>Ovarian cancer | 2007 (South Korea) |
| Lipo-Dox® [Taiwan Liposome] | Liposome | Doxorubicin | Kaposi's sarcoma, breast and ovarian cancer | 1998 (Taiwan) |
| Marqibo® [Talon] | Liposome | Vincristine | Acute lymphoid leukemia | 2012 (USA) |
| Mepact® [Takeda] | Liposome | Mifamurtide MTP-PE | Osteosarcoma | 2009 (EU) |
| Myocet® [Cephalon] | Liposome | Doxorubicin | Breast cancer (cyclophosphamide) | 2000 (Europe) |
| NanoTherm® [Magforce Nanotechnologies] | Iron oxide nanoparticle | | Thermal ablation glioblastoma | 2010 (Europe) |
| Oncaspar® [Enzon/Sigma-tau] | PEG protein conjugate | L-asparaginase | Leukemia | 2006 |
| Zinostatin stimalamer® (Zinostatin) [Yamanouchi] | Polymer protein conjugate | Styrene maleic anhydride neocarzinostatin (SMANCS) | Liver cancer<br>Renal cancer | 1994 (Japan) |

In addition to the approved nanomedicine, a total of 1575 nanomedicine formulations had been registered for clinical trials by December 2015 according to the registry maintained by clinicaltrials.gov. As many as 1381 of these are in the field of cancer therapy [3]. The following of this section summarized the varieties of nanomedicine formulations that have been in the process of clinical trial, which include polymer-drug conjugates (Table 1.2), polymer-based Nanocarriers (Table 1.3), and inorganic Nanocarriers (Table 1.4). In addition to the traditional nanoparticles, newly-developed nanomedicines with stimuli-responsiveness, and still in the

experimental stages, were also listed in Table 1.5.

Thousands of publications suggest that nanomedicine therapeutics are effective in cancer treatment. However, only very few nanomedicine formulations have successfully entered clinical trials. It is important to address the detailed characterization of nano-carriers, as well as the safety issues in developing optimized nanomedicine products for clinical use. The quality assessment of nanomedicine is important, which involves the characteristics such as structure, composition, size, surface properties, porosity, charge, and aggregation behavior that may impact the performance of the nanomedicine in vivo. Characterization of stability of the nanomedicine in interaction with biological fluids (such as serum), and from the storage aspects (shelf-life), are also of great importance. The intracellular fate of the nanomedicines, as well as the long-term toxicological studies, are aspects that should be addressed to elucidate the safety issues of the nanomedicine.

**Table 1.2**. Polymer-drug conjugates in clinical trials [1].

| Product [company] | Platform | Ligand (target) | Drug | Indication | Status |
|---|---|---|---|---|---|
| ADI-PEG 20 [Polaris] | PEG protein conjugate | | Arginine deaminase | Hepatocellular carcinoma, melanoma | Phase 2/3 |
| AP5280 [Access Pharmaceuticals] | HPMA drug conjugate | | Platinum | Solid tumors | Phase 1/2 |
| CT-2106 [CTI Biopharma] | Polyglutamic acid drug conjugate | | Camptothecin | Colon cancer, ovarian cancer | Phase 1/2 |
| DE-310 [Daiichi Pharmaceutical] | Carboxymethyldextran polyalcohol drug conjugate | | DX-8951 (camptothecin derivate) | Solid tumors | Phase 1 |
| Delimotecan (Men 4901/T-0128) | Carboxymethyldextran drug conjugate | | T-2513 (camptothecin analogue) | Solid tumors | Phase 1 |
| DOX-OXD (AD-70) | Dextran drug conjugate | | Doxorubicin | Solid tumors | Phase 1 |
| MAG-CPT (PNU166148/Mureletecan) [Pfizer] | HPMA drug conjugate | | Camptothecin | Solid tumors | Phase 1 |
| MTX-HSA | HSA drug conjugate | | Methotrexate | Kidney cancer | Phase 2 |
| NKTR-102 (Etirinotecan pegol) [Nektar] | PEG drug conjugate | | Irinotecan | Breast cancer, ovarian cancer, colorectal cancer | Phase 3 |
| NKTR-105 [Nektar] | PEG drug conjugate | | Docetaxel | Solid tumors, ovarian cancer | Phase 1/2 |
| Pegamotecan (EZ-246) [Enzon] | PEG drug conjugate | | Camptothecin | Gastric cancer | Phase 2 |
| PegAsys [Genentech]/PegIntron [Merck] | PEG protein conjugate | | IFNα2a/-IFNα2b | Melanoma, leukemia | Phase 2 |
| PEG-SN38 (EZN-2208) [Belrose Pharma/Enzon] | PEG drug conjugate | | SN38 (irinotecan derivate) | Solid tumors, breast cancer, lymphoma, colorectal cancer | Phase 2 |
| PK1 (FCE28068) [UK Cancer Research/Pfizer] | HPMA drug conjugate | | Doxorubicin | Breast cancer, lung cancer, colorectal | Phase 2 |
| PK2 (FCE28069) [UK Cancer Research/Pfizer] | HPMA drug conjugate | Galactosamine (lectin) | Doxorubicin | Hepatocellular carcinoma | Phase 2 |
| PNU166945 [Pfizer] | HPMA drug conjugate | | Paclitaxel | Solid tumors | Phase 1 |
| ProLindac (AP5346) | HPMA drug conjugate | | DACH-oxaliplatin | Ovarian cancer | Phase 2 |
| Taxoprexin [Protarga] | Docosahexaenoic acid drug conjugate | | Paclitaxel | Melanoma, liver cancer, adenocarcinoma, kidney cancer, non-small-cell lung cancer | Phase 2/3 |
| XMT-1001 [Mersana] | Fleximer drug conjugate | | Camptothecin | Gastric cancer, lung cancer | Phase 1 |
| Xyotax, Opaxio (CT-2103) [Cell Therapeutics] | Polyglutamic acid (polyglumex) drug conjugate | | Paclitaxel | Lung cancer, ovarian cancer | Phase 3 |

Abbreviation for Table 1.2: Poly(N-(2-Hydroxypropyl)methacrylamide) (HPMA); Human serum albumin (HSA); Poly(ethylene glycol) (PEG); poly-1-hydroxymethylethylene hydroxymethylformal (Fleximer).

**Table 1.3.** Polymer-based nanocarriers in clinical trials [4].

| Product [company] | Polymer | Ligand (target) | Drug | Indication | Status |
|---|---|---|---|---|---|
| ABI-008 [Abraxis/Celgene] | Albumin nanoparticle | | Docetaxel | Metastatic breast cancer, prostate cancer | Phase 2 |
| ABI-009 [Abraxis/Celgene] | Albumin nanoparticle | | Rapamycin | Solid tumors, bladder cancer | Phase 1/2 |
| ABI-011 [Abraxis/Celgene] | Albumin nanoparticle | | Thiocolchicine dimer | Solid tumors, lymphoma | Phase 1/2 |
| BIND-014 [Bind Therapeutics] | PEG-PLGA polymeric nanoparticle | Aptamer (PSMA) | Docetaxel | Non-small-cell lung cancer, prostate cancer | Phase 1/2 |
| CALAA-01 [Calando Pharmaceuticals] | Cyclodextrin polymeric nanoparticle | Transferrin (transferrin receptor) | siRNA targeting ribonucleotide reductase subunit 2 | Solid tumors | Phase 1 |
| CRLX-101 (IT-101) [Cerulean Pharma] | Cyclodextrin nanoparticle | | Camptothecin | Solid tumors, renal cell carcinoma, rectal cancer, non-small-cell lung cancer | Phase 1/2 |
| DHAD-PBCA-NP | Polybutylcyanacrylate nanoparticles | | Mitoxantrone | Hepatocellular carcinoma | Phase 2 |
| Docetaxel-PNP [Samyang Biopharmaceuticals] | PEG-PLA/taxane polymeric nanoparticle | | Docetaxel | Solid tumors | Phase 1 |
| Lipotecan (TLC388) [Taiwan Liposome] | Liposome with polylactone | | TLC388 (Camptothecin derivate) | Liver cancer, renal cancer | Phase 1/2 (orphan drug status) |
| Nanoxel [Fresenius Kabi Oncology] | Poly (N-isopropyl acrylamide-co-vinylpyrrolidone ) nanoparticle | | Paclitaxel | Advanced breast cancer | Phase 1 |
| NC-4016 [NanoCarrier] | Diaminocyclohexane polymer | | Oxaliplatin | Solid tumors, lymphoma | Phase 1 |
| NC-6004 (Nanoplatin) [NanoCarrier] | PEG-PGA polymeric micelle | | Cisplatin | Pancreas cancer | Phase 2/3 |
| NC-6300 (K-912) [NanoCarrier] | PEG-polyaspartate polymeric micelle | | Epirubicin | Solid tumors | Phase 1 (Japan) |
| NK-012 [Nippon Kayaku] | PEG-PGA polymeric micelle | | SN-38 (active metabolite of irinotecan) | Solid tumors, small cell lung cancer, breast cancer, | Phase 2 |
| NK-105 [NanoCarrier Nippon Kayaku] | PEG-PAA polymeric micelle | | Paclitaxel | Gastric cancer, breast cancer | Phase 2/3 |
| NK-911 [National Cancer Institute Japan/Nippon Kayaku] | PEG-PAA polymeric micelle | | Doxorubicin | Solid tumors | Phase 1 |
| SP1049C [Supratek Pharma] | Pluronic polymeric micelle | | Doxorubicin | Advanced adenocarcinoma | Phase 2/3 |
| Transdrug BA-003 (Livatag) [BioAlliance Pharma] | Polyisohexylcyanoacrylate nanoparticle | | Doxorubicin | Hepatocellular carcinoma | Phase 3 (2004 EU orphan drug status) |

**Table 1.4**. Inorganic nanocarrier under clinical trial [1].

| Product [company] | Platform | Ligand (target) | Application | Indication | Status |
|---|---|---|---|---|---|
| Aurimune (CYT-6091) CytImmune Sciences] | Colloidal gold | | Tumor necrosis factor delivery | Solid tumors | Phase 1/2 |
| AuroLase [Nanospectra] | Gold-coated silica nanoparticle | | Photothermal ablation | Head and neck cancer | Phase 1 |
| Ferumoxtran-10 (Sinerem/Combidex) [Guerbet/AMAG] | Iron oxide nanoparticle | | Magnetic resonance imaging | Prostate cancer | Phase 3 |
| Ferumoxytol (Feraheme) [MD Anderson/AMAG] | Iron oxide nanoparticle | | Magnetic resonance imaging | Head and neck cancer, lymph node cancer | Phase 1 |
| NanoXray (NBTXR3) [Nanobiotix] | Hafnium oxide nanoparticle | | Radiotherapy | Solid tumors | Phase 1 |
| Targeted SNP [Memorial Sloan Kettering Cancer Center] | Silica nanoparticle | cRGDY (integrin) | Lymph node imaging | Head and neck melanoma | Phase 0 |

**Table 1.5.** Novel polymeric nanoparticles in experimental stages [5].

| Polymer | Method | Physicochemical Characteristics (size, ζ-potential) | Stimuli | Drug/Disease |
|---|---|---|---|---|
| pullulan–DOX | dialysis | $<$100 nm, 25 mV | pH (hydrazone bond) | doxorubicin/cancer |
| chimeric polypeptides–DOX | spontaneous self-assembly | 42 nm | pH (hydrazone bond) | doxorubicin/cancer |
| poly(2-tetrahydropyranyl methacrylate) | emulsification solvent evaporation (o/w) | 314 nm, 21 mV | pH (acetal bond) | paclitaxel/cancer |
| poly(ethylene oxide)–poly(β-amino ester) | nanoprecipitation | 150–200 nm, 40 mV | pH (dissolution mechanism) | paclitaxel/cancer |
| poly(ethylenimine)–poly(methacryloyl sulfadimethoxine) (PSD)-*block*-PEG | self-assembly (electrostatic attraction) | 300 nm, ~0 mV | pH (sulfonamide group) | DNA/cancer |
| poly(ethylene glycol)–poly(L-histidine)–poly(L-lactide) | dialysis | 803 nm[a] | pH (imidazole group) | doxorubicin/cancer |
| chitosan–histidine–arginine | spontaneous self-assembly | 105 nm, 34 mV | pH (imidazole group) | DNA/cancer |
| (5-methyl-2-(2,4,6-trimethoxyphenyl)-[1,3]-5- dioxanylmethyl methacrylate) and (1,4-*O*-methacryloylhydroquinone) | mini-emulsion polymerization | 20–100 nm | pH (acetal bond) | paclitaxel/cancer |
| Ac-dextran-*g*-poly(oligoethylene glycol) methyl ether methacrylate | RAFT polymerization, self-assembly | 90 nm | pH (acetal bond) | doxorubicin/cancer |
| PEG–aldehyde functionalized dextran–DOX | self-assembly | 100 nm | pH (imine bonds) | doxorubicin/cancer |
| poly(oligoethylene glycol) methyl ether acrylate | RAFT polymerization, self-assembly | 10–20 nm | pH (imine bonds) | doxorubicin/cancer |
| poly(oligoethylene glycol) methyl ether acrylate | RAFT polymerization, self-assembly | 14 nm | pH (imine bonds) | Hsp 90 inhibitor/cancer |
| poly(oligoethylene methoxy acrylate) modified with NO donor molecules | RAFT polymerization, self-assembly | 32 nm, 3 mV | pH | NO/anti-biofilm activity |
| poly(acrylic acid-*co*-stearyl acylate) and poly(ethylene glycol) | dialysis | 100 nm | pH (carboxylic group) | indomethacin/anti-inflammatory |
| poly(lactic-*co*-glycolic acid) and Eudragit S-100 | emulsification solvent diffusion | 250 nm, 3.0 mV | pH (dissolution mechanism) | tenofovir/anti-HIV transmission |
| poly(ethylenimine)–pluronic F-127 | emulsification solvent evaporation (o/w) | 330 nm,[b] 11.7 mV[b] | temperature (hypothermia) | siRNA/cancer |
| poly(*N*,*N*-diethylacrylamide-*co* acrylamide)-*block*-poly(γ-benzyl-L-glutamate) | dialysis | 129 nm | temperature (hyperthermia) | paclitaxel/cancer |
| trimethyl chitosan-*g*-poly(*N*-isopropylacrylamide) | self-assembly (electrostatic attraction) | 200 nm,[c] ~0–5 mV[c] | temperature | DNA/cancer |
| poly(3,4-dihydroxycinnamic acid-*co*-4-hydroxycinnamic acid) | self-assembly (solvent mixing) | 420 nm[d] | light (photo-cross-linking, cleavage) | –/– |
| quinone-methide backbone-diamine spacer 4,5-dimethoxy-2-nitrobenzyl alcohol | emulsification solvent evaporation (o/w) | 170 nm | light (self-immolative system) | –/– |
| *o*-nitrobenzyl/methacrylate-functionalized poly(ethylenimine) | radical polymerization | 160 nm | light (photolytic degradation) | DNA/cancer |
| chitosan hydrochloride 4-oxo-4-(pyren-4-ylmethoxy)butanoic acid | self-assembly (electrostatic attraction) | 100 nm[e] | light (photolytic disassembly) | –/– |
| 4′-azobenzene dibenzoyl chloride/triethanolamine | dendrimer grafted nanosilica templates | 20–100 nm | light (*trans*/*cis* isomerization) | –/– |
| 2-nitrophenylethylene glycol/diamine | emulsification solvent evaporation (o/w) | 217–358 nm | light (photolytic degradation) | tagalsin G/cancer |
| poly(ethylene glycol)-*b*-poly(lactic acid) | emulsification solvent evaporation (o/w) | 374 nm[f] | redox (disulfide bond) | paclitaxel/cancer |
| poly(acrylamide)–poly(methacrylamide)–*N*,*N*′-bis-(acryloyl)cystamine | interfacial polymerization | 11.3 nm, 3.6–4.7 mV | redox (disulfide bond) | caspase-3/cancer |
| dimethylaminoethyl methacrylate/*N*,*N*-bis-(acryloyl)cystamine | RAFT polymerization, self-assembly | 35 nm, 29 mV | redox (disulfide bond) | siRNA/cancer |

### *1.2 Endocytosis of nanomedicine*

#### *1.2.1 General endocytosis pathway of polymeric delivery vehicles*

Small molecules such as ions, amino acids and oligosaccharide can directly enter cells through the membrane protein pumps or channels [6], driven by the transmembrane concentration gradient of the solute. On the other hand, macromolecules and nano-delivery vehicles must be internalized via endocytosis which involves the specific interaction with surface receptors on plasma membrane, the formation of membrane-bound vesicles and the consumption of ATP [7].

Endocytosis, the common pathway for the internalization of extracellular substances, can be divided in two major categories [8]: phagocytosis and pinocytosis. Phagocytosis occurs for the engulfment of nutrient, pathogens and cell debris, and is achieved by membrane-bound vacuoles known as phagosomes [9]. Phagocytosis is central to tissue homeostasis and immunity, and is restricted to some specialized cells such as macrophages, monocytes and neutrophils, etc. Pinocytosis is common in all cells in which the transportation of cargo is mediated by high-affinity receptors. The cargo first binds with the receptors on the surface of cells, which produces a localized decrease in the Gibbs free energy, and induces the plasma membrane to wrap around the cargo to form a closed-vesicle structure [8]. The vesicle eventually buds off the plasma membrane and fuses with endosomes and lysosomes [7]. The pinocytic pathway is classified into: macropinocytosis, clathrin-mediated endocytosis, caveolae-mediated endocytosis and clathrin- and caveolae-independent endocytosis, as suggested in Figure 1.2. The particular pathway that should be followed is driven by the physical, chemical and biological properties of the cargo molecules, as well as the

type of cells. In general, endocytosis plays an important role in the communication between cells and extracellular environment, and impact the intracellular fate of engulfed biomaterials.

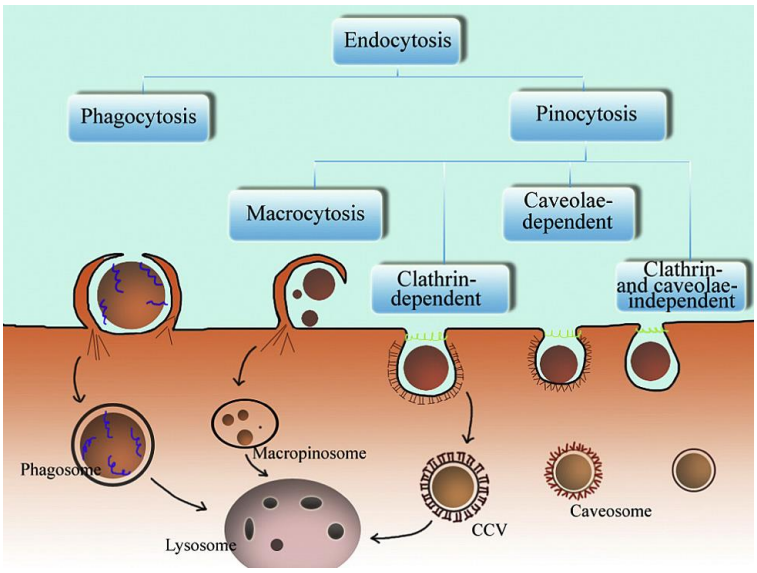


**Figure 1.2.** Schematic illustrations of different endocytosis pathways [10].

### *1.2.2 Clathrin-mediated endocytosis*

In clathrin-mediated endocytosis, a protein named clathrin-1 polymerizes on the cytosolic side of the plasma membrane where the cargo is internalized, and form clathrin coated vesicles that wrap around the cargo. The assembled vesicle (ca.120 nm) is pinched off from the plasma membrane by a small GTPase, dynamin [11]. Various accessory proteins like amphiphysin, Eps15 and intersectin, have been shown to act as scaffolds that connect the endocytic machinery with actin cytoskeleton. Actin defines the spatial regulation and movement of the endocytic vesicle towards the interior of the cells [12]. Within cells the clathrin coated vesicles migrate and fuse with

the early endosomes where they are sorted to late endosomes or lysosomes, to trans-Golgi network or to the recycling endosomes to be transported back to plasma membrane. Clathrin-mediated endocytosis is the most common pathway for the entry of nanoparticles. For example, poly(ethylene glycol-co-lactide) (PEG-co-PLA) nanoparticles with average diameter of 100 nm by HeLa cervical cancer cells [10], cationic chitosan nanoparticles (ca. 360 nm) by human lung carcinoma A549 cells [13], mesoporous silica nanoparticles (ca.110 nm) by human mesenchymal stem cells and fibroblasts [14], the entrance of above nanoparticles are all dependent on clathrin-mediated endocytosis.

### *1.2.3 Caveolae-mediated endocytosis*

Caveolae are abundant in muscle, endothelial cells, fibroblasts and adipocytes and absent in neurons and leukocytes. The definitive characteristic of caveolae is the presence of the hairpin-like membrane protein, caveolin. There are three isoforms of caveolin in mammalian cells. Caveolin-3 is muscle specific, while caveolin-1 and -2 are abundant in most non-muscle cells (such as endothelial cells, fibroblasts and adipocytes) and absent in neurons and leukocytes [8]. The binding of cargo molecules with surface receptors induces the formation of flask-shaped structure (60–80 nm) coated with caveolin [15], which is recognized as the hallmark for caveolae-mediated endocytosis. Other components of the caveolae endocytic machinery include proteins like cavin, which induces membrane curvature, dynamin, which enables vesicle scission, as well as vesicle-associated membrane protein (VAMP2) and synaptosome-associated protein (SNAP), which mediate subsequent vesicle fusion, etc [16]. After

budding off the plasma membrane, the caveolae vesicles transport and fuse with caveosomes or multivesicular body [15]. Caveolae-mediated endocytosis is involved in the internalization of several pathogens including Simian virus 40 and cholera toxin, and is reported to bypass the fusion with endolysosomes to prevent degradation of the pathogens [17]. In addition, polymeric nanoparticles were also reported to be internalized by cells via caveolae pathway. Poly(3-aminopropyl)siolxane nanoparticles modified with stearic acid and galactose were shown to selectively target caveolae in human aortic endothelial cells [18]. DOXIL®, a PEGylated liposomes loaded with doxorubicin, utilize caveolae-mediated endocytosis to enter human ovarian cancer cells [19].

### *1.2.4 Macropinocytosis*

Macropinocytosis is initiated by transient activation of receptor tyrosine kinases induced by growth factors. The receptor activation mediates a signaling cascade that leads to changes in the actin cytoskeleton and triggers formation of membrane ruffles [20]. These membrane ruffles protrude to engulf the surrounding fluid and nutrients in the extracellular environment. They can simply fuse with the plasma membrane or form an intracellular vacuole, termed as a macropinosome [21]. The macropinosomes are larger (0.5–10 μm) and distinct from other vesicles formed during pinocytosis. Many particles like bacteria, apoptotic bodies, necrotic cells and viruses can induce the ruffling behavior independently of the growth factors, and internalize in macropinosomes [20]. In macrophages, after pinching off from plasma membrane, macropinosomes fuse with lysosomes [22]. In contrast, in human A431 epidermoid

carcinoma cells, the macropinosomes travel back to the plasma membrane and release the cargos extracellularly [22]. The fate of engulfed cargos by macropinocytosis is highly dependent on cell types. Macropinocytosis was reported [23] to contribute to cellular entry of plasmid DNA complexed to polyhisidine and polylysine. Submicron-sized and greater particles [24], such as PLGA microparticles and polystyrene microparticles, are generally known to internalize the cells via macropinocytosis. However; most of the literature reported the nanoparticles undergo cellular internalization via more than one endocytic pathway. For example, Zhang et al. [25] reported nanoparticles from a core of albumin and a lecithin corona, were internalized by BT-474 human ductal carcinoma cells through both clathrin-dependent pinocytosis and macropinocytosis. The complexity of endocytic transport requires multiple quantitative techniques to elucidate the pathways involved.

### *1.2.5 CD44-mediated endocytosis*

CD44 is a cell surface glycoprotein that serves as the endocytic receptor for hyaluronic acid in keratinocytes, chondrocytes, and breast cancer cells [26]. Hyaluronic acid (HA) is a non-sulfated linear glycosaminoglycan composed of multiple copies of the disaccharide unit of D-glucuronic acid and N-acetyl-D-glucosamine. In addition to being one of the major component of extracellular matrix, HA is known to participate in a variety of physiological and pathophysiological processes, including tumor metastasis, wound healing and leukocyte extravasation at sides of inflammation, etc. [27] Internalization of HA through CD44 mediated endocytosis has been shown to require acylation of the CD44 cytoplasmic tail [26]. Palmitoylation of CD44 on two

cysteine residues, Cys286 in the transmembrane domain and Cys295 in the cytoplasmic domain, was found to be essential for lipid raft association [28], which further facilitated the internalization of HA.

CD44 is endogenously expressed at low levels on various cell types in normal tissues, but it requires activation before it can bind to HA. Importantly, the minimal size of HA fragments binding to CD44 are six monosaccharide units(HA6) [27]. Activated CD44 is overexpressed in solid tumors, but much less, or not at all on their non-tumorigenic counterparts [29]. Targeting HA-CD44 receptor interactions on tumor cells may identify promising therapeutic approaches in cancer treatment [29]. HA has also been formulated into a series of nano-features for biomedical application [30], such as polymeric nanoparticles from HA-modified poly(lactic-co-glycolic acid)(PLGA), HA-modified polycaroplactone (PCL) or HA-modified Poly(n-butyl cyanoacrylate) (PBCA); liposomes with HA surface coating; polymeric micelles from HA-grafted-5β-cholanic acid, HA grafted deoxycholic acid (DOCA) and HA grafted polyethyleneimine (PEI), HA grafted poly(histidine) (PHis) and d-α-tocopheryl polyethylene glycol 2000 succinate (TPGS2k), mulberry-like dual-drug complicated nanocarriers (MLDC) from hyaluronic acid nanoparticles, etc. As summarized in Table 1.6, HA based biomaterials have been reported as various delivery vehicles [31] for the tumor-targeting delivery of chemotherapeutics such as doxorubicin, epirubicin, paclitaxel, mitomycin, etc.

**Table 1.6**. HA based anti-tumor drug delivery systems [30].

| Type | HA constituents | Drug(s) | Administration route | Disease (site of growth) | Application | Tumor model |
|---|---|---|---|---|---|---|
| Micelles | HA-PHis/TPGS2k | doxorubicin | i.v. | Breast cancer (s.c.) | Imaging | MCF-7/ADR |
| Micelles | HA-ss-DOCA | paclitaxel | i.v. | Breast cancer (s.c.) | Imaging, antitumor effect, toxicity | MDA-MB-231 |
| Micelles | HA-ss-(OA-g-bPEI) | paclitaxel, AURKA siRNA | i.v. | Breast cancer (s.c.) | Imaging, antitumor effect | MDA-MB-231 |
| Micelles | HA-5β-cholanic acid | paclitaxel | i.v. | Squamous cell carcinoma (s.c.) | Antitumor effect | SCC7 |
| Micelles | FA-HA-C18 | paclitaxel | i.v. | Breast cancer (s.c.) | Pharmacokinetics, biodistribution | MCF-7 |
| Micelles | HA/ATRA-PEI | ATRA | i.v. | Colon cancer (s.c.) | Antitumor effect/immunomodulator | CT-26, HCT-8 |
| Micelles | MLDC | doxorubicin, ApoG2 | i.v. | Prostatic cancer (s.c.) | Biodistribution, antitumor effect | PC-3 |
| Liposomes | HA, phospholipids, cholesterol | mitomycin | i.v. | Different human models in mice | Toxicity, pharmacokinetics, biodistribution, antitumor effect | Different cancer cell lines |
| Liposomes | HA, phospholipids, cholesterol | doxorubicin | i.v. | Different human models in mice | Pharmacokinetics, biodistribution | Different cancer cell lines |
| Liposomes | HA-ceramide, phospholipids, cholesterol | doxorubicin -Magnevist | i.v. | Breast cancer (s.c.) | Imaging, pharmacokinetic | MDA-MB-231 |
| Polymeric nanoparticles | HA-PLGA | docetaxel | i.v. | Breast cancer (s.c.) | Pharmacokinetics, biodistribution, antitumor effect | MDA-MB-231 |
| Polymeric nanoparticles | HA-PEG-PLGA | doxorubicin | i.v. | Ehrlich ascites tumor (s.c.) | Toxicity, biodistribution, antitumor effect | EAT |
| Polymeric nanoparticles | HA-PEG-PCL | doxorubicin | i.v. | Ehrlich ascites tumor (s.c.) | Toxicity, biodistribution, antitumor effect | EAT |
| Polymeric nanoparticles | HA-PEG-PLGA | 5fluorouracil | i.v. | Ehrlich ascites tumor (i.p. | Toxicity, biodistribution, antitumor effect | EAT |
| Polymeric nanoparticles | HA-ss-PLGA | doxorubicin | i.v. | Breast cancer (s.c.) | Biodistribution | MDA-MB-231 |
| Polymeric nanoparticles | HA-ss-PLGA | doxorubicin, cyclopamine | i.p. | Breast cancer (s.c.) | Antitumor effect | MDA-MB-231 |
| Polymeric nanoparticles | HA-PCL | doxorubicin | i.v. | Squamous cell carcinoma (s.c.) | Biodistribution, antitumor effect | SCC7 |
| Polymeric nanoparticles | HA-PBCA | paclitaxel | i.v. | Sarcoma (s.c.) | Antitumor effect | S-180 |

### *1.2.6 Pathways for endosomal escape*

The sequestration of engulfed nanoparticles in endolysosomes result in bottleneck for the intracellular release of payloads as well as the fulfillment of the biological functions of the payloads. Techniques to achieve endosomal escape of internalized cargos have major impact on non-viral delivery systems for nucleic acid and proteins. The major mechanisms for sequestered cargos to escape endosomes are suggested in Figure 1.3.

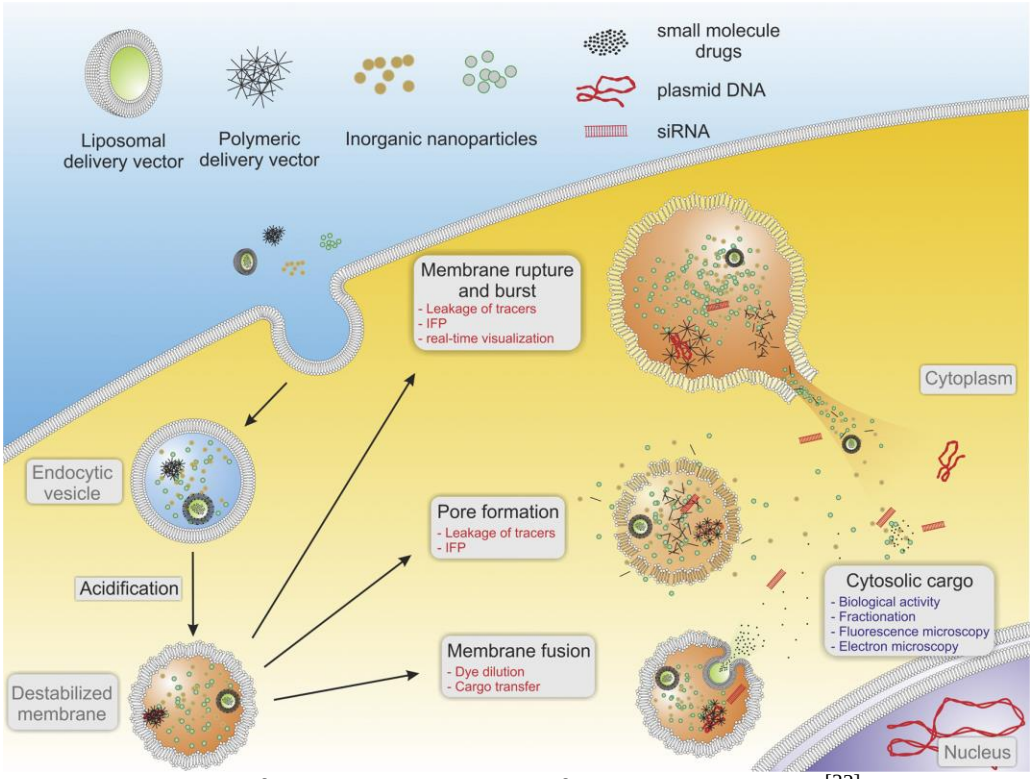


**Figure 1.3**. Pathways for endosomal escape of sequestered cargos [32].

*Flip-flop and pore formation*. The outer layers of endosomal membranes are composed of phospholipids with negative charge, the interaction between cationic cargos with the endosomal membrane is thought to induce a ‘‘flip-flop’’ mechanism [33], where anionic phospholipids from the cytosolic side will flip to the intraluminal side on the endosomal membrane. This charge-neutralized ion pair will result in non-lamellar phase changes and subsequent membrane destabilization [33]. The cationic charge can result from quaternary amine groups, such as cationic lipid 1,2-dioleyl-3-trimethylammonium-propane (DOTAP), or protonable amine groups from polymers such as poly(ethylene imine) (PEI), poly(L-lysine) (PLL) and chitosan. In the case of endosomal destabilizing peptide, pore formation is another mechanism [32]. GALA

peptide [34], which contains 30 amino acids, with glutamic acid-alanine-leucine-alanine repeating units and histidine, undergoes a pH-dependent conformational change to give a helical structure at acidic endosomal environment. Li et al. [34] proposed that GALA becomes incorporated into the vesicle bilayer and aggregates to form a pore with diameter ranges from 5 to 10 Å, which results in the leakage of endosomal content.

*Membrane fusion*. This mechanism highlighted the fusion of the membrane of cargos with the membrane of endosomes. For example, haemagglutin subunit (HA2) of influenza virus, is responsible for facilitating membrane fusion [35]. The C-terminal end is embedded in the viral membrane whereas the N-terminal end contains a fusion peptide with a sequence of hydrophobic amino acids. Once inside the endosomes, HA2 undergoes conformation change in response to the low pH environment and exposes the highly conserved hydrophobic region. Subsequently, this triggers the fusion of viral membrane with the endosomal membrane, leading to the leakage of viral genome to cytosol [35].

*Endosome rupture*. "proton sponge effect'', which is based on cationic polymers or lipids with excess uncharged protonable amine groups that can buffer endosomal acidification by absorbing protons in the endolysosomal compartment [36]. As long as ATP is present in the cytosol, ATPases will keep pumping protons against their electrochemical gradient across the endolysosomal membrane, with an associated influx of counterions to balance the transmembrane voltage difference [32]. The osmotic swelling leads to the rupture of endolysosomal membrane, followed by the subsequent release of cargos into cytosol.

Table 1.7 summarized the current non-viral delivery vehicles functionalized with the above modalities for endosomal escape. The cationic charges, fusogenic functional groups have been introduced to cholesterol lipids including DOPE (1,2-dioleoyl-sn-glycero-3- phosphoethanolamine), DOTAP (1,2-dioleyl-3-trimethylammonium-propane) and GAP-DMORIE (N-(3-aminopropyl)-N, N-dimethyl-2,3-bis(cis-9-tetradecenyloxy)-1-propanaminium bromide); PEG-PEI (polyethylene glycol-polyehtylenimine), poloxamer or polysaccharide based Nanocarriers. These delivery systems for nucleic acid have been in the process of clinical evaluations [37]. In addition to the aforementioned mechanisms, endosome rupture can also be achieved by photochemical internalization (PCI) technique, which will be discussed in details in the following section.

**Table 1.7.** Non-viral gene delivery vehicles with endosomal escape modalities under clinical evaluation [37].

| Delivery system | Gene therapy drug | Sponsor | Indications | Phase | Status |
|---|---|---|---|---|---|
| DOTAP–cholesterol | DOTAP–Chol-fus1 | MD Anderson Cancer Center | Non-small-cell lung cancer | I | Completed |
| | | | | I/II | Active |
| GAP-DMORIE–DPyPE | Tetravalent dengue vaccine | US Army Medical Research and Materiel Command | Dengue disease vaccine | I | Active |
| GL67A–DOPE–DMPE–PEG | pGM169/GL67A | Imperial College London | Cystic fibrosis | II | Active |
| PEI | BC-819/PEI | BioCancell Ltd. | Bladder cancer | II | Active |
| | BC-819 | BioCancell Ltd. | Ovarian cancer | I/II | Completed |
| | DTA-H19 | BioCancell Ltd. | Pancreatic cancer | I/II | Completed |
| | SNS01-T | Senesco Technologies, Inc. | Multiple myeloma and B cell lymphoma | I/II | Recruiting |
| | CYL-02 | University Hospital, Toulouse | Pancreatic ductal adenocarcinoma | I | Completed |
| PEG–PEI–cholesterol | EGEN-001 | Gynecologic Oncology Group | Ovarian, tubal and peritoneal cancers | I | Recruiting |
| | | | | II | Active |
| | EGEN-001-301 | EGEN, Inc. | Colorectal peritoneal cancer | I/II | Recruiting |
| PEI–mannose–dextrose | DermaVir/LC002 | Genetic Immunity | HIV vaccine | II | Active |
| Poloxamer CRL1005–benzalkonium chloride | ASP0113 | Astellas Pharma Inc. | CMV vaccine | III | Recruiting |
| | | | | II | Recruiting |
| | VCL-CB01 | Astellas Pharma Inc. | CMV vaccine | II | Completed |

### *1.3 Photochemical internalization (PCI) and photodynamic therapy (PDT)*

#### *1.3.1 Photosensitizing reaction*

Photosensitizers are molecules in which photosensitizing reaction occurs when activated by light irradiation. The photosensitizer is excited by absorption of photons with appropriate wavelength, and reaches the first excited singlet state. The deactivation of photosensitizer in singlet state via an intersystem crossing leads to the excited triplet state [38]. The lifetime of the triplet state is relatively long so that the excited photosensitizer has enough time to encounter other molecules and lead to two types of photosensitizing reactions [38], as illustrated in Figure 1.4. Firstly, the triplet photosensitizer can react directly with a substrate to form free radicals by transfer of a proton or an electron (type-1 reaction) [39]. These radicals can further interact with oxygen and form reactive oxygen species (ROS). Secondly, the triplet photosensitizer

can also transfer its energy directly to molecular oxygen, to form excited singlet oxygen (type-2 reaction) [39]. The production of singlet oxygen or ROS is considered to be a key factor to evaluating the efficacy of photosensitizing reactions.

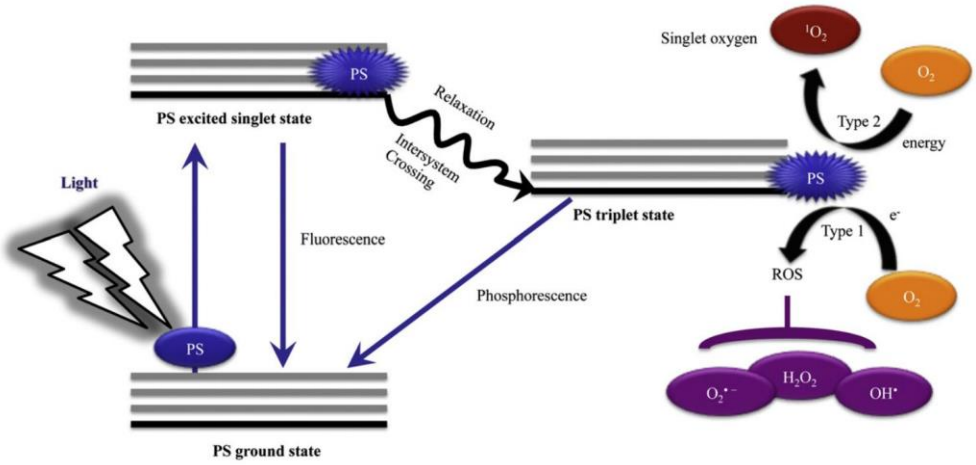


**Figure 1.4**. Schematic illustration of photosensizting reactions [39].

### *1.3.2 Photosensitizers for photodynamic therapy (PDT)*

Photodynamic therapy (PDT), a photosensitizer-based anti-tumor treatment, enables the localized therapeutic effect by the application of light, and provides a promising strategy as an alternative and complementary modality for the conventional chemotherapy [40]. In PDT, the administration of photosensitizers is followed by the application of light irradiation to the tumor site. Upon irradiation, photosensitizers generate ROS and singlet oxygen via photon-induced energy transfer, and anti-tumor effect is achieved via the direct inhibition of tumor cells, vasculature damage in tumor tissues, and enhancement of host immune process in response to PDT. The PDT efficacy is attributed to the chemical structures of the photosensitizers. Figure 1.5

shows the basic structure of the most commonly studied photosensitizers for PDT: porphyrin, chlorin, bacteriochlorin and phthalocyanine. The PDT photosensitizers are usually planar and aromatic. The core structure is called "macrocycle" which is composed of four pyrroles linked by azone bridges in the case of phthalocyanine or by methine bridges for the others [41]. The extensive aromatic structure (i.e. π-conjugation) enables photosensitizers to absorb light in the visible region of light spectrum. The absorption spectra among these compounds are similar with a strong peak at around 400 nm called Soret band and other weaker bands between 600 nm and 800 nm called Q-bands [42]. The extended π-conjugation in these molecules results in lower electronic repulsion and therefore lowers the energy of the molecular states involved. A lower transition energy (ΔE) results in longer absorption wavelength. As a result, the maximum absorption of porphyrin is around 630 nm, shorter than the peak absorption of chlorin at 650 nm and phthalocyanine at 670 nm [41].

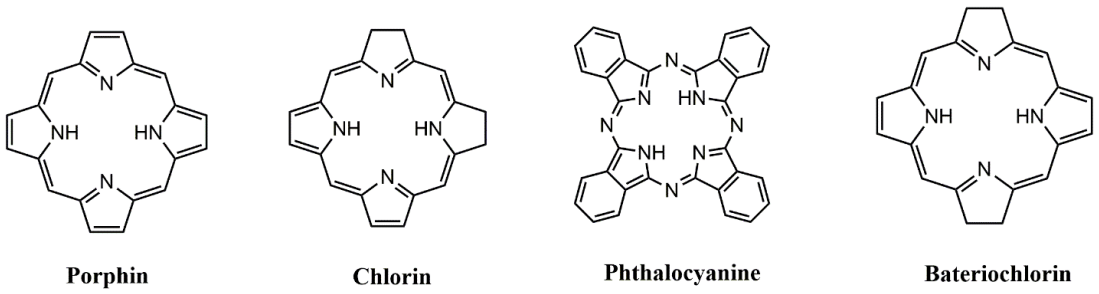


**Figure 1.5.** Common photosensitizers for photodynamic therapy.

### *1.3.3 Challenges for PDT photosensitizers*

A good photosensitizer should absorb photons efficiently, have a high quantum yield of triplet formation, and the triplet state should exhibit enough lifetime to react with neighboring target molecules such as molecular oxygen [42]. However,

aggregation is a common phenomenon for most chlorin and phthalocyanine based PDT-photosensitizer. The fluorescence and the singlet oxygen quantum yields of aggregated species are lower than those of monomeric form [43]. Aggregation of the photosensitizer reduce the probability of the photosensitizer to undergo intersystem crossing, and most of the energy in the excited state will be dissipated through non-radiative decay, producing only heat [44]. Even dimers of some photosensitizers could be photochemically inactive [43]. In addition, the formation of large-scale aggregates upon systemic injection of hydrophobic photosensitizer may considerably modify their pharmacokinetics as compared to monomer forms [45], and hence impact the PDT efficacy. Binding of photosensitizers to proteins, other macromolecules or nano-delivery vehicle, are reported [46] to increase the lifetime of the triplet state, enhance the monomerization of aggregated species, and improve the efficacy of PDT.

### *1.3.4 Nano-delivery vehicles for PDT*

Due to the minimized toxicity of photosensitizer in the absence of light, which reduces the risk of systemic toxicity in normal tissues, PDT provides a promising strategy as an alternative and complementary modality in addition to the conventional chemotherapy. Several PDT photosensitizers [47] such as Photofrin®, Levulan® and Visudyne®, have been clinically approved for the treatment of head and neck cancer, skin cancer, etc. However, there're also several challenges that impact the efficiency of PDT via direct administration of photosensitizers [45]. In addition to aggregation, most PDT photosensitizers are highly hydrophobic and difficult to be incorporated into intravenously deliverable formulations. Due to the lack of tumor selectivity, the

direct administration of PDT photosensitizers can lead to the accumulation of photosensitizers in easily light-exposed normal tissues like the eyes and skin, which in turn result in prolonged phototoxicity and photosensitivity in patients when exposed to ambient light.

The nano-delivery vehicles can provide an effective approach to resolve the challenges associated with intravenous administration and selective delivery of the photosensitizers to tumor tissues [48]. Enhanced tumor-specific delivery [36] can be achieved by nano-delivery vehicles that keep the photosensitizers in circulation for longer periods of time (by preventing renal clearance and non-specific uptake) and allow increased uptake within the tumors via extravasation through the tumor-associated leaky vasculature (the enhanced permeation and retention or EPR effect). Various nanoparticles [45] have been reported for the encapsulation and controlled release of photosensitizers. Table 1.8 summarized the nano-delivery vehicles for PDT photosensitizers that exhibited enhanced PDT efficiency in the inhibition of tumors both in vitro and in vivo.

**Table 1.8.** Studies reported on nanoparticle-based formulation of PDT photosensitizers [45].

| Photosensitizer | NP vehicle | Targeting motif | Cell type |
|---|---|---|---|
| Porphyrin derivatives (hematoporphyrin, porfimer sodium etc.) | PLGA nanoparticles | N/A (passive) | SW480 (human colon cancer) |
| | Polyacrylamide nanoparticles | F3 peptide | 9L (orthotopic rat glioma) |
| | Magnetic chitosan nanoparticles | N/A (passive) | SW480 (xenograft human colon) |
| | Silica nanoparticles | N/A (passive) | HeLa (human colon cancer) |
| | | | HCT 116 (human colon cancer) |
| | | | A549 (human lung cancer) |
| Chlorin derivatives (chlorin e6, mTHPC, pheophorbide etc.) | Human serum albumin nanoparticles | N/A (passive) | HT-29 (human colon cancer) |
| | Chitosan nanoparticles | N/A (passive) | HT-29 (human colon cancer) |
| | Iron oxide nanoparticles | N/A (passive) | MGC-803 (human gastric cancer) |
| | NaYF4:Yb,Er/NaGdF4 nanoparticles | N/A (passive) | U87MG (human glioma) |
| | Hyaluronic acid nanoparticles | Hyaluronic acid targeted to CD44 | HT-29 (human colon cancer) |
| | PLGA nanoparticles | N/A (passive) | Rhabdomyosarcoma (orthotopic) |
| | Polyacrylamide nanoparticles | N/A (passive) | Colon-26 (murine colon cancer) |
| Phthalocyanine derivatives (zinc (II) phthalocyanine, silicon phthalocyanine 4 etc.) | Mesoporous silica nanoparticles | N/A (passive) | H22 (human hepatoma) |
| | Dendrimers | N/A (passive) | A549 (human lung cancer) |
| | Gold nanoparticles | EGF | Gli36 (orthotopic human glioma) |
| Indocyanine green | Calcium phosphosilicate | Anti-CD117 antibody | 32D-p210-GFP (orthotopic murine chronic myeloid leukemia) |
| Methylene blue | Phosphonate-terminated silica nanoparticles | N/A (passive) | HeLa (human cervical cancer) |

### *1.3.5 Photosensitizers for photochemical internalization (PCI)*

Photochemical internalization (PCI), developed by Berg and colleagues [49], is a highly efficient technology which takes advantage of photochemical rupture of endocytic vesicles by light-activated photosensitizers and enables the cytosolic release of therapeutic agents. Different from PDT, PCI helps to further improve the anti-tumor efficacy of other therapeutic agents, instead of the photosensitizers themselves take the lead in the inhibition of tumors.

It was documented that many photosensitizers enter the cells via pinocytosis pathway, and target endolysosomes [50]. However, not all photosensitizers that localized in endolysosomes are suitable as PCI-photosensitizers. In the chemical structure of photosensitizers, the hydrophobic/hydrophilic balance is modulated by the presence of lipophilic and charged side-chains around the macrocycle. The general findings have shown that hydrophobic photosensitizers bearing a few negative charges can enter the cells via receptor-mediated endocytosis and redistribute between the membranes of endolysosomes, while hydrophilic photosensitizers with many positive

or negative charges are too polar to be inserted into the endolysosomal membrane [51]. PCI-photosensitizers are a class of amphiphilic phthalocyanine, porphine or chlorin derivatives, with proper number of polar substitution groups on the macrocycles, that exhibit specific affinity with the membrane of endolysosomes.

Typical PCI photosensitizers include aluminum phthalocyanine disulfonate (AlPcS2a), tetraphenylporphine disulfonate (TPPS2a) and tetraphenylchlorin disulfonate (TPCS2a or Amphinex), and their chemical structures are shown in Figure 1.6. The two sulfonate groups on the macrocycles render the amphiphilic properties of the PCI photosensitizers, and effective endolysosomal rupture upon light irradiation were reported [52]. The activation wavelength is 660 to 670 nm for AlPcS2a, and 430 – 450 nm for both TPPS2a and Amphinex [49]. In this regard, AlPcS2a may be preferable to TPPS2a or Amphinex for in vivo utilization, due to the better penetration depth of red light in tumor tissues.

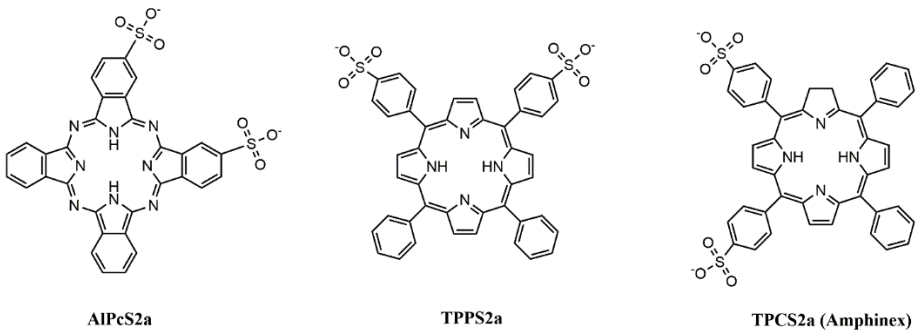


**Figure 1.6.** Chemical structures for typical PCI photosensitizers.

### *1.3.6 PCI-facilitated delivery of macromolecular therapeutics*

Membrane impermeable macromolecular therapeutics are internalized by cells via endocytosis and are usually sequestered in the endocytic vesicles before being

subsequently degraded by the digestive enzymes in lysosomes, hence greatly hinder their therapeutic efficacy. Photochemical rupture of endolysosomal membrane enables the release of such macromolecular therapeutics into cytosol, to further fulfill their biological functions. PCI effect has been demonstrated in >80 different cell lines and >10 different xenograft models of various cancers [51], and improve the delivery and efficacy of the following macromolecular therapeutics.

Gene delivery. PCI has been studied as a tool to facilitate gene delivery both with several non-viral and adenoviral vectors, by using reporter genes [53] such as genes encoding EGFP (enhanced green fluorescent protein) or p53 tumor suppression gene. In an in vivo study by Ndoye et al. [54], mice xenograft with p53-mutated head and neck squamous carcinomas was treated by intratumoral injection of the photosensitizer AlPcS2a and a plasmid encoding p53 complexed to a glycosylated polyethyleneimine, which resulted in dramatic tumor regression in all the transfected animals. Mice receiving plasmid DNA alone (without PCI) or receiving PCI treatment but not plasmid didn't exhibit any delay in tumor growth, which suggest that PCI-facilitated enhancement of gene delivery was essential to achieve good therapeutic effect.

Protein and peptide. Bleomycin is a water-soluble glycopeptidic antibiotic (1.4 kDa) used in a number of cancer chemotherapies, notably squamous carcinomas and malignant lymphomas [55]. As few as 500 bleomycin molecules that translocated to cytosol are sufficient to induce cell death in combination with electroporation in vitro [55]. However, bleomycin penetrates membrane structures poorly and accumulates in endocytic vesicles. Berg et al. [56] demonstrated the in vivo synergistic effect between bleomycin and the PCI effect by AlPcS2a on human squamous carcinoma xenograft

model, in which curative response was observed in 60% of the tumor bearing mice that received PCI of bleomycin, while tumor control was absent in animals receiving bleomycin only. In addition, the preclinical data indicated that PCI of bleomycin in combination with surgery or external-beam radiotherapy on patients is a promising treatment modality that may reduce the need for mutilating surgery or toxic radiation effects, and hence improved local tumor control [51].

Nano-delivery vehicles. Nano-delivery vehicles enter cells via endocytosis. Except ultra-small gold nanoparticles (2-10 nm) [57], which were identified in nucleus and cytoplasm, endolysosomal sequestration and subsequent degradation was inevitable if the nano-carriers are not engineered to escape endolysosomes. PCI also potentiate the intracellular delivery performance of nano-delivery vehicles. Yen et al. [58] reported an augmented anti-tumor efficiency of poly(ethylene glycol)-poly(lysine) (PEG-PLys) micelles conjugated with camptothecin via disulfide linkage, when endolysosomal escape was achieved from the PCI effect of free photosensitizer photofrin. Lu et al. [59] reported PEG-PLys micelles incorporated with zinc phthalocyanine dendrimer that exhibited light-facilitated reversal of doxorubicin resistance in MCF-7/ADR both in vitro and in vivo. The sequestration of cationic doxorubicin hydrochloride in acidic endocytic compartments of MCF-7/ADR cells was reported as one the mechanism for doxorubicin resistance in MCF-7/ADR cells, and the PCI-facilitated cytosolic release bypass the endolysosomal sequestration of doxorubicin, and effectively enhanced the antitumor efficiency compared to the groups treated with doxorubicin but not receiving PCI.

### *1.4 Antigen Cross-presentation and cancer immunotherapy*

#### *1.4.1 Antigen processing and presentation*

Unlike other immune cells, T cells receptor can only recognize antigen in the form of peptide binding with MHC (major histocompatibility complex) molecules on the surface of antigen presenting cells. To be recognized by T cells, protein antigens need to be degraded into peptide intracellularly, and the process is termed as antigen processing [60]. The complex assembled from degraded peptide and MHC molecules are displayed on the surface of antigen presenting cells such as dendritic cells, macrophages, and B cells, etc., and can be recognized by T cells. The process in which the complex of peptide /MHC molecules form, translocate to cell surface and communicating with T cells, is termed as antigen presentation [60]. The major pathways for antigen presentation, including MHC class I presentation and MHC class II presentation, are illustrated in Figure 1.7.

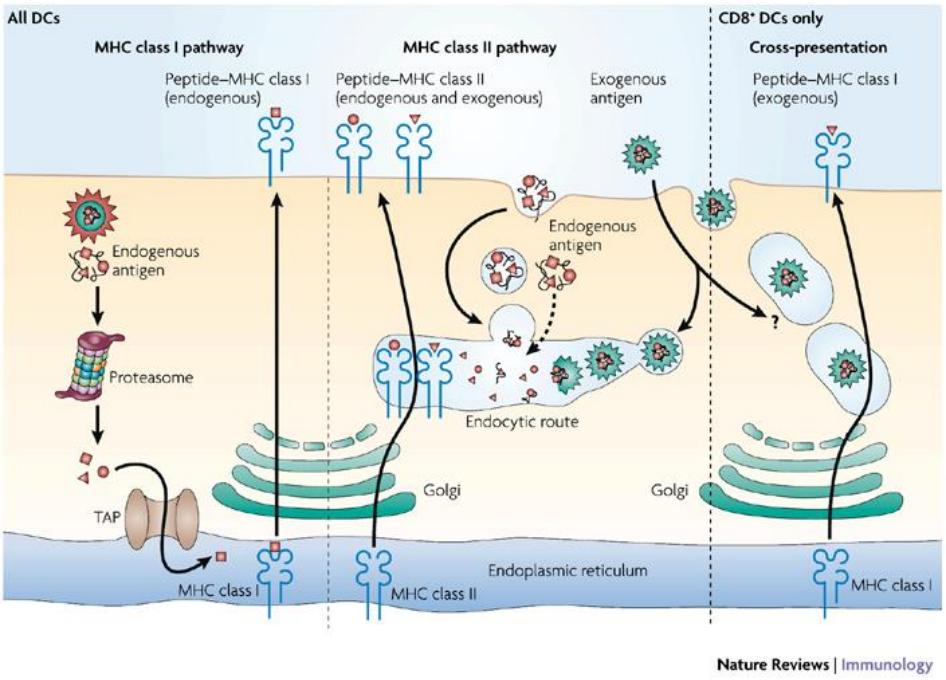


**Figure 1.7.** Pathways for antigen presentation [61].

### *1.4.2. MHC class I and class II pathway*

In MHC class I presentation pathway [62], endogenous protein antigens are degraded into peptides that can be bounded by MHC class I molecules and presented to CD8 T cells. Protein antigens in cytosol are degraded by a large barrel-shaped protein complex called the proteasome, which provide several different protease activities. The proteasome consists of 28 polypeptide subunits, each of 20-30 kDa. Antigenic peptide degraded by proteasome are transported into endoplasmic reticulum by transporter associated with antigen processing (TAP). Meanwhile, MHC class I heavy chains and β2-mircoglobulin are also translocated to the endoplasmic reticulum, where they assembled and bind with the degraded peptide. The peptide-bound MHC class I molecules are released from the endoplasmic reticulum and formed closed-

membrane vesicles before they are transported to the plasma membrane and present to CD8 T cells (killer T cells), the major function of which is to kill cells that have been infected with virus or pathogens.

Alternatively, most exogenous protein antigens are internalized by antigen presenting cells via pinocytosis or phagocytosis and presented by MHC class II pathway [63]. The internalized exogenous protein antigens are sequestered in endocytic vesicles which contains protease and hydrolase, and degraded to produce antigenic peptides. Meanwhile, MHC class II α and β chains are assembled with invariant chain, before they translocate to the endocytic vesicle, bind with the antigenic peptide and dissociated with invariant chain. The peptide-bound MHC class II molecules are delivered to plasma membrane by outgoing vesicles, and present to CD4 T cells (helper T cells), which help other cells in the immune system to respond to infection.

### *1.4.3. Cross-presentation for cell-based cancer immunotherapy*

The protein antigens for the above two are mostly virus-derived protein, infected cell bodies, etc. However, antigen presenting cells are also able to process exogenous antigen protein such as vaccines, by MHC class I pathway, and this presenting process is termed as cross-presentation, and potentiate CD8 T cell response. The cross-presentation of vaccines [64] also involves the endocytosis of the antigen, degradation of the antigen in proteasome, the display of immune complex from the degraded antigenic peptide on the surface of antigen presenting cells, and the communication with CD8 T cells. The cross-presentation implies some connection between class I (degradation of antigen occurs in cytosol, instead of endocytic vesicles) and class II

pathways (endocytosis of exogenous antigen), however, the detailed mechanism and signaling pathways for cross-presentation is still not clearly defined. Cross-presentation enables the induction of cytotoxic immunity by vaccine antigens, and provides rationale for cell-based cancer immunotherapy.

Ovalbumin is the model antigen to study cross-presentation. Cytosolic ovalbumin is degraded in proteasome to produce SIINFEKL peptide (OVA 257-264), SIINFEKL binds with murine MHC class I molecule H-2Kb and elicit cross-presentation and CD8 T cell response [65]. However, ovalbumin in endocytic vesicles is degraded into OVA 323-339 peptide, and the subsequent immune response is restricted to MHC class II pathway [66].

Suppression of immune response is common in tumor local environment [67], and cell-based immunotherapy takes advantage of tumor antigens to elicit CD8 T cell response in vivo. Many studies [68] have demonstrated that the generation of anti-tumor immunity depends on the cross-presentation of tumor antigens by dendritic cells. Studies [69] also suggested that dendritic cells can capture tumor antigens, and cross-present these antigens to T cells in tumor-draining lymph nodes. This results in the generation of tumor-specific CD8 T cells, or cytotoxic lymphocytes (CTLs) that contribute to tumor depletion.

### *1.4.4. Protein/peptide vaccines for cancer immunotherapy*

Epitope peptide and full-length proteins which binds to MHC molecules could have the potential to elicit tumor immunity. However, the immunogenicity of protein/peptide vaccine are usually low, and adjuvants become necessary component,

that functions to activate, mature, and recruit cells of the innate immunity, which in turn provide the stimulatory signals essential for the adaptive immune response to tumor [70]. For example, vaccination using a full-length recombinant MAGE-A3 protein with an immune-stimulant adjuvant GSK (a detoxified derivative of the lipopolysaccharide of the gram negative bacterium salmonella minnesota R595 strain) [71], showed superior induction of humoral and cellular responses in patients with resected non-small cell lung cancer and possibly clinical activity in patients with metastatic melanoma in phase 2 studies. Another novel vaccine design [72], containing a glycosylated Muc1 peptide, and the immuno-adjuvant Pam3CysSk4, a toll-like receptor 2 agonist, induced both humoral and cellular responses to glycosylated Muc1, and reduced tumor growth was observed in a mouse breast tumor model.

Heat shock proteins function as molecular chaperones that assist folding/unfolding and transport of proteins across membranes and prevent protein aggregation after environmental stress [73]. Extracellularly localized and membrane-bound heat shock proteins have been found to play key roles in eliciting antitumor immune responses by acting as carriers for tumor-derived immunogenic peptides, as adjuvants for antigen presentation, or as targets for the innate immune system [74]. The interaction of heat shock proteins with receptors on antigen-presenting cells promotes the maturation of dendritic cells, results in an upregulation of MHC class I and class II molecules, induces secretion of pro- and anti-inflammatory cytokines, chemokines, and immune modulatory nitric oxides, and thus integrates adaptive and innate immune phenomena [75]. Intratumoral delivery of exogenous heat shock protein Hsp70 in a rat glioblastoma model caused a significant inhibition of tumor progression [76], which as

accompanied by an increased cytotoxic activity of NK cells and CD8 T lymphocytes. A comparable therapeutic efficacy was also reported by Rafiee et al. [77] in which a complete tumor eradication following transfection of the hsp70.1 gene sequence into mouse tumor cells.

Other vaccines are also developed including cell-based vaccines [78] and neoantigens [79]. Ex vivo preparation of matured dendritic cells, or gene-modified whole tumor cells for improved immune-activation can also be included in combination with protein/peptide vaccine. In general, clinical efficacy of cancer immunotherapy is still challenged by the following issues [70], such as selection of antigen/epitope for optimal binding to MHC molecules; suitable adjuvant for immunogenicity and improved immunological outcome; presence of regulatory cells that suppress immune activation, etc.

### *1.4.5 Nano-delivery vehicles for protein based tumor vaccine*

Good delivery vehicles for protein based tumor vaccine should 1) mimic the composition and immunological processing of actual pathogens; 2) actively or passively target the antigen presenting cells such as dendritic cells; 3) protect the protein vaccine from premature degradation; 4) induce the maturation of antigen presenting cells and direct the subsequent immune response. Nanoparticle based vaccine delivery system has been developed to overcome limitations that include inherent instability of soluble antigens, low internalization efficiency of soluble antigens, and insufficient cross-presentation to activate CD8 T cells. Nanoparticle based vehicles provided protection against premature degradation of payloads, and

exhibited targeted delivery and sustained release of protein antigens, controllable interaction with antigen presenting cells, and multivalent presentation, etc. The polymeric based nano-delivery systems for various antigens were summarized in Table 1.9, and poly (γ-glutamic acid) (PGA), N-trimethyl chitosan (TMC), poly(lactide-co-glycolide) (PLGA) are most extensively studied polymers as nanocarriers for vaccine delivery.

**Table 1.9**. Polymeric nanocarriers as delivery systems for antigens [80].

| Polymer | Antigen | Model‡ | Response | Route(s) |
|---|---|---|---|---|
| Chitosan/TMC | OVA | BALB/c | IgG | intraduodenally |
| TMC | OVA | BALB/c | IgG | ID |
| TMC | OVA | BALB/c | IgG | IM |
| TMC | OVA | BALB/c | IgG, IgA | IN |
| TMC (+ *LPS/CTB/ $PAM_3CSK_4$/MDP/CpG*) | OVA | BALB/c | IgG, IgA | ID/IN |
| TMC–hyaluronic acid | OVA | BALB/c | IgG | IN/ID |
| TMC | HBsAg | BALB/c | IgG/IgA | IN |
| TMC | DT | BALB/c | IgG | ID |
| TMC | Influenza A subunit H3N2 | C57BL/6 | IgG/IgA | IM/IN |
| TMC-MCC | TT | BALB/c | IgG | IN |
| TMC-alginate | Urease | Kunming mice | IgG/IgA | SC/oral |
| γ-hPGA | Listeriolysin peptide | C57BL/6 | Survival | Rear footpad |
| γ-hPGA | Tax peptide | C3H mice | Cytotoxic T cells | SC |
| γ-hPGA | gp100 peptide | C57BL/6 | IFN-γ | SC |
| γ-hPGA | EphA2 peptide | C57BL/6 | IFN-γ, cytotoxic T cells | IP |
| γ-hPGA | OVA | C57BL/6 | Cytotoxic T cells | SC |
| γ-hPGA | OVA | C57BL/6 | IgG, cytotoxic T cells | Rear footpad |
| γ-hPGA | Influenza HA | BALB/c | IFN-γ, IL-4, IL-6, IgG, cytotoxic T cells | SC |
| γ-hPGA | Influenza HA | BALB/c | IFN-γ, IL-4, IL-6, IgG/IgA | SC/IN |
| PLA | HBsAg | Wistar rats | IFN-γ, IgG | IM |
| PLGA | Allergen Bet v 1 | BALB/c | IFN-γ, IL-10, decreased IgG1 | SC |
| PLGA (+ *7-acyl lipid A*) | TRP-2 peptide | C57BL/6 | $CD8^+$-derived IFN-γ | SC |
| PLGA, PLGA/TMC | OVA | BALB/c | IgG | IM |
| PLGA (+ *7-acyl lipid A*) | OVA | BALB/c | IFN-γ, $CD4^+$, $CD8^+$ T cells | IP/SC |
| PLGA (+ *MPL*) | OVA | BALB/c | IgG, IgA | Orally |
| PLGA (+ *CpG*) | TT | C57BL/6 | IFN-γ, IgG | SC |
| PLGA | *B. pertussis* toxoid and filamentous HA | BALB/c | IFN-γ, IL-5, IgG | IP/orally |

In the study by Shima et al. [81], nanoparticles from amphiphilic poly (γ-glutamic acid)-graft-L-phenylalanine ethyl ester (γ-PGA-Phe) were developed as the delivery vehicles for ovalbumin. By modulating the hydrophobicity (the grafting ratio of

phenylalanine) of the amphiphilic polymer, optimized encapsulation of ovalbumin was achieved and the activation of dendritic cells, as well as the induction of antigen-specific cellular immunity-based immune responses, were also dependent on the chemical/physical properties of the nano-carriers. γ-PGA-Phe nanoparticles with 65% to 71% grafting degree of phenylalanine resulted in optimized encapsulation of ovalbumin, and stimulated maximum level of cellular immunity in dendritic cells, by enhancing the secretion of various cytokines (TNF-α, IL-6, and IL-12, etc). The activated cellular immunity by γ-PGA-Phe (65%-71%) was 30-hold higher than the free antigen. Reddy et al. [82] developed ovalbumin loaded polypropylene sulfide nanoparticles and reported a size-dependent immunity in mice, in which they proved that interstitial flow transported ultra-small nanoparticles (25 nm) highly efficiently into lymphatic capillaries and draining lymph nodes, which was much efficient than greater nanoparticles (100 nm) in targeting the lymph node residing dendritic cells. In addition, the surface functional group also impact the efficiency to induce the maturation of dendritic cells and the activation of subsequent immunity. The 25 nm nanoparticles with polyhydroxylated surface induced significantly enhanced dendritic cell maturation compared to the polymethylated or polycarboxylated counterparts. The effect of vaccination of ovalbumin loaded 25-nm polyhydroxylated nanoparticles was comparable to that of LPS, which is a typical immunogenic effector and ligand for toll-like receptor 4. Shen et al. [83] developed poly(lactide-co-glycolide) (PLGA) nanoparticles encapsulated with ovalbumin which enhanced the cellular uptake of ovalbumin and induced T cell responses. While macropinocytosis of soluble ovalbumin leads to poor MHC class I presentation by dendritic cells, phagocytosis of

ovalbumin-loaded PLGA nanoparticles enhanced cross presentation, leading to potent responses of CD8 T cells. The MHC class I presentation of ovalbumin-loaded PLGA nanoparticles stimulated T cell interleukin-2 secretion at 1000-fold lower concentration than free ovalbumin.

### *1.5 Conclusions*

In the design of polymeric delivery carriers for chemotherapeutics, photosensitizers or vaccines, it is critical to elucidate the intracellular fate and specific interaction between nano-carriers and cells. The cell-vesicles interactions proved rationale for the design of environmental responsive and site-specific delivery system in response to a series of endogenous cues (enzyme, acidic pH, redox potential, etc.) as well as exogenous stimuli (light, temperature, ultrasounds, electric field, etc).

### *References:*


[1] A. Wicki, D. Witzigmann, V. Balasubramanian, J. Huwyler, *J. Controlled Release* **2015**, *200*, 138.

[2] S. Mura, J. Nicolas, P. Couvreur, *Nat. Mater.* **2013**, *12*, 991.

[3] A service of the U.S. National Institutes of HealthRetrieved Dec. 2015 http:// clinicaltrials.gov2015.

[4] H. Priya James, R. John, A. Alex, K. R. Anoop, *Acta Pharm. Sin. B* **2014**, *4*, 120.

[5] C. I. C. Crucho, *ChemMedChem* **2015**, *10*, 24.

[6] J. L. Goldstein, R. G. W. Anderson, M. S. Brown, *Nature* **1979**, *279*, 679.

[7] I. Mellman, *Annu. Rev. Cell Dev. Biol.* **1996**, *12*, 575.

[8] G. J. Doherty, H. T. McMahon, *Annu. Rev. Biochem.* **2009**, *78*, 857.

[9] A. Aderem, D. M. Underhill, *Annu. Rev. Immunol.* **1999**, *17*, 593.

[10] Z. Mao, X. Zhou, C. Gao, *Biomater. Sci.* **2013**, *1*, 896.

[11] T. J. Pucadyil, S. L. Schmid, *Science* **2009**, *325*, 1217.

[12] V. I. Slepnev, P. De Camilli, *Nat. Rev. Neurosci.* **2000**, *1*, 161.

[13] M. Huang, Z. Ma, E. Khor, L.-Y. Lim, *Pharm. Res.* **2002**, *19*, 1488.

[14] T.-H. Chung, S.-H. Wu, M. Yao, C.-W. Lu, Y.-S. Lin, Y. Hung, C.-Y. Mou, Y.-C. Chen, D.-M. Huang, *Biomaterials* **2007**, *28*, 2959.

[15] I. R. Nabi, P. U. Le, *J. Cell Biol.* **2003**, *161*, 673.

[16] J. E. Schnitzer, J. Liu, P. Oh, *J. Biol. Chem.* **1995**, *270*, 14399.

[17] L. Pelkmans, J. Kartenbeck, A. Helenius, *Nat. Cell Biol.* **2001**, *3*, 473.

[18] T. Nishikawa, N. Iwakiri, Y. Kaneko, A. Taguchi, K. Fukushima, H. Mori, N. Morone, J. Kadokawa, *Biomacromolecules* **2009**, *10*, 2074.

[19] G. Sahay, J. O. Kim, A. V. Kabanov, T. K. Bronich, *Biomaterials* **2010**, *31*, 923.

[20] J. P. Lim, P. A. Gleeson, *Immunol. Cell Biol.* **2011**, *89*, 836.

[21] J. A. Swanson, *Nat. Rev. Mol. Cell Biol.* **2008**, *9*, 639.

[22] S. Falcone, E. Cocucci, P. Podini, T. Kirchhausen, E. Clementi, J. Meldolesi, *J. Cell Sci.* **2006**, *119*, 4758.

[23] C. Goncalves, *Mol. Ther.* **2004**, *10*, 373.

[24] G. Sahay, D. Y. Alakhova, A. V. Kabanov, *J. Controlled Release* **2010**, *145*, 182.

[25] L. Zhang, S. Zhang, S. Ruan, Q. Zhang, Q. He, H. Gao, *Acta Pharmacol. Sin.* **2014**, *35*, 846.

[26] R. F. Thorne, *J. Cell Sci.* **2003**, *117*, 373.

[27] S. Misra, V. C. Hascall, R. R. Markwald, S. Ghatak, *Front. Immunol.* **2015**, *6*, 201.

[28] S. P. Thankamony, W. Knudson, *J. Biol. Chem.* **2006**, *281*, 34601.

[29] S. Song, H. Qi, J. Xu, P. Guo, F. Chen, F. Li, X. Yang, N. Sheng, Y. Wu, W. Pan, *Pharm. Res.* **2014**, *31*, 2988.

[30] F. Dosio, S. Arpicco, B. Stella, E. Fattal, *Adv. Drug Deliv. Rev.* **2016**, *97*, 204.

[31] A. Mero, M. Campisi, *Polymers* **2014**, *6*, 346.

[32] A. K. Varkouhi, M. Scholte, G. Storm, H. J. Haisma, *J. Control. Release Off. J. Control. Release Soc.* **2011**, *151*, 220.

[33] T. F. Martens, K. Remaut, J. Demeester, S. C. De Smedt, K. Braeckmans, *Nano Today* **2014**, *9*, 344.

[34] W. Li, F. Nicol, F. C. Szoka, *Adv. Drug Deliv. Rev.* **2004**, *56*, 967.

[35] J. M. White, S. E. Delos, M. Brecher, K. Schornberg, *Crit. Rev. Biochem. Mol. Biol.* **2008**, *43*, 189.

[36] Y. W. Cho, J.-D. Kim, K. Park, *J. Pharm. Pharmacol.* **2003**, *55*, 721.

[37] H. Yin, R. L. Kanasty, A. A. Eltoukhy, A. J. Vegas, J. R. Dorkin, D. G. Anderson, *Nat. Rev. Genet.* **2014**, *15*, 541.

[38] A. P. Castano, T. N. Demidova, M. R. Hamblin, *Photodiagnosis Photodyn. Ther.* **2004**, *1*, 279.

[39] M. DeRosa, *Coord. Chem. Rev.* **2002**, *233–234*, 351.

[40] D. E. J. G. J. Dolmans, D. Fukumura, R. K. Jain, *Nat. Rev. Cancer* **2003**, *3*, 380.

[41] S. Swavey, M. Tr, In *Recent Advances in the Biology, Therapy and Management of Melanoma*; Davids, L., Ed.; InTech, 2013.

[42] L. B. Josefsen, R. W. Boyle, *Met.-Based Drugs* **2008**, *2008*, 1.

[43] M. Lilletvedt, H. H. Tønnesen, A. Høgset, S. A. Sande, S. Kristensen, *Pharm.* **2011**, *66*, 325.

[44] D. Wróbel, A. Dudkowiak, *Mol. Cryst. Liq. Cryst.* **2006**, *448*, 15/[617].

[45] A. Master, M. Livingston, A. Sen Gupta, *J. Control. Release Off. J. Control. Release Soc.* **2013**, *168*, 88.

[46] I. Yoon, J. Z. Li, Y. K. Shim, *Clin. Endosc.* **2013**, *46*, 7.

[47] R. R. Allison, K. Moghissi, *Clin. Endosc.* **2013**, *46*, 24.

[48] S. S. Lucky, K. C. Soo, Y. Zhang, *Chem. Rev.* **2015**, *115*, 1990.

[49] K. Berg, P. K. Selbo, L. Prasmickaite, T. E. Tjelle, K. Sandvig, J. Moan, G. Gaudernack, O. Fodstad, S. Kjølsrud, H. Anholt, G. H. Rodal, S. K. Rodal, A. Høgset, *Cancer Res.* **1999**, *59*, 1180.

[50] A. A. Rosenkranz, D. A. Jans, A. S. Sobolev, *Immunol. Cell Biol.* **2000**, *78*, 452.

[51] P. K. Selbo, A. Weyergang, A. Høgset, O.-J. Norum, M. B. Berstad, M. Vikdal, K. Berg, *J. Controlled Release* **2010**, *148*, 2.

[52] K. Berg, M. Folini, L. Prasmickaite, P. Selbo, A. Bonsted, B. Engesaeter, N. Zaffaroni, A. Weyergang, A. Dietzea, G. Maelandsmo, E. Wagner, O.-J. Norum, A. Hogset, *Curr. Pharm. Biotechnol.* **2007**, *8*, 362.

[53] A. Høgset, L. Prasmickaite, T. E. Tjelle, K. Berg, *Hum. Gene Ther.* **2000**, *11*, 869.

[54] A. Ndoye, G. Dolivet, A. Hogset, A. Leroux, A. Fifre, P. Erbacher, K. Berg, J. Behr, F. Guillemin, J. Merlin, *Mol. Ther.* **2006**, *13*, 1156.

[55] C. Y. Calvet, D. Famin, F. M. André, L. M. Mir, *OncoImmunology* **2014**, *3*, e28131.

[56] K. Berg, A. Dietze, O. Kaalhus, A. Høgset, *Clin. Cancer Res. Off. J. Am. Assoc. Cancer Res.* **2005**, *11*, 8476.

[57] L. Shang, K. Nienhaus, G. Nienhaus, *J. Nanobiotechnology* **2014**, *12*, 5.

[58] H.-C. Yen, H. Cabral, P. Mi, K. Toh, Y. Matsumoto, X. Liu, H. Koori, A. Kim, K. Miyazaki, Y. Miura, N. Nishiyama, K. Kataoka, *ACS Nano* **2014**, *8*, 11591.

[59] H.-L. Lu, W.-J. Syu, N. Nishiyama, K. Kataoka, P.-S. Lai, *J. Control. Release Off. J. Control. Release Soc.* **2011**, *155*, 458.

[60] Janeway CA Jr, Travers P, Walport M, In *Immunobiology: The Immune System in Health and Disease*; Garland Science, 2001.

[61] J. A. Villadangos, P. Schnorrer, *Nat. Rev. Immunol.* **2007**, *7*, 543.

[62] E. W. Hewitt, *Immunology* **2003**, *110*, 163.

[63] T. ten Broeke, R. Wubbolts, W. Stoorvogel, *Cold Spring Harb. Perspect. Biol.* **2013**, *5*, a016873.

[64] G. T. Belz, F. R. Carbone, W. R. Heath, *Crit. Rev. Immunol.* **2002**, *22*, 439.

[65] S. M. Standley, Y. J. Kwon, N. Murthy, J. Kunisawa, N. Shastri, S. J. Guillaudeu, L. Lau, J. M. J. Fréchet, *Bioconjug. Chem.* **2004**, *15*, 1281.

[66] T. Mizuochi, S.-T. Yee, M. Kasai, T. Kakiuchi, D. Muno, E. Kominami, *Immunol. Lett.* **1994**, *43*, 189.

[67] W. Zou, *Nat. Rev. Cancer* **2005**, *5*, 263.

[68] C. M. Fehres, W. W. J. Unger, J. J. Garcia-Vallejo, Y. van Kooyk, *Front. Immunol.* **2014**, *5*.

[69] N. P. Restifo, M. E. Dudley, S. A. Rosenberg, *Nat. Rev. Immunol.* **2012**, *12*, 269.

[70] K. K. Wong, W. A. Li, D. J. Mooney, G. Dranoff, In *Advances in Immunology*; Elsevier, 2016; Vol. 130, pp. 191–249.

[71] J. Vansteenkiste, M. Zielinski, A. Linder, J. Dahabreh, E. E. Gonzalez, W. Malinowski, M. Lopez-Brea, T. Vanakesa, J. Jassem, H. Kalofonos, J. Perdeus, R. Bonnet, J. Basko, R. Janilionis, B. Passlick, T. Treasure, M. Gillet, F. F. Lehmann, V. G. Brichard, *J. Clin. Oncol. Off. J. Am. Soc. Clin. Oncol.* **2013**, *31*, 2396.

[72] V. Lakshminarayanan, P. Thompson, M. A. Wolfert, T. Buskas, J. M. Bradley, L. B. Pathangey, C. S. Madsen, P. A. Cohen, S. J. Gendler, G.-J. Boons, *Proc. Natl. Acad. Sci.* **2012**, *109*, 261.

[73] A. Murshid, J. Gong, M. A. Stevenson, S. K. Calderwood, *Expert Rev. Vaccines* **2011**, *10*, 1553.

[74] D. R. Ciocca, N. Cayado-Gutierrez, M. Maccioni, F. D. Cuello-Carrion, *Curr. Mol. Med.* **2012**, *12*, 1183.

[75] M. Shevtsov, G. Multhoff, *Front. Immunol.* **2016**, *7*.

[76] M. A. Shevtsov, E. Y. Komarova, D. A. Meshalkina, N. V. Bychkova, N. D. Aksenov, S. V. Abkin, B. A. Margulis, I. V. Guzhova, *Oncotarget* **2014**, *5*, 3101.

[77] M. Rafiee, J. R. Kanwar, R. W. Berg, K. Lehnert, K. Lisowska, G. W. Krissansen, *Cancer Gene Ther.* **2001**, *8*, 974.

[78] E. Gilboa, S. K. Nair, H. K. Lyerly, *Cancer Immunol. Immunother.* **1998**, *46*, 82.

[79] T. N. Schumacher, R. D. Schreiber, *Science* **2015**, *348*, 69.

[80] S. A. Ferreira, F. M. Gama, M. Vilanova, *Nanomedicine Nanotechnol. Biol. Med.* **2013**, *9*, 159.

[81] F. Shima, T. Akagi, T. Uto, M. Akashi, *Biomaterials* **2013**, *34*, 9709.

[82] S. T. Reddy, A. J. van der Vlies, E. Simeoni, V. Angeli, G. J. Randolph, C. P. O'Neil, L. K. Lee, M. A. Swartz, J. A. Hubbell, *Nat. Biotechnol.* **2007**, *25*, 1159.

[83] H. Shen, A. L. Ackerman, V. Cody, A. Giodini, E. R. Hinson, P. Cresswell, R. L. Edelson, W. M. Saltzman, D. J. Hanlon, *Immunology* **2006**, *117*, 78.

# CHAPTER 2

# A PSEUDO-PROTEIN BASED BIODEGRADABLE MICELLAR PLATFORM FOR THE DELIVERY OF ANTI-CANCER DRUG: PHOTO-ENHANCED STRUCTURAL STABIITY, UNIQUE INTRACELLULAR TRAFFICKING AND IN VITRO THERAPEUTIC EFFECT IN HUMA COLON CANCER CELLS

## *2.1 Abstract*

Amino acid based poly (ester amide)s (AA-PEA) is a new family of biodegradable polymers that exhibits "pseudo-protein" characteristics and the structural varieties of AA-PEAs make them hold great potential in multiple biomedical applications. In this study, a lysine-phenylalanine based AA-PEA is developed as the self-assembled nano-micellar carrier for efficient delivery of doxorubicin (DOX). The lysine moieties from the pseudo-protein provided available sites for further functionalization, and methylcoumarin was introduced for easy and photo-controllable crosslinking, to effectively improve the micellar stability in serum containing environment and against dilution. However, photo-crosslinks did not bring in any barrier for the intracellular release of DOX. DOX release was significantly accelerated by the presence of proteolytic enzyme, due to the biodegradability of pseudo-protein micelles. In addition, pseudo-protein delivery system exhibited unique interactions with HCT116 human colon cancer cells. DOX loaded in pseudo-protein micelles co-localized with mitochondria and endolysosomes, while free DOX was distributed only in the nuclei. Beside the difference in intracellular trafficking, DOX-loaded pseudo-protein micelles stimulated increased level of intracellular reactive oxygen species and mitochondrial damage. Free DOX induced conditional apoptosis in HCT116 cells between 0.5-2 μM, while DOX loaded in pseudo-protein micelles induced apoptosis over a higher/broader concentration range (2-10 μM).

## *2.2 Introduction*

Polymeric micelles as nano-carriers for chemotherapeutics have gained considerable popularity in the study of cancer treatment. The micellar carriers provide physical or chemical encapsulation of drugs in their hydrophobic cores, and have the potential to improve the pharmacological [1]. However, polymeric micelles are facing several practical challenges that significantly limit their therapeutic efficacy. One of the major challenge lies in their instability in physiological environment [2]. Self-assembled polymeric micelles are thermodynamically in equilibrium with their unimers. After intravenous

administration, micellar carriers receive instant dilution below their critical micelle concentration (CMC), which leads to significant disintegration of the micellar structure [3]. In addition, the interaction with blood components, such as plasma proteins, is reported to disrupt the thermodynamic equilibrium between micelles and unimers, resulting in unwanted micelle collapse [4]. The loss of structural integrity causes the premature release of drugs from the carrier, which generates toxicity and adverse effects in normal organs.

Chemical crosslinking of micelle is one of the most common approaches to overcome the physiological destabilization forces. By introducing polymerizable moieties, multifunctional reactive agents [5], or functional groups for host-guest interactions [6], crosslinking can be established in the shell, core or intermediate layer of micelles. Coumarin-based photochemical crosslinking is a newly emerged crosslinking technique which takes advantage of the reversible photodimerization of coumarin activated by UV irradiation at two different wavelengths [7]. As demonstrated by Zhao et al. [8], micelle stabilization was achieved by the formation of photo controllable core-crosslinks between coumarin functionalized poly(methyl methacrylate) chains. Other studies [9-12] also incorporated coumarin photo-crosslinks to improve the stability of various nanocarriers, including a series of biodegradable or non-degradable polymers. However, since crosslinking brings in barriers for the encapsulated molecules to diffuse out of the micelles, it causes slow/insufficient release of payloads inside cancer cells and hinders the potency of micellar carriers.

The pitfall of the crosslinking approach to stabilize micelles makes the concept “stabilization-on-demand” [8] quite appealing, and provides an incentive for the development of smart delivery systems that can be destabilized upon intracellular signals. By modulating polymer characteristics, such as the susceptibility towards intracellular stimuli (acidic pH, redox potential or specific enzymes, etc.) [13, 14], rapid release of payloads in cancer cells can be achieved, while the extracellular stability is still maintained. Numerous design

concepts and tailor-made polymers have therefore emerged, and biodegradable polymeric micelles [15-17] are an attractive option over the non-degradable ones due to the unelucidated long term toxicity of the latter.

Amino acid based poly (ester amide)s (AA-PEA) is a new family of synthetic pseudo proteins recently developed for several biomedical applications ranging from synthetic skin, coating for drug-eluting stents, to drug delivery vehicles. The details have recently been given in several review articles [18-20]. AA-PEA is synthesized from 3 building blocks: amino acids, diols and diacids, and has both ester and amide groups on the polymer backbone as available sites for enzymatic degradation. AA-PEA exhibits both protein and non-protein characteristics, and our previous work have demonstrated the unique advantages of AA-PEA, which include reproducible synthetic routes, versatile structural design, enzymatic biodegradation, excellent biocompatibility, and muted inflammatory response, etc. By selecting different types of amino acids, diols, and adjusting the number of hydrocarbons between ester and amide groups, AA-PEA materials are tunable in charge density, hydrophobicity/hydrophilicity, as well as the reactive sites for further chemical functionalization. Chu et al. have demonstrated that arginine or lysine based PEAs facilitated the penetration through cell membrane and worked as effective delivery systems for therapeutic agents including genes [21-24].

The aim of the study is to develop a novel biodegradable pseudo protein micelle as an intracellular drug delivery vehicle. Lysine-phenylalanine PEA is chosen based on our preliminary study [21]. And to improve the extracellular stability, coumarin functional groups is introduced into the hydrophobic segments of the polymer chains so that reversible photo-crosslinking can be established. The modified pseudo protein is abbreviated as Lys-Phe-PEAcou-PEG. Doxorubicin (DOX), one of the most typical anticancer drugs employed in the clinical use, is chosen as the model drug for examining the delivery performances. Previous work suggested the apoptotic death of HCT116 colon cancer cells is conditional with respect to the concentration of DOX [25, 26].

However, of the biodegradable micellar systems investigated so far in the literatures, very few studies addressed the dose-dependent interaction between DOX-loaded micelles and cancer cells. In this contribution, we not only study the effect of photo-crosslinking on the stability of the Lys-Phe-PEAcou-PEG micelles, as well as the effect of enzymatic degradation on the in vitro release of DOX from the crosslinked micelles. But we also focus on the endocytosis, subcellular distribution, and the dose-dependent interaction between DOX-loaded Lys-Phe-PEAcou-PEG micelles and HCT116 colon cancers cells.

### *2.3. Experimental*

#### *2.3.1 Chemicals and cells*

N-Hydroxysulfosuccinimide-polyoxyethylene-maleimide (NHS-PEG-MAL, MW=2000 Da) was from JenKem Technology (Allen, TX). 7-(carboxymethoxy)-4-methylcoumarin, thionyl chloride, nile red, 3-(4,5-dimethylthiazol-2-yl)-2,5-diphenyltetrazolium bromide (MTT), α-chymotrypsin (Type II, from bovine pancreas), methyl-β-cyclodextrin, cobalt chloride, carbonyl cyanide 3-chlorophenylhydrazone (CCCP) and QuantiPro BCA Assay Kit were from Sigma Aldrich (Milwaukee, WI). Dimethyl sulfoxide (DMSO), ethyl acetate and other HPLC grade solvents were from JT Baker (Phillipsburg, NJ). Dipeptide cysteine-lysine with amidation at C-terminus of cysteine was synthesized by GL Biochem Ltd. (Shanghai, China). Doxorubicin hydrochloride was from Lancrix Chemicals (Shanghai, China). Mitotracker deep red FM, Mitotracker green, Lysotracker deep red, Lysotraker green, Hoechst 33342, SYTOX Red dead cell stain, DiL (1,1'-dioctadecyl-3,3,3',3'-Tetramethylindocarbocyanine perchlorate) and DiO (3,3'-dioctadecyloxacarbocyanine perchlorate) were from Molecular Probes (Eugene, OR). Nystatin, chloropromazine, amiloride hydrochloride, JC-1 mitochondrial membrane potential assay kit, dihydroethidium (DHE), and calcein AM were from Cayman Chemical (Ann Arbour, MI). Annexin V apoptosis detection kit was from eBioscience (San Diego, CA). Cleaved caspase 3 western blot kit

were from Cell Signaling Technology (Beverly, MA). Snakeskin dialysis tubing (MWCO=3.5 kDa or 10 kDa) and NHS-Rhodamine were from Pierce (Rockford, IL). Z-LysNCA (ε-(benzyloxycarbonyl)-L-lysine N-carboxyanhydride), Phe-4 (di-p-toluenesulfonic acid salt of bis-L-phenylalanine butane-1, 4-diester) and NA (di-p-nitrophenyl adipate) were synthesized from our previous study [21].

HCT116 human colon carcinoma cell line was maintained in McCoy's 5A medium (Lonza, Walkersville, MD) supplemented with 10% fetal bovine serum (Hyclone, Logan, UT), 2 mM L-glutamine, 100 units/mL penicillin, and 100 μg/mL streptomycin (Lonza, Walkersville, MD) at 37 °C in 5% $CO_2$.

### *2.3.2 Characterization*

$^1$H NMR spectra were recorded on a Varian Unity Inova 400 MHz spectrometer (Palo Alto, CA), and deuterated dimethyl sulfoxide (DMSO-d6, Cambridge Isotope Laboratories) was used as the solvent. The chemical shifts were calibrated against solvent signals. The morphology of micelles was observed on a FEI Tecnai Spirit T12 TEM (FEI Co., Hillsboro, OR) at an operating voltage of 120 kV. Zeta potential and the size of the micelles were characterized at room temperature on a Zetasizer NanoZS system (Malvern, UK). UV-vis spectroscopy was performed on a Lambda Bio40 spectrophotometer (Perkin-Elmer, Norwalk, CT). Fluorescence spectra was recorded on a PTI spectrofluorometer (Photon Technology International, South Brunswick, NJ). For the microplate assay, the absorbance or relative fluorescence units were read on a Synergy HT microplate reader (BioTek, Winooski, VT). Cells were visualized with a Zeiss LSM710 confocal microscope (Carl Zeiss MicroImaging, Thornwood, NY). Flow cytometry was performed on a BD FACSAria fusion fluorescence activated cell sorter (BD Biosciences, Franklin Lakes, NJ).

### *2.3.3 Synthesis of Lys-Phe-PEAcou-PEG polymer*

*Synthesis of lysine- phenylalanine based PEA (Lys-Phe-PEA).* The synthesis of Lys-Phe-PEA with pendent amino groups was based on our published studies [21]. Z-LysNCA (1.28 g, 4.14 mmol) was mixed with Phe-4 (5.78 g, 7.93 mmol) in N, N-dimethylacetamide (DMA, 30 mL) and stirred at 40 °C for 3 hrs before the temperature was raised to 80 °C and kept for 24 hrs in nitrogen atmosphere. The reaction was subsequently cooled to room temperature. NA (3.08 g, 7.93 mmol) and trimethylamine (2.41 mL, 17.45 mmol) were added and stirred at 80 °C for 24 hrs in nitrogen atmosphere. The feed ratio between Z-LysNCA, Phe-4 and NA was 1:1.9:1.9 [21]. The resulting solution was precipitated into cold ethyl acetate and dried in vacuo. The as prepared polymer (5 g) was dissolved in trifluoroacetic acid (20 mL) and stirred for 1 hr at room temperature before methanesulfonic acid (1.30 mL) dissolved in anisole (2.6 mL) was added. After stirring for additional 1 hr, the solution was precipitated into cold diethyl ether. The polymer was dissolved in DMA, neutralized with triethylamine, and precipitated into ethyl acetate. The de-protected polymer, Lys-Phe-PEA, was dialyzed against ethanol for 48 hrs (MWCO=3.5 kDa), and dried in vacuo.

*Synthesis of polyethylene glycol grafted Lys-Phe-PEA (Lys-Phe-PEA-PEG).* Lys-Phe-PEA polymers with various grafting ratio of polyethylene glycol were synthesized for PEGylation. To functionalize 45% of the total repeating units on Lys-Phe-PEA with PEG, Lys-Phe-PEA (100 mg) was dissolved in DMSO (20 mL) containing 178 mg of heterofunctional PEG (NHS-PEG-MAL, MW=2000) and stirred at room temperature for 24 hrs. The reaction mixture was precipitated into ethyl acetate for three times and dried in vacuo.

*Synthesis of methylcoumarin grafted Lys-Phe-PEA-PEG (Lys-Phe-PEAcou).* 7-(chlorocarbonylmethoxy)-4-methylcoumarin was prepared from 7-(carboxymethoxy)-4-methylcoumarin and thionyl chloride based on published procedure [10]. To functionalize 5% of the total repeating units on Lys-Phe-PEA-PEG with methylcoumarin, Lys-Phe- PEA-PEG from last step was dissolved in

THF (20 mL) with trimethylamine (13 μL). 7-chlorocarbonylmethoxy-4-methylcoumarin (3 mg) in THF (1 mL) was added and stirred overnight in dark at room temperature. The resulted solution was precipitated three times into methanol and dried in vacuo. The purified polymer was dissolved in degassed DMSO (20 mL). Cysteine-lysine dipeptide (25 mg) in degassed DI water (2 mL) was added, stirred overnight at room temperature and dialyzed against DI water (MWCO=3.5 kDa) for 48 hrs. The purified Lys-Phe-PEAcou-PEG was lyophilized.

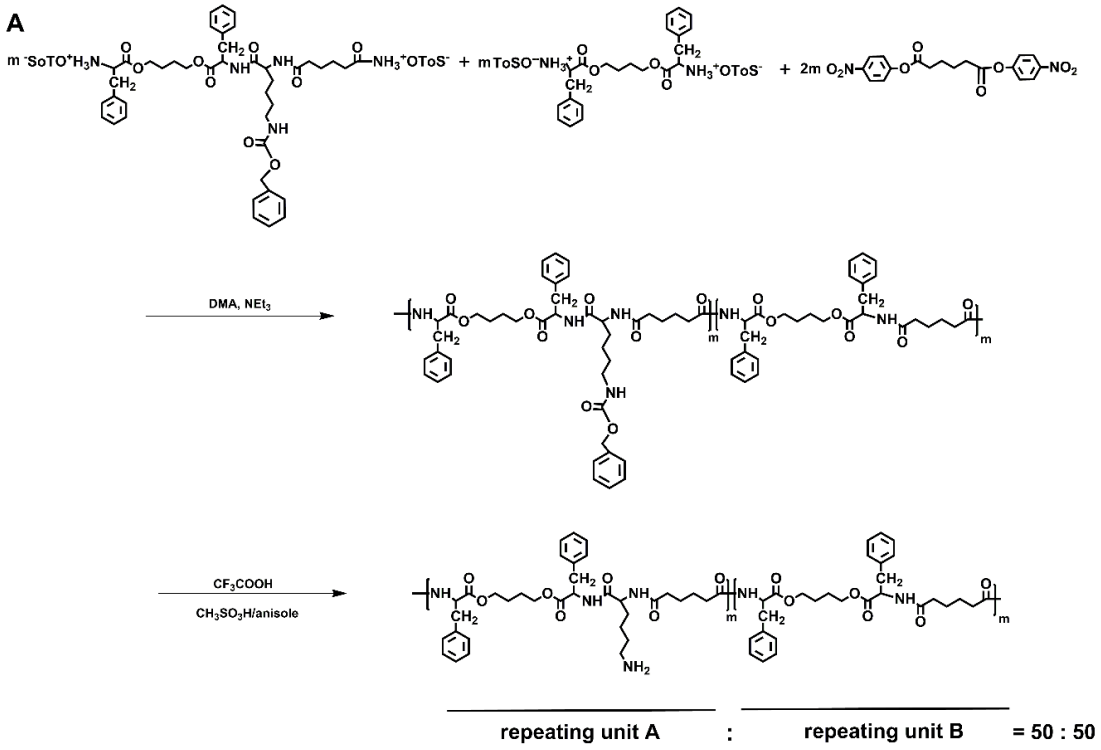

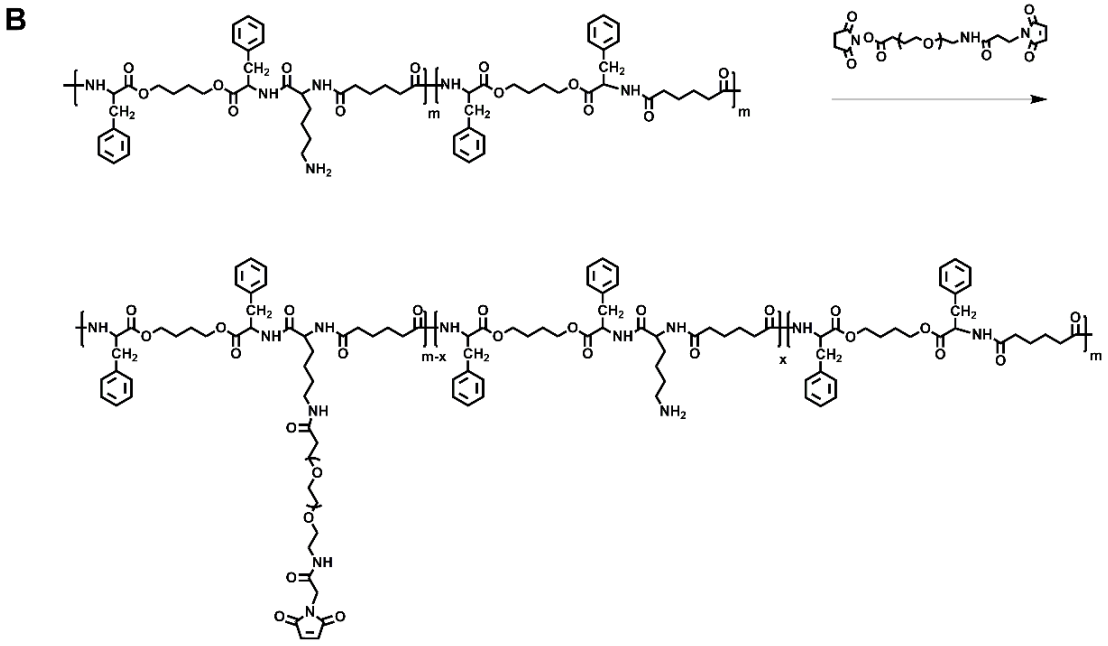
B

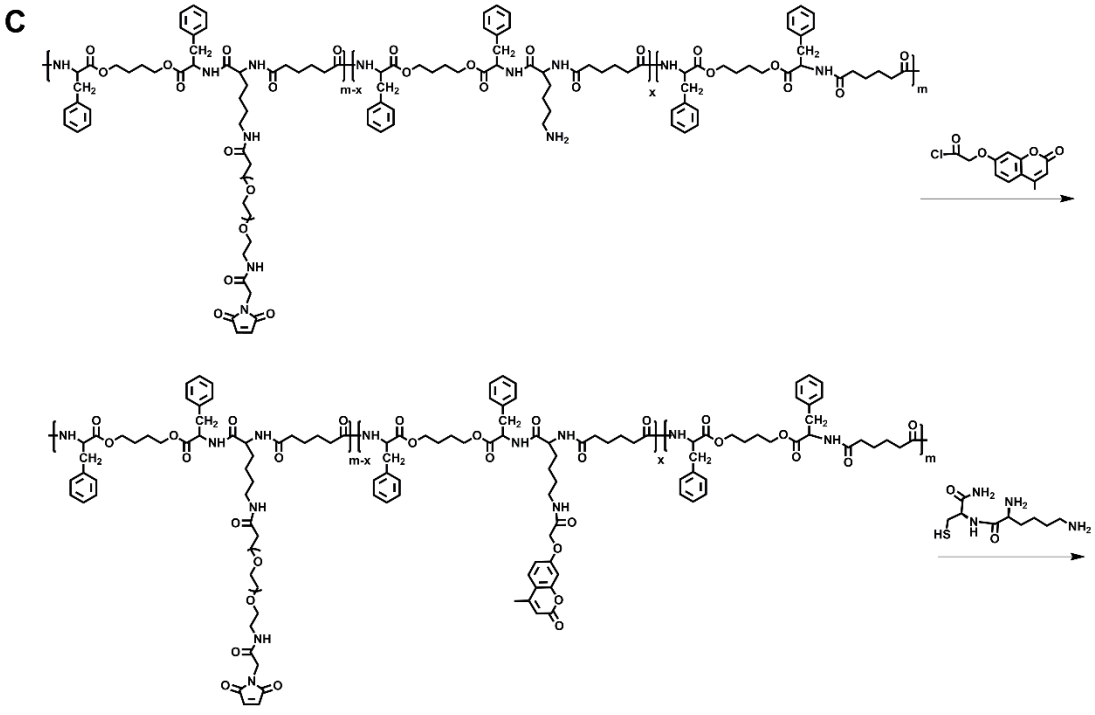
C

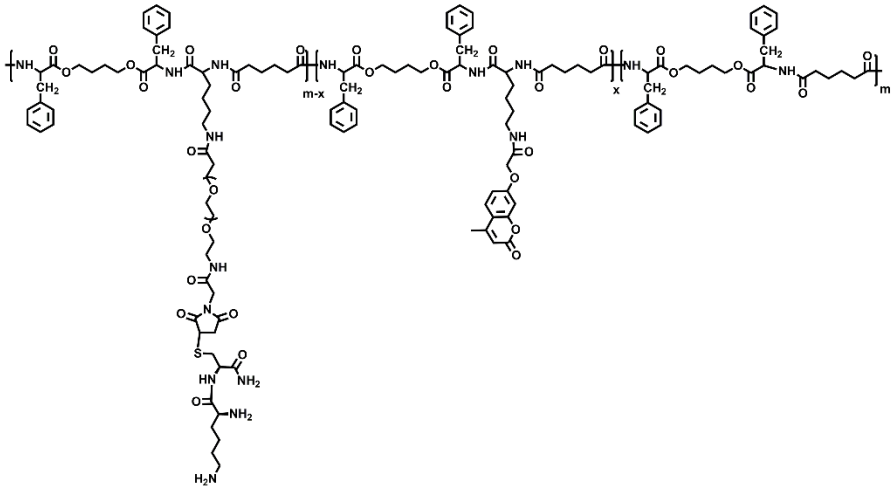

**Figure 2.1.** Synthesis scheme for A) lysine-phenylalanine based PEA (Lys-Phe-PEA), B) polyethylene glycol grafted Lys-Phe-PEA (Lys-Phe-PEA-PEG), and C) methylcoumarin grafted Lys-Phe-PEA-PEG (Lys-Phe-PEAcou-PEG).

### *2.3.4 Preparation and characterization of photo-crosslinked Lys-Phe-PEAcou-PEG micelles*

Aqueous dispersion of Lys-Phe-PEAcou-PEG micelles (1 mg/mL) was exposed to 365 nm irradiation (model B-100AP; UVP, Upland, CA) for 3 hrs at room temperature. The photo-crosslinking process was monitored with UV-vis spectroscopy. To prepare the de-crosslinked micelles, aqueous dispersion of completely crosslinked Lys-Phe-PEAcou-PEG micelle (1 mg/mL) was exposed to 254 nm irradiation (model UVGL-25; UVP, Upland, CA) for 1 hr. The critical micelle concentration (CMC) of the Lys-Phe-PEAcou-PEG micelles was determined with nile red assay according to previous study [27].

### *2.3.5 Effect of serum and enzyme on the stability of micelles*

Lys-Phe-PEAcou-PEG (10 mg) was dissolved in DMSO followed by addition of DiO (100 μg) and DiL (100 μg). The mixture was stirred for 30 min and dialyzed (MWCO=3.5 kDa) against DI water for 24 hrs. The dialyzed

solution was filtered through a 0.45 μm microfilter and subjected to UV irradiation to prepare the crosslinked FRET micelles.

To evaluate the effect of serum on micellar stability, the crosslinked or uncrosslinked FRET micelles were dispersed in 10 mM PBS (pH=7.4) and mixed with fetal bovine serum (FBS) (1:9 v/v, with the final micelle concentration of 0.1 mg/mL) at 37°C for up to 48 hrs,

To evaluate the effect of proteolytic enzyme on micellar stability, crosslinked or uncrosslinked FRET micelles were dispersed in 10 mM PBS containing 0.2 mg/mL α-chymotrypsin for up to 48 hrs.

The fluorescence emission spectra of FRET micelles after incubation with FBS or enzyme was measured (λex=470 nm). And FRET ratio was calculated as follows:

$$\text{FRET ratio} = \frac{I_{DiL}}{I_{DiL} + I_{DiO}}$$

where $I_{DiL}$ represents the fluorescence intensity at 565 nm and $I_{DiO}$ represents the fluorescence intensity at 501 nm.

### *2.3.6 Preparation of doxorubicin-loaded crosslinked Lys-Phe-PEAcou-PEG micelles*

Doxorubicin hydrochloride (15 mg) was dissolved in DMSO (5 mL) with trimethylamine (7.2 μL) and stirred overnight, followed by the addition of Lys-Phe-PEAcou-PEG (100 mg) in DMSO (10 mL). The mixture was stirred for another 2 hrs before DI water (6 mL) was added dropwise. DMSO and unloaded drug were removed by dialysis (MWCO=10 kDa) against DI water for 48 hrs. The dialyzed solution was filtered through a 0.45 μm microfilter, and subjected to UV irradiation at 365 nm as described in section 2.4 to prepare DOX-loaded crosslinked Lys-Phe-PEAcou-PEG micelles.

To determine the drug loading content (DLC) and encapsulation efficiency (EE), the solution of crosslinked DOX-loaded Lys-Phe-PEAcou-PEG micelles was irradiated by 254 nm UV light for 1 hr to facilitate the photo-cleavage of

methylcoumarin dimer. The de-crosslinked micelles were then lyophilized and dissolved in DMSO. DOX content was determined by fluorescence spectroscopy (λex=480 nm) and calibrated with DOX standard curve.

### *2.3.7 In vitro DOX release from Lys-Phe-PEAcou-PEG micelles*

DOX release from Lys-Phe-PEAcou-PEG micelles were examined in 10 mM phosphate buffer (pH 5.5) with or without the presence of α-chymotrypsin. DOX-loaded Lys-Phe-PEAcou-PEG (5 mg, either crosslinked or uncrosslinked) dissolved in 10 mM phosphate buffer (pH 5.5, 5mL) with α-chymotrypsin (0.2 mg/mL) was dialyzed (MWCO=10 kDa) against phosphate buffer (pH 5.5, 30 mL) at 37 °C under shaking (100 rpm). At pre-determined time intervals, 5 mL of buffer outside the dialysis tubing was withdrawn and replaced by 5 mL of fresh buffer. Release profile of DOX-loaded micelles dispersed in phosphate buffer (pH 5.5) without enzyme was also tested. DOX concentration in collected samples was determined by spectrofluorometer (λex=480 nm) and calibrated with DOX standard curve. The percentage of cumulatively released DOX was plotted vs. time. Each test was performed in triplicate.

### *2.3.8 Cytotoxicity studies*

Cytotoxicity of DOX-loaded crosslinked Lys-Phe-PEAcou-PEG micelles was assessed by MTT assay as described previously [28]. HCT116 cells were incubated with blank crosslinked micelles, free DOX, or DOX-loaded crosslinked Lys-Phe-PEAcou-PEG micelles for 48 hrs, with equivalent DOX concentration ranging from 0.05 to 20 μM. And the experiments were run in six replicates. The absorbance at 570 nm was recorded and normalized to untreated control to give the percentage of cell survival.

### *2.3.9 Endocytosis and subcellular localization study*

*Accumulated endocytosis study*. HCT116 cells were seeded in 6-well plate (3 x $10^5$ cells/well) and pre-incubated for 24 hrs. Free DOX or DOX-loaded crosslinked Lys-Phe-PEAcou-PEG micelles with 2 μM equivalent DOX concentration were added and incubated for 1, 4, 8, 12 or 24 hrs, before the cells were harvested for flow cytometry test. The mean fluorescence from cellular DOX were plotted vs. time. The tests were performed in triplicate.

*Endocytosis inhibition assay*. HCT116 cells were seeded in 6-well plate (3 x $10^5$ cells/well) and pre-incubated for 24 hrs. The cells were treated with inhibitors that block different endocytic pathways (nystatin, 50 μg/mL; chloropromazine, 30 μM; amiloride hydrochloride, 50 μM; or methyl-β-cyclodextrin, 3 mg/mL) [29, 30] for 0.5 hr before DOX-loaded crosslinked Lys-Phe-PEAcou-PEG micelles with equivalent DOX concentration of 2 μM was added and incubated for another 4 hrs. The cells were harvested for flow cytometry test. Cells incubated with DOX-loaded micelles at 37°C but not treated with any inhibitor were tested as control. The mean fluorescence intensity for each sample was recorded and normalized to control. The tests were performed in triplicate.

*Subcellular distribution*. 3 x $10^5$ HCT116 cells were seeded in a 35 mm glass bottomed petri dish (3 x $10^5$ cells/well, MaTek, Ashland, MA) and pre-incubated for 24 hrs. Blank crosslinked micelles labelled with rhodamine, free DOX or DOX-loaded crosslinked Lys-Phe-PEAcou-PEG micelles with equivalent DOX concentration of 5 μM was added and incubated for 4 hrs. Cells were stained with specific organelle markers including Lysotracker (50 nM), Mitotracker (500 nM) or Hoechst 33342 (1 μg/mL) and imaged alive by confocal microscopy. The Pearson's coefficient was determined with Fiji software (National Institutes of Health).

### *2.3.10 Measurement of cellular reactive oxygen species (ROS)*

The cellular ROS level was measured by dihydroethidium (DHE) probe [31]. HCT116 cells were seeded in black 96-well plate (0.5 x $10^4$ cells/well) and pre-incubated for 24 hrs. Blank crosslinked micelles, DOX-loaded crosslinked Lys-Phe-PEAcou-PEG micelles, or free DOX with various DOX concentrations were added and incubated for 24 hrs. The cells were then stained with 1 μM DHE for 20 min [32]. The endpoint relative fluorescence unit was recorded (λex=530±25 nm, λem=590±35 nm). Cells treated with DOX only but not DHE probe were also tested and the DOX fluorescence was subtracted from the total fluorescence. The result was normalized to untreated control and plotted as a function of DOX concentration. The experiments were performed in triplicate.

### *2.3.11 Assessment of MMP and MPTP*

Mitochondria membrane potential (MMP) assay. HCT116 cells were seeded in a 6-well plate (3 x $10^5$ cells/well) and pre-incubated for 24 hrs. Blank crosslinked micelles, free DOX or DOX-loaded crosslinked Lys-Phe-PEAcou-PEG micelles with various DOX concentrations were added and incubated for another 24 hrs. The cells were stained with JC-1 probe as per manufacturer's instruction and analysed by flow cytometry. Negative control (untreated cells) and positive control (cells treated with mitochondria uncoupler CCCP) were also tested. Each experiment was performed in triplicate. The percentage of cell population stained with higher level of JC-1 monomer and lower level of J-aggregates was recorded.

Mitochondrial permeability transition pore (MPTP) assay. HCT116 cells were seeded in 35 mm glass bottomed petri dish (3 x $10^5$ cells/well) and pre-incubated for 24 hrs. Blank crosslinked micelles, free DOX or DOX-loaded crosslinked Lys-Phe-PEAcou-PEG micelles with various DOX concentrations were added and incubated for 24 hrs. Cells were then incubated with calcein AM (1 μM) for 15 min at 37 °C with the presence of cobalt chloride (1 mM). The quenching of mitochondrial calcein fluorescence was visualized by

confocal microscopy. The fluorescence intensity normalized to the total number of cells was analysed with Fiji software (National Institutes of Health), expressed as the percentage to untreated control and plotted as a function of DOX concentration.

### *2.3.12 Caspase assay and annexin V apoptosis assay*

*Caspase 3/7 activity*. HCT116 cells were seeded in a black 96-well plate ($0.5 \times 10^4$ cells/well) and incubated for 24 hrs. Blank crosslinked micelles, free DOX or DOX-loaded crosslinked Lys-Phe-PEAcou-PEG micelles with various DOX concentrations were added and incubated for another 48 hrs. Caspase 3/7 activity was assessed by Apo-ONE Homogeneous Caspase-3/7 assay kit (Promega, Madison, WI) as per manufacturer's instruction. The fluorescence intensity was recorded ($\lambda ex=485\pm20$ nm, $\lambda em=528\pm20$ nm) and normalized to untreated control. Each experiment was performed in triplicate.

*Western blot for cleaved caspase 3*. HCT116 cells incubated with blank crosslinked micelles, DOX-loaded crosslinked Lys-Phe-PEAcou-PEG micelles, or free DOX with various DOX concentrations were harvested, lyzed in RIPA buffer. Cell lysates, quantified with BCA assay, were separated by SDS-PAGE on tris-glycine gel (4-20%, Novex, San Diego, CA) and transferred to PVDF membranes (Bio-Rad Laboratories, Hercules, CA). The protein bands were immunostained and visualized with cleaved caspase-3 western detection kit (Cell Signaling Technology, Beverly, MA) as per manufacturer's instruction.

*Annexin V assay*. HCT116 cells were seeded in a 6-well plate ($3 \times 10^5$ cells/well) and incubated for 24 hrs. Free DOX or DOX-loaded crosslinked Lys-Phe-PEAcou-PEG micelles with various DOX concentrations were added and incubated for another 48 hrs. Cells ($1 \times 10^6$) were harvested, stained with annexin V-FITC assay reagent (5 μL) in annexin binding buffer (100 μL), and further stained with SYTOX Red (5 nM). The percentage of early apoptotic cells (annexin V-FITC positive, SYTOX Red negative) was determined by flow cytometry. Each experiment was performed in triplicate.

### *2.3.13 Statistical analysis*

The data are presented as mean values with standard deviations (SD). All data were analysed with one-way ANOVA, followed by Tukey's multiple comparison tests, and $p < 0.05$ is considered statistically significant.

## *2.4. Results and Discussion*

### *2.4.1 Synthesis and characteristics of Lys-Phe-PEAcou-PEG micelles*

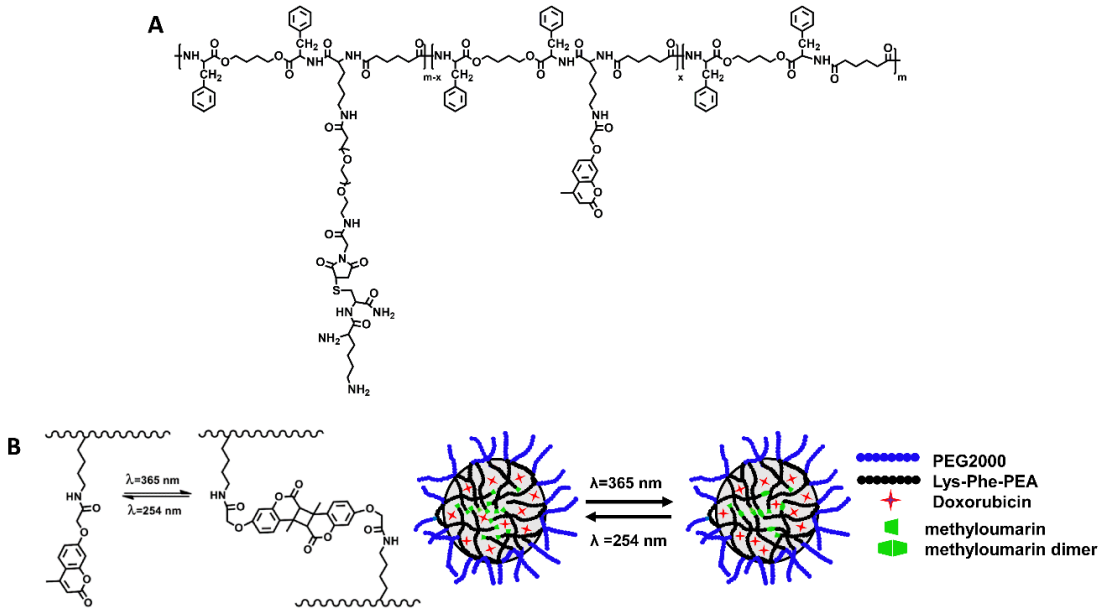


**Figure 2.2.** A) Chemical structure and the formation of photo-crosslinked micelles from lysine-phenylalanine based poly (ester amide)s grafted with polyethylene glycol and methylcoumarin (Lys-Phe-PEAcou-PEG). B) Graphic illustration of the reversible photo-crosslinking/de-crosslinking process of DOX-loaded Lys-Phe-PEAcou-PEG micelles.

In the ungrafted Lys-Phe-PEA polymer, the Lys moieties accounts for 33% of total amino acid units in the polymer, based on calculation from $^{1}$H NMR.

And the ratio between the two repeating units (repeating unit A and B as indicated in Figure 2.1A) in the polymer chains of Lys-Phe-PEA, was calculated to be 50:50 [21]. Molecular weight of Lys-Phe-PEA was determined as $M_n$=14.1 kDa, PDI=1.43. The characterization results of Lys-Phe-PEA polymer are consistent with our previously published data [21]. Figure 2.2 shows the generic chemical structure of the Lys-Phe-PEAcou-PEG with pendant methylcoumarin (MCM) in the Lys moiety as well as the schematic illustration of the reversible photo-crosslinking process.

Figure 2.3 shows the $^1$H NMR spectrum for Lys-Phe-PEAcou-PEG polymer. Typical peak for PEG was observed at 3.3 to 3.5 ppm, and typical peaks for methycoumarin functional group were observed at 2.42, 6.23, 6.95 and 7.73 ppm, which prove the successful grafting of the two molecules into the polymer. The PEG content can be roughly calculated by comparing the peak area at 3.3 to 3.5 ppm (-$CH_2CH_2O$- from PEG) to the peak area at 7.2 to 7.4 ppm (hydrogens from phenyl groups in Phe moieties). The content of methylcoumarin can be calculated by absorption at 320 nm in UV-vis spectrum of the sample calibrated with standard curve of 7-(carboxymethoxy)-4-methylcoumarin. Combining the results from $^1$H NMR and UV-vis spectrum, the molar amount of PEG or methylcoumarin divided by the total molar amount of repeating units was calculated, and defined as the grafting ratio. From the calculated grafting ratios listed in Table 2.1, the contents of PEG and methylcoumarin in the polymer can be controlled by adjusting the feed ratio of NHS-PEG-MAL and 7-(chlorocarbonylmethoxy)-4-methylcoumarin to Lys-Phe-PEA.

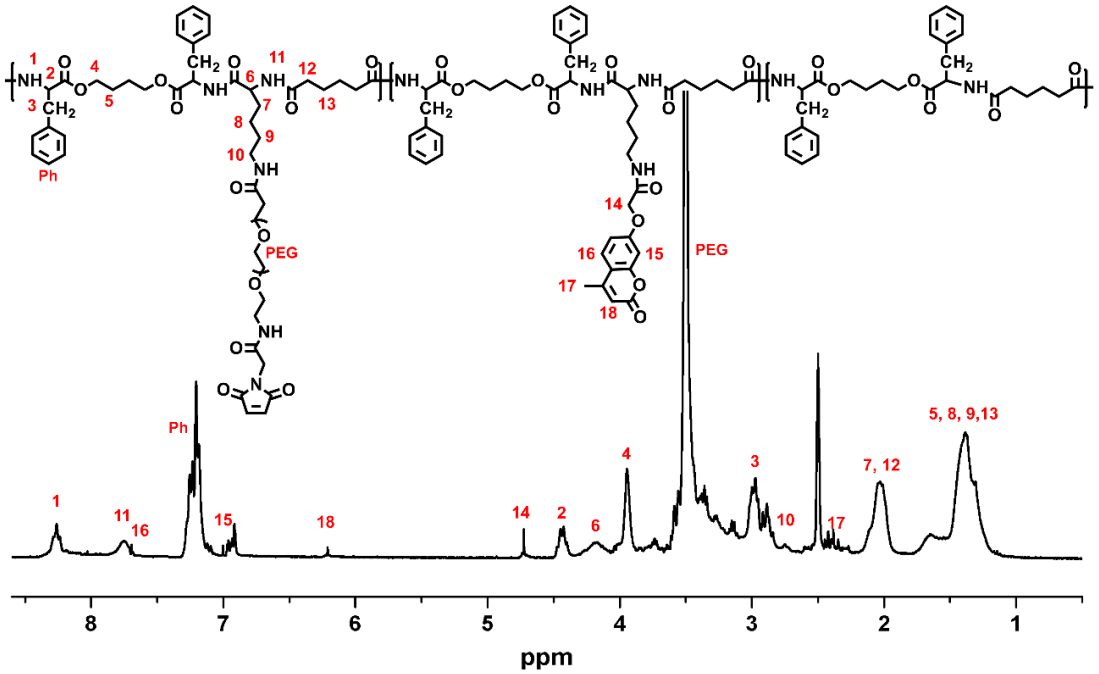


**Figure 2.3**. $^{1}$H NMR spectrum of Lys-Phe-PEAcou-PEG.

As shown in Figure 2.1 and 2.2, the Lys-Phe-PEAcou-PEG polymer is amphiphilic, and can self-assemble into spherical micellar structure in aqueous solution. The influence of grafting ratio on micelle sizes was examined and the results are shown in Table 2.1. A higher methylcoumarin content leads to an increase in Lys-Phe-PEAcou-PEG micelle size due to the hydrophobicity of methylcoumarin molecules. It's also reported that excessive amount of methylcoumarin could result in interparticle crosslinking [10] and further increase the size of assembled structure. The Lys-Phe-PEAcou-PEG micelles are designed for the intracellular delivery of chemotherapeutics, and Sakurai et al. [33] reported that drug carriers less than 200 nm resulted in more effective delivery because they are less likely to be captured by reticuloendothelial system (RES) than larger particles. Based on the above consideration, the Lys-Phe-PEAcou-PEG micelles with 43% grafting ratio for PEG and 5% grafting ratio for methylcoumarin is chosen for the rest of the study.

**Table 2.1**. Size data of uncrosslinked (unXL) Lys-Phe-PEAcou-PEG micelles with various grafting ratio of PEG and methylcoumarin (MCM).

| Expected grafting ratio | Actual grafting ratio[a] | DLS size of unXL Lys-Phe-PEAcou-PEG micelles /nm |
|---|---|---|
| 45% PEG + 5%MCM | 43%PEG + 5% MCM | 197.13 ±7.60 |
| 35% PEG + 15%MCM | 31%PEG + 12% MCM | 400.22 ± 17.69 |
| 25% PEG + 25%MCM | 23%PEG + 29% MCM | 592.13 ± 5.90 |
| 15% PEG + 35%MCM | 9%PEG + 40% MCM | 762.00 ± 11.23 |

a. Grafting ratio is defined as the molar amount of PEG or MCM divided by the total molar amount of repeating units in Lys-Phe-PEA.

### *2.4.2 Characterization of the photo-crosslinked Lys-Phe-PEAcou-PEG micelles*

The process of photo-crosslinking and de-crosslinking of Lys-Phe-PEAcou-PEG micelles was monitored by UV-vis spectra and shown in Figure 2.4. Methylcoumarin monomer exhibits a unique absorption peak at 320 nm. A decrease in absorbance at 320 nm was observed when the micelle solution was subjected to 365 nm irradiation, suggesting the formation of methylcoumarin photodimer. After 3 hrs irradiation, no further decrease at 320 nm peak was observed, indicating most available methylcoumarin monomers have been converted into dimers. The dimerization degree of methylcoumarin in crosslinked Lys-Phe-PEAcou-PEG micelles, defined as $(1\text{-}A320_{initial}/A320_{end})$, is calculated to be 71%. The recovery of absorbance peak at 320 nm was also observed when the micelle solution was subjected to 254 nm irradiation. The de-crosslinking process was complete within 1 hr as no further recovery was detected, and the degree of dimerization dropped to 7%, which means more than

90% of the methylcoumarin photodimer have been photo-cleaved. This reversible change of methylcoumarin monomers vs. dimers observed in the UV-vis spectra in Figure 2.4 demonstrates the successful manipulation of crosslinking and de-crosslinking in Lys-Phe-PEAcou-PEG micelle system. In addition to being photo-controllable, coumarin-based photo-crosslinking technique is easy to apply, and with no need to introduce purification steps to remove any by-products. In this research we aim to take advantage of the photo-crosslinking to improve micellar stability, and the de-crosslinking process was only applied in the test of drug loading content to facilitate the complete dissolution of DOX-loaded micelles.

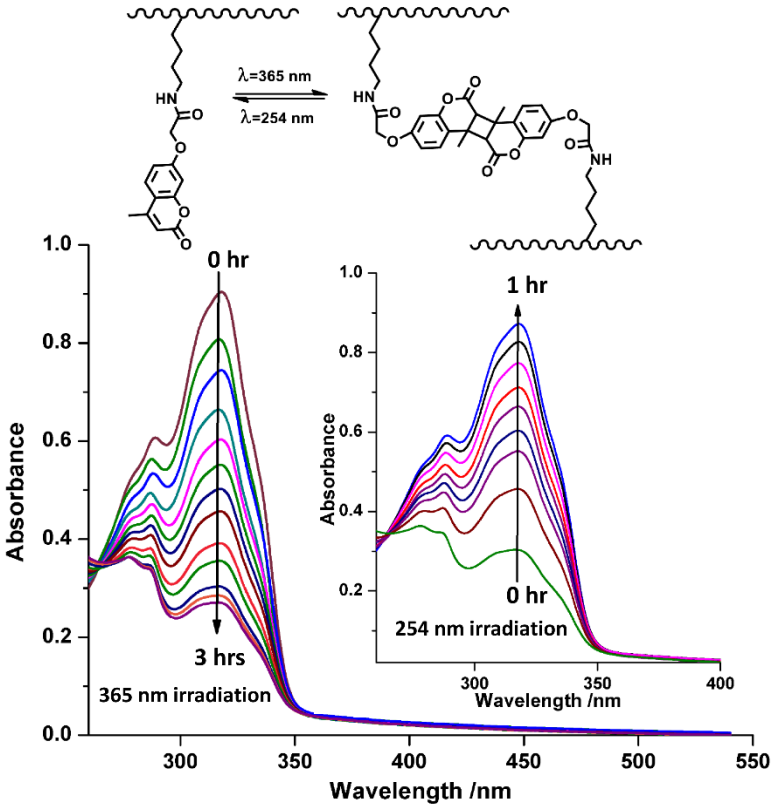


**Figure 2.4**. Monitoring the process of photo-crosslinking (irradiated by 365 nm UV light) and de-crosslinking (irradiated by 254 nm UV light) of Lys-Phe-PEAcou-PEG micelles via UV-Vis spectroscopy. The decrease in the

absorbance peak at 320 nm represents the formation of methylcoumarin photodimer.

The size characterization for Lys-Phe-PEAcou-PEG micelles after photo-crosslinking is listed in Table 2.2. The average DLS diameter of the Lys-Phe-PEAcou-PEG micelles decreased to 157.03 ± 4.5 nm after crosslinking, compared to the 191.37 ± 7.6 nm for the uncrosslinked one. The surface charge is not affected by crosslinking, as both crosslinked and uncrosslinked Lys-Phe-PEAcou-PEG were cationic (8.99 ± 0.23 mV and 7.47 ± 0.51mV, respectively), due to the covalently attached cysteine-lysine dipeptide. The major purpose for introducing dipeptide is to block the unreacted maleimide functional group and prevent unwanted interactions with any thiol containing molecules in cells or biological fluids. In future applications, the dipeptide can also be replaced by other bio-active molecules to introduce functionality. The critical micelle concentration (CMC) of the uncrosslinked Lys-Phe-PEAcou-PEG was detected to be 20.4 mg/L. And CMC was non-detectable for the crosslinked Lys-Phe-PEAcou-PEG micelles with nile red probe. Micelles with lower CMC can better maintain structural integrity against dilution, which is a common practice of intravenous administration of drugs. Therefore, we conclude that the photo-crosslinked Lys-Phe-PEAcou-PEG micelles can effectively improve the structural stability of Lys-Phe-PEAcou-PEG micelles against dilution.

**Table 2.2**. Characterization of Lys-Phe-PEAcou-PEG micelles before and after photo-crosslinking.

| Micelles | DLS size/nm | PDI | Zeta potential /mV | CMC[a] / mg/L | DLC[b] | EE[b] |
|---|---|---|---|---|---|---|
| unXL Lys-Phe- | 191.37 ± 7.6 | 0.167±0.009 | 7.47±0.51 | 20.4 | | |

| | | | | | | |
|---|---|---|---|---|---|---|
| PEAcou-PEG | | | | | | |
| XL Lys-Phe-PEAcou-PEG | 157.03 ± 3.5 | 0.151 ±0.06 | 8.99±0.23 | | | |
| unXL Lys-Phe-PEAcou-PEG/DOX | 168.76 ± 11.8 | 0.209 ±0.05 | 7.08±0.67 | | 7.6% | 65.7% |
| XL Lys-Phe-PEAcou-PEG/DOX | 139.08 ± 11.2 | 0.187 ±0.06 | 7.23±0.69 | | 8.2% | 71.2% |

a. Critical micelle concentration (CMC) is the lowest concentration for micelle formation.

b. DLC (drug loading content) and EE(encapsulation efficiency) were determminded for DOX-loaded crosslinked (XL) or uncrosslinked (unXL) Lys-Phe-PEAcou-PEG micelles.

### *2.4.3 Effect of serum and enzyme on the stability of Lys-Phe-PEAcou-PEG micelles*

TEM morphology of the photo-crosslinked Lys-Phe-PEAcou-PEG micelles (Figure 2.5A) further confirmed the formation of spherical assembly from the amphiphilic polymer in an aqueous solution.

Previous research demonstrated that the presence of serum protein impacted the structural integrity of PEGylated micelles [34, 35]. The structural

stability of Lys-Phe-PEAcou-PEG micelles in serum-containing environment, was determined by measuring the Forster Resonance Energy Transfer (FRET) of DiL/DiO pair. When encapsulated in the hydrophobic interior of micelles, the FRET pair is close enough to ensure efficient energy transfer. However, upon micelle disintegration, the FRET pair is released to the media and the distance between them is beyond the permissible range for FRET [36]. The FRET ratio reflects the level of micelle disintegration [37]. As shown in Figure 2.5C, in the absence of FBS, a slight decrease in FRET ratio (5%-10%) was observed for both crosslinked and uncrosslinked micelles, suggesting that both micelles retained their stability in phosphate buffer. However, FRET ratio decreased to 0.6 when uncrosslinked micelles were incubated with whole FBS for 48 hrs, which suggest the leakage of FRET pairs into aqueous media. The disintegration of the uncrosslinked Lys-Phe-PEAcou-PEG micelles in FBS containing environment can be attributed to the lack of an internal stabilizing force so that the serum protein disrupted the original interactions between unimers and pulled the micelles apart. The crosslinked Lys-Phe-PEAcou-PEG micelles, on the other hand, remained stable, as FRET ratio was 0.83 after 48 hrs incubation with FBS. The cross-links between methylcoumarin-containing segments help to maintain the structural integrity.

We also examined the stability of micelles incubated with α-chymotrypsin, an enzyme which preferentially attacks the hydrophobic amino acids such as phenylalanine, and cleaves the amide bonds. From Figure 2.5D, FRET ratio decreased to 0.64 and 0.61 respectively, for crosslinked and uncrosslinked micelles, after incubated with α-chymotrypsin for 48 hrs. The results indicate that the crosslinked Lys-Phe-PEAcou-PEG micelles are still sensitive to proteolytic enzyme. The destabilization of crosslinked micelles after enzymatic degradation is further substantiated by TEM image in Figure 2.5B, as no spherical assembled structure was observed.

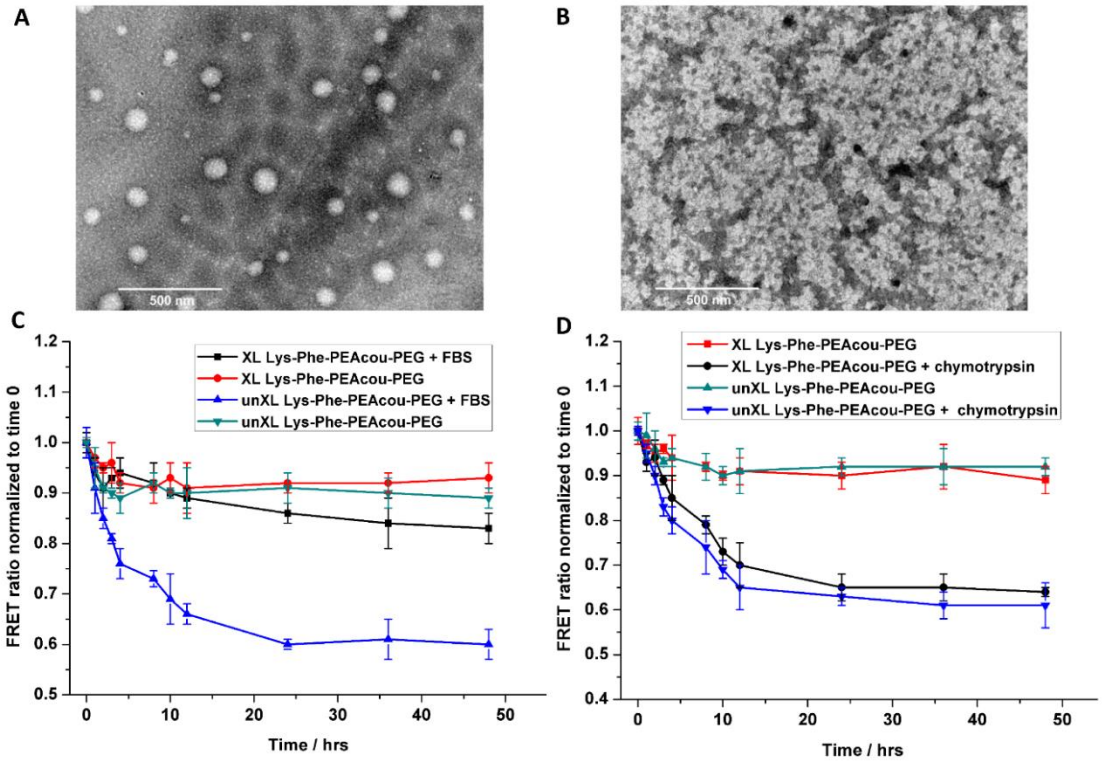


**Figure 2.5**. A) TEM image of crosslinked Lys-Phe-PEAcou-PEG micelles dispersed in phosphate buffer (pH=7.4). B) TEM image of crosslinked Lys-Phe-PEAcou-PEG micelles after 48 hrs incubation with 0.2 mg/mL α-chymotrypsin. C) Stability of crosslinked or uncrosslinked Lys-Phe-PEAcou-PEG micelles incubated with FBS. The FRET ratio was measured for micelles after incubation in phosphate buffer or whole FBS. D) Stability of crosslinked or uncrosslinked Lys-Phe-PEAcou-PEG micelles incubated with α-chymotrypsin. The FRET ratio was measured for micelles after incubation with phosphate buffer or 0.2 mg/mL α-chymotrypsin. Values represent the average ± SD (n=3).

### *2.4.4 In vitro drug release of DOX from Lys-Phe-PEAcou-PEG micelles*

The Lys-Phe-PEAcou-PEG micelles were then evaluated as the delivery vehicles for DOX. The encapsulation efficiency for DOX was 65.7 % in crosslinked Lys-Phe-PEAcou-PEG micelles and 71.2 % in uncrosslinked micelles (Table 2.2). Effective encapsulation was achieved in the Lys-Phe-

PEAcou-PEG micelles, and the efficiency is comparable to other biodegradable micelle systems [15, 16].

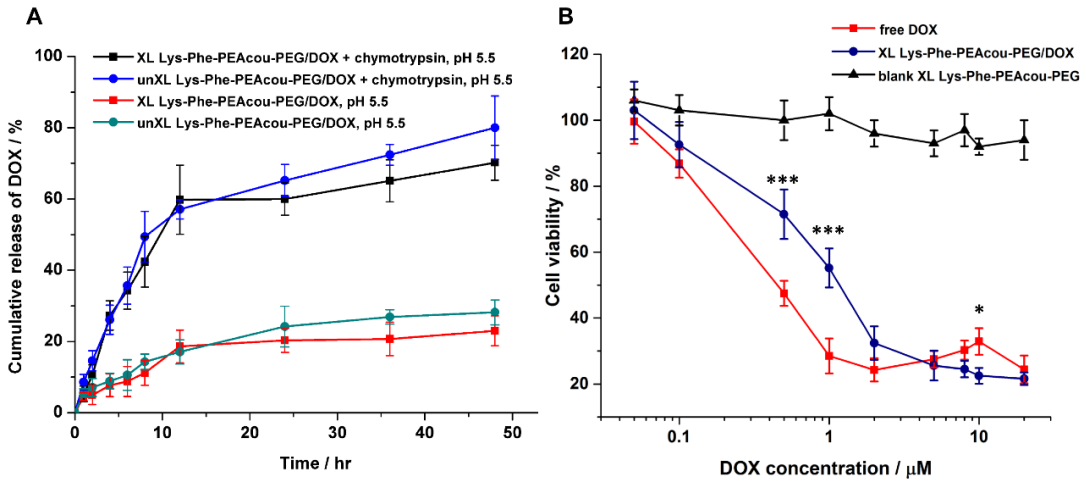


**Figure 2.6**. A) In vitro release profile of DOX from Lys-Phe-PEAcou-PEG micelles in pH 5.5 phosphate buffer with or without the presence of 0.2 mg/mL α-chymotrypsin. Values represent the average ± SD (n=3). B) Viability of HCT116 cells after 48 hrs incubation with blank crosslinked micelles, DOX-loaded crosslinked Lys-Phe-PEAcou-PEG micelles, or free DOX with various DOX concentrations. Values represent the average ± SD (n=6). Statistical significance was compared between micellar DOX treated group and free DOX treated control: *, $p < 0.05$; **, $p < 0.01$; ***, $p < 0.001$.

To examine the in vitro release of DOX from Lys-Phe-PEAcou-PEG micelles, 10 mM phosphate buffer (pH 5.5) with the presence of α-chymotrypsin was chosen as the release media, which would work as an artificial mimic of the endolysosomal environment due to the endolysosomal entrapment of of Lys-Phe-PEAcou-PEG micelles (Figure 2.8A). The release profiles of DOX are shown in Figure 2.6A. First, at the end of 48 hrs, the crosslinked micelles had 70% cumulative DOX release in the presence of α-chymotrypsin (black curve), while only less than 25% cumulative was achieved without any enzyme (red curve). The results indicate that DOX release was

effectively accelerated by enzymatic degradation of the crosslinked carrier. Second, no significant difference was observed in the release of DOX from crosslinked and uncrosslinked micelles with the presence of enzyme. It can be concluded that enzymatic degradation has the major impact on the release kinetics, and the effect of photo-crosslinking is relatively minor.

As demonstrated in section 3.3, the structural stability of the uncrosslinked Lys-Phe-PEAcou-PEG micelles is poor in serum containing environment. In addition, the uncrosslinked micelles would disassociate when an equivalent DOX concentration was lower than 2.7 μM, i.e., inadequate for the proposed DOX dose-dependent study. On the other hand, photo-crosslinking significantly improved the stability of the Lys-Phe-PEAcou-PEG micelles, and the crosslinked micelles maintained their structural stability at DOX concentrations lower than 0.5 μM. Considering the fact that photo-crosslinks did not cause any barrier for DOX release when enzyme was present, we decided to focus on the crosslinked Lys-Phe-PEAcou-PEG micelles to investigate the dose-dependent effect at various DOX concentrations in the subsequent studies.

### *2.4.5 Cytotoxicity of DOX-loaded crosslinked Lys-Phe-PEAcou-PEG micelles in HCT116 cells*

Cytotoxicity of both blank micelles and DOX-loaded micelles toward both HCT116 human colon cancer cells (Figure 2.6B) were examined. From the data in Figure 2.6B, no cytotoxicity from the blank crosslinked Lys-Phe-PEAcou-PEG micelles toward HCT116 cells was observed at all the testing concentrations. We concluded that cytotoxicity induced by DOX-loaded micelles should be attributed to the released DOX, instead of the carriers.

The cytotoxicity of DOX-loaded crosslinked Lys-Phe-PEAcou-PEG micelles on HCT116 cells was then tested, and compared with free DOX, with equivalent concentrations of DOX ranging from 0.05 to 20 μM. The data in Figure 2.6B demonstrates that, at high DOX concentration (10 μM), DOX-loaded crosslinked Lys-Phe-PEAcou-PEG micelles showed significantly higher

cytotoxicity than free DOX. However, at lower DOX concentration (< 2 μM), free DOX still statistically outcompeted micellar DOX. No significant difference was detected at 2-8 μM or 20 μM. The IC50 was 1.22 μM for DOX-loaded crosslinked Lys-Phe-PEAcou-PEG micelles and 0.41 μM for free DOX, respectively.

### *2.4.6 Uptake study of DOX-loaded crosslinked Lys-Phe-PEAcou-PEG micelles*

Inhibition study was performed to explore the endocytosis pathway of Dox-loaded crosslinked Lys-Phe-PEAcou-PEG micelles, and the data is shown in Figure 2.7A. Incubation of HCT116 cells with DOX-loaded crosslinked micelles at 4 °C for 4 hrs resulted in a 40% decrease in the intracellular DOX level. Similarly, inhibition of macropinocytosis (by amiloride) and the clathrin-mediated pathway (by chloropromazine) also resulted in a significant inhibition of DOX transmigration. On the other hand, inhibition of caveolae (by nystatin) and lipid raft mediated endocytosis (by methyl-β-cyclodextrin), resulted in no significant difference in intracellular DOX level compared to control. We therefore conclude that the translocation of DOX-loaded crosslinked Lys-Phe-PEAcou-PEG micelles into HCT116 cells is energy-dependent and involves both macropinocytosis and clathrin-mediated endocytosis. This is in contrast to the passive diffusion of free DOX across cell membrane [38], which is not dependent on either ATP consumption or transport vesicles.

To study the intracellular DOX level vs. time, we monitored the uptake of DOX-loaded crosslinked Lys-Phe-PEAcou-PEG micelles or free DOX by HCT116 cells within 24 hrs. At the first 4 hrs, average fluorescence from HCT116 cells treated with micellar DOX was 50% lower than free DOX, and the difference was statistically significant. But after 12 hrs to 24 hrs incubation, no statistically significant difference was detected, as shown in Figure 7B. Two possible explanations are proposed for this result. First, the endocytosis of micellar DOX generally takes longer time than the passive diffusion of free

DOX. Second, DOX was located in the hydrophobic interior of micelles and it also takes time for the migration of DOX out of the carriers to achieve similar level of intracellular fluorescence as free DOX.

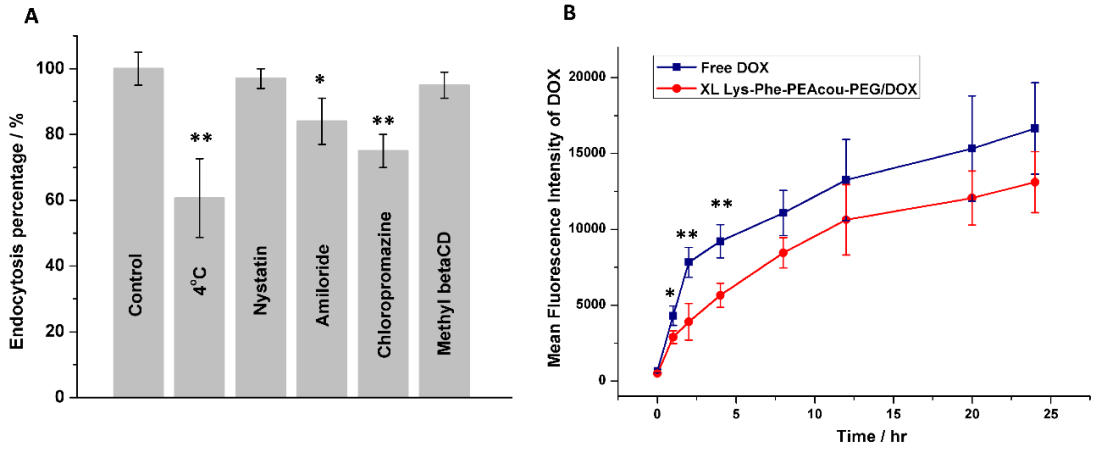


**Figure 2.7**. A) Endocytosis inhibition studies. HCT116 cells pre-treated with various endocytosis inhibitors were incubated with DOX-loaded crosslinked Lys-Phe-PEAcou-PEG micelles (2 μM equivalent DOX concentration) for 4 hrs. Mean fluorescence from cellular DOX was recorded by flow cytometry and normalized to the DOX level in control (cells not treated with any inhibitor). Values represent the average ± SD (n=3). Statistical significance was compared between inhibitor treated group and control. B) Mean fluorescence of HCT116 cells incubated with free DOX or DOX-loaded crosslinked Lys-Phe-PEAcou-PEG (2 μM equivalent DOX concentration) vs. incubation time. Values represent the average ± SD (n=3). Statistical significance was compared between micellar DOX treated group and free DOX treated control: *, $p < 0.05$; **, $p < 0.01$.

### *2.4.7 Subcellular distribution of DOX-loaded crosslinked Lys-Phe-PEAcou-PEG micelles*

First, we identified the subcellular distribution of blank crosslinked micelles (no DOX loaded). No distinguishable fluorescence from the methylcoumarin moieties was detected when exited at 405 nm at regular level

of laser power (data not shown). This can be attributed to the low methylcoumarin concentration in HCT116 cells. Since methylcoumarin is a relatively weak fluorophore compared to other fluorescent dyes used for cell imaging, and the formation of photodimer would further quench its fluorescence. As a result, we characterized the subcellular distribution of blank crosslinked Lys-Phe-PEAcou-PEG micelles labelled with rhodamine, as shown in Figure 2.8A and Table 2.3. After 4 hrs incubation with HCT116 cells, a high level of co-localization was observed between the blank micelles and endolysosomes, with a Pearson's coefficient of 0.90 ± 0.08, which indicates that the blank micelles were largely entrapped in endolysosomes. No significant level of co-localization was observed with either nuclei or mitochondria. Endolysosomal compartments provide the sequestration of various proteolytic enzymes, which can accelerate the intracellular release of DOX from the crosslinked Lys-Phe-PEAcou-PEG micelles due to the enzymatic biodegradability of the pseudo protein micelles.

Co-localization study was performed to identify the intracellular distribution of DOX loaded in crosslinked Lys-Phe-PEAcou-PEG micelles. By comparing the DOX fluorescence with specific organelle markers for the nuclei (Hoechst), mitochondria (Mitotracker) or endolysosomes (Lysotracker), DOX-loaded crosslinked micelles exhibited different distribution profile than free DOX. As shown in Figure 2.8B, a high level of co-localization (yellow) was observed between the red fluorescence from DOX loaded in crosslinked micelles and the green pseudo-color from Lysotracker or Mitotracker. The Pearson's coefficient was calculated to be 0.63 ± 0.16 for DOX/Lysotracker, and 0.89 ± 0.10 for DOX/Mitotracker. The correlation coefficients also confirm that DOX from crosslinked micelles was located in both mitochondria and endolysosomes. Considering the subcellular distribution of the blank micelles, it is reasonable to conclude that the DOX released from the biodegraded micelle further migrated out of endolysosomes and co-localized with mitochondria. No overlap between DOX and the nuclei was observed, indicating that DOX from

crosslinked micelles did not translocate into the nuclei. Free DOX (Figure 2.8C), on the other hand, significantly co-localized with the nuclei, as the Pearson's coefficient was 0.75 ± 0.11; but not with either mitochondria or endolysosomes.

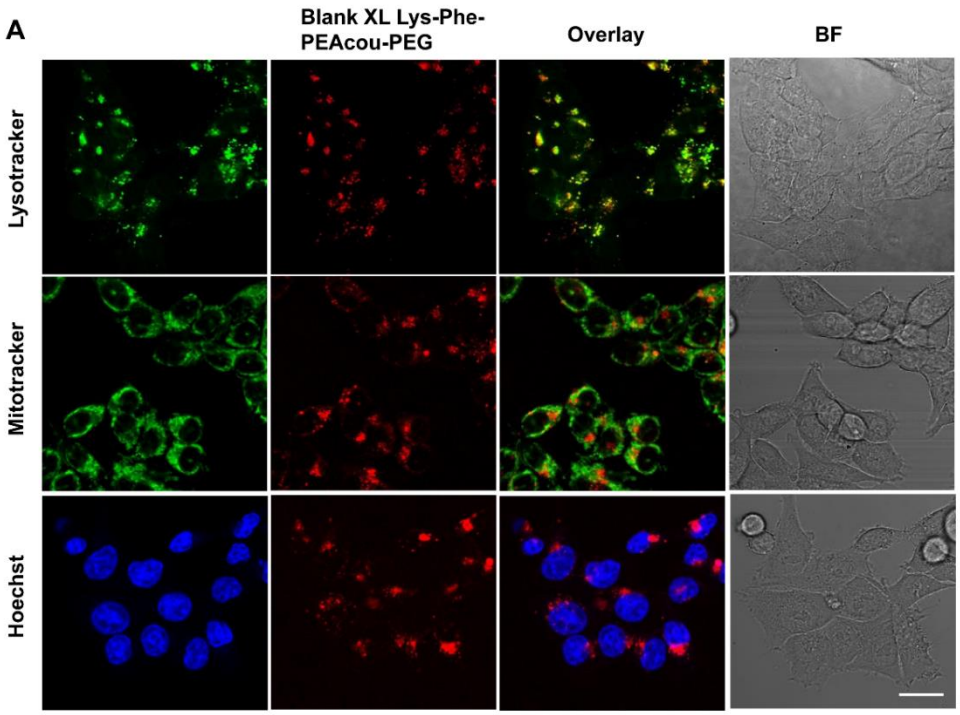

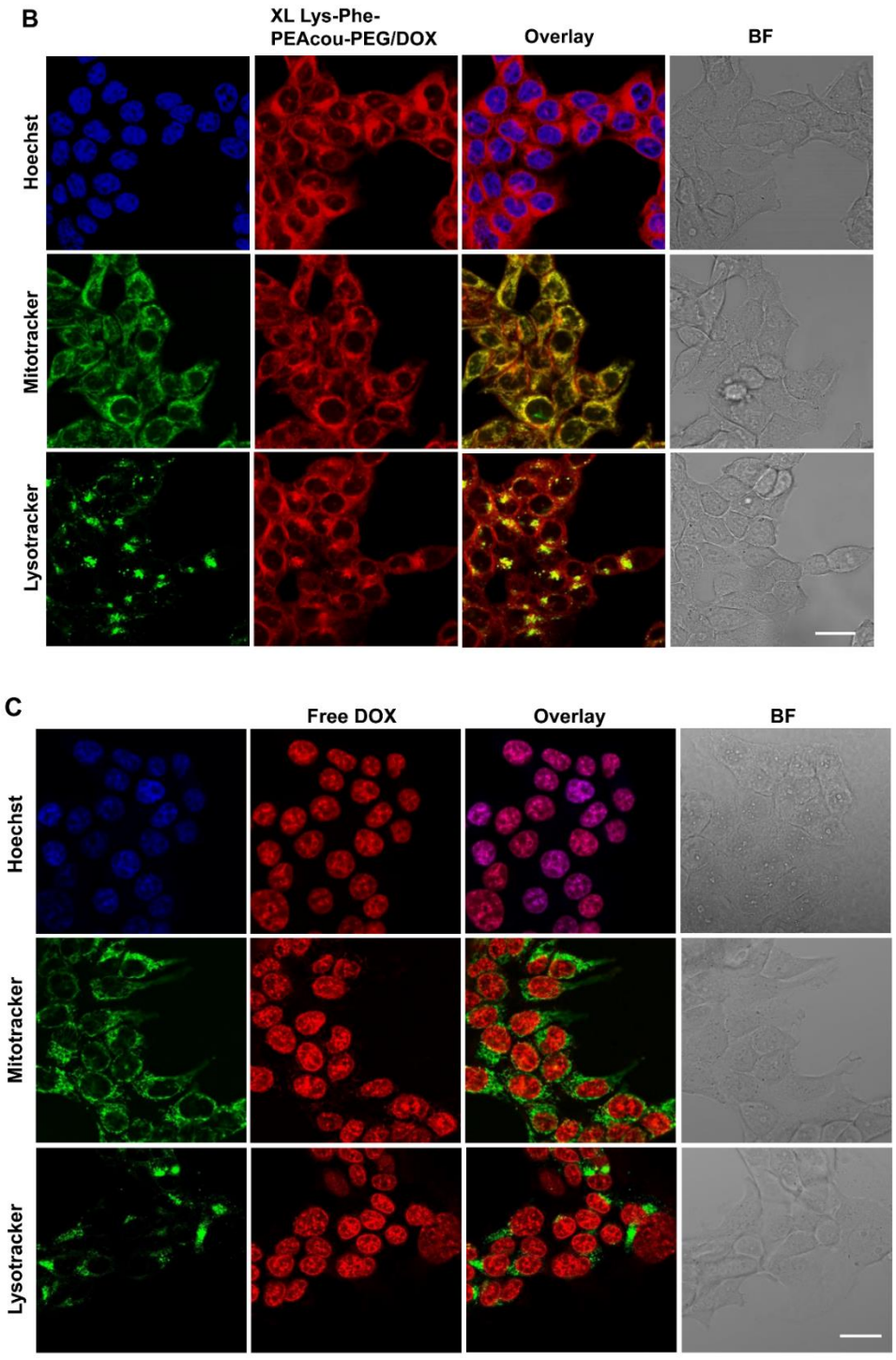


**Figure 2.8**. Subcellular distribution in HCT116 colon cancer cells after 4 hrs incubation with A) Rhodamine labeled blank crosslinked Lys-Phe-PEAcou-PEG micelles. The nuclei, mitochondria and endolysosomes were labelled with specific

organelle markers, Hoechst 33342 (blue), Mitotracker green and Lysotracker green, respectively. B) DOX loaded in crosslinked Lys-Phe-PEAcou-PEG micelles. C) free DOX. The equivalent concentration of DOX is 5 μM. The nuclei, mitochondria and endolysosomes were labelled with specific organelle markers, Hoechst 33342 (blue), Mitotracker deep red FM (green pseudo-color) and Lysotracker deep red (green pseudo-color), respectively. Scale bar represents 20 μm.

**Table 2.3**. Pearson's coefficient for the co-localization of DOX or blank crosslinked Lys-Phe-PEAcou-PEG micelles with organelle markers in HCT116 colon cancer cells

| | Hoechst | Lysotracker | Mitotracker |
|---|---|---|---|
| Blank XL Lys-Phe -PEAcou-PEG micelles | 0.20 ± 0.09 | 0.90 ± 0.08 | 0.51 ± 0.10 |
| DOX loaded in XL Lys-Phe-PEAcou-PEG micelles | 0.20 ± 0.04 | 0.63 ± 0.16 | 0.89 ± 0.10 |
| Free DOX | 0.75 ± 0.11 | 0.13 ± 0.05 | 0.21 + 0.13 |

### *2.4.8 Mitochondria damage and oxidative stress induced by DOX-loaded crosslinked Lys-Phe-PEAcou-PEG micelles*

Mitochondria play an important role in signalling and regulation of cell death [39, 40]. The opening of mitochondrial permeability transition pore (MPTP) as well as the loss of mitochondrial membrane potential (MMP) are crucial events in apoptotic cell death. As co-localization was observed between micellar DOX and mitochondria, we further characterized the mitochondrial damage in HCT116 cells.

MPTP is a protein pore that forms in the inner membrane of the mitochondria, their opening represents the loss of membrane integrity of mitochondria, and will further induce the release of mitochondrial components.

As demonstrated in Figure 2.9A and 2.9B, cobalt chloride, a specific quencher for calcein fluorescence, only quenched the cytosolic calcein fluorescence in untreated cells or blank micelles treated cells. Calcein fluorescence from the mitochondria was observed in healthy cells as no MPTP formed and the mitochondrial membrane maintained their integrity to prevent the permeation of cobalt chloride. However, in HCT116 cells treated with DOX-loaded crosslinked Lys-Phe-PEAcou-PEG micelles, the quenching of mitochondrial calcein fluorescence was observed, which suggested the opening of MPTP and the subsequent permeation of cobalt chloride into mitochondria was significant. The DOX concentration that induced mitochondrial calein quenching and MPTP opening for micellar DOX was between 2 to 10 μM (as shown in Figure 2.9C). In the case of free DOX, MPTP opening was detected at lower DOX concentrations (0.5 to 2 μM).

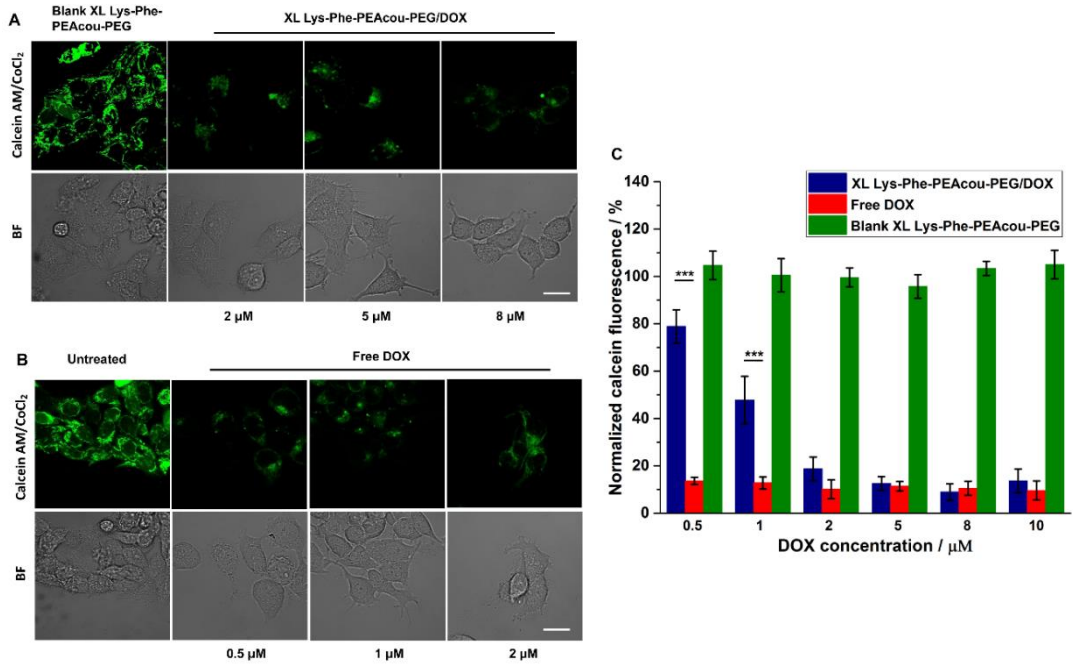


**Figure 2.9**. A) Confocal images of mitochondrial permeability transition pore (MPTP) opening in HCT 116 cells incubated with A) DOX-loaded crosslinked Lys-Phe-PEAcou-PEG/DOX micelles or B) free DOX for 24 hrs with various DOX

concentrations. Calcein AM/ cobalt chloride were used to visualize MPTP. Untreated cells or cells incubated with blank micelles were also characterized. C) The fluorescence intensity of calcein AM normalized to total number of cells, expressed as the percentage to untreated control and plotted as a function of DOX concentration. Statistical significance was compared between micellar DOX treated group and free DOX treated control: *, $p < 0.05$; **, $p < 0.01$; ***, $p < 0.001$.

As illustrated in Figure 2.10A, when treated with blank crosslinked micelles, less than 2% of HCT116 cells were detected with depolarized mitochondria (quadrant 3, lower level of J aggregates and higher level of JC-1 monomer). No significant difference was observed between blank micelles treated cells or untreated cells, which demonstrates the biological safety of the blank Lys-Phe-PEAcou-PEG micelles to mitochondria. The data in Figure 2.10B shows the percentage of HCT116 cells which lost their MMP upon 24 hrs incubation with either free DOX, or DOX-loaded crosslinked Lys-Phe-PEAcou-PEG micelles. At the DOX concentration between 2 to 10 μM, a significantly higher percentage of the HCT116 cells with depolarized mitochondria was detected when treated with micellar DOX, compared to free DOX. The loss of MMP marks the dysfunction of mitochondria, and can be associated with the release of apoptogenic factors, an early event that initiates apoptosis. However, it's also reported that the loss of MMP can be a consequence of apoptotic-signalling pathway[41]. So far we can only conclude from the MPTP and MMP results that DOX-loaded crosslinked Lys-Phe-PEAcou-PEG micelles generally caused higher level of mitochondria damage, compared to free DOX, at the same duration and concentration of drug exposure.

Since mitochondria are the major source of ROS generation, we subsequently examined the ROS production in HCT116 cells, which is another event that closely related to apoptosis. The intracellular ROS induced by micellar DOX was comparable to that induced by free DOX at 0.5 and 1 μM (Figure 2.10C); but at higher DOX concentrations (2-8 μM), micellar DOX

induced significantly higher levels of ROS than free DOX. Although the mean ROS level induced by micellar DOX at 10 μM was greater than free DOX, the difference was statistically insignificant at $p < 0.05$.

The difference in intracellular ROS level can be attributed to the difference in their subcellular distribution. Since mitochondria function as the major domain for ROS generation, it is reasonable that micellar DOX interacted with mitochondria and produced more ROS at relatively higher DOX concentration (2-8 μM). Overproduction of ROS in cells can cause damage to proteins and DNA that further initiates apoptosis[42]. Therefore, the MMP, MPTP and ROS data suggest that HCT116 cells treated with DOX-loaded crosslinked Lys-Phe-PEAcou-PEG micelles, are presumed to be more susceptible to apoptotic cell death at higher DOX concentration.

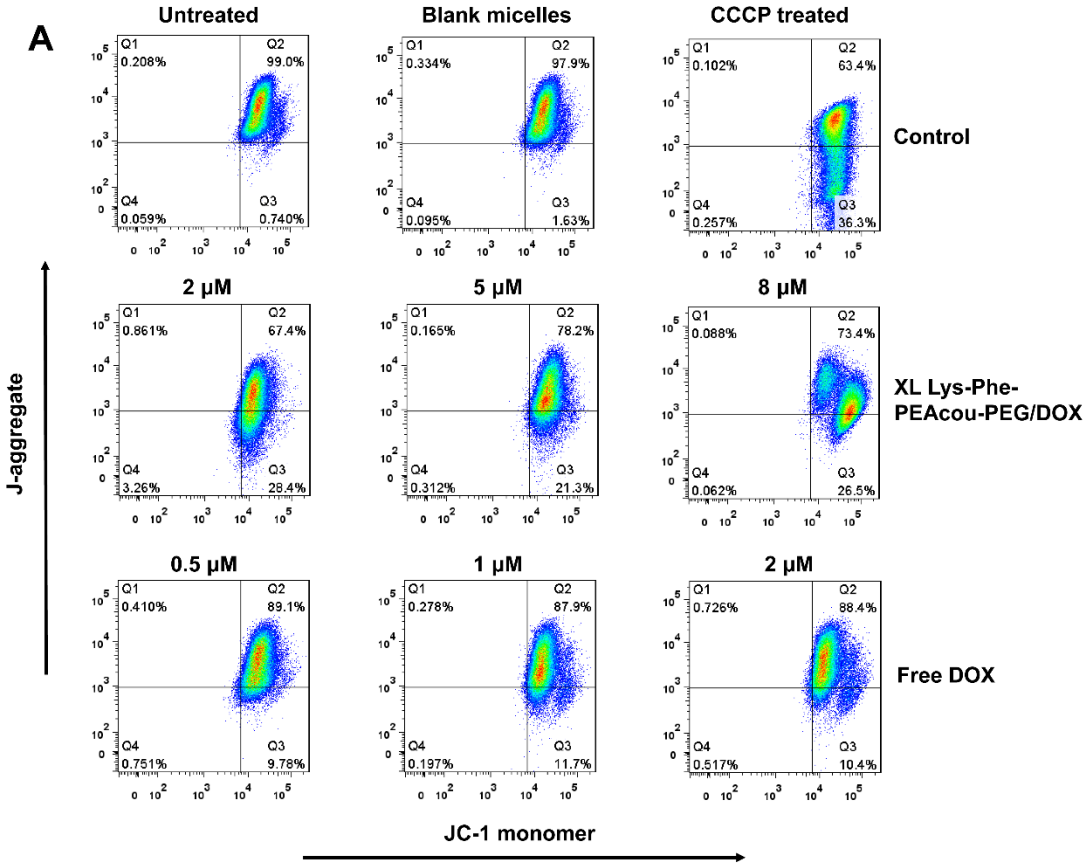

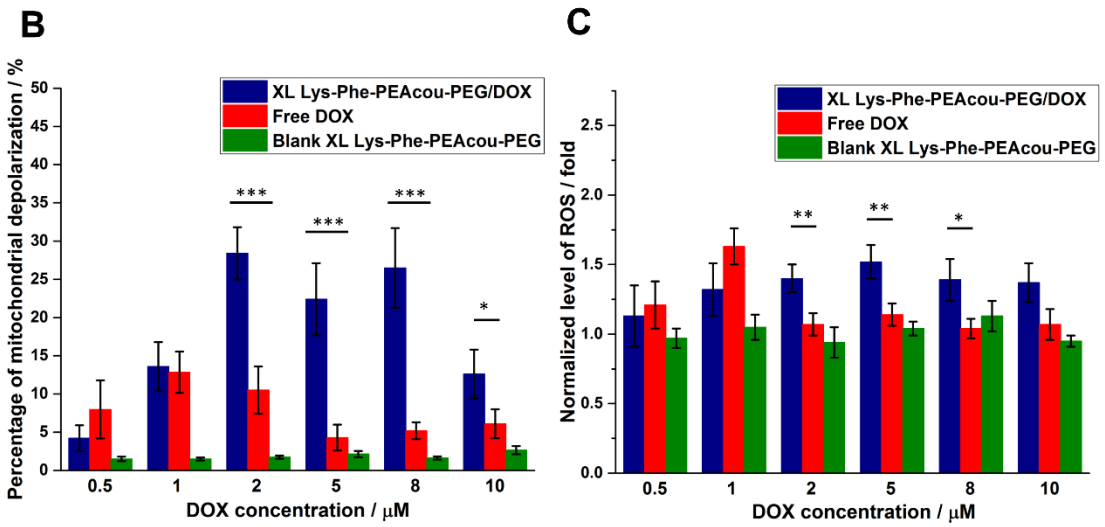


**Figure 2.10**. A) Flow cytometry detection of mitochondrial membrane potential (MMP) of HCT116 colon cancer cells by JC-1 assay. HCT116 cells were treated for 24 hrs with either DOX-loaded crosslinked Lys-Phe-PEAcou-PEG micelles or free DOX with various DOX concentrations, cells incubated with blank crosslinked Lys-Phe-PEAcou-PEG micelles, or CCCP treated cells were also tested. B) The percentage HCT116 cells with depolarized mitochondria (quadrant 3) in JC-1 assay were recorded and plotted as a function of DOX concentration. C) The intracellular reactive oxygen species (ROS) were probed by dihydroethidium (DHE). HCT116 cells were treated for 24 hrs with blank crosslinked micelles, DOX-loaded crosslinked Lys-Phe-PEAcou-PEG micelles or free DOX with various DOX concentrations. The level of ROS was normalized to the untreated control. Values represent the average ± SD (n=3). Statistical significance was compared between micellar DOX treated group and free DOX treated control: *, $p < 0.05$; **, $p < 0.01$; ***, $p < 0.001$.

### *2.4.9 Dose-dependent apoptosis by DOX-loaded crosslinked Lys-Phe-PEAcou-PEG micelles*

To determine whether the overproduction of ROS and mitochondria damage could actually lead to increased apoptosis in HCT116 cells treated with micellar DOX, we further examined the dose dependent apoptosis. Figure 2.11A shows the confocal images of the apoptotic HCT116 cells by annexin-V

staining. In the apoptotic HCT116 cells induced by DOX-loaded crosslinked Lys-Phe-PEAcou-PEG micelles, the red fluorescence from DOX still distributed in the cytoplasm, while apoptotic cells treated with free DOX exhibited DOX fluorescence only in the nuclei. Micellar DOX with higher DOX concentration (5-10 μM) also exhibited similar distribution in the cytoplasm instead of in the nuclei (data not shown). These results suggest that, instead of intercalating in nuclear DNA, DOX from crosslinked micelles stayed away from the nuclei throughout the apoptotic process, which can be a possible indication of potentially different pathway in inducing apoptosis between micellar DOX and free DOX. Similar results were also reported by Kopeck et al. [43, 44], in which DOX bounded with N-(2-hydroxypropyl) methacrylamide (HPMA) polymer showed different distribution pattern and induced apoptosis in ovarian carcinoma cells by the disruption of mitochondrial function.

The data in Figures 2.11C shows the percentage of early apoptotic cells detected with flow cytometry. For DOX-loaded crosslinked Lys-Phe-PEAcou-PEG micelles, the percentage of apoptotic cells was much lower than free DOX, when the DOX concentration is less than 2 μM. The result is consistent with the lower cytotoxicity data shown in Figure 2.6B, suggesting that at lower DOX concentration, free DOX is more lethal toward HCT116 cells than micellar DOX. However, the difference in apoptosis percentage disappeared at 2 μM DOX concentration as no statistical difference between free DOX and micellar DOX was observed. This trend was reversed when the DOX concentration was > 2 μM, as significantly increased percentage of apoptosis was detected in HCT116 cells treated with micellar DOX. Free DOX, demonstrated by Yokochi et al. [25], induces necrosis at higher dose in HCT116 cells, which explains the reduced apoptosis percentage detected in cells treated with free DOX with concentration > 2 μM. Micellar DOX, on the other hand, was not observed to induce necrotic cell death in the concentration range between 2 to 10 μM.

Cleaved caspase 3 (17-19 kDa) is an active enzyme in the execution of apoptosis. Western blot data in Figure 2.11B suggest that the cleaved caspase 3

was present in HCT116 cells treated with micellar DOX with the DOX concentrations of 2 to 8 μM, or free DOX treated cells with the DOX concentration of 0.5 to 2 μM. The caspase 3/7 activity was further quantified and the data in Figure 2.11D is consistent with the result of apoptosis percentage. For HCT116 cells treated with free DOX, increased caspase 3/7 activity was detected only when DOX concentration was between 0.5-2 μM, and was significantly lower than DOX-loaded crosslinked Lys-Phe-PEAcou-PEG micelles at the DOX concentration > 2 μM. The result of dose-dependent apoptosis in HCT116 cells shows the similar trend with the data in Figure 2.9 and 2.10, which suggests the correlation between apoptosis, MPTP, ROS and MMP, and that the concentration range to induce apoptosis in HCT116 cells is different between micellar DOX and free DOX. Yokochi et al. [25] reported the conditional apoptosis by free DOX in several cancer cell lines, and related the dose-dependent behaviour to DNA methyltransferase. However, detailed molecular biological characterization are required to further elucidate the mechanism of how DOX loaded in crosslinked Lys-Phe-PEAcou-PEG micelles translocated to the mitochondria, and their specific signalling pathway in inducing apoptosis, which would be the focus of our following study.

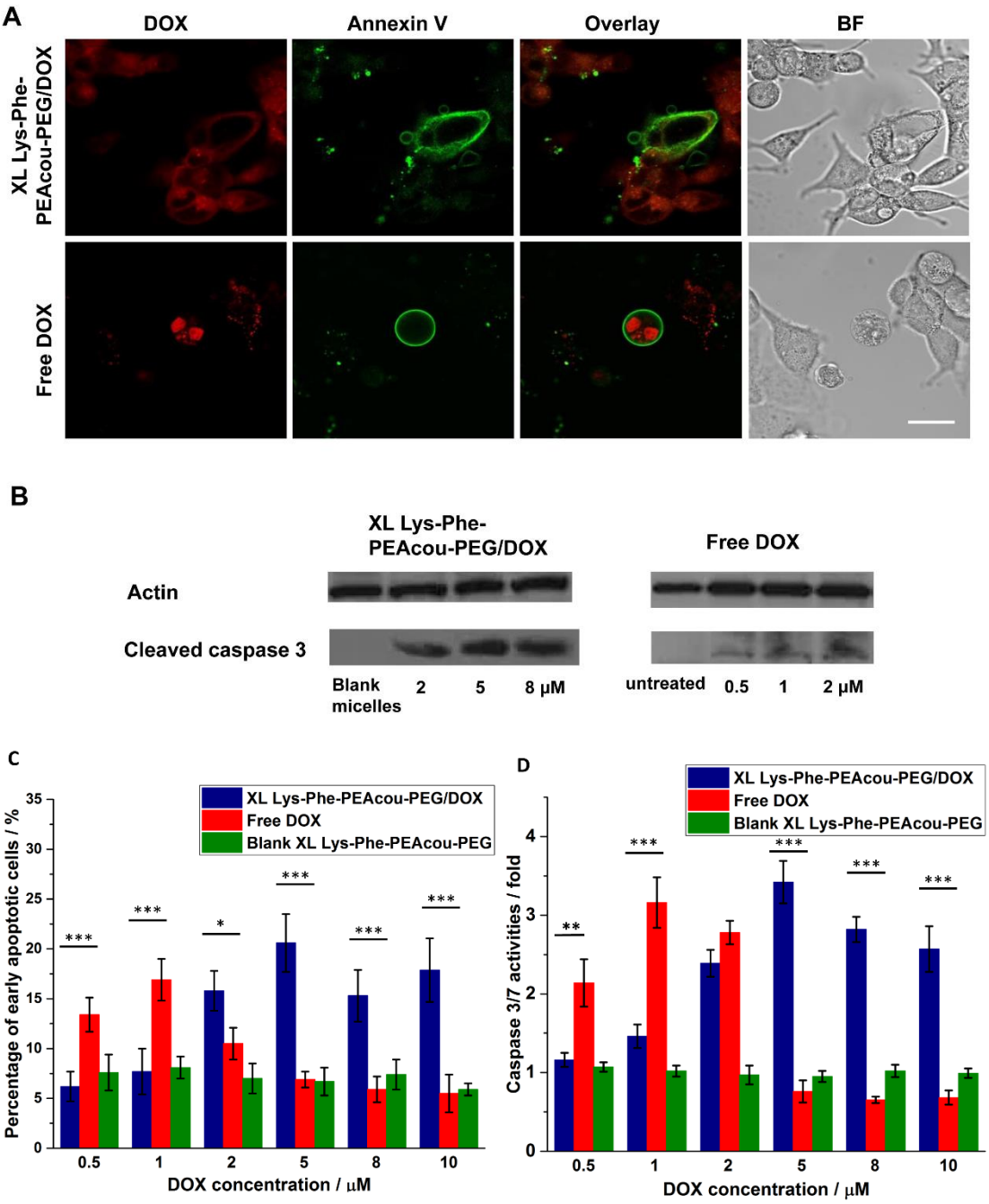


**Figure 2.11**. A) Annexin V staining of apoptotic HCT116 cells treated with DOX-loaded crosslinked Lys-Phe-PEAcou-PEG micelles or free DOX for 48 hrs with equivalent DOX concentration of 2 μM. Red fluorescence is from DOX and the green fluorescence is from annexin V-FITC. Scale bar represents 20 μm. B) Western blot to identify the presence of cleaved caspase 3 (17 – 19 kDa) in the lysate of HCT116 cells

after incubation with DOX-loaded crosslinked Lys-Phe-PEAcou-PEG micelles or free DOX. Untreated cells or cells incubated with blank crosslinked micelles were also characterized. C) Percentage of early apoptotic HCT116 cells (annexin V positive and SYTOX Red negative cells) detected by flow cytometry. HCT116 cells were treated with blank crosslinked micelles, DOX-loaded crosslinked Lys-Phe-PEAcou-PEG micelles or free DOX with various DOX concentrations for 48 hrs. D) Caspase 3/7 activity assay for HCT116 cells treated with blank crosslinked micelles, free DOX or DOX-loaded crosslinked Lys-Phe-PEAcou-PEG micelles with various concentrations of DOX for 48 hrs. Values represent the average ± SD (n=3). Statistical significance was compared between micellar DOX treated group and free DOX treated control: *, $p < 0.05$; **, $p < 0.01$; ***, $p < 0.001$.

### *2.5 Conclusions*

A lysine-phenylalanine based pseudo-protein micelles with photo-crosslinkable methylcoumarin moieties were synthesized for the intracellular delivery of DOX. The major conclusions of this study are: A) The crosslinked micelles exhibited significantly better structural stability in serum containing media and were able to counter the dilution-induced micelle disintegration; B) The in vitro release of DOX was not hindered by crosslinking, and can be accelerated by enzymatic degradation due to the biodegradability of the pseudo protein micelles, suggesting the stabilization-on-demand capability; C) DOX-loaded crosslinked Lys-Phe-PEAcou-PEG micelles co-localized to a large extent with mitochondria and endolysosomes in HCT116 cells, while free DOX localized only in the nuclei; D) DOX-loaded crosslinked Lys-Phe-PEAcou-PEG micelles induced apoptosis in HCT116 cells at higher and broader drug concentration range than free DOX, and the difference in inducing apoptosis showed a correlation with mitochondrial depolarization, MPTP opening and ROS generation. This research brings a novel perspective in the study of in vitro therapeutic effect of micellar drug delivery systems. The pseudo protein

micelles also exhibit versatile promise as a “stabilization-on-demand” delivery carrier, and can be further functionalized with targeting moieties and other bioactive agents. Furthermore, this study provides researchers with new insight into the design of micellar delivery vehicles and could have the potential in developing new nanocarriers for the mitochondria-targeting delivery of payloads.

**References:**


[1] K. Miyata, R. J. Christie and K. Kataoka, *Reactive and Functional Polymers*, **2011**, 71, 227-234.

[2] A. P. R. Johnston, G. K. Such, S. L. Ng and F. Caruso, *Current Opinion in Colloid & Interface Science*, **2011**, 16, 171-181.

[3] Y. H. Bae and H. Yin, *Journal of Controlled Release*, **2008**, 131, 2-4.

[4] T. Riley, T. Govender, S. Stolnik, C. D. Xiong, M. C. Garnett, L. Illum and S. S. Davis, *Colloids and Surfaces B: Biointerfaces*, **1999**, 16, 147-159.

[5] A. Rösler, G. W. M. Vandermeulen and H.-A. Klok, *Advanced Drug Delivery Reviews*, **2012**, 64, 270-279.

[6] J. Zhang, H. Sun and P. X. Ma, *ACS Nano*, **2010**, 4, 1049-1059.

[7] J. Jiang, B. Qi, M. Lepage and Y. Zhao, *Macromolecules*, **2007**, 40, 790-792.

[8] J. He and Y. Zhao, *Dyes and Pigments*, **2011**, 89, 278-283.

[9] Q. Jin, X. Liu, G. Liu and J. Ji, *Polymer*, **2010**, 51, 1311-1319.

[10] J. W. Chung, K. Lee, C. Neikirk, C. M. Nelson and R. D. Priestley, *Small*, **2012**, 8, 1693-1700.

[11] J. He, X. Tong and Y. Zhao, *Macromolecules*, **2009**, 42, 4845-4852.

[12] Y. Shao, C. Shi, G. Xu, D. Guo and J. Luo, *ACS Applied Materials & Interfaces*, **2014**, 6, 10381-10392.

[13] A. S. Hoffman, *Advanced Drug Delivery Reviews*, **2013**, 65, 10-16.

[14] H. Wei, R. X. Zhuo and X. Z. Zhang, *Progress in Polymer Science*, **2013**, 38, 503-535.

[15] X. Shuai, H. Ai, N. Nasongkla, S. Kim and J. Gao, *Journal of Controlled Release*, **2004**, 98, 415-426.

[16] K. Kataoka, T. Matsumoto, M. Yokoyama, T. Okano, Y. Sakurai, S. Fukushima, K. Okamoto and G. S. Kwon, *Journal of Controlled Release*, **2000**, 64, 143-153.

[17] J. S. Chawla and M. M. Amiji, *International Journal of Pharmaceutics*, **2002**, 249, 127-138.

[18] C. C. Chu, in *Biodegradable Polymers: New Biomaterial Advancement and Challenges*, ed. C. C. Chu, Nova Science Publisher, **2015**, vol. 2.

[19] C. C. Chu, *Journal of Fiber Bioengineering and Informatics*, **2012**, 5, 1-31.

[20] C. C. Chu, in *Biomaterials – Principles and Practices*, eds. J. Y. Wong, J. D. Bronzino and D. R. Peterson, CRC Press, **2012**.

[21] M. Deng, J. Wu, C. A. Reinhart-King and C. C. Chu, *Biomacromolecules*, **2009**, 10, 3037-3047.

[22] H. Song and C. C. Chu, *Journal of Applied Polymer Science*, **2012**, 124, 3840-3853.

[23] J. Wu, D. Yamanouchi, B. Liu and C. C. Chu, *Journal of Materials Chemistry*, **2012**, 22, 18983.

[24] D. Q. Wu, J. Wu, X. H. Qin and C. C. Chu, *J. Mater. Chem. B*, **2015**, 3, 2286-2294.

[25] T. Yokochi, *Molecular Pharmacology*, **2004**, 66, 1415-1420.

[26] R. Lüpertz, W. Wätjen, R. Kahl and Y. Chovolou, *Toxicology*, **2010**, 271, 115-121.

[27] P. J. G. Coutinho, E. M. S. Castanheira, M. Céu Rei and M. E. C. D. Real Oliveira, *The Journal of Physical Chemistry B*, **2002**, 106, 12841-12846.

[28] J. Wu and C. C. Chu, *Acta Biomaterialia*, **2012**, 8, 4314-4323.

[29] H. Silva, F. Frézard, E. J. Peterson, P. Kabolizadeh, J. J. Ryan and N. P. Farrell, *Molecular Pharmaceutics*, **2012**, 9, 1795-1802.

[30] D. Colin, E. Limagne, S. Jeanningros, A. Jacquel, G. Lizard, A. Athias, P. Gambert, A. Hichami, N. Latruffe, E. Solary and D. Delmas, *Cancer Prevention Research*, **2011**, 4, 1095-1106.

[31] P. H. Hoet, B. Nemery and D. Napierska, *Nano Today*, **2013**, 8, 223-227.

[32] A. Wojtala, M. Bonora, D. Malinska, P. Pinton, J. Duszynski and M. R. Wieckowski, in *Methods in Enzymology*, Elsevier, **2014**, 542, 243-262.

[33] E. Sakurai, H. Ozeki, N. Kunou and Y. Ogura, *Ophthalmic Research*, **2001**, 33, 31-36.

[34] P. Opanasopit, M. Yokoyama, M. Watanabe, K. Kawano, Y. Maitani and T. Okano, *Journal of Controlled Release*, **2005**, 104, 313-321.

[35] R. Savić, T. Azzam, A. Eisenberg and D. Maysinger, *Langmuir*, **2006**, 22, 3570-3578.

[36] B. A. Aguilar-Castillo, J. L. Santos, H. Luo, Y. E. Aguirre-Chagala, T. Palacios-Hernández and M. Herrera-Alonso, *Soft Matter*, **2015**, 11, 7296-7307.

[37] J. Lu, S. C. Owen and M. S. Shoichet, *Macromolecules*, **2011**, 44, 6002-6008.

[38] G. Speelmans, R. W. H. M. Staffhorst, B. de Kruijff and F. A. de Wolf, *Biochemistry*, **1994**, 33, 13761-13768.

[39] M. Han, M. R. Vakili, H. Soleymani Abyaneh, O. Molavi, R. Lai and A. Lavasanifar, *Molecular Pharmaceutics*, **2014**, 11, 2640-2649.

[40] S. R. Jean, D. V. Tulumello, C. Riganti, S. U. Liyanage, A. D. Schimmer and S. O. Kelley, *ACS Chemical Biology*, **2015**, 10, 2007-2015.

[41] J. D. Ly, D. R. Grubb and A. Lawen, *Apoptosis*, **2003**, 8, 115-128.

[42] H. U. Simon, A. Haj-Yehia and F. Levi-Schaffer, *Apoptosis*, **2000**, 5, 415-418.

[43] A. Malugin, P. Kopečková and J. Kopeček, *Molecular Pharmaceutics*, **2006**, 3, 351-361.

[44] T. Minko, P. Kopečková and J. Kopeček, *Journal of Controlled Release*, **2001**, 71, 227-237.

# CHAPTER 3

# BIODEGRADABLE NANOCOMPLEX FROM HYALURONIC ACID AND ARGININE BASED POLY(ESTER AMIDE)S AS THE DELIVERY VEHICLES FOR IMPROVED PHOTODYNAMIC THERAPY OF MULTIDRUG RESISTANT TUMOR CELLS: AN IN VITRO STUDY OF THE PERFORMANCE OF CHLORIN E6 PHOTOSENSITIZER

### *3.1 Abstract*

Photodynamic therapy (PDT), which enables the localized therapeutic effect by the application of light, provides a promising strategy as an alternative and complementary modality for the treatment of tumor. However, the aggregation of photosensitizers in acidic microenvironment of tumor and the non-targeted distribution of photosensitizers in normal tissues significantly affect the PDT efficiency. In this study, we developed a biodegradable nanocomplex from hyaluronic acid and arginine based poly(ester amide)s (HA-Arg-PEA) as the nano-carrier for chlorin e6 (Ce6). Hyaluronic acid (HA) in the nanocomplex enhanced the tumor-specific endocytosis mediated by the overexpression of CD44 receptor. Arginine-based PEA (Arg-PEA) not only provide electrostatic interaction with HA to form self-assembled nanostructure, but also improve the monomerization of the loaded Ce6. HA-Arg-PEA nanocomplex significantly reduced the aggregation of Ce6 at physiological pH as well as mildly acidic pH, compared to free Ce6. The biodegradable characteristic of HA-Arg-PEA nanocomplex enabled the intracellular delivery of Ce6, in which its release and generation of singlet oxygen can be accelerated by enzymatic degradation of the carrier. The in vitro PDT efficiency of Ce6-loaded HA-Arg-PEA nanocomplex was examined in CD44 positive MDA-MB-435/MDR multidrug resistant melanoma cells. CD44-mediated uptake of Ce6-loaded HA-Arg-PEA nanocomplex significantly improved Ce6 level in MDA-MB-435/MDR cells within a short incubation time (4 hrs), and the PDT efficiency in the inhibition of multidrug resistant tumor cells was also enhanced at higher Ce6 concentrations.

### *3.2 Introduction*

Different from traditional chemotherapy, photodynamic therapy (PDT) offers an alternative approach to treat tumor, in which the administration of photosensitizers is followed by the application of light irradiation to the tumor site [1]. Upon irradiation, photosensitizers generate reactive oxygen species (ROS) and singlet oxygen via photon-induced energy transfer, and further induce the localized oxidative damage to tumor cells. Most tumor cells with chemotherapy-resistance are not reported to develop cross-resistance to PDT photosensitizers including chlorin e6 (Ce6) [2,3], chloroaluminum tetrasulfonate phthalocyanine (AlPcS) [4], and protoporphyrin IX (PpIX) [5], etc. Many studies have demonstrated the independence of intracellular accumulation of these photosensitizers from the overexpression of multidrug transporter protein, P-glycoprotein [6,7], and PDT is also reported to have the potential to reverse multidrug resistant phenotype [8]. However, current photodynamic treatments are still facing several practical challenges that impact their efficacy. Most photosensitizers are of poor water solubility and difficult to be directly administered via intravenous injection. Besides, the accumulation of photosensitizers in normal tissue was also observed [9], and the non-targeted distribution of photosensitizer not only affects PDT potency, but also bring in skin photo-sensitivities to patients. Patients receiving photodynamic treatment are restricted from sunlight exposure in order to minimize side effects [10].

Considering the above disadvantages for direct administration of free photosensitizers, targeted delivery of photosensitizers to the site of action with a suitable delivery vehicle is a promising strategy to improve PDT efficacy, and

simultaneously reduce the risk of side effect or toxicity. Various polymeric nano-vehicles [11] have been reported as the delivery carriers for PDT, and bring in additional advantages to PDT, such as protection of photosensitizer from degradation, improving their circulating time in blood, selective targeting and controlled release of photosensitizer in tumor tissue, etc. Hyaluronic acid (HA) is a natural and biodegradable polysaccharide formed by D-glucuronic acid and N-acetyl-D-glucosamine repetitive units [12]. Identified as the ligand molecule for CD44 receptors [13], HA has attracted considerable research interests in the field of tumor-targeting delivery, due to the overexpression of CD44 receptors on many types of tumor cells. HA-based nano-carriers exhibited enhanced binding and endocytosis by tumor cells, and have been developed to improve the potency of various therapeutic agents [14]. HA was reported as the delivery vehicles for multiple PDT-photosensitizers including hematoporphyrin [15], chlorin derivatives [16], phthalocyanine derivatives [17], and significantly improved therapeutic efficiency was reported when compared to the direct administration of free photosensitizer. However, of the published studies on delivery systems for PDT, few of them addressed the aggregation issue of the loaded photosensitizer, as aggregation is one of general limitations for PDT efficacy in acidic tumor environment [18].

Synthetic amino acid based poly (ester amide)s (AA-PEA) is a new family of biodegradable polymers synthesized from 3 building blocks: amino acids, dialcohol, diacids. AA-PEAs have been engineered into nanofibrous membranes, 3D microporous hydrogels, coating for suture and cardiovascular stent, and drug delivery vehicles for multiple biomedical applications. The

current research on AA-PEAs have recently been reviewed [19–21]. Previous published studies have demonstrated the unique advantages of AA-PEA, which includes reproducible synthetic routes, versatile structural design, enzymatic biodegradability, excellent biocompatibility, and muted inflammatory response, etc. By selecting different types of amino acids, diols, and adjusting the number of hydrocarbons between ester and amide groups, AA-PEA materials are tuneable in charge density, hydrophobicity/hydrophilicity, as well as the reactive sites for further chemical functionalization. Among the amino acids for AA-PEA synthesis, arginine (Arg) retains cationic charge over a wide range of pH, suitable to form electrostatic complex with other negatively charged materials or payloads [22]. Chu et al. have recently demonstrated that cationic Arg-PEAs facilitated the penetration through cell membrane and worked as effective delivery systems for therapeutic agents including genes [23].

In this research, we aim to develop a biodegradable nanocarrier for the targeted delivery of photosensitizers, and address the following issues associated with PDT treatment of tumor: 1) to improve the selective endocytosis of photosensitizer by tumor cells, instead of normal cells.; 2) to reduce the aggregation of photosensitizer in an acidic environment.

Chlorin e6 (Ce6), a commonly investigated photosensitizer with activation wavelength at 660 to 670 nm, is chosen as the payload to be delivered. Three peripherally attached carboxylic groups on Ce6 exist in different ionic forms, depending on the pH. Prior published studies [24,25] suggested that Ce6 aggregated predominantly at acidic pH, which lead to reduced sensitizing efficiency, and

adversely impact the therapeutic effect. In this contribution, nano-sized delivery carrier is designed from both HA and Arg-PEA, in which HA component provides targeting modality to achieve selective endocytosis by CD44 positive tumor cells. The cationic Arg-PEA component not only formed electrostatic self-assembled structure with HA, but also provided advantages for the improving photosensitizing efficiency for Ce6. We focused on investigating the level of Ce6 monomerization in interaction with the carrier at both physiological and acidic environment. Intracellular trafficking and in vitro PDT efficacy of Ce6-loaded nanocomplex in multidrug resistant MDA-MB-435/MDR melanoma cells were also studied to investigate its potential as the delivery system for PDT.

### *3.3. Experimental*

#### *3.3.1 Chemicals and cells*

Sodium hyaluronate (MW= 10 to 20 kDa) was purchased from Lifecore Biomedical (Chaska, MN). N-hydroxysuccinimide (NHS), N-(3-dimethylaminopropyl)-N'-ethylcarbodiimide hydrochloride (EDC), tetrabutylammonium bromide, p-nitrosodimethyl aniline (RNO), methyl-β-cyclodextrin, ninhydrin, QuantiPro BCA assay kit and hyaluronidase from bovine testes were from Sigma Aldrich (Milwaukee, WI). Amberlite IR-120 $H^+$ ion exchange resin was from Alfa Aesar (Ward Hill, MA). Dimethyl sulfoxide (DMSO), methanol and other HPLC grade solvents were from JT Baker (Phillipsburg, NJ). Chlorin e6 was from Frontier Scientific (Logan, UT). Nystatin, chloropromazine, amiloride hydrochloride were from Cayman Chemical (Ann Arbor, MI). Anti-human CD44

antibody (clone IM7) and annexin V apoptosis detection kit were from eBioscience (San Diego, CA). Lysotracker green was from Cell Signaling Technology (Beverly, MA). Snakeskin dialysis tubing (MWCO = 10 kDa) and NHS-rhodamine were from Pierce (Rockford, IL). The monomer Arg-4 (tetra-p-toluenesulfonic acid salt of bis-L-arginine butane-1, 4-diester) and NA (di-p-nitrophenyl adipate) were synthesized according to our previously studies [26,27].

MDA-MB-435/MDR multidrug resistant melanoma cells were donated by Dr. Robert Clarke (Georgetown University, Washington, D.C.) and MD Anderson Cancer Center (Houston, TX). MDA-MB-435/MDR cells were maintained at 37 ºC with 5% $CO_2$ in Minimum Essential Medium (Richter's modification) containing 2mM L-glutamine, phenol red, 10% fetal bovine serum, and 1% penicillin/streptomycin. NIH 3T3 fibroblasts were maintained in Dulbecco's Modified Eagle Medium (DMEM) supplemented with phenol red, 10% fetal bovine serum, and 1% penicillin/streptomycin.

### *3.3.2 Synthesis of amine terminated arginine based PEA*

The synthesis of amine-terminated Arg-PEA was based on our previously published study [26]. As depicted in Figure 3.1, excessive amount of Arg-4 (0.82 g, 1.0 mmol) was mixed with NA (0.31 g, 0.8 mmol) in 1.5 mL DMSO, and heated to 75 ºC under stirring to obtain a uniform mixture. Triethylamine (0.31 mL, 2.2 mmol) was added under vigorous stirring. The reaction was kept for 12 hrs at 75 ºC. The resulting Arg-PEA polymer with amine end groups was precipitated in cold ethyl acetate, dissolved in DI water, and repeated concentrated in Macrosep centrifugal device

(MWCO=1 kDa, Pall Filtron, Northborough, MA). The purified amine-terminated Arg-PEA was lyophilized. Ninhydrin assay was performed as per manufacturer's instruction to estimate the content of primary amine end groups, and calibrated against a standard curve from free arginine.

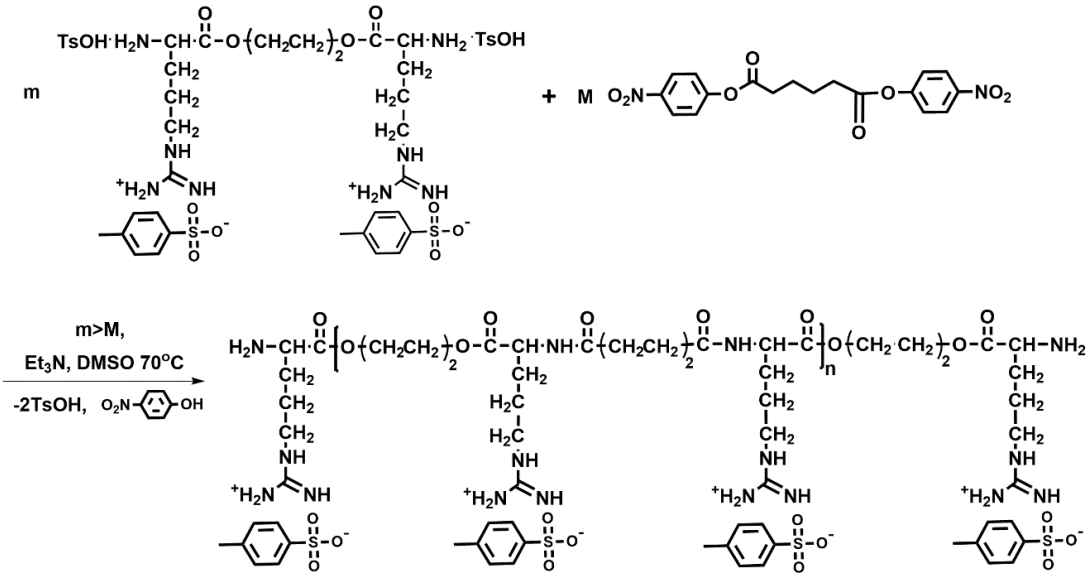


**Figure 3.1**. Synthesis scheme of amine terminated arginine based poly(ester amide)s (Arg-PEA).

### *3.3.3 Preparation of Ce6 loaded HA-Arg-PEA nanocomplex*

*Preparation of blank HA-Arg-PEA nanocomplex.* To improve the solubility of hyaluronic acid in organic solvents, sodium hyaluronate was converted to tetra-N-butylammonium hyaluronate (HA-TBA) via ion exchange method [28]. Amberlite IR-120 $H^+$ resin was washed with methanol and deionized water, neutralized with 1 M NaOH, washed with deionized water and then immersed in 0.25 M aqueous tetra-N-butylammonium bromide solution overnight. The resulting ion exchange resin was

then added to an aqueous solution of sodium hyaluronate (20 mg/mL) and stirred overnight at room temperature. The resin was then removed by filtration, and the aqueous solution was lyophilized to give HA-TBA. To prepare the nanocomplex from Arg-PEA and HA-TBA, 100 mg HA-TBA was dissolved in 5 mL DMSO/$H_2O$ (1:1 v/v), the carboxyl groups on HA were activated with NHS/EDC (-COOH: NHS: EDC = 1:5:1.2, molar ratio). 100 mg amine terminated Arg-PEA dissolved in 5 mL DMSO was then added dropwise. The mixture solution was stirred overnight, dialyzed (MWCO = 10 kDa) against DI water for 24 hrs, and repeated concentrated in Macrosep centrifugal device (MWCO=100 kDa, Pall Filtron, Northborough, MA). Purified HA-Arg-PEA nanocomplex was then lyophilized. The morphology of HA-Arg-PEA nanocomplex was observed on a FEI Tecnai Spirit T12 TEM (FEI Co., Hillsboro, OR) at an operating voltage of 120 kV. Zeta potential and size of the nanocomplex were characterized at room temperature on a Zetasizer NanoZS system (Malvern, UK).

*Preparation of Ce6-loaded HA-Arg-PEA nanocomplex.* Ce6 (20 mg) and amine terminated Arg-PEA (100 mg) were dissolved in 5 mL DMSO and stirred for 30 min in dark. The mixed solution of Ce6/Arg-PEA was then added dropwise to the activated HA-TBA solution as prepared above and stirred overnight in dark. The mixture solution was subjected to dialysis and centrifugal concentration, then filtered through a 0.45 μm microfilter. The filtered solution was lyophilized. To determine the loading content (LC) and encapsulation efficiency (EE) of Ce6, 5 mg lyophilized Ce6-loaded HA-Arg-PEA nanocomplex was first digested in 0.1 M NaOH (2.5 mL) at room temperature overnight, before another 2.5 mL of DMSO was added. The mixed

solution was centrifuged at 14000 rcf. The fluorescence intensity (λex=405 nm, λem=672 nm) of the supernatant was recorded on a PTI spectrofluorometer (Photon Technology International, South Brunswick, NJ).

### *3.3.4 Detection of monomerization of Ce6 in interaction with Arg-PEA*

Due to the difficulty to directly probe the UV-Vis spectrum of Ce6 loaded in the nanocomplex, the mixture of Arg-PEA and Ce6 in aqueous solution was studied to illustrate the monomerization of Ce6 in interaction with Arg-PEA. A mixture of Arg-PEA and Ce6 (10:1 w/w) was dispersed at an equivalent Ce6 concentration of 50 μM in phosphate buffer with various pH ranging from 4.5 to 10.0. Free Ce6 was tested as control. UV-Vis spectra were obtained for each sample on a Lambda Bio40 spectrophotometer (Perkin-Elmer, Norwalk, CT), and the absorbance at 672 nm and 645 nm were recorded. Absorbance at 672 nm represents the monomeric form of Ce6, while absorbance at 645 nm represents the aggregated form of Ce6 [29]. The ratio between $A_{672}$ and $A_{645}$, an indication of Ce6 monomerization, was calculated and plotted vs. pH.

### *3.3.5 Detection of singlet oxygen generation*

The generation of singlet oxygen from Ce6 upon irradiation was quantitatively evaluated by RNO bleaching assay. Free Ce6 or Ce6-loaded HA-Arg-PEA nanocomplex (HA-Arg-PEA/Ce6) was dissolved in a mixed solution of DMSO and PBS (1:10 v/v) with or without the presence of 120 unit/mL hyaluronidase, and incubated at 37 ºC for 24 hrs. The equivalent concentration of Ce6 in each sample was

100 μM. After incubation, 400 μL the above solution was added to 3.6 mL phosphate buffer (pH 7.4 or pH 6.5) containing 5.58 mg L-histidine and 0.377 mg RNO. The final concentration of Ce6 was 10 μM. Each solution was subjected to light irradiation by 120 LED arrays at 660 nm (Elixa, Albuquerque, NM) and the power density was 25 mW/cm$^2$. The absorbance of RNO in each sample was measured at 440 nm by UV-Vis spectroscopy as a function of irradiation time. Each test was performed in triplicate.

### *3.3.6 Endocytosis Ce6-loaded HA-Arg-PEA nanocomplex*

*Endocytosis inhibition assay*. MDA-MB-435/MDR cells were seeded in a 6-well plate (3 x $10^5$ cells per well) and pre-incubated for 24 hrs. The cells were treated with inhibitors that block different endocytic pathways (nystatin, 50 μg/mL; chloropromazine, 30 μM; amiloride hydrochloride, 50 μM; methyl-β-cyclodextrin, 3 mg/mL or anti-CD44 antibody as per manufacturer's instruction) for 0.5 hr before rhodamine labelled blank HA-Arg-PEA nanocomplex was added and incubated for another 4 hrs. The cells were then washed with PBS, harvested and subjected to flow cytometry assay on FACSAria fusion fluorescence activated cell sorter (BD Biosciences, Franklin Lakes, NJ). The effect of low temperature (4°C) on endocytosis was also studied. Cells incubated with HA-Arg-PEA nanocomplex at 37°C but not treated with any inhibitor were tested as control. The mean fluorescence intensity for each sample was recorded and normalized to control. The tests were performed in triplicate.

*Accumulated endocytosis study*. MDA-MB-435/MDR cells were seeded in a 6-well plate (3 x $10^5$ cells per well) and pre-incubated for 24 hrs followed by the addition of free Ce6 or Ce6-loaded HA-Arg-PEA nanocomplex of an equivalent Ce6 concentration 5 μM and incubated for 1, 2, 4, 8, 12 or 24 hrs. The cells were washed with PBS, harvested and lysed in 0.4 mL 0.5% Triton-X. 0.2 mL of the cell lysate was added to 1 mL DMSO and the fluorescence intensity (λex = 405 nm, λem = 672 nm) was recorded to quantify the Ce6 level in each sample. The other 0.2 mL of cell lysate from the same sample was subject to BCA assay to determine the total protein content as per manufacturer's instruction. The fluorescence intensity for each sample was normalized to total protein content and each test was performed in triplicate. The accumulated endocytosis study on 3T3 fibroblasts (CD44 negative) was also performed in the same procedure as described above.

### *3.3.7 Subcellular distribution of Ce6-loaded HA-Arg-PEA nanocomplex*

To determine the expression of CD44 in MDA-MB-435/MDR cells, immunostaining was performed to untreated MDA-MB-435/MDR cells with anti-human CD44 antibody, as per manufacturer's instruction. The expression of CD44 receptor on MDA-MB-435/MDR cells was visualized on a Zeiss LSM710 confocal microscope (Carl Zeiss MicroImaging, Thornwood, NY).

To study the subcellular distribution of Ce6-loaded HA-Arg-PEA nanocomplex in MDA-MB-435/MDR cells, 3 x $10^5$ MDA-MB-435/MDR cells were seeded in a glass bottomed petri dish (P35G-0-10-C, MaTek, Ashland, MA) and pre-incubated for

24 hrs. Free Ce6 or Ce6-loaded HA-Arg-PEA nanocomplex with equivalent Ce6 concentration of 2 μM was added and incubated for 24 hrs. Cells were then washed three times with PBS and imaged alive by confocal microscopy. To study the subcellular distribution of blank HA-Arg-PEA nanocomplex labelled with rhodamine, MDA-MB-435/MDR cells were incubated with blank nanocomplex for 4 hrs and stained with Lysotracker green as per manufacturer's instruction. The cells were imaged alive with confocal microscopy.

### *3.3.8 Phototoxicity of Ce6 loaded HA-Arg-PEA towards MDA-MB-435/MDR cells*

MDA-MB-435/MDR cells were seeded in a 96-well plate ($5 \times 10^3$ cells per well) and pre-incubated for 24 hrs. Free Ce6 or Ce6-loaded HA-Arg-PEA nanocomplex with various Ce6 concentration were added and incubated for 4 hrs. The cells were washed three times with PBS and incubated for another 20 hrs in fresh culture media. Light irradiation was applied by LED arrays for 2 min at 660 nm with light dose of 3 J/cm$^2$. After a further incubation for another 24 hrs, the viability of cells was determined by MTT assay. The absorbance at 570 nm was recorded and normalized to untreated control. Each experiment was run in six replicates.

### *3.3.9 Annexin V assay*

MDA-MB-435/MDR cells were seeded in a 6-well plate ($3 \times 10^5$ cells per well) and pre-incubated for 24 hrs. Blank HA-Arg-PEA nanocomplex, free Ce6 or Ce6-loaded HA-Arg-PEA nanocomplex with equivalent Ce6 concentration of

2 μM or 10 μM were added and incubated for 4 hrs. The cells were washed three times with PBS and incubated for another 20 hrs in fresh culture media. Light irradiation was applied by LED arrays at 660 nm for 2 min with light dose of 3 J/cm$^2$. Annexin-V/PI double staining was performed 24 hrs post light irradiation, as per manufacturer's instruction. The percentage of dead/apoptotic cells were analysed by flow cytometry, and each experiment was performed in triplicate.

### *3.3.10 Statistical analysis*

The data are presented as mean values with standard deviations (SD). All data were analyzed using one-way ANOVA, followed by Tukey's multiple comparison tests, and $p < 0.05$ was used for statistical significance.

## *3.4 Results and discussion*

### *3.4.1 Preparation of amine terminated Arg-PEA*

Amine terminated Arg-PEA was prepared from solution polycondensation, in which excess amount of nucleophilic Arg-4 monomer was reacted with electrophilic NA monomer to result in free amine groups on both ends of polymer chain. We also reported a amine terminated phenylalanine based PEA from the same synthesis method [26]. $^1$H NMR spectrum was obtained to characterize the amine terminated Arg-PEA, and typical chemical shifts were observed at 8.25 ppm (-**NH**-CO-), 4.23 ppm (-**CH$_2$**-O-CO-) and 3.09 ppm (-NH-CO-**CH$_2$**-). The molecular weight of the amine terminated Arg-PEA was 6.5 kDa with PDI =1.36, as detected by GPC. The amine-

terminated Arg-PEA exhibits strong cationic charge when dispersed in pH 7.4 phosphate buffer, and the zeta potential for the 1 mg/mL solution was + 22.5 ± 3.9 mV. The content of free amine was 0.25 mmol/g in Arg-PEA, as detected by ninhydrin assay.

### *3.4.2 Characterization of Ce6-loaded HA-Arg-PEA nanocomplex*

HA-Arg-PEA nanocomplex was formed from electrostatic self-assembly between HA (anionic) and Arg-PEA (cationic) as shown in Figure 3.2, and further stabilized via covalent crosslinking between -$NH_2$ end groups in Arg-PEA and -COOH groups in HA. Negative surface charge (- 17.6 to -22.4 mV) was detected for all HA-Arg-PEA nanocomplex with various HA to Arg-PEA ratios, and the size of the nanocomplex increased with higher HA contents, e.g., from 114.04 ± 5.92 nm (HA/Arg-PEA= 1:1 w/w) to 530.58 ± 3.80 nm (HA/ Arg-PEA= 4:1 w/w). In addition, the loading content of Ce6 was also affected by HA to Arg-PEA ratio. Increased HA component lead to a decrease in the loading content of Ce6, e.g., 9.0% (HA/Arg-PEA= 1:1 w/w) vs. 3.2% (HA/ Arg-PEA= 4:1 w/w), which can be attributed to the reduced electrostatic interactions between Ce6 and Arg-PEA. Nanocarriers with smaller size resulted in more effective delivery because they are less likely to be captured by reticuloendothelial system (RES) than larger particles in systemic circulation [30]. HA-Arg-PEA nanocomplex with HA/Arg-PEA ratio of 1:1 was chosen for the following study.

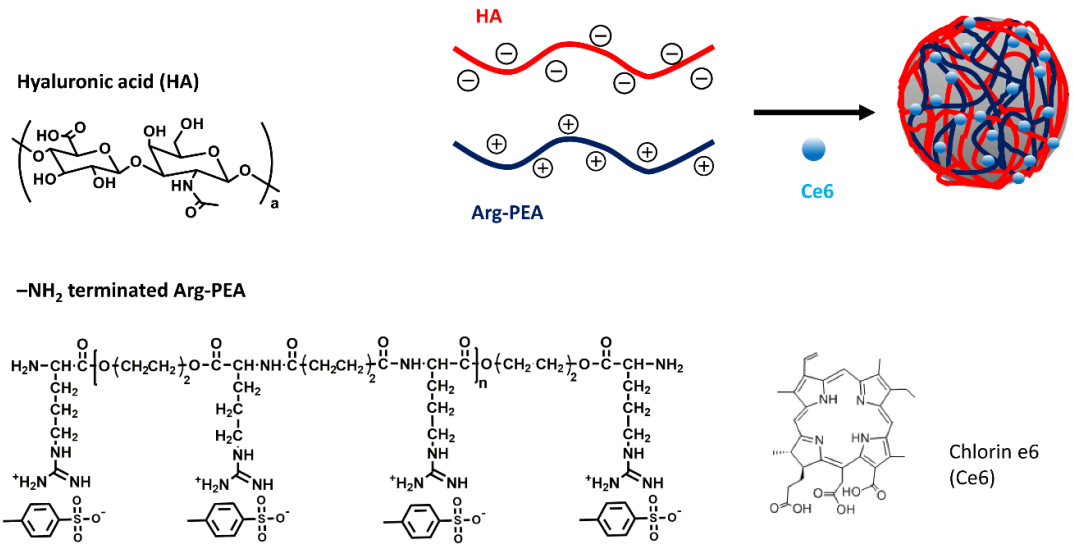


**Figure 3.2**. Chemical structure of tetra-N-butylammonium hyaluronate (HA-TBA), amine-terminated arginine based poly(ester amide)s (Arg-PEA) and chlorin e6 (Ce6). And the graphic illustration of Ce6-loaded HA-Arg-PEA nanocomplex.

Electrostatically self-assembled microparticles from HA and unsaturated Arg-PEA was previously reported by Potuck et al [31]. They reported the assembled structure with average feature size of 2.49−15 μm from high molecular weight HA (1,000 kDa) and unsaturated Arg-PEA (30 to 60 kDa). In this current study, much smaller nanocomplex can be formed by using HA with low molecular weight (10 to 20 kDa) and amine-terminated Arg-PEA (6.5 kDa).

The characteristics of Ce6-loaded HA-Arg-PEA nanocomplex (HA-Arg-PEA/Ce6) are listed in Table 3.1. The LC and EE for Ce6 were 9.0% and 90.3%, respectively. The incorporation of Ce6 into HA-Arg-PEA nanocomplex didn't significantly changed the size and surface charge. The TEM image in Figure 3.3A

confirmed the spherical structure of Ce6-loaded HA-Arg-PEA nanocomplex. After incubation with hyaluronidase (120 unit/mL) for 24 hrs [32], the spherical morphology of Ce6-loaded HA-Arg-PEA nanocomplex disappeared (Figure 3.3B) due to the enzymatic breakdown of HA.

**Table 3.1**. Characteristics of HA-Arg-PEA nanocomplex (HA/Arg-PEA = 1:1 w/w).

| | **DLS diameter (nm)** | **PDI** | **Zeta potential (mV)** | **Loading Content (%)** | **Encapsulation Efficiency (%)** |
|---|---|---|---|---|---|
| **HA-Arg-PEA** | 130.58 ± 7.87 | 0.184 ± 0.055 | -22.4 ± 1.2 | | |
| **HA-Arg-PEA/ Ce6** | 114.04 ± 5.92 | 0.159 ± 0.072 | -20.6 ± 2.5 | 9.0 | 90.3 |

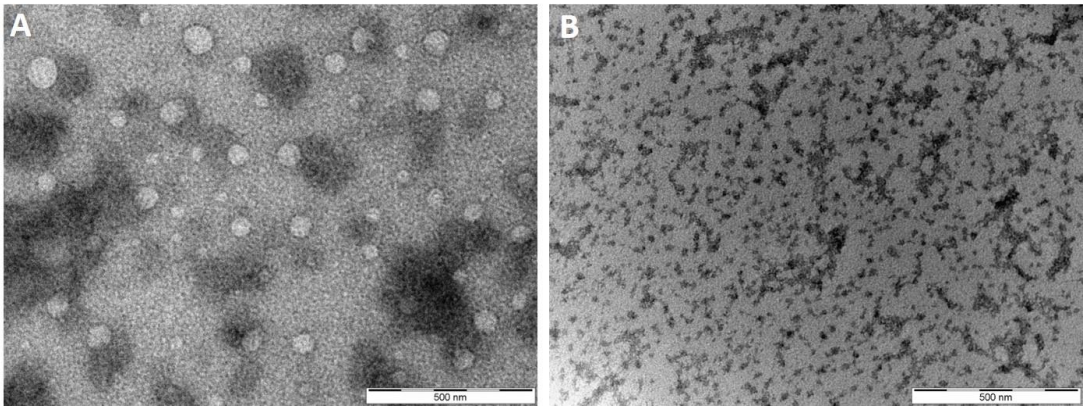


**Figure 3.3**. TEM image of A) Ce6-loaded HA-Arg-PEA nanocomplex in pH 7.4 phosphate buffer, B) Ce6-loaded HA-Arg-PEA nanocomplex after 24 hrs incubation

with 120 unit/mL hyaluronidase in pH 7.4 phosphate buffer.

### *3.4.3 Evaluation of Ce6 monomerization*

Ce6 aggregates in acidic pH (6.5-6.9) that is common in tumor microenvironment [33]. The aggregation can lead to reduced photosensitizing effect, and adversely affects the PDT efficiency. To characterize the monomerization level of Ce6, two typical absorbance peaks at 672 nm (representing Ce6 in monomer state) and 645 nm (representing Ce6 in aggregated state) in the Q-band of UV-vis spectrum were investigated and the $A_{672}/A_{645}$ ratio was evaluated as an index for Ce6 monomerization [29]. Due to the difficulty in directly probing the UV-Vis spectra of Ce6 loaded in HA-Arg-PEA, as indicated in Figure 3.4A. At the same Ce6 concentration, the absorbance peaks of free Ce6 at 672 nm and 645 nm were overlapped and indistinguishable from the Ce6 loaded in HA-Arg-PEA, this can be attributed to the fact that Ce6 was entrapped in the interior of the nanocomplex which impacted the UV-Vis absorbance. Therefore, we studied the $A_{672}/A_{645}$ ratio of the mixture of Ce6 and the Arg-PEA component of the HA-Arg-PEA nanocomplex in an aqueous solution, as the absorption peaks of Ce6 at 672 nm and 645 nm were more evident and clear in Figure 3.4A.

As shown in Figure 3.4B, the $A_{672}/A_{645}$ ratio for free Ce6 reached the highest value (i.e., highest level of Ce6 monomerization) at pH 10, then decreased with reduced pH, and reached the lowest value at pH 4.5. The monomerization of free Ce6 as a function of pH are consistent with previous study [34] that Ce6 molecules in alkaline aqueous media and polar organic solvents stay predominantly in the

monomeric form. An increasing fraction of aggregated Ce6 was observed at acidic pH due to the non-ionized carboxylic groups in Ce6 and the formation of intermolecular hydrogen bonding [29]. On the other hand, the fraction of Ce6 monomer in complex with Arg-PEA was significantly higher than free Ce6 at pH ranging from 4.5 to 7.4. No statistical difference between Ce6-loaded Arg-PEA and free Ce6 in the $A_{672}/A_{645}$ ratio was found at pH 10.

It is suggested that Arg-PEA provided alkaline and polar environment for Ce6, and the interaction between Arg-PEA and Ce6 further interrupted the intermolecular bonding between Ce6 molecules, which leads to increased fraction of Ce6 monomer. In the PDT treatment for tumor, aggregation of Ce6 can be anticipated in acidic microenvironment of tumor [35]. Therefore, it's important to incorporate proper delivery carriers that can compensate the disadvantage of Ce6 aggregation. Arg-PEA enhanced Ce6 monomerization at a relatively low weight ratio (10:1), which is comparable to polyvinylpyrrolidone, an additive used to enhance therapeutic activity of Ce6 in the formulation of Pholon® [24,29]. Contrary to the non-biodegradability of polyvinylpyrrolidone, Arg-PEAs are enzymatic biodegradable and exhibit excellent biocompatibility towards a wide range of cells [36–40]. Therefore, the Arg-PEA component in the nanocomplex is expected to provide additional advantages as the delivery vehicles for Ce6.

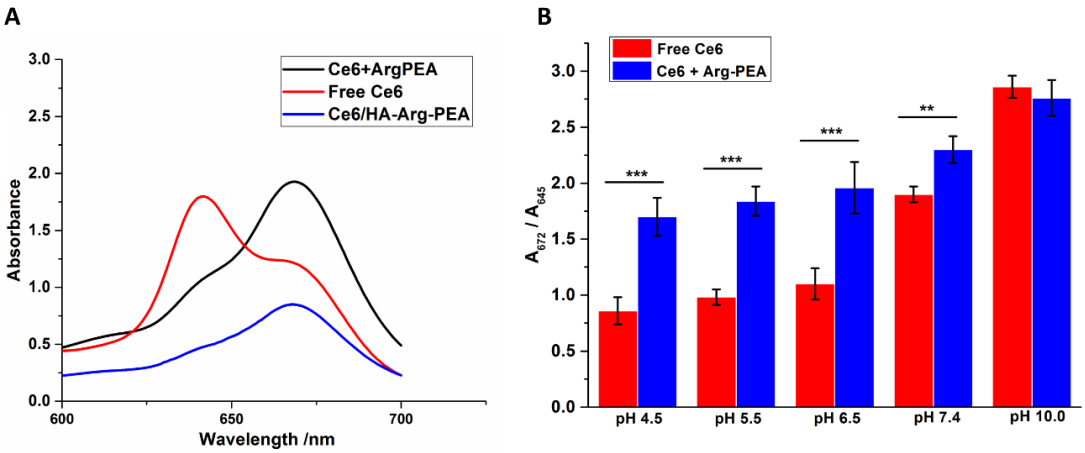


**Figure 3.4**. A) The UV-Vis spectra of free Ce6, mixture of Arg-PEA and Ce6, and Ce6-loaded HA-Arg-PEA nanocomplex in an aqueous dispersion (pH 4.5). B) The effect of pH on Ce6 monomerization in interaction with Arg-PEA. The ratio between the absorbance at 672 nm (representing Ce6 in the monomer state) and 645 nm (representing Ce6 in the aggregation state) from UV-Vis spectra obtained from mixture of Arg-PEA and Ce6 (with equivalent Ce6 concentration of 50 µM) dispersed in phosphate buffer with various pH. Free Ce6 was tested as control. Values represent the average ± SD (n=3). Statistical significance: *, $p < 0.05$; **, $p < 0.01$, ***, $p < 0.001$.

### *3.4.4 In vitro generation of singlet oxygen*

To illustrate the effect of enzymatic degradation on photosensitizing effect of Ce6 in HA-Arg-PEA nanocomplex, the production of singlet oxygen species was probed by RNO bleaching assay. RNO bleaching is a consequence of singlet oxygen captured by the imidazole ring, resulting in the formation of a trans-annular peroxide

intermediate with reduced absorbance at 440 nm [41]. As shown in Figure 3.5A, in the absence of hyaluronidase, Ce6 loaded in HA-Arg-PEA nanocomplex (red curve) exhibited a delayed release of singlet oxygen when comparing to free Ce6 (blue curve) at physiological pH. The result suggested that when entrapped in the interior of HA-Arg-PEA nanocomplex, the sensitizing efficiency of Ce6 was suppressed towards 660 nm light irradiation to produce singlet oxygen. However, after incubation with hyaluronidase for 24 hrs, a rapid generation of singlet oxygen was observed for Ce6-loaded HA-Arg-PEA nanocomplex (black curve) due to the release of Ce6 from the nanocomplex, and the rate for singlet oxygen generation was comparable to free Ce6 (blue curve). Consistent with the morphological changes of HA-Arg-PEA nanocomplex in Figure 3.3, Ce6 released from the degraded nanocomplex is responsible for the rapid generation of singlet oxygen, and hyaluronidase can provide an effective intracellular signal to accelerate the release of Ce6 within tumor cells.

At pH 6.5 (Figure 3.5B), slower rate of singlet oxygen generation from free Ce6 (blue curve) was observed than pH 7.4 (Figure 3.5A), as 74% of RNO was maintained after 60 min irradiation. Ce6-loaded HA-Arg-PEA nanocomplex without degradation still exhibited a lower level of singlet oxygen generation (red curve) than free Ce6, but the difference was significantly reduced at acidic pH. In the case of Ce6-loaded HA-Arg-PEA nanocomplex after enzymatic degradation (black curve), accelerated RNO bleaching was observed (54% of RNO remained after 60 min irradiation), when compared to either free Ce6 or Ce6-loaded HA-Arg-PEA without degradation. Considering the result of Ce6 monomerization in Figure 3.4, and that singlet oxygen generation is positively correlated to the degree of Ce6 monomerization, it is

reasonable to attribute the accelerated singlet oxygen generation to the interaction between Ce6 and Arg-PEA component in the nanocomplex.

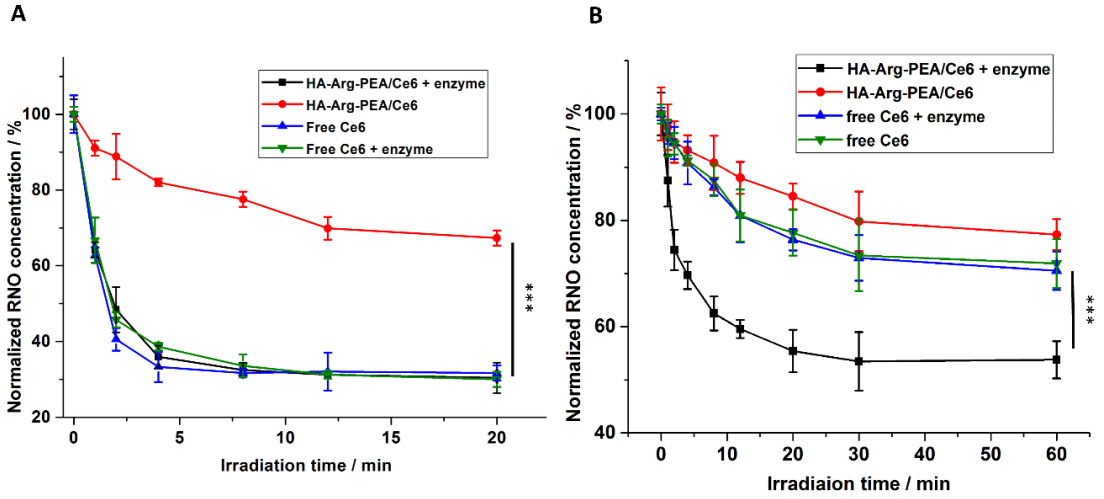


**Figure 3.5**. The production of singlet oxygen from Ce6-loaded HA-Arg-PEA nanocomplex after 24 hrs incubation with hyaluronidase, and diluted in phosphate buffer with different pH: A) pH 7.4, and B) pH 6.5. The final concentration of Ce6 in each sample was 10 μM Light irradiation at 660 nm was applied. The generation of singlet oxygen was monitored vs. irradiation time by measuring RNO bleaching at 440 nm. Values represent the average ± SD (n=3). Statistical significance: ***, $p < 0.001$.

### *3.4.5 Subcellular distribution of Ce6-loaded HA-Arg-PEA nanocomplex*

The expression of CD44 receptor on MDA-MB-435/MDR cells was first confirmed by anti-CD44 staining, as shown in Figure 3.6. The overexpression of CD44 receptor on MDA-MB-345 cells was also evidenced by Sun et al. [42]. Therefore, it is reasonable to select MDA-MB-435/MDR melanoma cells as CD44 positive in vitro model to examine the antitumor effect of Ce6-loaded HA-Arg-PEA.

Figure 3.6A also showed the subcellular distribution of Ce6 loaded in HA-Arg-PEA nanocomplex and free Ce6; and both were identified in the cytoplasm of MDA-MB-435/MDR cells after 4 hrs incubation. The subcellular distribution of the blank HA-Arg-PEA nanocomplex was also studied and shown in Figure 3.6B. The red fluorescence of rhodamine-labelled nanocomplex was identified to be co-localized with endolysosomes, as yellow pixels were observed in the overlay images. The results suggested that HA-Arg-PEA nanocomplex was entrapped in endolysosomes which have a series of digestive enzymes to be able to accelerate the release of Ce6 from the nanocomplex due to the biodegradation of the carrier by endolysosomal enzymes, as indicated in Figure 3.3 and Figure 3.5. It can be concluded that the distribution of the biodegradable HA-Arg-PEA nanocomplex in the endolysosomes may lead to release of Ce6 which was accelerated by enzymatic biodegradation of the carrier, and Ce6-loaded in the nanocomplex exhibited the same subcellular distribution compared to free Ce6, where they can fulfill their biological functions.

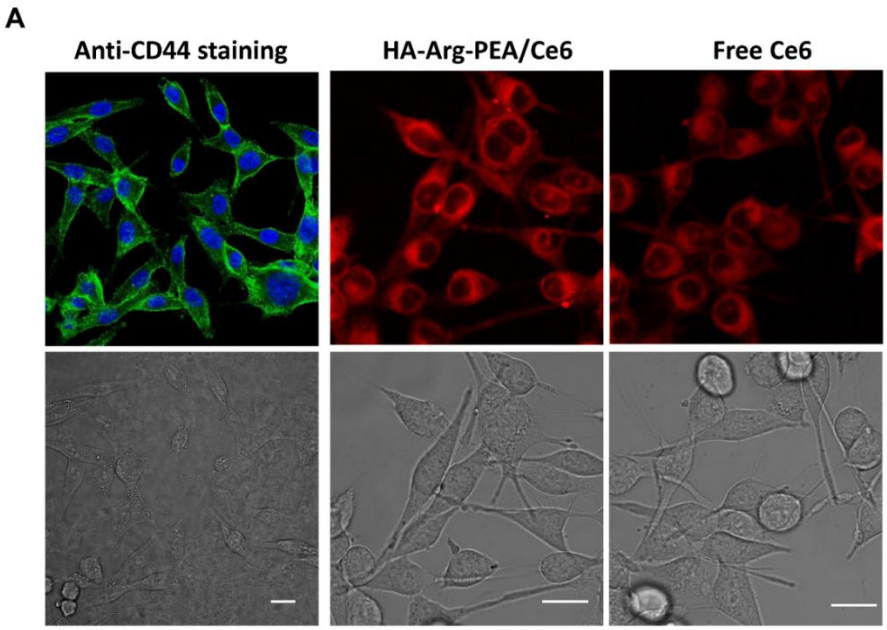

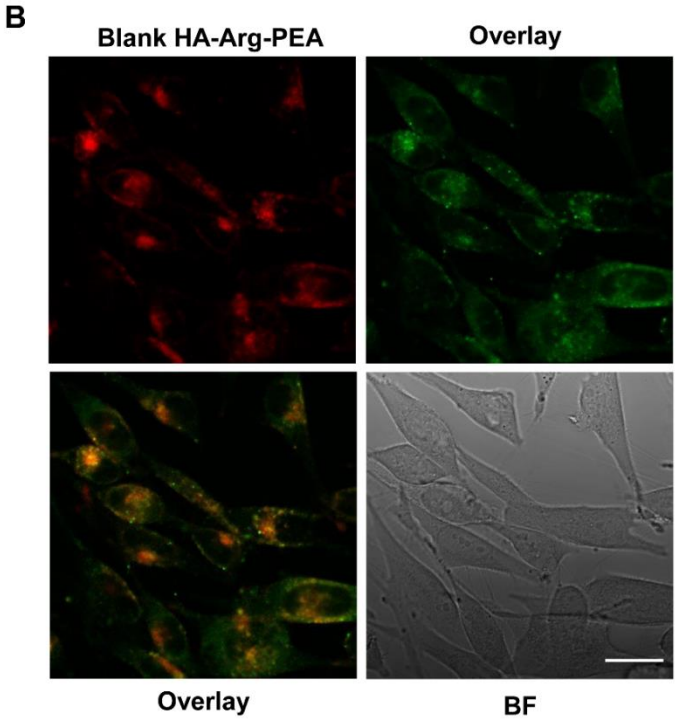


**Figure 3.6**. A) Confocal images of subcellular distribution of Ce6-loaded HA-Arg-PEA nanocomplex in MDA-MB-435/MDR cells after 24 hrs incubation. Left column: MDA-MB-435/MDR cells stained with anti-human CD44 antibody (green), the nuclei were counterstained with DAPI (blue). Middle column: intracellular fluorescence from MDA-MB-435/MDR cells treated with Ce6-loaded HA-Arg-PEA nanocomplex (red). Right column: intracellular fluorescence from MDA-MB-435/MDR cells after treated with free Ce6 (red). B) Confocal images of subcellular distribution of blank HA-Arg-PEA nanocomplex labelled with rhodamine (red) after 4 hrs incubation. The endolysosomes of MDA-MB-435/MDR cells were labelled with Lysotracker (green). Overlay of green and red fluorescence, and the bright filed (BF) images were provided. Scale bar represents 20 μm.

### *3.4.6 Endocytosis of HA-Arg-PEA nanocomplex by MDA-MB-435/MDR cells*

Inhibition study was performed to probe the endocytosis pathway of the blank HA-Arg-PEA nanocomplex in MDA-MB-435/MDR cells, and the data are shown in Figure 3.7A. The uptake of HA-Arg-PEA nanocomplex was decreased by 38% in MDA-MB-435/MDR cells pre-treated with anti-CD44 antibody, indicating that the entry of HA-Arg-PEA nanocomplex was mediated by CD44 receptor. Figure 3.7A also suggested that incubation of MDA-MB-435/MDR cells at 4 °C resulted in 60% decrease in the intracellular accumulation of rhodamine labelled nanocomplex, indicating that the internalization of HA-Arg-PEA nanocomplex is energy-dependent. The inhibition of lipid raft mediated endocytosis by methyl-β-cyclodextrin (methyl-betaCD) and clathrin mediated endocytosis by chloropromazine lead to the reduction of intracellular HA-Arg-PEA nanocomplex by 15% and 22%, respectively. The results suggested that both the clathrin mediated and lipid raft mediated endocytosis were involved in the internalization of HA-Arg-PEA nanocomplex into the MDA-MB-435/MDR cells. The lipid-raft dependent endocytosis pathway of was also reported by Qhattal et al. [43]. They suggested that HA grafted nanoparticles can rapidly recruit CD44s to the lipid raft fraction, and depletion of cholesterol by methyl-betaCD lead to shedding of CD44s, which reduced the uptake of HA nanoparticles.

However, the inhibition of macropinocytosis and the caveolae-mediated pathways by amiloride or nystatin in Figure 3.7A showed no significant

reduction in the transmigration of HA-Arg-PEA nanocomplex, indicating that the internalization of the blank HA-Arg-PEA nanocomplex was independent of macropinocytosis or caveolae pathway. The entry of free Ce6 into tumor cells, on the other hand, is a complicated process which involves binding with multiple plasma protein and lipoprotein, and LDL(low density lipoprotein) receptor mediated endocytosis was also evident for the internalization of free Ce6 [44].

In addition to the study of endocytosis pathway, the accumulated level of intracellular Ce6 were also monitored in both MDA-MB-435/MDR cells (CD44 positive) and 3T3 fibroblasts (CD44 negative), as shown in Figure 3.7B. When MDA-MB-435/MDR cells were incubated with Ce6-loaded HA-Arg-PEA nanocomplex, a significantly higher Ce6 level was observed at the first 4 hrs (blue curve), the highest among all the testing samples including free Ce6 (black curve). But the difference disappeared at longer incubation time (8 hrs and thereafter). Therefore, it's reasonable to conclude that the CD44 receptor mediated endocytosis of HA-Arg-PEA nanocomplex was more effective to improve the internalization efficiency of loaded Ce6 at a shorter exposure time.

In CD44 negative 3T3 fibroblasts, the accumulated level of intracellular Ce6 from free Ce6 (red curve) did not exhibit any statistical difference from the Ce6 level in MDA-MB-435/MDR cells (blue curve), suggesting no selectivity between normal and tumor cells. The lack of selectivity in the endocytosis of free Ce6 into cancer cells was also reported by Yoon et al. **[45]** in their study of HT29 colorectal tumor cells. In the case of Ce6-loaded HA-Arg-PEA

nanocomplex, the intracellular Ce6 level in MDA-MB-435/MDR cells (blue curve) was 1.8 fold higher than 3T3 fibroblasts (green curve) after 24 hrs incubation. HA-Arg-PEA remarkably enhanced the selectivity of Ce6 internalization by CD44 overexpressed tumor cells, and provides promising potential as the tumor-targeted delivery vehicles in PDT treatments.

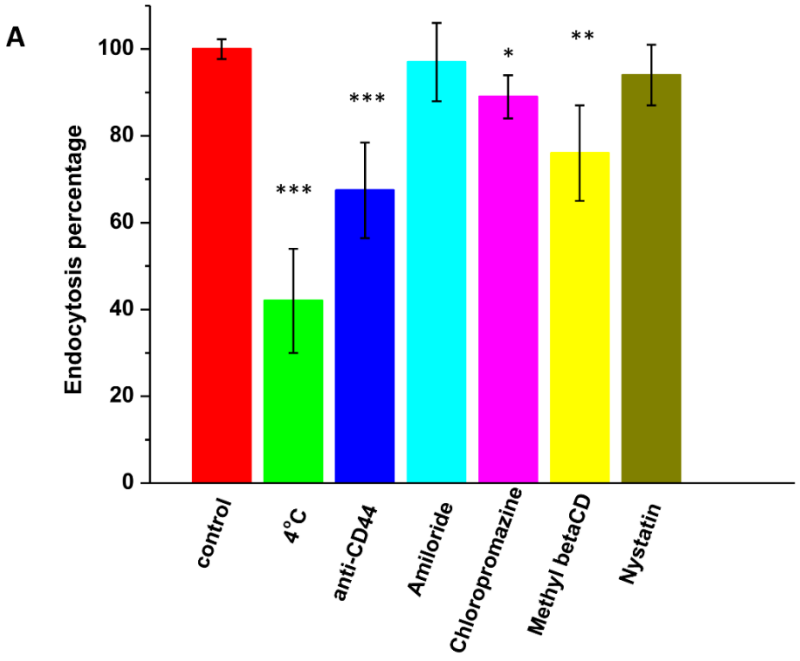

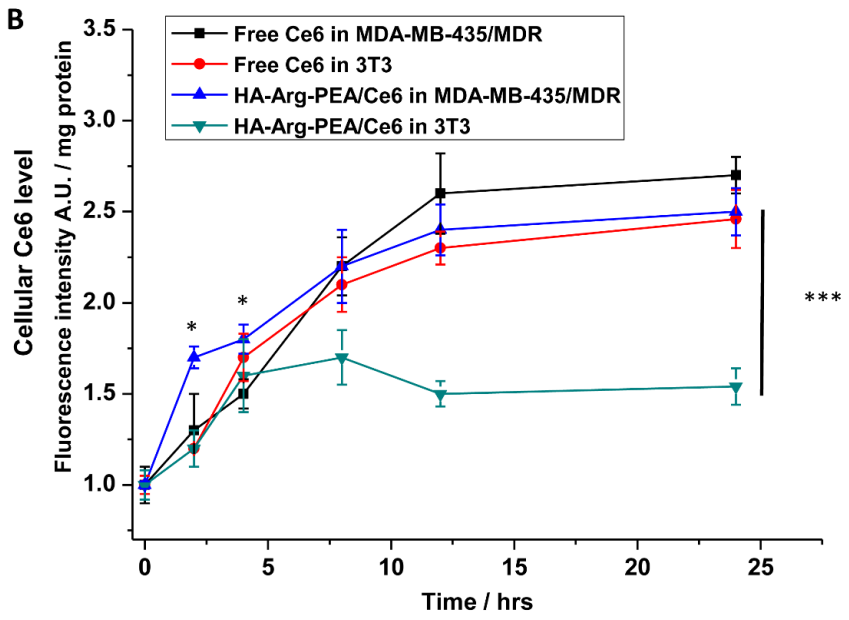


**Figure 3.7**. A) Endocytosis pathway inhibition studies. MDA-MB-435/MDR cells pre-treated with various endocytosis inhibitors or low temperature were incubated with rhodamine labelled HA-Arg-PEA nanocomplex for 4 hrs. Mean cellular fluorescence was recorded by flow cytometry and normalized to control (cells incubated with nanocomplex but not treated by any inhibitor). Values represent the average ± SD (n=3). Statistical significance was compared with control. B) Mean fluorescence of MDA-MB-435/MDR cells (CD44 positive) or 3T3 fibroblasts (CD44 negative) incubated with free Ce6 or Ce6-loaded HA-Arg-PEA nanocomplex (5 μM equivalent Ce6 concentration) was plotted vs. incubation time. Values represent the average ± SD (n=3). Statistical significance was compared between free Ce6 and Ce6-loaded HA-Arg-PEA nanocomplex treated groups, *, $p < 0.05$; **, $p < 0.01$, ***, $p < 0.001$.

### *3.4.7 Phototoxicity of Ce6-loaded HA-Arg-PEA nanocomplex*

Cytotoxicity of blank HA-Arg-PEA nanocomplex (without loaded Ce6) was first examined in MDA-MB-435/MDR cells to determine the biocompatibility of the carrier. As shown in Figure 3.8A, no significant cytotoxicity from the blank nanocomplex was observed at the concentration range from 1 to 100 μg/mL，which correlated to equivalent Ce6 concentration between 0.15 to 15 μM that was used in cytotoxicity study in Figure 3.8B. Therefore, the phototoxicity of Ce6-loaded HA-Arg-PEA nanocomplex can be solely attributed to the loaded Ce6 photosensitizer, instead of the carrier.

The phototoxicity of Ce6-loaded HA-Arg-PEA nanocomplex toward MDA-MB-435/MDR cells was then studied and the results are given in Figure 3.8B. The light dose of 3 J/cm$^2$ was selected based on the previous research on chlorin PDT. Chung et al. [46] and Luo et al. [47] suggested the range of light dose (1 – 5 J/cm$^2$) in both HCT116 human colon cancer cells and Tca8113 human tongue squamous cancer cells. In our preliminary study, we tested different light doses of 1 J/cm$^2$, 3 J/cm$^2$ and 5 J/cm$^2$, and only 3 J/cm$^2$ (120 sec) light dose resulted in a gradual increase in cellular toxicity as a function of the concentration of Ce6. At a lower light dose (1 J/cm$^2$, 40 sec) the cytotoxicity induced by both free Ce6 and Ce6-loaded nanocomplex was not significant (MDA-MB-435/MDR viability was greater than 70%) throughout the tested concentration range of Ce6 (1 – 10 μM). At a higher light dose (5 J/cm$^2$, 200 sec), the phototoxicity effect by free Ce6 and Ce6-loaded nanocomplex dominated from 0.5 to 10 μM, and the difference between free Ce6 and Ce6-loaded nanocomplex was not detectable due to the overdose of light irradiation that masked the difference.

When a light dose of 3 J/cm$^2$ was applied at 660 nm, enhanced toxicity was observed for both free Ce6 and Ce6-loaded HA-Arg-PEA nanocomplex, due to the production of singlet oxygen by photosensitizer shown in Figure 3.5B. Ce6-loaded HA-Arg-PEA nanocomplex induced significantly enhanced toxicity towards MDA-MB-435/MDR cells than free Ce6 at higher Ce6 concentrations (5-15 μM). However, the difference in phototoxicity between the two treatments disappeared at concentrations lower than 2 μM. The $IC_{50}$ was calculated to be 4.3 μM for free Ce6 and 2.6 μM for Ce6-loaded HA-Arg-PEA nanocomplex, respectively.

The enhanced cytotoxicity towards MDA-MB-435/MDR cells by Ce6-loaded nanocomplex at higher Ce6 concentrations can be attributed to the enhanced level of Ce6 monomerization and efficiency in generating singlet oxygen as indicated in Figure 3.4 and 5B. As Ce6 monomerization positively correlated to the photosensizting effect which induced phototoxicity [48], the interaction between Arg-PEA and Ce6, which is favorable for Ce6 monomerization, lead to the improved PDT efficiency of Ce6-loaded HA-Arg-PEA nanocomplex. At diluted condition (less than 2 μM), Ce6 maintained their monomeric form and the interaction with nanocomplex had less impact on their therapeutic efficiency.

The enhanced phototoxicity by Ce6-loaded HA-Arg-PEA nanocomplex is also closely related to the accumulated cellular Ce6 level described in Figure 3.7B. In addition, CD44 mediated endocytosis of HA-Arg-PEA nanocomplex facilitated the internalization of Ce6 by MDA-MB-435/MDR cells within a shorter incubation time (Figure 3.7B), and the higher intracellular Ce6 level also contributed to the improved phototoxicity of Ce6-loaded HA-Arg-PEA nanocomplex.

Phototoxicity of free Ce6 and Ce6-loaded HA-Arg-PEA nanocomplex was also detected on wild type MDA-MB-435 cells without multidrug resistance. At a light dose of 3 J/cm$^2$, the $IC_{50}$ was 5.0 μM for free Ce6 and 2.4 μM for Ce6-loaded HA-Arg-PEA nanocomplex. Comparing the $IC_{50}$ values between wild type vs. multidrug resistant phenotype, MDA-MB-435/MDR cells did not exhibit cross-resistance to photodynamic treatment in the case of both free Ce6 and Ce6-loaded HA-Arg-PEA nanocomplex. Since the presence of drug efflux pump does not adversely affect the therapeutic performance of Ce6-loaded HA-Arg-PEA nanocomplex, it can be applied as an alternative/complementary treatment for multidrug resistant tumor with improved therapeutic efficiency.

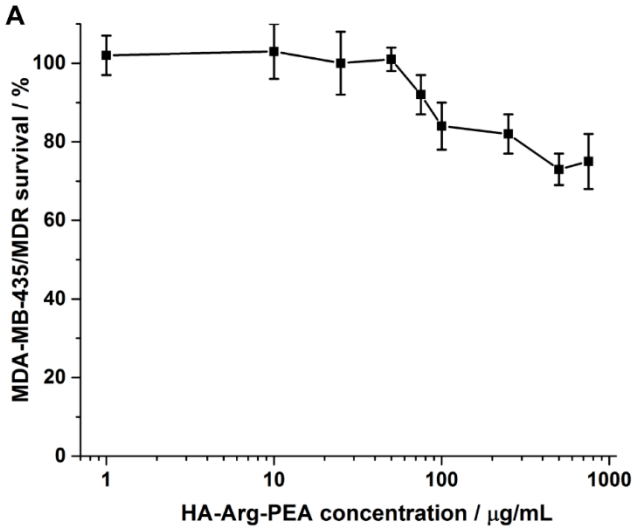

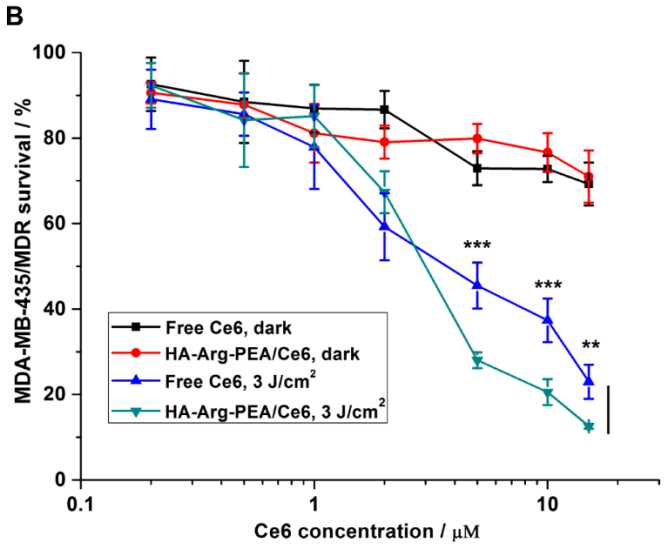


**Figure 3.8**. A) Viability of MDA-MB-435/MDR cells treated by blank HA-Arg-PEA nanocomplex. B) Viability of MDA-MB-435/MDR cells treated by Ce6-loaded HA-Arg-PEA nanocomplex and free Ce6 at various Ce6 concentrations with and without irradiation. The MDA-MB-435/MDR cells were incubated with Ce6 for 4 hrs, washed and further incubated for another 20 hrs in fresh media, before light irradiation was applied (660 nm, 3 J/cm$^2$). Cell viability was determined 24 hrs post-irradiation. Values represent the average ± SD (n=6). Statistical significance: *, $p < 0.05$; **, $p < 0.01$, ***, $p < 0.001$.

### *3.4.8 Apoptosis study on PDT-treated MDA-MB-435/MDR cells*

To further characterize cell death in PDT-treated MDA-MB-435/MDR cells, flow cytometry results for annexin V/PI assay were shown in Figure 3.9A. The percentages of cell population in each quadrant were obtained as: live cells (PI$^{-/}$annexin V$^-$, the lower left quadrant), dead cells (PI$^+$/annexin$^+$ and PI$^+$/annexin V$^-$, both the upper right and upper left quadrant), early apoptotic cells (PI$^-$/annexin V$^+$, the lower right

quadrant), and listed in Figure 3.9B. Blank HA-Arg-PEA nanocomplex didn't induce significant cell death, as 83.6% of cells was alive. The result suggested the biocompatibility of the blank nanocomplex. Cell death induced by two different Ce6 concentrations (2 μM and 10 μM) was then detected for both free Ce6 and Ce6-loaded HA-Arg-PEA nanocomplex. It can be concluded that any cytotoxicity should be attributed to the loaded Ce6 instead of the carrier.

At a higher Ce6 concentration (10 μM), neither Ce6-loaded nanocomplex nor free Ce6 induced early apoptosis. When treated with Ce6-loaded HA-Arg-PEA nanocomplex, the majority of the cell population (79.6 %) was detected as dead cells, and a minor population of live cells was detected (20.0%). These results suggest a trend of necrotic death of MDA-MB-435/MDR cells when treated with a higher dose of Ce6-loaded HA-Arg-PEA nanocomplex. Free Ce6 at a similar concentration (10 μM) induced a significantly lower level of cell death, as 46.7% of cells were alive. These results further suggest that the Ce6-loaded HA-Arg-PEA nanocomplex was more potent than free Ce6 at a higher Ce6 concentration.

At a lower Ce6 concentration (2 μM), the Ce6-loaded HA-Arg-PEA nanocomplex did not induce cell death as effectively as free Ce6, i.e., 64.3% of cells were alive in the Ce6-loaded nanocomplex treatment vs. 56.7% live cells treated with free Ce6. However, 16.7% of cells were subjected to early apoptosis in the Ce6-loaded HA-Arg-PEA nanocomplex treatment, the highest among all 4 testing groups, indicating a potentially different cell death mechanism at this particular treatment condition.

At higher Ce6 concentration (10 μM), Ce6-loaded HA-Arg-PEA nanocomplex

outperformed than free Ce6. Higher Ce6 concentration lead to a greater tendency to form Ce6 aggregates in the absence of a proper carrier. At diluted condition, Ce6 monomer would dominate irrespective of the carrier, and bring in therapeutic effectiveness. In general, the annexin V/PI assay provided consistent results with the phototoxicity data in Figure 3.8, in which enhanced PDT efficiency was observed for Ce6-loaded HA-Arg-PEA nanocomplex at higher Ce6 concentrations (5 to 15 μM). The in vitro cell work was performed at physiological pH, and it's reasonable to predict that Ce6-loaded HA-Arg-PEA can exhibit enhanced potency than free Ce6 in acidic microenvironment of tumor in the in vivo study.

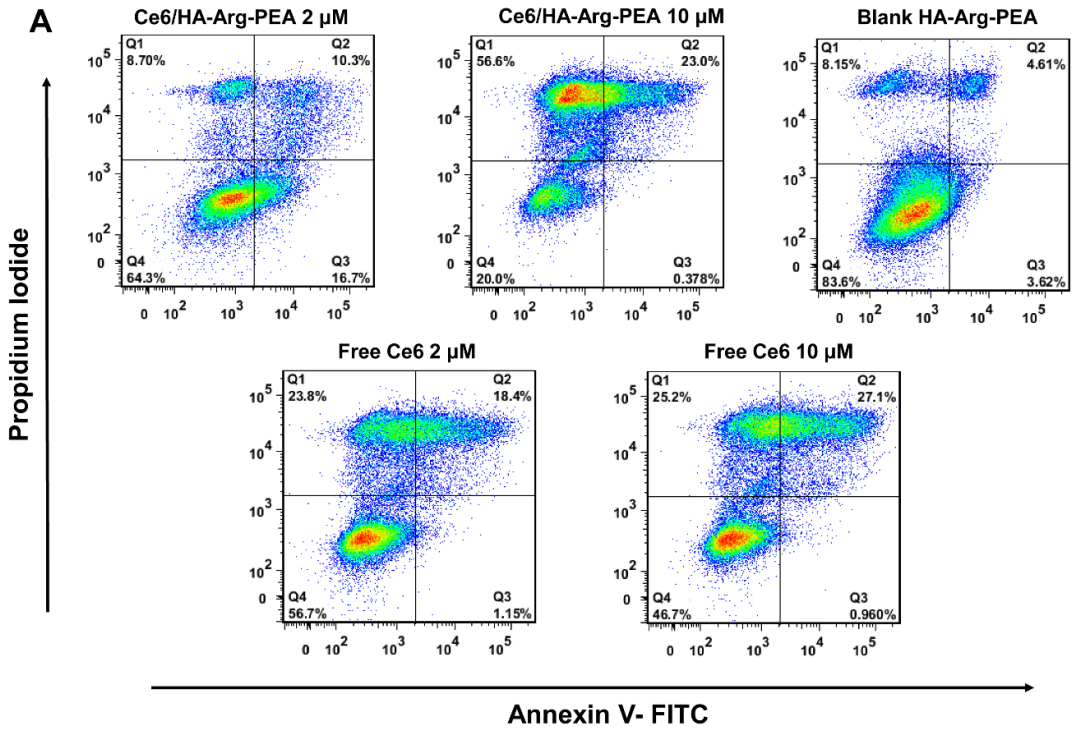

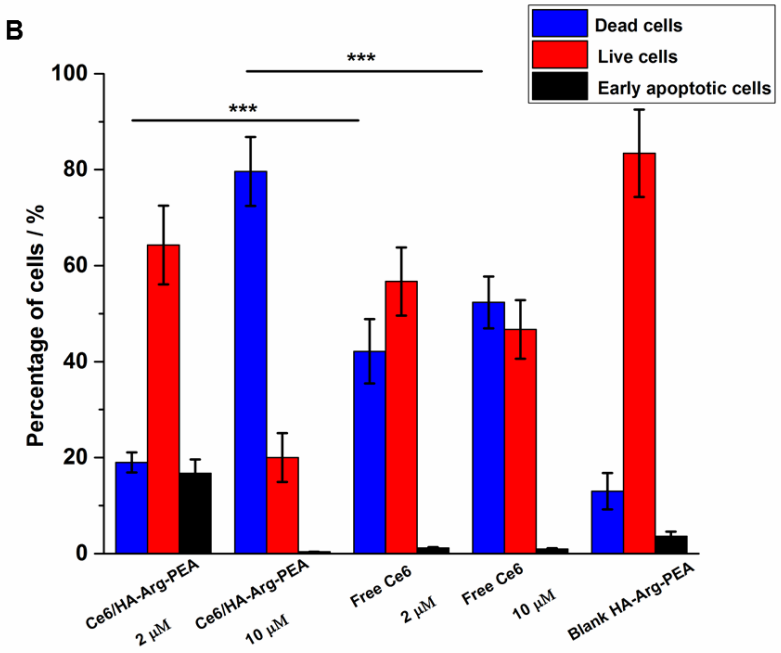


**Figure 3.9**. Photosensitizer-induced apoptosis of MDA-MB-435/MDR cells by Annexin V/PI Staining. A) Flow cytometry plots of annexin V/PI staining of MDA-MB-435/MDR cells. Blank HA-Arg-PEA nanocomplex, free Ce6 or Ce6-loaded HA-Arg-PEA nanocomplex with equivalent Ce6 concentrations (2 and 10 μM) were incubated with MDA-MB-435/MDR cells for 4 hrs before the photosensitizer was washed off and cells were incubated for another 20 hrs in fresh media. Light irradiation was then applied (660 nm, 3 J/cm$^2$). Annexin-V/PI double staining was performed 24 hrs post irradiation. B) The percentage of cell population in each quadrant was determined by flow cytometry, values represent the average ± SD (n=3). Statistical significance: ***, $p < 0.001$.

### *3.5 Conclusions*

Self-assembled nanocomplex was formed from anionic HA and cationic Arg-

PEA, and further stabilized via covalent bonding. The Arg-PEA component in the nanocomplex facilitated the formation of Ce6 monomer with enhanced photosensitizing efficiency, while the HA component achieved targeted delivery of Ce6 in CD44 positive tumor cells. The monomerization of loaded Ce6 was maintained in acidic environment compared to free Ce6, and the efficiency of singlet oxygen generation was also improved. The biodegradability of HA-Arg-PEA nanocomplex enabled enzymatic-triggered release of Ce6. The CD44-mediated endocytosis of Ce6-loaded nanocomplex significantly improved the selectivity and the intracellular Ce6 level in CD44 positive MDA-MB-435/MDR cancer cells within a shorter incubation time. The PDT efficiency in tumor cell inhibition was also enhanced compared to free Ce6, especially at higher Ce6 concentrations. Therefore, the biodegradable HA-Arg-PEA nanocomplex could be a promising delivery vehicle in the application of photodynamic therapy for tumors.

**References:**


[1] D. E. J. G. J. Dolmans, D. Fukumura, R. K. Jain, *Nat. Rev. Cancer* **2003**, *3*, 380.

[2] S. Horibe, J. Nagai, R. Yumoto, R. Tawa, M. Takano, *J. Pharm. Sci.* **2011**, *100*, 3010.

[3] V. P. Savitskiy, V. P. Zorin, M. P. Potapnev, *Exp. Oncol.* **2005**, *27*, 47.

[4] D. L. Frazier, M. A. Barnhill, X. Lu, E. Jones, G. Niemeyer, L. Mishu, C. D. Lothrop, *Lasers Surg. Med.* **1993**, *13*, 511.

[5] W. Li, W. J. Zhang, K. Ohnishi, I. Yamada, R. Ohno, K. Hashimoto, *J. Photochem. Photobiol. B* **2001**, *60*, 79.

[6] Q. Wu, Z. Yang, Y. Nie, Y. Shi, D. Fan, *Cancer Lett.* **2014**, *347*, 159.

[7] B. Q. Spring, I. Rizvi, N. Xu, T. Hasan, *Photochem Photobiol Sci* **2015**, *14*, 1476.

[8] A. Casas, G. Di Venosa, T. Hasan, null Al Batlle, *Curr. Med. Chem.* **2011**, *18*, 2486.

[9] R. R. Allison, G. H. Downie, R. Cuenca, X.-H. Hu, C. J. Childs, C. H. Sibata, *Photodiagnosis Photodyn. Ther.* **2004**, *1*, 27.

[10] A. E. O'Connor, W. M. Gallagher, A. T. Byrne, *Photochem. Photobiol.* **2009**, *85*, 1053.

[11] A. Master, M. Livingston, A. Sen Gupta, *J. Controlled Release* **2013**, *168*, 88.

[12] K. Y. Choi, H. Chung, K. H. Min, H. Y. Yoon, K. Kim, J. H. Park, I. C. Kwon, S. Y. Jeong, *Biomaterials* **2010**, *31*, 106.

[13] L. Schaefer, D. P. Reinhardt, *Adv. Drug Deliv. Rev.* **2016**, *97*, 1.

[14] F. Dosio, S. Arpicco, B. Stella, E. Fattal, *Adv. Drug Deliv. Rev.* **2016**, *97*, 204.

[15] J. Shi, R. Ma, Lei Wang, J. Zhang, Ruiyuan Liu, Y. Liu, X. Yu, J. Gao, L. Li, Hou, Z. Zhang, *Int. J. Nanomedicine* **2013**, 2361.

[16] M. Gary-Bobo, D. Brevet, N. Benkirane-Jessel, L. Raehm, P. Maillard, M. Garcia, J.-O. Durand, *Photodiagnosis Photodyn. Ther.* **2012**, *9*, 256.

[17] H. Y. Yoon, H. Koo, K. Y. Choi, S. J. Lee, K. Kim, I. C. Kwon, J. F. Leary, K. Park, S. H. Yuk, J. H. Park, K. Choi, *Biomaterials* **2012**, *33*, 3980.

[18] T. Debele, S. Peng, H.-C. Tsai, *Int. J. Mol. Sci.* **2015**, *16*, 22094.

[19] C.-C. Chu, In *Biodegradable Polymers: New Biomaterial Advancement and Challenges*; Chu, C.-C., Ed.; Nova Science Publisher, 2015; Vol. 2.

[20] C.-C. Chu, In *Biomaterials – Principles and Practices*; Wong, J. Y.; Bronzino, J. D.; Peterson, D. R., Eds.; CRC Press, 2012.

[21] C. C. Chu, *J. Fiber Bioeng. Inform.* **2012**, *5*, 1.

[22] C.C.Chu, In *L-Arginine – Structure, Dietary Sources and Beneficial Effects*; Nova Science Publisher: New York, In Press.

[23] J. Wu, D. Yamanouchi, B. Liu, C.-C. Chu, *J. Mater. Chem.* **2012**, *22*, 18983.

[24] H. A. Isakau, M. V. Parkhats, V. N. Knyukshto, B. M. Dzhagarov, E. P. Petrov, P. T. Petrov, *J. Photochem. Photobiol. B* **2008**, *92*, 165.

[25] E. Zenkevich, E. Sagun, V. Knyukshto, A. Shulga, A. Mironov, O. Efremova, R. Bonnett, S. P. Songca, M. Kassem, *J. Photochem. Photobiol. B* **1996**, *33*, 171.

[26] J. Wu, C.-C. Chu, *Acta Biomater.* **2012**, *8*, 4314.

[27] H. Song, C. C. Chu, *J. Appl. Polym. Sci.* **2012**, *124*, 3840.

[28] J. Dahlmann, A. Krause, L. Möller, G. Kensah, M. Möwes, A. Diekmann, U. Martin, A. Kirschning, I. Gruh, G. Dräger, *Biomaterials* **2013**, *34*, 940.

[29] S. Paul, S. Selvam, P. W. S. Heng, L. W. Chan, *J. Fluoresc.* **2013**, *23*, 1065.

[30] S. A. Kulkarni, S.-S. Feng, *Pharm. Res.* **2013**, *30*, 2512.

[31] A. N. Potuck, B. L. Weed, C. A. Leifer, C. C. Chu, *Biomacromolecules* **2015**, *16*, 564.

[32] H. Harada, M. Takahashi, *J. Biol. Chem.* **2007**, *282*, 5597.

[33] B. Čunderlíková, L. Gangeskar, J. Moan, *J. Photochem. Photobiol. B* **1999**, *53*, 81.

[34] H. A. Isakau, M. V. Parkhats, V. N. Knyukshto, B. M. Dzhagarov, E. P. Petrov, P. T. Petrov, *J. Photochem. Photobiol. B* **2008**, *92*, 165.

[35] M. Shen, Y. Huang, L. Han, J. Qin, X. Fang, J. Wang, V. C. Yang, *J. Controlled Release* **2012**, *161*, 884.

[36] G. Gakhar, H. Liu, R. Shen, D. Scherr, D. Wu, D. Nanus, C.-C. Chu, *Anticancer Res.* **2014**, *34*, 3981.

[37] K. A. Hernandez, R. C. Hooper, T. Boyko, A. R. Golas, M. van Harten, D. Q. Wu, A. Weinstein, C. C. Chu, J. A. Spector, *J. Biomed. Mater. Res. B Appl. Biomater.* **2015**, *103*, 457.

[38] J. Wu, C.-C. Chu, *J Mater Chem B* **2013**, *1*, 353.

[39] J. Wu, M. A. Mutschler, C.-C. Chu, *J. Mater. Sci. Mater. Med.* **2011**, *22*, 469.

[40] D. Yamanouchi, J. Wu, A. N. Lazar, K. C. Kent, C.-C. Chu, B. Liu, *Biomaterials* **2008**, *29*, 3269.

[41] W. Bors, C. Michel, M. Saran, *Eur. J. Biochem.* **1979**, *95*, 621.

[42] X. Sun, P. Ma, X. Cao, L. Ning, Y. Tian, C. Ren, *Drug Deliv.* **2009**, *16*, 357.

[43] H. S. S. Qhattal, X. Liu, *Mol. Pharm.* **2011**, *8*, 1233.

[44] H. Mojzisova, S. Bonneau, C. Vever-Bizet, D. Brault, *Biochim. Biophys. Acta BBA - Biomembr.* **2007**, *1768*, 2748.

[45] H. Y. Yoon, H. Koo, K. Y. Choi, S. J. Lee, K. Kim, I. C. Kwon, J. F. Leary, K. Park, S. H. Yuk, J. H. Park, K. Choi, *Biomaterials* **2012**, *33*, 3980.

[46] C.-W. Chung, C. W. Choi, Y. Jeong, D. H. Kang, *J. Nanosci. Nanotechnol.* **2016**, *16*, 1379.

[47] W. Luo, R.-S. Liu, J.-G. Zhu, Y.-C. Li, H.-C. Liu, *Oncol. Lett.* **2014**.

[48] M. Hädener, I. Gjuroski, J. Furrer, M. Vermathen, *J. Phys. Chem. B* **2015**, *119*, 12117.

# CHAPTER 4

# LIGHT-FACILITATED REDUCTION-RESPONSIVE DRUG DELIVERY SYSTEM FROM BIODEGRADABLE PSEUDO PROTEIN/HYAURONIC ACID NANOCOMPLEX WITH IMPROVED ANTI-TUMOR EFFECT

### *4.1 Abstract*

Reduction-sensitive nanomedicine is a promising strategy to achieve controlled release of payloads in response to intracellular reductive milieu. However, endolysosomal sequestration of internalized carriers and insufficient redox potential in endolysosomes may delay the release of payloads and impact their therapeutic efficacy. Photochemical internalization (PCI), which takes advantage of light-induced endolysosomal rupture, is an effective technique for endosomal escapes and cytosolic release of cargos. In this study, a biodegradable and reduction-sensitive nanocomplex was developed from arginine based poly(ester amide)s and hyaluronic acid (HA), and the PCI-photosensitizer AlPcS2a was conjugated to the surface of the nanocomplex (ArgPEA-ss-HA(AP)). The PCI effect of ArgPEA-ss-HA(AP) nanocomplex was validated in both monolayers and 3D spheroid models of MDA-MB-231 breast cancer cells. Synergism was detected between PCI effect and doxorubicin-loaded nanocomplex in the inhibition of MDA-MB-231 cells. In addition, the ArgPEA-ss-HA(AP) nanocomplex also provided enhanced intratumoral penetration in 3D spheroids compared to free AlPcS2a. The in vivo results suggested that the conjugation of AlPCs2a in the nanocomplex enabled the consistent and preferential accumulation of both doxorubicin and AlPcS2a in tumor site. Light-enhanced anti-tumor effect was observed for doxorubicin-loaded nanocomplex at well-tolerable dosage. ArgPEA-ss-HA(AP) nanocomplex, as a reduction-responsive delivery vehicle, can hold great potential to achieve spatio-temporally controllable anti-tumor effect.

### *4.2 Introduction*

Stimuli-responsive nanomedicine with controlled release profile and minimal side effect have gained considerable popularity in the study of anti-cancer drug delivery [1]. Smart nano-carriers enable the site-specific release of payloads in response to a series of biological cues in tumor local environment (enzyme, acidic pH, redox potential, etc.) as well as other physical stimuli (light, temperature, ultrasounds, electric field, etc) [2]. Among various smart nanomedicines, reduction-sensitive nano-

vehicles provide a promising strategy for intracellular drug delivery, in which the release of payloads is predominantly triggered by thiol/disulfide exchange induced by the intracellular reducing agent such as glutathione[3].

The internalization of nanomedicine by tumor cells involves transporter-mediated endocytosis [4]. The nanoparticles are wrapped around by the plasma membrane, and closed-vesicle structures are formed, followed by fusion with endolysosomes. Except ultra-small gold nanoparticles (2-10 nm), which were identified in nucleus and cytoplasm [5,6], endolysosomal sequestration and subsequent degradation was inevitable if the nano-carriers are not engineered to escape endolysosomes [7]. For reduction-responsive nanomedicine, the therapeutic potency can be challenged due to the absence of reductive milieu in endolysosomes [8]. Augmentation in therapeutic effect resulted from endolysosomal escape of reduction-sensitive nanomedicine were reported [9,10].

Photochemical internalization (PCI), developed by Berg and colleagues [11], is a highly efficient technology which takes advantage of photochemical rupture of endocytic vesicles and enables the cytosolic release of therapeutic agents [12]. PCI-photosensitizers are amphiphilic molecules which contain hydrophobic fused rings and hydrophilic sulfonate groups, and exhibit specific affinity with the membrane of endocytic vesicles where they generate singlet oxygen upon irradiation to induce the permeabilization of endocytic vesicles. PCI-photosensitizers are non-toxic in the absence of light, and spatio-temporally controlled tumoricidal effect can be achieved by the application of light irradiation. PCI has been demonstrated to enhance the efficacy of various therapeutic agents, such as macromolecular [11]. In addition, PCI was also documented to enhance the delivery performance of polymer-based nano-carriers[13]. Yen et al. [14] reported an augmented anti-tumor efficiency of poly(ethylene glycol)-poly(lysine) (PEG-PLys) micelles conjugated with camptothecin via disulfide linkage, when endolysosomal escape was achieved from the PCI effect of free photosensitizer photofrin.

The concentration of PCI-photosensitizers and therapeutic agents, light dosage, the time interval between the administration of drug and the application of light are the

key factors that contribute to the efficacy of PCI [15]. In the current research, PCI-photosensitizers and the therapeutics were administered separately. The discrepancy in their biodistribution and pharmacokinetic profiles can impact the efficiency of PCI-facilitated treatment. It is of particular interest to develop a biodegradable vehicle for the co-delivery of both PCI-photosensitizer and therapeutic agents.

Amino acid based poly (ester amide)s (AA-PEA) is a family of biodegradable pseudo-proteins synthesized from 3 building blocks: amino acids, dialcohol, diacids. By selecting different amino acids, AA-PEAs are tunable in their chemical/physical properties and have been engineered into coatings for cardiovascular stent, nanofibers, nanoparticles, hydrogels for multiple biomedical applications. The advantages for AA-PEAs include biodegradability, biocompatibility, and muted inflammatory response, etc., and current research on AA-PEAs have recently been reviewed [16–19]. Among the amino acids for AA-PEA synthesis, arginine retains cationic charge over a wide range of pH, suitable to form electrostatic complex with other negatively charged materials such as hyaluronic acid (HA) [19–21]. HA-based nanomedicine provided considerable therapeutic potency in the field of tumor-targeting delivery, due to the overexpression of CD44 receptors on many types of tumor cells [22]. Choi et al [23] suggested that low degree of PEGylation on HA nanoparticles improved their blood circulation time, resulted in an enhanced retention of the nanoparticles in tumor site.

In this contribution, we aimed to develop a biodegradable and reduction-responsive nanocomplex from arginine based PEA and hyaluronic acid, and functionalized the surface of the nanocomplex with PCI-photosensitizer AlPcS2a (aluminum phthalocyanine disulfonate) via PEG (polyethylene glycol) spacer. AlPcS2a is one of the most commonly studied PCI-photosensitizers with activation wavelength of 660 -670 nm. As evidenced by previous studies, phthalocyanine derivatives maintained the photosensizting effect after being conjugated with PEG [24] or small molecules [25], which provides rationale for the PCI-effect induced by conjugated AlPcS2a. However, efficiency for the endocytosis of free AlPcS2a by tumor cells or the penetration in solid tumor can challenge the therapeutic efficacy, as the general incubation time of free AlPcS2a and various 2D tumor cells was reported

[16] at 12-18 hrs before PCI effect was achieved. It is important to develop a delivery system with improved endocytosis/penetration of AlPcS2a. In this study, the AlPcS2a-cojugated nano-carriers exhibited enhanced uptaken efficiency on both 2D monolayer of MDA-MB-231 breast cancer cells, and 3D multicellular spheroids, compared to free AlPcS2a. The PCI effect in combination with doxorubicin(DOX)-loaded nanocomplex was investigated to illustrate the impact of endosomal escape on the anti-tumor efficacy of reduction-sensitive nanomedicine both *in vitro* and *in vivo*.

### *4.3 Experimental*

#### *4.3.1 Chemicals and cells*

Sodium hyaluronate (MW= 10 to 20 kDa) was from Lifecore Biomedical (Chaska, MN). Tetrabutylammonium bromide, thionyl chloride, cystamine dihydrochloride, 1-ethyl-3-(3-dimethylaminopropyl)-carbodiimide hydrochloride (EDC), 1-hydroxybenzotriazole (HOBT), dithiothreitol (DTT), and glutathione (GSH) were from Sigma Aldrich (Milwaukee, WI). Amberlite IR-120 $H^+$ ion exchange resin was from Alfa Aesar (Ward Hill, MA). Dimethyl sulfoxide (DMSO), methanol and other HPLC grade solvents were from JT Baker (Phillipsburg, NJ). Lysotracker green and Hoechst 33342 were from Molecular Probes (Eugene, OR). Aluminum phthalocyanine disulfonate (AlPcS2a) was from Frontier Scientific (Logan, UT). Doxorubicin hydrochloride was from Lancrix Chemicals (Shanghai, China). Maleimide-polyoxyethylene-amine (MAL-PEG-$NH_2$, MW= 5 kDa) was from JenKem Technology (Allen, TX). Snakeskin dialysis tubing (MWCO = 10 kDa), SPDP (N-succinimidyl 3-(2-pyridyldithio) propionate) crosslinker were from Pierce (Rockford, IL). Arg-2 (tetra-p-toluenesulfonic acid salt of bis-L-arginine ethane diester) and NSu (di-p-nitrophenyl succinate) were synthesized from our previous study [26].

MDA-MB-231 cancer cells were maintained in Dulbecco's modified Eagle medium (Lonza, Walkersville, MD) supplemented with 10% fetal bovine serum (Hyclone, Logan, UT), 2 mM L-glutamine, 100 unit/mL penicillin, and 100 μg/mL streptomycin (Lonza, Walkersville, MD) at 37 °C in 5% $CO_2$.

### *4.3.2 Synthesis of polymers*

*Synthesis of AlPcS2a dichloride*. AlPcS2a (50mg, 63.6 µM) was dissolved in thionyl chloride (5 mL); the mixture was refluxed for 8 hrs [25,27]. The excess of thionyl chloride was evaporated under vacuum and the residue was washed with dichloromethane and dried to give dichlorosulfonyl phthalocyanine.

*Synthesis of HA-SH conjugated with PEG and AlPcS2a (HA-SH(AP))*. HA-SH with degree of thiolation of 23% was synthesized according to the published procedures [28]. Tetrabutylammonium salt of HA-SH (HA-SH-TBA) was prepared as previously described [29]. As illustrated in Figure 4.1B, MAL-PEG-$NH_2$ (70 mg) and triethylamine (5.6 mg) was dissolved in DMF (5 mL), AlPcS2a dichloride (11 mg) was added and reacted overnight at a room temperature. Ethanol (0.5 mL) was then added and the reaction mixture was purged with nitrogen for 1 hr before it was added to a solution of HA-SH-TBA (165 mg) in DMF (10 mL) under nitrogen protection. The reaction was stirred at room temperature overnight, dialyzed (MWCO=3.5 kDa) against DMF/$H_2O$ (3:7, v/v) for 24 hrs and DI water for another 24 hrs. The resulted aqueous solution of HA-SH(AP) was stirred with 25 mM DTT for 2 hrs, precipitated in ethanol, re-dissolved in 10 mL DI water and lyophilized. The above procedures were performed in dark. UV-Vis spectra of HA-SH(AP) in aqueous solution was examined on a Lambda Bio40 spectrophotometer (Perkin-Elmer, Norwalk, CT).

*Preparation of $NH_2$-ArgPEA-$NH_2$*. The synthesis of amine-terminated Arg-PEA was according to published study [30]. As illustrated in Figure 4.1A, an excessive amount of monomers Arg-2 (1.0 mmol) was mixed with monomer NSu (0.8 mmol) in DMSO (1.5 mL), and heated to 75 ºC under stirring. Triethylamine (0.31 mL) was added until the monomers were completely dissolved. The reaction was kept for 12 hrs at 75 ºC. The resulting $NH_2$-ArgPEA-$NH_2$ was precipitated in cold ethyl acetate twice, re-dissolved in DI water, and repeatedly concentrated in Macrosep centrifugal device (MWCO=1 kDa, Pall Filtron, Northborough, MA) for purification. Ninhydrin assay was performed to estimate the content of primary amine, calibrated with a standard curve obtained from free arginine.

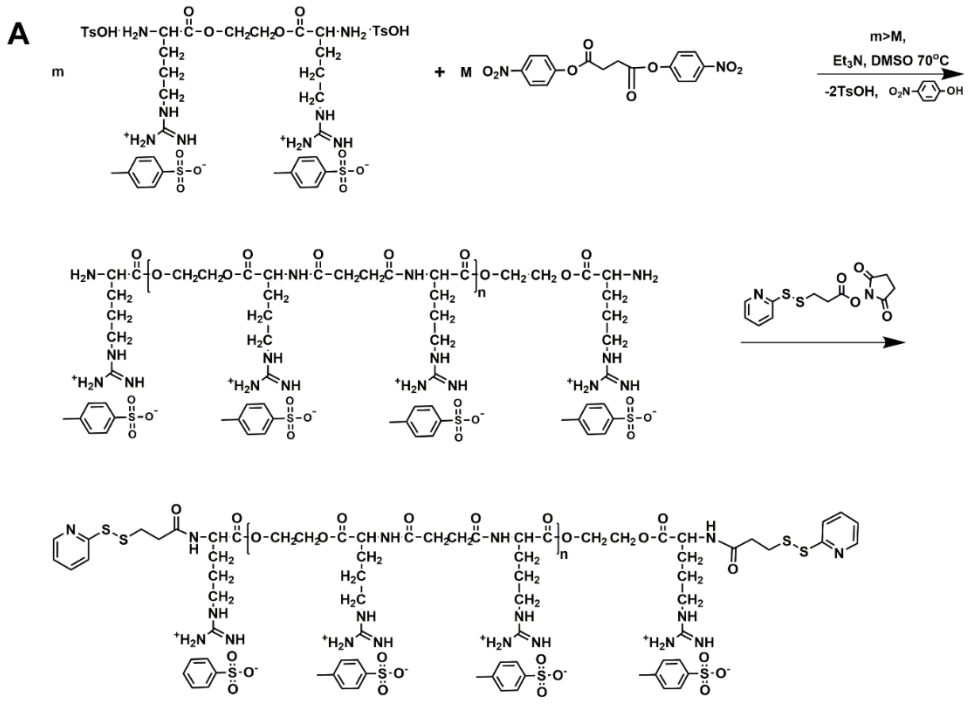


SPDP activated $NH_2$-ArgPEA-$NH_2$

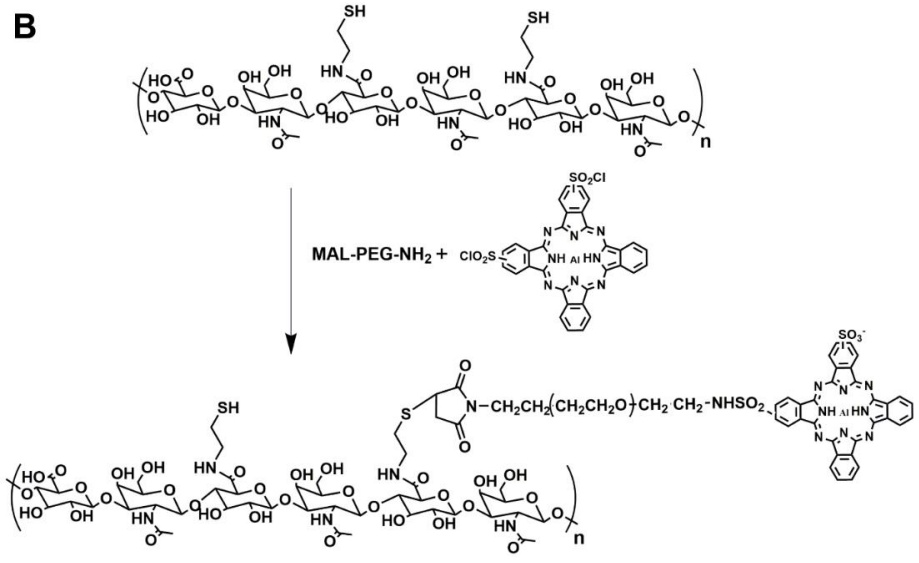


HA-SH(AP) thiolated hyaluronic acid conjugated with PEG and AlPcS2a

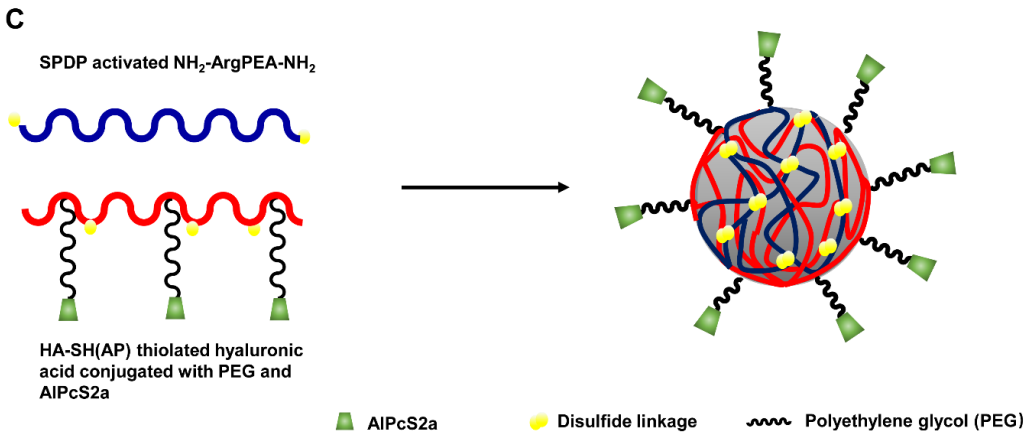


**Figure 4.1.** Synthesis scheme for A) arginine based poly(ester amide)s (ArgPEA) with amino end groups ($NH_2$-ArgPEA-$NH_2$), and activation of amino groups with SPDP crosslinker; B) thiolated hyaluronic acid (HA-SH) functionalized with polyethylene glycol (PEG) and AlPcS2a photosensitizer (HA-SH (AP)); and C) A) the formation of reduction-sensitive nanocomplex ArgPEA-ss-HA(AP) from $NH_2$-ArgPEA-$NH_2$ activated by SPDP and HA-SH(AP) via disulfide linkage.

### *4.3.3 Preparation and characterization of DOX-loaded ArgPEA-ss-HA (AP) nanocomplex*

To prepare the DOX-loaded ArgPEA-SS-HA(AP) nanocomplex (Figure 4.1C), $NH_2$-ArgPEA-$NH_2$ (50 mg) was dissolved in DMSO (5 mL), SPDP (13 mg) was added and stirred for 2 hrs at room temperature. HA-SH(AP) in DI water (176 mg, 20 mg/mL) was further added and stirred for 2 hrs. 20 mg doxorubicin hydrochloride was then added and stirred overnight. The resulted nanocomplex was dialyzed against DI water (MWCO=10 kDa) for 48 hrs, repeatedly concentrated in Macrosep centrifugal filter (MWCO=100 kDa), and lyophilized. To determine the contents of AlPcS2a in the nanocomplex, ArgPEA-ss-HA (AP) nanocomplex (10 mg) was digested in 0.1 M NaOH (1 mL) overnight. The fluorescence of AlPcS2a was

determined on a PTI spectrofluorometer (Photon Technology International, South Brunswick, NJ) at λex=605 nm, λem=660-790 nm, and calibrated with an AlPcS2a standard curve.

To determine the loading contents of DOX in the nanocomplex, 10 mg of DOX-loaded ArgPEA-ss-HA (AP) nanocomplex was dissolved in 25 mM aqueous solution of DTT and stirred overnight. The solution was centrifuged at 14000 rcf and DOX concentration was determined by spectrofluorometer at λex=480 nm, λem=590 nm and calibrated with a DOX standard curve. Drug loading content (DLC) and encapsulation efficiency (EE) were calculated.

The morphology of the nanocomplex was observed on a FEI Tecnai Spirit T12 TEM (FEI Co., Hillsboro, OR) at an operating voltage of 120 kV. Zeta potential and the size profile were characterized on a NanoZS Zetasizer (Malvern, UK).

### *4.3.4 Oxygen consumption rate of ArgPEA-ss-HA(AP) nanocomplex*

The oxygen consumption rate of blank ArgPEA-ss-HA(AP) nanocomplex was measured using a Clark-type oxygen electrode (Hansatech Instruments Ltd, UK) as previously described [31]. The microelectrode was inserted into the PBS solution of free AlPcS2a or blank ArgPEA-ss-HA(AP) with equivalent AlPcS2a concentration. 10% FBS was also present in each sample as receptor for reactive oxygen species. LED arrays (660 nm, 25 mW/cm$^2$, Elixa Ltd, Albuquerque, NM) was used for light irradiation. Before each measurement, the system was calibrated in PBS bubbled with air. Fold of oxygen consumption was acquired by normalizing the measured oxygen pressure in each sample to untreated PBS bubbled with air, and the result was plotted as a function of irradiation time. Oxygen consumption rate of non-irradiated solution of free AlPcS2a or blank ArgPEA-ss-HA(AP) were also tested.

### *4.3.5 In vitro release of DOX from ArgPEA-ss-HA(AP) nanocomplex*

*In vitro* release profiles of DOX from the ArgPEA-ss-HA(AP) nanocomplex were examined in 10 mM phosphate buffer (pH 7.4) with or without the presence of 10 mM glutathione(GSH) for 48 hrs at 37 °C. The

DOX-loaded ArgPEA-ss-HA(AP) nanocomplex in PBS (5mg/mL, 5mL) with 10 mM GSH was placed in dialysis tubing (MWCO = 10 kDa) and immersed against same buffer (30 mL) at 37 °C under shaking (100 rpm). At pre-determined time intervals, buffer outside the dialysis tubing (5 mL) was withdrawn and replaced by fresh buffer. DOX concentration in collected samples were determined on spectrofluorometer at λex=480 nm, λem=590 nm, the percentage of released DOX was plotted vs. time. Each test was performed in triplicate.

### *4.3.6 In vitro endocytosis and endosomal escape of ArgPEA-ss-HA(AP) nanocomplex*

*Endocytosis*. MDA-MB-231 cells incubated with blank ArgPEA-ss-HA(AP) nanocomplex or free AlPcS2a for predetermined time intervals. Flow cytometry was performed on FACSAria fusion fluorescence activated cell sorter (BD Biosciences, Franklin Lakes, NJ), and each test was run in 3 replicates.

*Endosomal escape*. MDA-MB-231 cells were seeded in a 35 mm glass-bottomed-dish (3 x $10^5$ cells/well, MaTek, Ashland, MA) and incubated for 24 hrs. Blank ArgPEA-ss-HA(AP) nanocomplex (c(AlPcS2a) = 5 μM) was added and incubated for 4 hrs. The cells were washed and labeled with Lysotracker green (50 nM) as per manufacturer's instruction, and imaged alive by confocal microscopy (Zeiss LSM710, Carl Zeiss MicroImaging, Thornwood, NY). Light irradiation was then applied by LED arrays at 660 nm with light dosages of 0 J/cm$^2$, 0.5 J/cm$^2$, 1.5 J/cm$^2$ or 3 J/cm$^2$. The Pearson's coefficient for co-localization between the blank ArgPEA-ss-HA(AP) nanocomplex and Lysotracker before and 0.5 hr after irradiation was determined with Fiji software (National Institutes of Health), 30 images were analyzed for each group.

### *4.3.7 Cytotoxicity of DOX-loaded ArgPEA-ss-HA(AP) nanocomplex in MDA-MB-231 monolayers*

MDA-MB-231 cells were seeded in 96-well plate (5 x $10^3$ cells/well) and pre-incubated for 24 hrs. Blank ArgPEA-ss-HA(AP) nanocomplex, DOX-loaded ArgPEA-ss-HA(AP) nanocomplex, free DOX with various DOX concentration were added and incubated for 4 hrs. The cells were washed with PBS and incubated for another 4 hrs in fresh DMEM. Light irradiation was applied by LED arrays (120 arrays, 25 mW/cm$^2$, Elixa Ltd, Albuquerque, NM) at 660 nm with light dosages of 0, 0.5, 1.5 or 3 J/cm$^2$. After further incubation for another 24 hrs, the cell viability was determined with WST-1 assay (Roche Diagnostics, Mannheim, Germany). The results were normalized to the viability of untreated cells to give the percentage of viability. Each experiment was run in 6 replicates. Factor α [32] was calculated from the survival fraction (SF) of different groups to evaluate the level of synergism (α>1 synergistic; α=1 simply additive; α<1 antagonistic).

$$\alpha = \frac{SF(free\ \ DOX) \times SF\ \ (ArgPEA - ss - HA(AP))}{SF\ \ (ArgPEA - ss - HA(AP)/DOX)}$$

### *4.3.8 Anti-tumor effect of DOX-loaded ArgPEA-ss-HA(AP) nanocomplex in MDA-MB-231 spheroids*

MDA-MB-231 multicellular spheroids were developed from the published protocols [33]. MDA-MB-231 cells were harvested and resuspended in DMEM containing 2.5% matrigel (BD Bioscience, San Jose, CA). Cells were seeded in ultra-low-attachment 96-well plate (CellCarrier, Perkin Elmer, Waltham, MA) at 0.5 x $10^4$ cells/well, centrifuged at 1000 rcf for 10 min and incubated for 3 days. Spheroids were treated with blank ArgPEA-ss-HA(AP) nanocomplex, DOX-loaded ArgPEA-ss-HA(AP) nanocomplex, free DOX or free AlPcS2a for 8 hrs, (with equivalent c(DOX)

= 5 μM, c(AlPcS2a) = 2.55 μM). Light irradiation was applied at 660 nm, 1.5 J/cm$^2$. Confocal Z-stack images were obtained with 20 μm interval between slices. The total fluorescence intensity for each Z-stacks was analyzed with Fiji software (National Institutes of Health) and normalized to the cross-sectional area of the spheroid. Each test was performed in 10 replicates.

*Spheroid viability assay*. MDA-MB-231 spheroids were treated with blank ArgPEA-ss-HA(AP) nanocomplex, DOX-loaded ArgPEA-ss-HA(AP) nanocomplex, free DOX or free AlPcS2a (with equivalent c(DOX) = 1 μM, c(AlPcS2a) = 0.51 μM) for 8 hrs The spheroids were then washed, chased for another 4 hrs, and light irradiation was applied at 660 nm, 1.5 J/cm$^2$. 7 days post irradiation, the viability of spheroids was determined with WST-1 assay. The results were normalized to the viability of untreated spheroids to give the percentage of viability, and each test was run in 10 replicates.

### *4.3.9 Ex-vivo examination of biodistribution of ArgPEA-ss-HA(AP) nanocomplex*

The female BALB/c nude mice were provided by the Vital Laboratory Animal Center (Beijing, China). All care of the animals was performed under specific pathogen free (SPF) conditions with free access to standard food and water, and all the animal experiments were conducted with the approval of the Ethics Committee of Shanghai University of Traditional Chinese Medicine.

To establish MDA-MB-231 xenograft model, MDA-MB-231 cells were harvested from confluent culture and re-suspended in DMEM containing 30% matrigel. $3\times10^6$ cells (100 μL) were injected subcutaneously into right flank area of each mouse. When tumors grew to 500 – 1000 mm$^3$ in volume, blank ArgPEA-ss-HA(AP) or free AlPcS2a was injected into the mice via tail vein (with equivalent AlPcS2a dose of 10 mg/kg). Mice were sacrificed 24 hrs post-injection, major organs and tumors were excised and observed with IVIS imaging system (Caliper Life Science, Hopkinton, MA). The protocol reported by Lee et al. [34] was used to determine the fluorescence intensity of AlPcS2a in each organ. Major organs and tumors were washed with saline and blotted dry, digested with 0.1 M NaOH (10 mL/

0.l g tissue) for 4 hrs at 50 °C and centrifuged. The fluorescence intensity of AlPcS2a in supernatant was determined with spectrofluorometer (λex=605 nm, λem=660-790 nm). The results were expressed as fluorescence intensity per unit mass of organs, and each test was run in 4 replicates.

#### *4.3.10 In vivo antitumor effect of DOX-loaded ArgPEA-ss-HA(AP) nanocomplex*

The *in vivo* antitumor efficacy of the DOX-loaded ArgPEA-ss-HA(AP) nanocomplex was evaluated on the MDA-MB-231 xenograft model. $3\times10^{6}$ cells (100 μL) were injected subcutaneously into right flank area of each BALB/c nude mice. When the tumor sizes reached approximately 100 $mm^3$, the mice were randomly divided into 5 groups (n=6) and intravenous (i.v.) injection was given with saline, free DOX (1.5 mg/kg/week), blank ArgPEA-ss-HA(AP) nanocomplex with irradiation, DOX-loaded ArgPEA-ss-HA(AP) nanocomplex (with equivalent DOX dosage of 1.5 mg/kg/week) with or without light irradiation. 3 injections were given at day 1, day 8 and day 15. 24 hrs post-injection, tumor tissues were irradiated by 671 nm He-Ne laser (100 $mW/cm^2$, 30 $J/cm^2$). Tumors were measured with a caliper, and tumor volume was calculated as following: $V_{tumor} = (a \times b^2)/2$, where a is the maximum length and b is the minimal width. The weight of tumor-bearing nude mice was also monitored. At day 28, all mice were sacrificed and the weight of the tumor was measured.

#### *4.3.11 Statistical analysis*

The data are presented as mean values with standard deviations (SD). All data were analyzed using one-way ANOVA, followed by Tukey's multiple comparison tests, and $p < 0.05$ was considered statistically significant.

### *4.4 Results and discussion*

#### *4.4.1 Characterization of ArgPEA-ss-HA(AP) polymers*

The amine terminated Arg-PEA ($NH_2$-ArgPEA-$NH_2$) was prepared from a

solution polycondensation, in which excess amounts of nucleophilic Arg-2 monomer reacted with electrophilic NSu monomer to result in free amine groups at both ends of the Arg-PEA chain. $^{1}$H NMR spectrum (Figure 4.2A) was obtained to characterize the amine terminated Arg-PEA, and typical chemical shifts were observed at 8.25 ppm (-**NH**-CO-), 4.23 ppm (-**CH$_2$**-O-CO-) and 3.09 ppm (-NH-CO-**CH$_2$**-). The molecular weight of the amine-terminated Arg-PEA by GPC was 6.5 kDa with PDI =1.36. The amine-terminated Arg-PEA exhibits strong cationic charge, and the zeta potential for the 1 mg/mL solution was + 22.5 ± 3.9 mV. The content of free -$NH_2$ was 0.25 mmol/g in Arg-PEA, as detected by ninhydrin assay.

Conjugation with polyethylene glycol (PEG) was reported [23] to elongate the blood circulation time of HA nanoparticles, prevent the nanoparticles from being captured by reticuloendothelial system, and still maintain the CD44-mediated tumor-targeting property of HA. The optimized PEGylation ratio was reported to be 5% [35]. In this study, PEGylation was also introduced to HA via thiol-maleimide chemistry. As shown in Figure 4.2B, the typical peaks for methylene protons in PEG chain (-**CH$_2$CH$_2$**O-) was observed at 3.4 to 3.9 ppm. The integral for methylene groups from PEG and methyl groups from HA was calculated. The grafting ratio of PEG, defined as the ratio between the molar amount of PEG and the molar amount of hyaluron repeating units, was estimated to be 5.8% which is in line with the optimized PEGylation ratio reported by Choi et al.[23] PEGylation of HA not only provides enhanced tumor-specific delivery property, but also introduces available -$NH_2$ groups for further functionalization. AlPcS2a was converted to its sulfonylchloride form by reaction with thionyl chloride [25,27] before it was reacted with the -$NH_2$ groups on PEG and resulted in thiolated HA conjugated with AlPcS2a (HA-SH(AP)). The chemical reaction between PEG and AlPcS2a was evidenced by centrifugation method. AlPcS2a conjugated with PEG or AlPcS2a physically mixed with PEG were dispersed in ethanol and centrifuged at 10, 000 rcf for 20 min. Due to the poor solubility of free AlPcS2a in ethanol, significant precipitation was observed in the physical mixture. However, uniform solution was observed after centrifugation in the case of AlPcS2a conjugated with PEG, as PEG improved the solubility of the

photosensitizer. Absorbance peaks were also observed at 667 nm and 605 nm in the UV-vis spectrum of HA-SH(AP), which corresponded to the Q-bands of phthalocyanine, and further proved the presence of AlPcS2a in the modified HA-SH(AP) polymers.

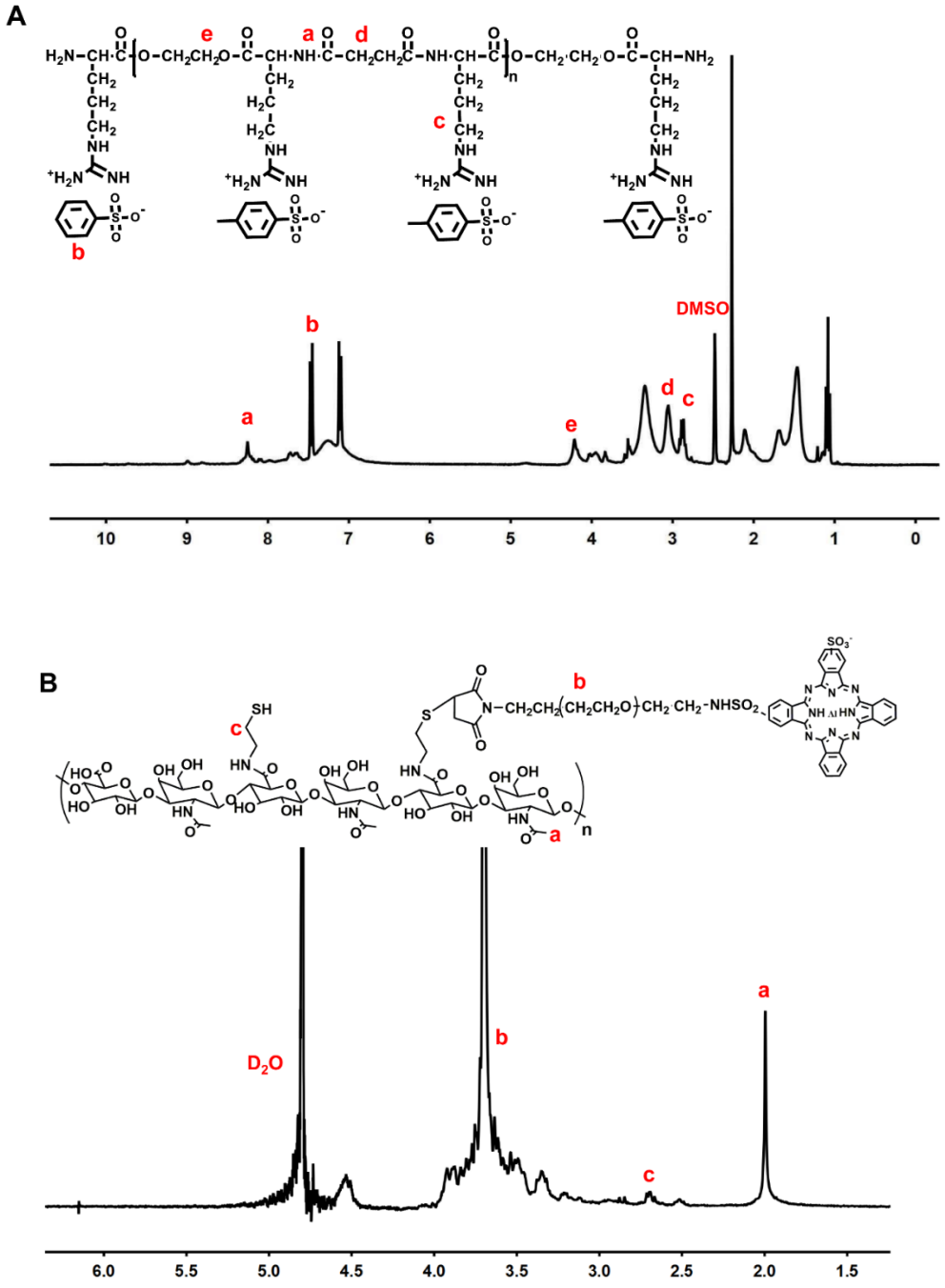

**Figure 4.2**. $^{1}$H NMR spectra of A) $NH_2$-ArgPEA-$NH_2$; B) HA-SH functionalized with PEG and AlPcS2a (HA-SH(AP)).

### *4.4.2 Characterization of ArgPEA-ss-HA(AP) nanocomplex*

ArgPEA-ss-HA(AP) nanocomplex was formed from self-assembly between HA and ArgPEA, as shown in Figure 4.1C and Figure 4.3A, and further stabilized via the disulfide linkage between the pyriyldithiol groups in SPDP-activated Arg-PEA and -SH groups in HA. Since amphiphilic AlPcS2a localized specifically in the lipid bilayer in the endolysosomes [15], the light-induced photochemical rupture should be limited to the endolysosomal membrane, instead of other subcellular compartments. The conjugation of AlPcS2a on the surface of ArgPEA-ss-HA(AP) nanocomplex via PEG spacer enabled the close contact between AlPcS2a and endolysosomal membrane, as illustrated in Figure 4.3B.

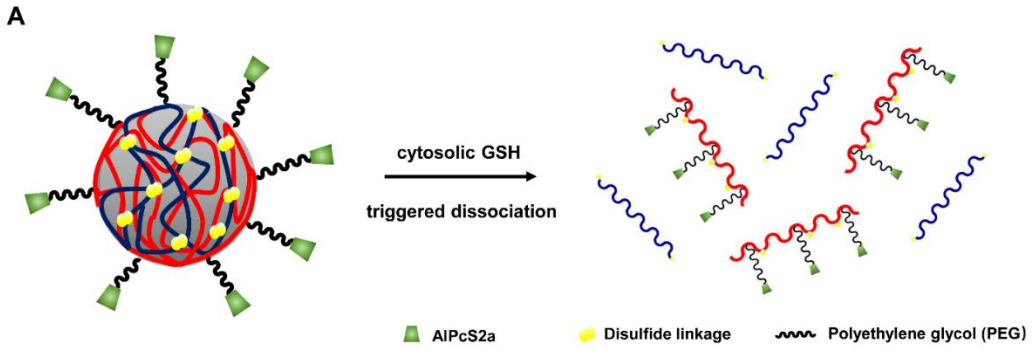

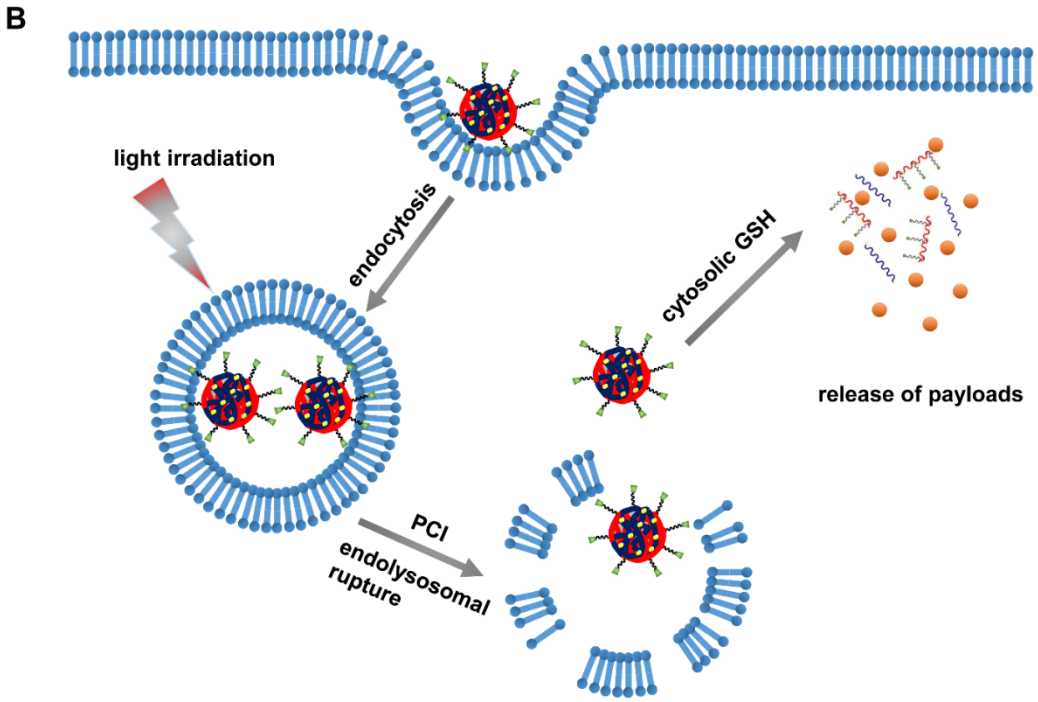


**Figure 4.3**. Illustration of A) dissociation of reduction-sensitive ArgPEA-ss-HA(AP) nanocomplex triggered by glutathione (GSH); and B) endosomal escape of ArgPEA-ss-HA(AP) nanocomplex and cytosolic release of payloads.

Spherical assembled structure was observed for ArgPEA-ss-HA(AP) nanocomplex, as suggested by the transmission electron microscope (TEM) image in Figure 4.4A. For ArgPEA-ss-HA(AP) nanocomplex with HA/ArgPEA = 2:1 (w/w) in feed, the average DLS (dynamic light scattering) diameter was detected as 109.9 ± 5.7 nm, with a PDI of 0.135. We also synthesized a series of ArgPEA-ss-HA(AP) nanocomplex with various HA to ArgPEA feed ratios, and a higher HA to ArgPEA ratio led to an increased size of the nanocomplex, i.e., 286.2 ± 7.9 nm for HA/ArgPEA=4:1 (w/w) vs. 109.9 ± 5.7 nm for HA/ArgPEA=2:1 (w/w).

The UV-Vis spectrum of the ArgPEA-ss-HA(AP) in an aqueous solution was shown in Figure 4.4C. The Q-bands of phthalocyanine groups in the nanocomplex were observed at 667 nm and 605 nm, respectively, with similar peak profile as free AlPcS2a. *Brasseur et al.* [24] suggested that the absorbance peak at 667 nm (A667) represents the monomeric form of AlPcS2a, while the peak at 605 nm (A605)

represents the aggregated form of AlPcS2a. The ratio of A667/A605 was calculated to be 4.45 for free AlPcS2a and 5.92 for the ArgPEA-ss-HA(AP) when the equivalent concentration of AlPcS2a in PBS was 10 μM. Aggregation was reported [36] as one of the challenges in photosensitizer-related cancer therapy, because it can reduce the photochemical sensitizing efficiency of the photosensitizer. Therefore, the higher A667/A605 ratio in the ArgPEA-ss-HA(AP) nanocomplex can be an indication of enhanced monomerization level of AlPcS2a in ArgPEA-ss-HA(AP), hence enhanced its photosensitizing efficiency. In Figure 4.4C, we also compared the UV-Vis spectra of ArgPEA-ss-HA(AP) (chemical conjugation of AlPcS2a) vs. AlPcS2a loaded in the ArgPEA-ss-HA nanocomplex (physical encapsulation of AlPcS2a). With equivalent concentration, AlPcS2a physically encapsulated in the interior of the nanocomplex exhibited significantly reduced absorbance at 667 nm, compared to the chemically conjugated counterpart. The absorbance of encapsulated AlPcS2a can be shielded by the carriers, however, AlPcS2a conjugated to the nanocomplex exhibited similar absorbance profile as the free ones, which provided evidence that AlPcS2a was localized on the surface of the nanocomplex, instead of the interior.

Oxygen consumption rate. As the photosensitizing effect of AlPcS2a involves the photo-induced generation of free radical, and further interact with oxygen molecules to form ROS. The rate of oxygen consumption positively correlates with the efficiency of ROS generation by ArgPEA-ss-HA nanocomplex. As shown in Figure 4.4D, oxygen consumption by ArgPEA-ss-HA(AP) increased with irradiation time, and the fold of oxygen consumption was 0.98 (with light dose of 0.5 J/cm$^2$), 0.91 (1.5 J/cm$^2$), and 0.79 (3 J/cm$^2$), respectively. In addition, the oxygen consumption profile by ArgPEA-ss-HA nanocomplex was almost identical to that of free AlPcS2a at the first 120 sec of irradiation at 660 nm (25 mW/cm$^2$). The results suggested that ArgPEA-ss-HA(AP) complex was as competent as free AlPcS2a in ROS generation, and could provide equivalent potential to initiate PCI. With longer irradiation time, ArgPEA-ss-HA(AP) exhibited higher rate of oxygen consumption than free AlPcS2a, which could be attributed to the enhanced monomerization level of the photosensitizer when conjugated with the nanocomplex (Figure 4.4C). Low level of oxygen consumption

was observed for non-irradiated groups in Figure 4.4D, which further validated the light-induced consumption of oxygen and generation of ROS by ArgPEA-ss-HA(AP) nanocomplex. Aluminum phthalocyanine conjugated with PEG and polyvinyl alcohol was previously reported [24] and the generation of reactive oxygen species by light irradiation was not affected by conjugation, which lead to similar conclusions as the oxygen consumption profile in Figure 4.4D, and provided the rationale for our following study.

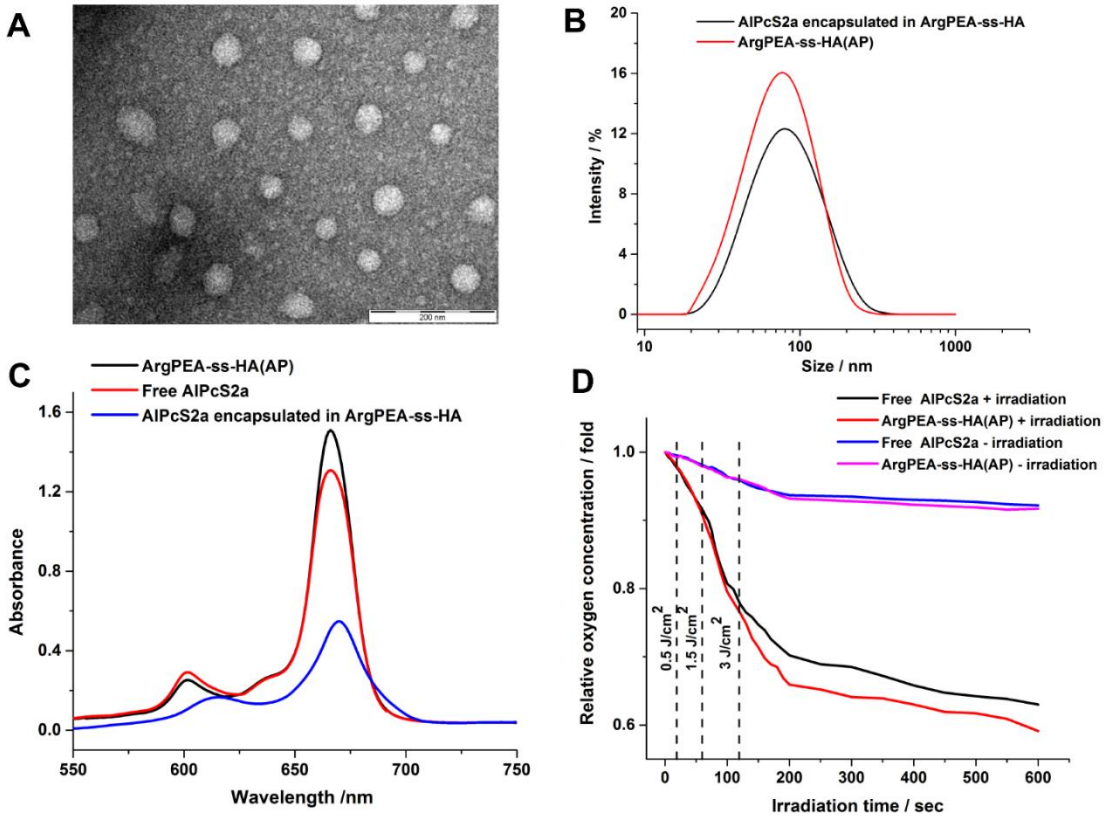


**Figure 4.4**. A) TEM images of blank ArgPEA-ss-HA(AP) nanocomplex, scale bar represents 200 nm. B) Distribution histogram of blank ArgPEA-ss-HA(AP) nanocomplex or AlPcS2a encapsulated in the interior of ArgPEA-ss-HA nanocomplex. C) UV-vis spectra of blank ArgPEA-ss-HA(AP) nanocomplex, free AlPcS2a or AlPcS2a encapsulated in the interior of ArgPEA-ss-HA nanocomplex in PBS with c(AlPcS2a) = 10 μM. D) Oxygen consumption vs. irradiation time for

ArgPEA-ss-HA(AP) nanocomplex or free AlPcS2a in PBS containing 10% FBS under irradiation (660 nm, 25 mW/cm2), the fold of oxygen consumption was obtained by normalizing the oxygen pressure of testing samples to that of untreated PBS. Irradiation time that result in light dose of 0.5, 1.5 or 3 J/cm$^2$ were marked as dotted lines.

### *4.4.3 Characterization of DOX-loaded ArgPEA-ss-HA(AP) nanocomplex*

The DOX-loaded ArgPEA-ss-HA(AP) nanocomplex of various HA/ArgPEA feed ratio were characterized and the data are shown in Table 1. Slightly negative surface charge (-4.31 to -5.89 mV) was observed for all DOX-loaded nanocomplex. HA/ArgPEA ratio also affected the size of the self-assembled nanocomplex, and a higher HA content in feed lead to an increased size of the nanocomplex, i.e. 272.7 nm for HA/ArgPEA=4:1(w/w) vs. 97.2 nm for HA/ArgPEA=2:1 (w/w). Nano-carriers of smaller size (< 200 nm) were found to be more effective in drug delivery because they are less likely to be captured by reticuloendothelial system than larger particles during systemic circulation [37].

At the same feed ratio of DOX, the DOX loading content (DLC) was 9.2% for the nanocomplex at the HA/ArgPEA=2:1 (w/w), while the DLC of DOX decreased to 5.1% for the nanocomplex at HA/ArgPEA=1:1 (w/w). The reduced DLC in nanocomplex of a lower HA/ArgPEA ratio can be attributed to the fact that doxorubicin hydrochloride is cationic and binds preferentially with anionic hyaluronic acid. Therefore, ArgPEA-ss-HA(AP) nanocomplex with the HA/ArgPEA ratio of 2:1 (w/w) was chosen for the following studies. The content of conjugated AlPcS2a in this DOX-loaded ArgPEA-ss-HA(AP) nanocomplex was detected as 5.9 wt%.

The release of DOX from ArgPEA-ss-HA(AP) nanocomplex with the presence of glutathione (GSH) was studied to investigate the sensitivity of the nanocomplex to reductive condition. As demonstrated in Figure 4.5, the cumulative percentage of DOX release in the presence of GSH was consistently and significantly higher than in the phosphate buffer saline (PBS, pH 7.4) over the whole duration of study. The accelerated release of DOX from the nanocomplex triggered by GSH provided

possibilities for PCI-enhanced therapeutic performances.

**Table 1**. Characterization of DOX-loaded ArgPEA-ss-HA(AP) nanocomplex with various HA to ArgPEA ratio.

| HA to ArgPEA ratio (w/w) [a] | 1:1 | 2:1 | 4:1 |
|---|---|---|---|
| DLS diameter / nm | 90.8 ± 4.29 | 97.25 ± 8.42 | 272.7 ± 6.78 |
| PDI | 0.152 ± 0.03 | 0.147 ± 0.04 | 0.144 ± 0.04 |
| Zeta potential / mV | - 4.3 ± 0.78 | -3.62 ± 0.99 | -5.89 ± 1.27 |
| AlPcS2a content / %wt | 2.9 | 4.7 | 6.2 |
| DOX DLC /% | 5.1 | 9.2 | 10.4 |
| DOX EE /% | 57.4 | 83.5 | 82.6 |

a. The weight ratio here indicated the feed ratio between HA-SH and $NH_2$-ArgPEA-$NH_2$ in the formulation of the nanocomplex.

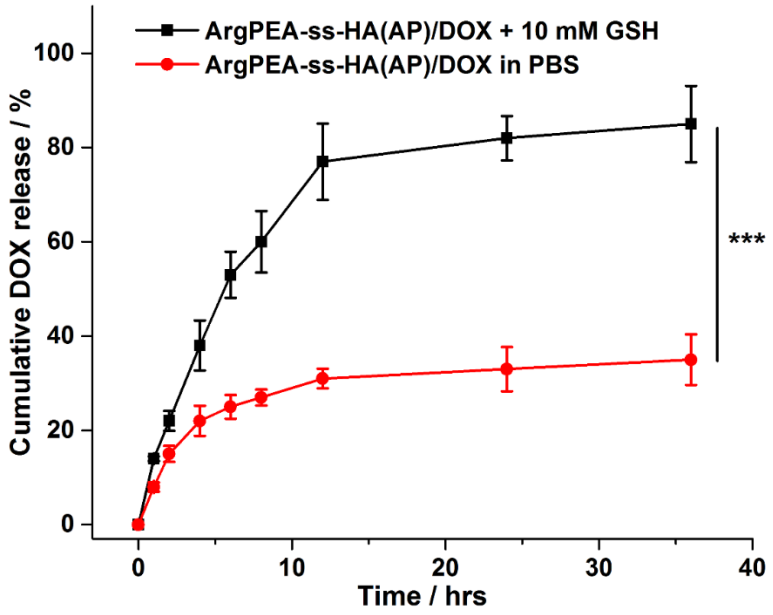


**Figure 4.5**. In vitro release of DOX from DOX-loaded ArgPEA-ss-HA(AP) nanocomplex dispersed in PBS with or without the presence of 10 mM GSH. All the

results were obtained from ArgPEA-ss-HA(AP) nanocomplex with HA/ArgPEA=2:1 (w/w). Statistical significance: *** $p < 0.001$.

### *4.4.4 Light-facilitated endosomal escape of ArgPEA-ss-HA(AP) nanocomplex*

To optimize the incubation time of ArgPEA-ss-HA(AP) nanocomplex with MDA-MB-231 monolayers, we studied the endocytosis of the nanocomplex as a function of time. As illustrated in Figure 4.6A, a distinct difference in intracellular AlPcS2a fluorescence was observed between ArgPEA-ss-HA(AP) nanocomplex and free AlPcS2a at the first 12 hrs, and the fluorescence intensity from the nanocomplex-treated MDA-MB-231 cells was 3-fold higher than the free AlPcS2a at 4 hrs. The fluorescence signals from the free AlPcS2a, however, gradually increased with time until the difference in intracellular fluorescence between the two treatments narrowed at 18-20 hrs. Free AlPcS2a contains two sulfonate groups and exhibits negative charge in biological environment due to the low pKa value, resulting in a slower rate of internalization [38]. ArgPEA-ss-HA(AP) nanocomplex significantly enhanced the internalization efficiency of AlPcS2a in MDA-MB-231 cells especially at the first 4 hrs. Subsequent incubation didn't result in significant increase in the intracellular level of the nanocomplex, and 4 hrs was hence chosen for the following study in MDA-MB-231 monolayers.

Co-localization study was performed to investigate the endosomal escape of ArgPEA-ss-HA(AP) nanocomplex in MDA-MB-231 monolayers. First, in the absence of light irradiation, MDB-MB-231 cells were incubated with blank ArgPEA-ss-HA(AP) nanocomplex for 4 hrs and stained with Lysotracker green before cells were imaged alive with confocal microscopy (Zeiss LSM710, Carl Zeiss MicroImaging, Thornwood, NY). The red pixels of ArgPEA-ss-HA(AP) nanocomplex overlapped with the green pixels of endolysosomes (Figure 4.6B), and Pearson's coefficient between green and red fluorescence, was determined as 0.63 (Figure 4.6C), indicating the endolysosomal sequestration of the nanocomplex. After another 0.5 hr incubation in dark, no significant change in fluorescence profile or Pearson's coefficient were observed. The results demonstrated that without irradiation, the blank ArgPEA-ss-

HA(AP) nanocomplex was largely entrapped inside endolysosomes.

When 660 nm irradiation at 1.5 J/cm$^2$ was applied with LED arrays (25 mW/cm$^2$, Elixa Ltd, Albuquerque, NM), the confocal image before and 0.5 hr post irradiation were recorded. The endosomal escape of the nanocomplex was evident, as less level of yellow pixels was observed, and non-overlapping red pixels from ArgPEA-ss-HA(AP) nanocomplex was observed to be diffused into cytosol. Significant difference in Pearson's coefficient was also observed before and 0.5 hr post irradiation, which further proved the endosomal escape of the nanocomplex induced by 660 nm irradiation. The effect of light dose on the endosomal escape in the ArgPEA-ss-HA(AP) nanocomplex was also investigated, as shown in Figure 4.6C. At a lower light dose (0.5 J/cm$^2$), the difference in Pearson's coefficient before and after irradiation was not statistically significant, which suggested that 0.5 J/cm$^2$ was not sufficient to result in endosomal escape of the nanocomplex. However, at higher light doses of 1.5 J/cm$^2$ and 3 J/cm$^2$, distinct endosomal escape was observed. The results also correlated well with Figure 4.4D, in which the oxygen consumption by 0.5 J/cm$^2$ was minor, while significant oxygen consumption was observed in the case of 1.5 J/cm$^2$ and 3 J/cm$^2$. In general, the light-induced translocation of ArgPEA-ss-HA(AP) from endolysosomal compartments into the reductive cytosol may result in enhanced intracellular release of DOX, as suggested in Figure 4.5, and we further studied the impact of light dose on the in vitro inhibition of MDA-MB-231 cells.

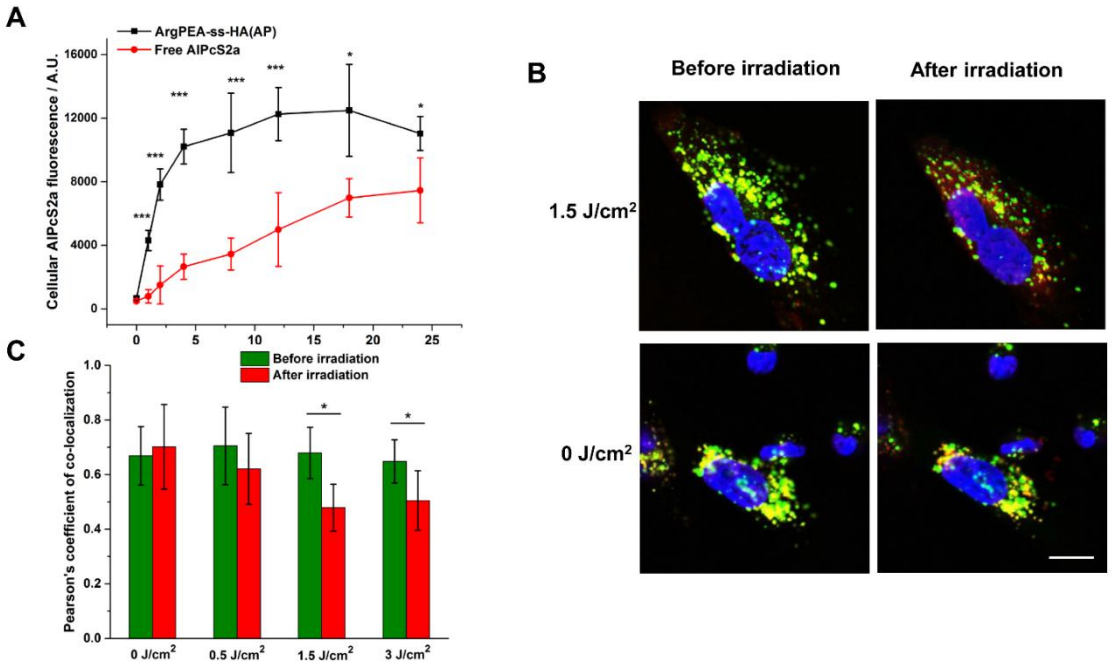


**Figure 4.6.** A) Mean fluorescence of free AlPcS2a and blank ArgPEA-ss-HA(AP) nanocomplex (c(AlPcS2a) = 5 μM) in MDA-MB-231 cells over incubation time in hrs. Values represent the average ± SD (n=3). B) Confocal images of MDA-MB-231 cells incubated with blank ArgPEA-ss-HA(AP) nanocomplex (c(AlPcS2a) = 5 μM) for 4 hrs before and after light irradiation at 660 nm (1.5 J/cm$^2$), Cells were labelled with Lysotracker green for lysosome, Intracellular fluorescence of Lysotracker (green), ArgPEA-ss-HA(AP) nanocomplex (red), and nuclei (blue) was recorded before irradiation and 0.5 hr post irradiation at 660 nm (1.5 J/cm$^2$). C) Pearson's coefficient for co-localization degree between blank ArgPEA-ss-HA(AP) nanocomplex and Lysotracker before and 0.5 hr after irradiation was applied at various light dose. Values represent the average ± SD (n=30). Statistical significance: *, $p < 0.05$; **, $p < 0.01$; ***, $p < 0.001$.

### *4.4.5 Light-enhanced anti-tumor effect of DOX-loaded ArgPEA-ss-HA(AP) nanocomplex in MDA-MB-231 monolayers*

The dosage of light and drug, intervals between drug administration and light

application, contributed to the anti-tumor efficiency of PCI-facilitated treatments. As described in the endocytosis rate of the ArgPEA-ss-HA(AP) nanocomplex (Figure 4.6A), 4 hrs incubation lead to significantly enhanced intracellular level of the nanocomplex, and was chosen as incubation time of DOX-loaded nanocomplex. Cytotoxicity in MDA-MB-231 monolayers treated with DOX-loaded ArgPEA-ss-HA(AP) nanocomplex were then studied for screening the proper light dose and DOX concentration that could enable maximum level of synergism. The results are shown in Figure 4.7. Based on the weight content of conjugated AlPcS2a and the DLC of DOX in the nanocomplex, the equivalent concentration of both DOX and AlPcS2a was indicated in Figure 4.7.

In the absence of light irradiation (Figure 4.7A), blank ArgPEA-ss-HA(AP) nanocomplex didn't induce significant toxicity. Cytotoxicity was observed in MDA-MB-231 cells treated with DOX-loaded ArgPEA-ss-HA(AP) nanocomplex, with an IC50 of 2.3 μM. However, The DOX-loaded nanocomplex was still less potent than free DOX in the inhibition of tumor cells. The IC50 for free DOX was determined as 1.1 μM.

In the absence of light irradiation (Figure 4.7A), blank ArgPEA-ss-HA(AP) nanocomplex didn't induce significant toxicity. Cytotoxicity was observed in MDA-MB-231 cells treated with DOX-loaded ArgPEA-ss-HA(AP) nanocomplex, with an IC50 of 2.3 μM. However, The DOX-loaded nanocomplex was still less potent than free DOX in the inhibition of tumor cells. The IC50 for free DOX was determined as 1.1 μM.

When light irradiation was applied (Figure 4.7B, C and D), no variation was observed in the cytotoxicity induced by free DOX, as the IC 50 of free DOX was detected between 1.1 to 1.3 μM. In addition, cytotoxicity was observed in the case of blank ArgPEA-ss-HA(AP) nanocomplex, at higher AlPcS2a concentration and higher light dose. When 3 J/cm$^2$ irradiation was applied (Figure 4.7D), MDA-MB-231 cell survival was less than 50% at c(AlPcS2a) = 1 to 5.1 μM. Cytotoxicity induced by irradiated blank nanocomplex can be related to the overproduction of reactive oxygen species by the conjugated AlPcS2a, which lead to oxidative damage and cell death.

However, PCI-facilitated drug delivery highlighted the photosensitizing effect to enhance the therapeutic effect of delivered payloads, instead of the photosensitizer itself taking the lead in the inhibition of tumor.

The IC50 for DOX-loaded nanocomplex at 1.5 J/cm$^2$ and 3 J/cm$^2$ was 0.71 μM and 0.62 μM, respectively, suggesting that light irradiation significantly enhanced the cytotoxicity of DOX-loaded nanocomplex. Factor α [32] was evaluated from the survival fraction (SF) to distinguish whether this augment was from simple addition, or from synergism induced by PCI (α>1 synergistic; α=1 simply additive; α<1 antagonistic).

At all testing groups, we only observed α >1 (synergism) for DOX-loaded ArgPEA-ss-HA(AP) with c(DOX) = 0.5 μM (with equivalent c(AlPcs2a) = 0.26 μM), and c(DOX) = 1 μM (with equivalent c(AlPcS2a) = 0.51 μM), when 660 nm irradiation was applied at 1.5 J/cm$^2$. The finding was consistent with the study by Matthew et al. [32] in which the optimized level of synergism was observed between bleomycin (0.25 μg/mL) and non-conjugated AlPcS2a (1.37 μM, 1 J/cm$^2$, 670 nm) in MDA-MB-231 cells. And we focused on DOX-loaded ArgPEA-ss-HA(AP) nanocomplex with c(DOX) = 1 μM (equivalent c(AlPcS2a) = 0.51 μM), and irradiated by 660 nm light at 1.5 J/cm$^2$ for the following in vitro study.

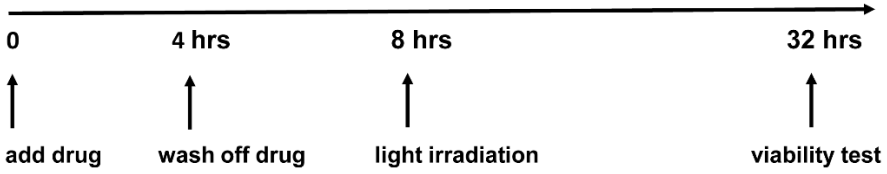

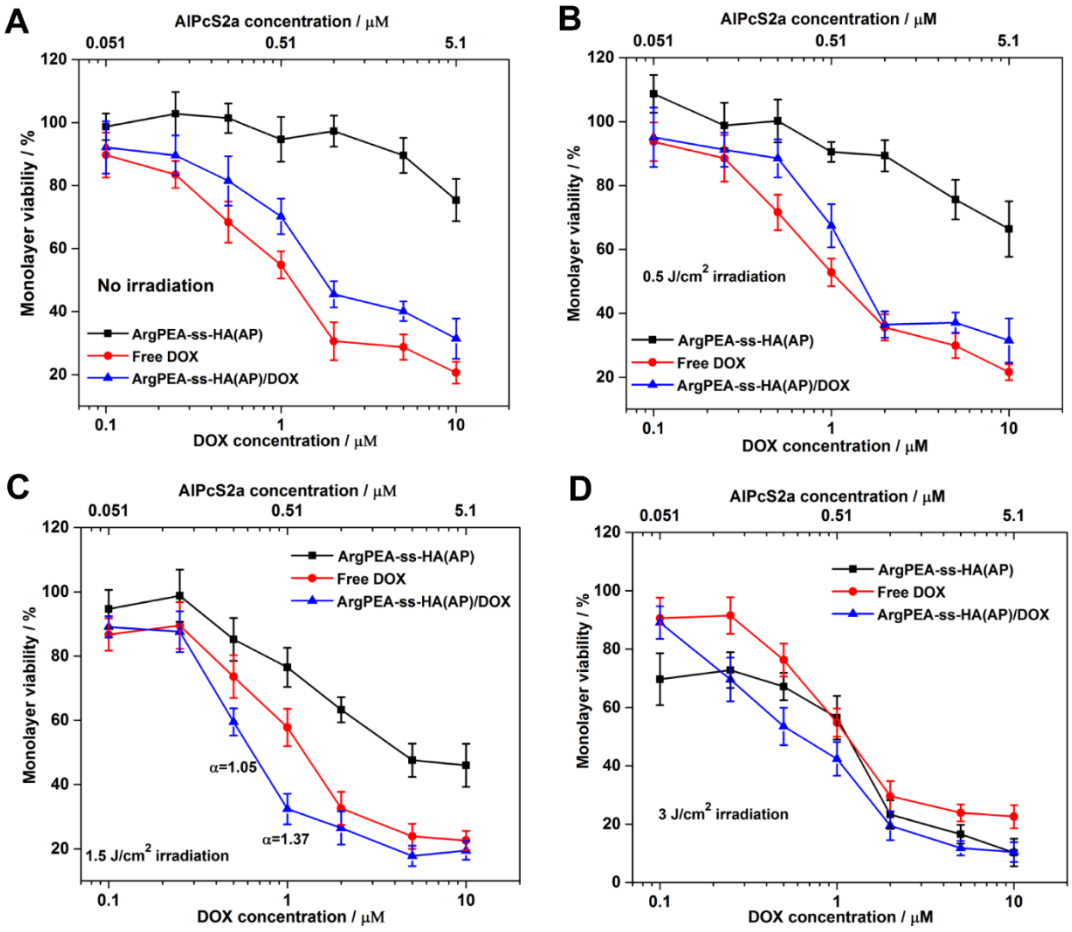


**Figure 4.7.** MDA-MB-231 cells were incubated with blank ArgPEA-ss-HA(AP) nanocomplex, DOX-loaded ArgPEA-ss-HA(AP) nanocomplex or free DOX with various DOX concentration for 4 hrs, washed off, chased for another 4 hrs before 660 nm irradiation was applied at A) no irradiation; B) 0.5 J/cm$^2$; C) 1.5 J/cm$^2$; D) 3 J/cm$^2$. Viability of cells was determined 24 hrs post irradiation and normalized to untreated control. Values represent the average ± SD (n=6). The equivalent concentration of AlPcS2a in DOX-loaded nanocomplex was also indicated in each diagram. Factor α was evaluated for the level of synergism.

### *4.4.6 Enhanced penetration and anti-tumor effect of DOX-loaded ArgPEA-ss-HA(AP) nanocomplex in MDA-MB-231 spheroids*

In addition to 2D monolayer, we extended our studies to 3D multicellular

spheroids, which correlated closely with in vivo outcomes [39]. To evaluate the ability of DOX-loaded ArgPEA-ss-HA(AP) nanocomplex to access the intratumoral space, confocal Z-stack was acquired from MDA-MB-231 spheroids after 8 hrs incubation with the blank ArgPEA-ss-HA(AP) nanocomplex or free AlPcS2a with equivalent concentration. Total fluorescence intensity was calculated and normalized to the cross-sectional area of the spheroids. As shown in Figure 4.8A and 4.8C, free AlPcS2a displayed the weakest fluorescence intensity, and the fluorescence disappeared at 100 to 120 μm from the top of the spheroids, suggesting free AlPCs2a was incompetent in penetration. The less efficient intratumoral migration of free AlPcS2a correlated with the endocytosis results in Figure 4.6A and can be attributed to its negative charge. In the case of blank ArgPEA-ss-HA(AP) nanocomplex without irradiation, the fluorescence from conjugated AlPcS2a disappeared 140 to 160 μm from the top of the spheroids, and significantly enhanced fluorescence intensity was also detected, comparing to free AlPcS2a. When 660 nm irradiation was applied at 1.5 J/cm$^2$, both the fluorescence intensity and penetration depth of the blank nanocomplex was significantly higher than free AlPcS2a; however, no significant difference was observed between irradiated vs. non-irradiated nanocomplex.

We further studied the distribution of DOX in the spheroids. Free DOX penetrated easily into the spheroids, as suggested in Figure 4.8B and 8C, the fluorescence from free DOX was observed as 160 to 180 μm into the spheroids, and the fluorescence intensity outcompeted the DOX-loaded nanocomplex with or without irradiation. DOX-loaded ArgPEA-ss-HA(AP) exhibited an effective level of penetration depth and fluorescence intensity in the absence of irradiation. When 1.5 J/cm$^2$ irradiation was applied, significantly increased fluorescence intensity was observed for DOX-loaded nanocomplex comparing to the non-irradiated counterpart. The released DOX was reported by Zhu et al. and Zheng et al.[40,41] to exhibit stronger fluorescence intensity than DOX entrapped in the carriers. Therefore, the increase in DOX fluorescence intensity after irradiation could be attributed to the translocation of the nanocomplex into the cytosol and the liberation of DOX from the carrier.

Blank ArgPEA-ss-HA(AP) nanocomplex, DOX-loaded nanocomplex, free DOX

or free AlPcS2a were incubated with MDA-MB-231 spheroids for 8 hrs, and the equivalent concentration of DOX (1 μM) and AlPcS2a (0.51 μM) was derived from the inhibition study in Figure 4.7. The nanocomplex was then washed off, chased for 4 hrs, before 660 nm irradiation was applied at 1.5 J/cm$^2$. Viability assay was performed 6 days post irradiation. As shown in Figure 4.8D, blank ArgPEA-ss-HA(AP) nanocomplex and free AlPcS2a didn't exhibit significant toxicity with or without irradiation, as more than 80% viability was detected. In the case of DOX-loaded nanocomplex, remarkably enhanced toxicity was observed in irradiated group when comparing to the non-irradiated counterpart. The therapeutic efficiency of irradiated DOX-loaded ArgPEA-ss-HA(AP) nanocomplex was equivalent to free DOX.

The enhanced therapeutic effect from DOX-loaded ArgPEA-ss-HA(AP) nanocomplex in both monolayer and spheroid suggested the potency of the PCI effect to overcome the sequestration of internalized carriers in endocytic compartments. The PCI-facilitated delivery of chemotherapeutics was also reported for other drug carriers. For example, Lu et al.[42] reported the use of dendrimer phthalocyanine to enhance the therapeutic effect of free DOX in multidrug resistant breast tumor MCF-7/ADR. Yen et al. [14] reported reduction-sensitive PEG-PLys conjugated with camptothecin, and the chemotherapy on AY27 urothelial carcinoma was augmented by co-administration of photofrin. However, in both studies, the photosensitizer and chemotherapeutics were administered separately, and the different blood circulation profiles might lead to a discrepancy in their biodistribution. We further investigate the in vivo distribution of ArgPEA-ss-HA(AP) nanocomplex, as a co-delivery system for both DOX and AlPcS2a.

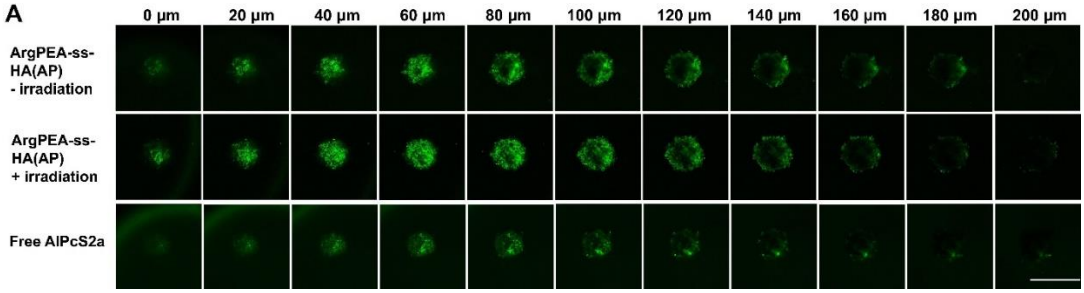

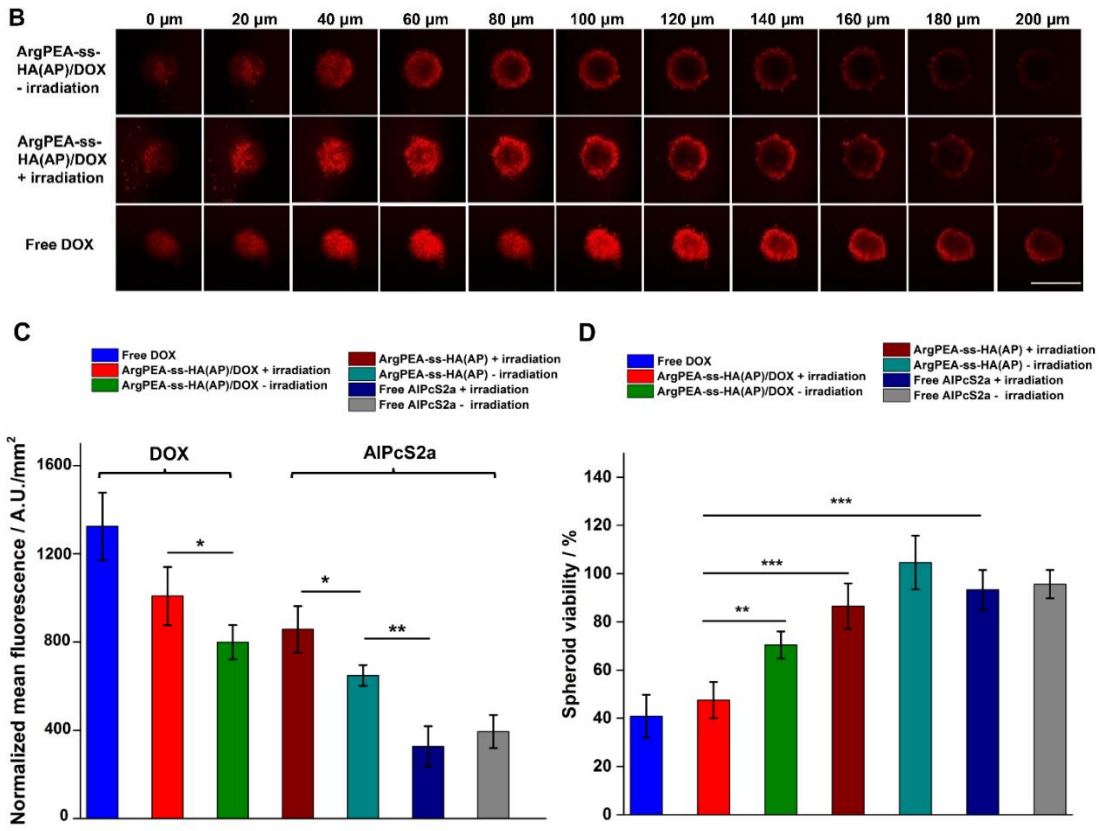


**Figure 4.8.** MDA-MB-231 multicellular spheroids incubated with A) blank ArgPEA-ss-HA(AP) nanocomplex or free AlPcS2a; B) DOX-loaded ArgPEA-ss-HA(AP) nanocomplex or free DOX for 8 hrs. The nanocomplex was then washed off, chased for 4 hrs, before 660 nm irradiation was applied at 1.5 J/cm$^2$. Confocal Z-stacks from 0 to 200 µm was obtained before and 4 hrs post irradiation, to evaluate the penetration depth of nanocomplex in tumor spheroids. AlPcS2a was pseudo-colored as green and DOX fluorescence was pseudo-colored as red. Scale bar represents 500 µm. C) Total DOX fluorescence or AlPcS2a fluorescence from Z-stacks was quantified and normalized to the cross-sectional area of the spheroid. Values represent the average ± SD (n=10). D) MDA-MB-231 multicellular spheroids incubated with blank ArgPEA-ss-HA(AP) nanocomplex, DOX-loaded ArgPEA-ss-HA(AP) nanocomplex, free DOX for 8 hrs, washed off, before 660 nm light irradiation was applied (1.5 J/cm$^2$. The equivalent concentration in each group: c (DOX) = 1 µM, and c(AlPcS2a) = 0.51 µM.

Viability of spheroids was determined 6 days post irradiation, and normalized to untreated control. Values represent the average ± SD (n=10). Statistical significance was compared: *, $p < 0.05$; **, $p < 0.01$; ***, $p < 0.001$.

### *4.4.7 Biodistribution of ArgPEA-ss-HA(AP) nanocomplex in mice xenograft model*

Blank ArgPEA-ss-HA(AP) nanocomplex or free AlPcS2a (5 mg/kg) was intravenously (i.v.) injected in BALB/c nude mice with MDA-MB-231 tumor xenograft. 24 hrs post-injection, tumor and other major organs were harvested and ex-vivo examination was performed as shown in Figure 4.9A and 4.9B. Chemical extraction of AlPcS2a in homogenized tissues were also performed, and the fluorescence intensity per unit mass of tissue was shown in Figure 4.9C. Free AlPcS2a was identified largely in liver and spleen, and this trend was also reported in previous study [43]. The normalized fluorescence intensity of free AlPcS2a in liver and spleen was 5-fold higher than tumor tissue, which suggested the efficiency for direct administration of free photosensitizer was incompetent. The distribution of the blank ArgPEA-ss-HA(AP) nanocomplex in tumor, on the other side, was more than 4-fold higher when comparing to free AlPcS2a, when equivalent dose was applied. Therefore, the ArgPEA-ss-HA(AP) nanocomplex exhibited enhanced tumor-specific accumulation of photosensitizer, and is expected to induce PCI effect in the tumor site. The level of free AlPcS2a in skin tissue was 6-fold higher compared to ArgPEA-ss-HA(AP) nanocomplex. The reduced distribution of conjugated AlPcS2a in skin could result in reduced risk of skin photosensitivity.

Distribution of DOX in different organs was also examined 24 hrs post i.v. injection. As the data shown in Figure 4.9D, kidney was the only organ that had the higher drug concentration from free DOX compared to DOX-loaded nanocomplex, which is consistent with the prior study that free DOX can be rapidly eliminated from blood circulation and excreted via kidney [44]. The concentration of free DOX was generally lower in other major organs including liver and spleen when comparing to DOX-loaded ArgPEA-ss-HA(AP) nanocomplex. The difference was the most significant in the tumor tissue, in which DOX-loaded nanocomplex exhibited 3.7-fold

higher concentration than free DOX. The enhanced distribution of both DOX and AlPcS2a in tumor site delivered by the nanocomplex can be attributed to the tumor-specific circulating properties of based nanocarriers [35], and could provide substantial advantages in the in vivo therapeutic effect.

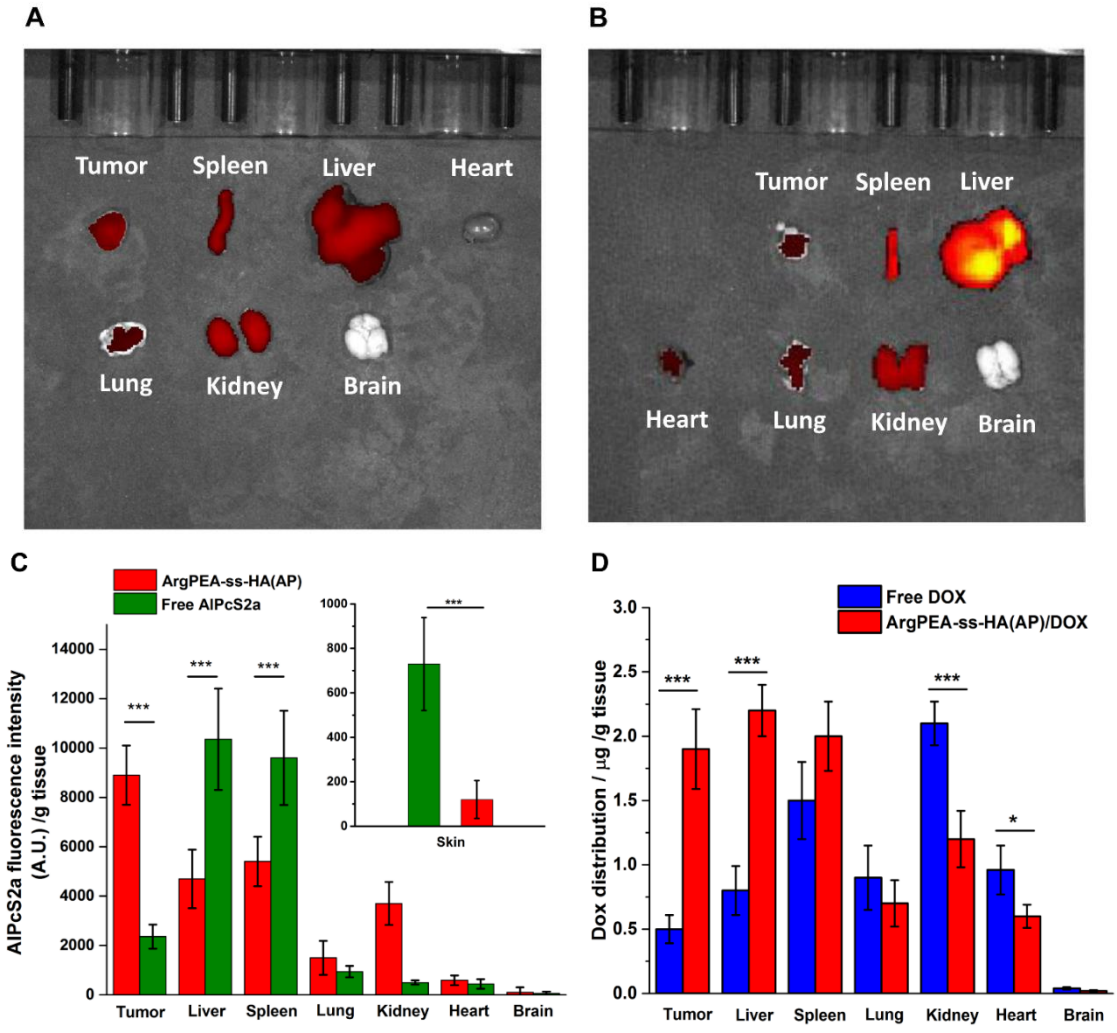


**Figure 4.9.** A) Ex-vivo examination of the biodistribution of A) blank ArgPEA-ss-HA(AP) nanocomplex and B) free AlPcS2a in different organs 24 hrs post i.v. injection. C) Normalized AlPcS2a fluorescence in the extraction of homogenized organs 24 hrs post i.v. injection of blank ArgPEA-ss-HA(AP) nanocomplex or free AlPcS2a (5 mg/kg). D) DOX concentration in the extraction of homogenized organs 24 hrs post i.v. injection of DOX-loaded ArgPEA-ss-HA(AP) nanocomplex or free

DOX (5 mg/kg). Values represent the average ± SD (n=4). Statistical significance: *, $p < 0.05$; **, $p < 0.01$, *** $p < 0.001$.

### *4.4.8 Light-enhanced anti-tumor effect by DOX-loaded ArgPEA-ss-HA(AP) nanocomplex in vivo*

The PCI effect on in vivo anti-tumor efficiency of DOX-loaded nanocomplex was further evaluated on MDA-MB-231 mice xenografts. i.v. injection of blank nanocomplex, DOX-loaded nanocomplex or free DOX were performed on day 1, 8 and 15, with equivalent DOX dosage of 2 mg/kg/week. The light dose of 50 J/cm$^2$ by 671 nm He-Ne laser (100 mW/cm$^2$) was used, and the time interval between i.v. injection and light irradiation was chosen as 24 hrs, according to the in vivo study of PCI on mice xenograft by Berg et al [45]. The growth of tumor was monitored over 28 days, and the results were illustrated in Figure 4.10A. Free DOX didn't exhibit any antitumor effect, as the tumor growth curve was almost identical to saline-treated control. Minor tumor suppression was observed in the group treated with blank ArgPEA-ss-HA(AP) nanocomplex with irradiation. Major anti-tumor effect was observed in groups treated with DOX-loaded ArgPEA-ss-HA(AP) nanocomplex both without or with irradiation. The final volume of tumor on day 28 by irradiated DOX-loaded nanocomplex was 180 mm3(normalized to the tumor volume on day 0), which suggested an 78% of reduction in tumor volume compared to saline-treated control. In addition, the rate of tumor suppression was significantly higher for the irradiated DOX-loaded nanocomplex, compared to the non-irradiated counterpart. The treatments were well tolerated as no statistically significant loss in body weight was observed in any of the groups (Figure 4.10B).

Skin photosensitivity [46] is an important challenge associated with photosensitizer-related treatment. As indicated in Figure 4.10B, free AlPcS2a resulted in 6-fold higher distribution in skin than AlPcS2a conjugated with the nanocomplex. The result can be attributed to the unique circulating properties [47] of the nano-carriers and the preferential accumulation in tumor tissues. The significantly reduced level of

AlPcS2a by ArgPEA-ss-HA(AP) in skin is expected to reduce the risk of light-induced disorder, damage or immune response in skin tissue [48]. In the groups treated by DOX-loaded ArgPEA-ss-HA(AP), minor edema and erythema were observed right after irradiation was applied, but was reversed in 2-3 days. No wound or scar was observed by the end of the treatment (day 28), which positively related to the low distribution of photosensitizer in skin tissue, and further proved the biosafety of the PCI-facilitated ArgPEA-ss-HA(AP) delivery vehicles.

It is worth pointing out that the reduction in weight/size of the exercised tumors (Figure 4.10C and 10D) occurred in groups treated with both irradiated non-irradiated DOX-loaded ArgPEA-ss-HA(AP) nanocomplex. The difference in tumor inhibition between irradiated and non-irradiated groups was statistically significant, which suggested that PCI effectively enhanced the anti-tumor activity of the reduction-sensitive DOX-loaded nanocomplex.

The advantages of light-facilitated delivery of chemotherapeutics were also discussed in previous literature [42,49], in which the photosensitizer DPc/m or Photofrin was administrated separately with the chemotherapeutics. The major improvement in this study was the covalent conjugation of the aluminum phthalocyanine disulfonate (AlPcS2a) photosensitizer on the reduction-responsive nano-vehicles, which enabled the preferential distribution of the photosensitizer in tumor site, and provided an effective tumor suppression at a low dosage of DOX (2 mg/kg/week). In addition to the current in vivo results, screening for the optimized treatment in vivo models would be the focus of our future study, including the dosage of light and DOX, the time interval between drug administration and light irradiation, etc., to further enhance the therapeutic effect and to achieve more precise manipulation of the spatio-temporally controllable anti-tumor effect.

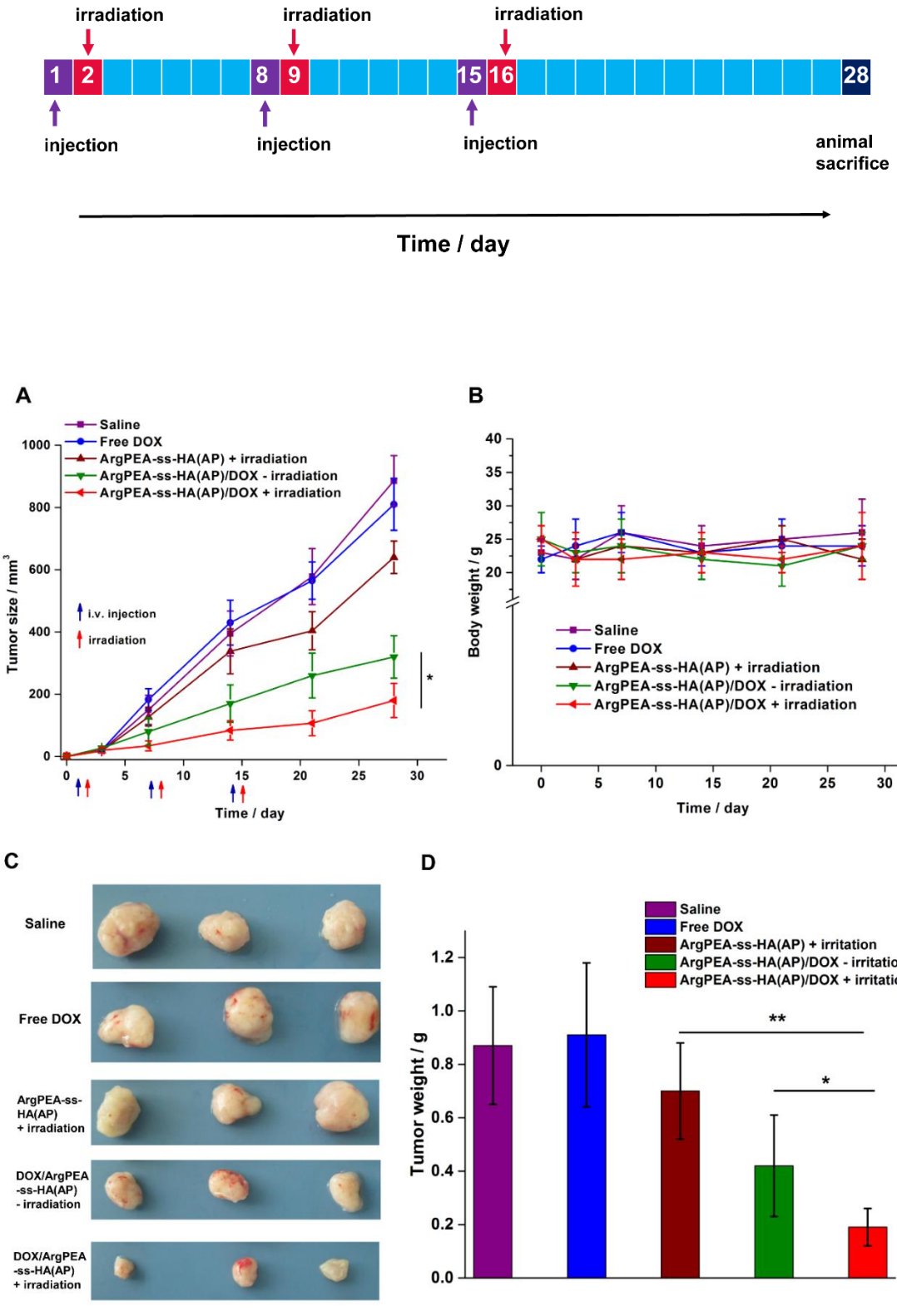


**Figure 4.10**. *In vivo* anti-tumor effect of blank ArgPEA-ss-HA(AP) nanocomplex,

DOX-loaded ArgPEA-ss-HA(AP) nanocomplex or free DOX (with equivalent DOX dosage of 1.5 mg/kg/week) treated female BALB/c nude mice. Light irradiation at 660 nm was applied 24 hrs post i.v. injection at 30 J/cm$^2$. A) Tumor volume was monitored vs. time. B) Body weight of tumor-bearing mice was monitored vs. time. C) Representative tumor images from different treatment group at day 28. D) Tumor weight from different treatment group at day 28. Statistical significance was compared: * $p < 0.05$; ** $p < 0.01$.

### *4.5 Conclusions*

A biodegradable and reduction-sensitive nanocomplex was developed from hyaluronic acid and arginine based PEA, and crosslinked with disulfide linkage. Photosensitizer, AlPcS2a, was conjugated via PEG spacer, and enabled the light-enhanced therapeutic effect of DOX-loaded nanocomplex. The data from both *in vitro* and *in vivo* studies lead to the following conclusions: A) The conjugated AlPcS2a induced endolysosomal rupture in MDA-MB-231 monolayers upon light irradiation, the sequestered nanocomplex was translocated into cytosol so that the release of DOX was accelerated by cytosolic GSH. B) PCI enhanced the *in vitro* inhibition of MDA-MB-231 cells by DOX-loaded nanocomplex, and synergism was detected at lower concentrations of DOX and AlPcS2a, with a moderate level of light irradiation. C) The AlPcS2a conjugated nanocomplex exhibited enhanced penetration in MDA-MB-231 spheroids compared to free AlPcS2a, and PCI-enhanced DOX release as well as augmented therapeutic effect were also observed in the spheroid model. D) *In vivo* results suggested a consistent and preferential accumulation of both AlPcS2a and DOX in tumor tissues, as delivered by the nanocomplex. PCI amplified the efficiency of the nanocomplex in tumor suppression, with a well-tolerable dosage of drug and light irradiation. This study provided insights in designing reduction-sensitive nano- carriers, and suggested the potential to develop smart nanomedicine responsive to both endogenous and exogenous cues to achieve spatio-temporal manipulation of the therapeutic effect.

**References:**


[1] H. Priya James, R. John, A. Alex, K. R. Anoop, *Acta Pharm. Sin. B* **2014**, *4*, 120.

[2] S. Mura, J. Nicolas, P. Couvreur, *Nat. Mater.* **2013**, *12*, 991.

[3] M. Huo, J. Yuan, L. Tao, Y. Wei, *Polym Chem* **2014**, *5*, 1519.

[4] G. Sahay, D. Y. Alakhova, A. V. Kabanov, *J. Controlled Release* **2010**, *145*, 182.

[5] A. K. Varkouhi, M. Scholte, G. Storm, H. J. Haisma, *J. Controlled Release* **2011**, *151*, 220.

[6] L. Shang, K. Nienhaus, G. Nienhaus, *J. Nanobiotechnology* **2014**, *12*, 5.

[7] L. Kou, J. Sun, Y. Zhai, Z. He, *Asian J. Pharm. Sci.* **2013**, *8*, 1.

[8] C. D. Austin, X. Wen, L. Gazzard, C. Nelson, R. H. Scheller, S. J. Scales, *Proc. Natl. Acad. Sci.* **2005**, *102*, 17987.

[9] A. M. Sauer, A. Schlossbauer, N. Ruthardt, V. Cauda, T. Bein, C. Bräuchle, *Nano Lett.* **2010**, *10*, 3684.

[10] S. A. Mackowiak, A. Schmidt, V. Weiss, C. Argyo, C. von Schirnding, T. Bein, C. Bräuchle, *Nano Lett.* **2013**, *13*, 2576.

[11] P. K. Selbo, A. Weyergang, A. Høgset, O.-J. Norum, M. B. Berstad, M. Vikdal, K. Berg, *J. Controlled Release* **2010**, *148*, 2.

[12] F. Ghetti, A. G. Griesbeck, M. Oelgemöller, *CRC handbook of organic photochemistry and photobiology*; CRC Press: Boca Raton, FL, 2012.

[13] A. Martinez de Pinillos Bayona, C. M. Moore, M. Loizidou, A. J. MacRobert, J. H. Woodhams, *Int. J. Cancer* **2016**, *138*, 1049.

[14] H.-C. Yen, H. Cabral, P. Mi, K. Toh, Y. Matsumoto, X. Liu, H. Koori, A. Kim, K. Miyazaki, Y. Miura, N. Nishiyama, K. Kataoka, *ACS Nano* **2014**, *8*, 11591.

[15] K. Berg, A. Weyergang, L. Prasmickaite, A. Bonsted, A. Høgset, M.-T. R. Strand, E. Wagner, P. K. Selbo, In *Photodynamic Therapy*; Gomer, C. J., Ed.; Humana Press: Totowa, NJ, 2010; Vol. 635, pp. 133–145.

[16] C.-C. Chu, In *Biodegradable Polymers: New Biomaterial Advancement and Challenges*; Chu, C.-C., Ed.; Nova Science Publisher, 2015; Vol. 2.

[17] C.-C. Chu, In *Biomaterials – Principles and Practices*; Wong, J. Y.; Bronzino, J. D.; Peterson, D. R., Eds.; CRC Press, 2012.

[18] Chih-Chang Chu, In *L-Arginine: Structure, Dietary Sources and Beneficial Effects*; Nova Science Publisher: New York, In Press.

[19] C. C. Chu, *J. Fiber Bioeng. Inform.* **2012**, *5*, 1.

[20] D.-Q. Wu, J. Wu, C.-C. Chu, *Soft Matter* **2013**, *9*, 3965.

[21] A. N. Potuck, B. L. Weed, C. A. Leifer, C. C. Chu, *Biomacromolecules* **2015**, *16*, 564.

[22] F. Dosio, S. Arpicco, B. Stella, E. Fattal, *Adv. Drug Deliv. Rev.* **2016**, *97*, 204.

[23] K. Y. Choi, H. Y. Yoon, J.-H. Kim, S. M. Bae, R.-W. Park, Y. M. Kang, I.-S. Kim, I. C. Kwon, K. Choi, S. Y. Jeong, K. Kim, J. H. Park, *ACS Nano* **2011**, *5*, 8591.

[24] N. Brasseur, R. Ouellet, C. La Madeleine, J. E. van Lier, *Br. J. Cancer* **1999**, *80*, 1533.

[25] C. M. Allen, R. Langlois, W. M. Sharman, C. La Madeleine, J. E. Van Lier, *Photochem. Photobiol.* **2002**, *76*, 208.

[26] H. Song, C. C. Chu, *J. Appl. Polym. Sci.* **2012**, *124*, 3840.

[27] J. K. Joseph, S. L. Jain, B. Sain, *Ind. Eng. Chem. Res.* **2010**, *49*, 6674.

[28] X. Z. Shu, Y. Liu, Y. Luo, M. C. Roberts, G. D. Prestwich, *Biomacromolecules* **2002**, *3*, 1304.

[29] J. Dahlmann, A. Krause, L. Möller, G. Kensah, M. Möwes, A. Diekmann, U. Martin, A. Kirschning, I. Gruh, G. Dräger, *Biomaterials* **2013**, *34*, 940.

[30] J. Wu, C.-C. Chu, *Acta Biomater.* **2012**, *8*, 4314.

[31] W.-D. Jang, Y. Nakagishi, N. Nishiyama, S. Kawauchi, Y. Morimoto, M. Kikuchi, K. Kataoka, *J. Controlled Release* **2006**, *113*, 73.

[32] M. S. Mathews, V. Vo, E.-C. Shih, G. Zamora, C.-H. Sun, S. J. Madsen, H. Hirschberg, *J. Environ. Pathol. Toxicol. Oncol. Off. Organ Int. Soc. Environ. Toxicol. Cancer* **2012**, *31*, 49.

[33] A. Ivascu, M. Kubbies, *J. Biomol. Screen.* **2006**, *11*, 922.

[34] C. C. Lee, B. W. Pouge, R. R. Strawbridge, K. L. Moodie, L. R. Bartholomew, G. C. Burke, P. Jack Hoopes, *Photochem. Photobiol.* **2007**, *74*, 453.

[35] K. Y. Choi, K. H. Min, H. Y. Yoon, K. Kim, J. H. Park, I. C. Kwon, K. Choi, S. Y. Jeong, *Biomaterials* **2011**, *32*, 1880.

[36] Z. Jiang, J. Shao, T. Yang, J. Wang, L. Jia, *J. Pharm. Biomed. Anal.* **2014**, *87*, 98.

[37] E. Sakurai, H. Ozeki, N. Kunou, Y. Ogura, *Ophthalmic Res.* **2001**, *33*, 31.

[38] H. Chen, L. Xiao, Y. Anraku, P. Mi, X. Liu, H. Cabral, A. Inoue, T. Nomoto, A. Kishimura, N. Nishiyama, K. Kataoka, *J. Am. Chem. Soc.* **2014**, *136*, 157.

[39] T. T. Goodman, C. P. Ng, S. H. Pun, *Bioconjug. Chem.* **2008**, *19*, 1951.

[40] D. Zhu, Z. Wang, S. Zong, H. Chen, X. Wu, Y. Pei, P. Chen, X. Ma, Y. Cui, *Nanoscale* **2014**, *6*, 8155.

[41] M. Huang, Z. Chen, K. Zheng, R. Li, X. Zhou, Y. Zhang, P. Hu, Y. Huang, *Int. J. Nanomedicine* **2015**, 5327.

[42] H.-L. Lu, W.-J. Syu, N. Nishiyama, K. Kataoka, P.-S. Lai, *J. Controlled Release* **2011**, *155*, 458.

[43] W. S. Chan, J. F. Marshall, R. Svensen, J. Bedwell, I. R. Hart, *Cancer Res.* **1990**, *50*, 4533.

[44] P. B. Johansen, *Cancer Chemother. Pharmacol.* **1981**, *5*, 267.

[45] O.-J. Norum, P. K. Selbo, A. Weyergang, K.-E. Giercksky, K. Berg, *J. Photochem. Photobiol. B* **2009**, *96*, 83.

[46] M. B. Vrouenraets, G. W. M. Visser, G. B. Snow, G. A. M. S. van Dongen, *Anticancer Res.* **2003**, *23*, 505.

[47] H. Maeda, H. Nakamura, J. Fang, *Adv. Drug Deliv. Rev.* **2013**, *65*, 71.

[48] D. E. J. G. J. Dolmans, D. Fukumura, R. K. Jain, *Nat. Rev. Cancer* **2003**, *3*, 380.

[49] P.-S. Lai, P.-J. Lou, C.-L. Peng, C.-L. Pai, W.-N. Yen, M.-Y. Huang, T.-H. Young, M.-J. Shieh, *J. Control. Release Off. J. Control. Release Soc.* **2007**, *122*, 39.

# CHAPTER 5

# INCLUSION COMPLEX FROM CYCLODEXTRIN-GRAFTED HYALURONIC ACID AND PSEUDO PROTEIN AS A BIODEGRADABLE NANO-DELIVERY VEHICLES FOR GAMBOGIC ACID

### *5.1 Abstract*

β-Cyclodextrin can form inclusion complex with a series of guest molecules including phenylalanine, and has gained considerable popularity in the study of supramolecular nanostructure. In this study, a biodegradable nano-delivery vehicle was developed from β-cyclodextrin grafted hyaluronic acid and phenylalanine based pseudo protein (HA(CD)-4Phe4 nanocomplex). Gambogic acid (GA), a naturally-derived chemotherapeutics from Garcinia hanburyi tree resin, was loaded in the nanocomplex and the delivery performance was evaluated in vitro. The 4Phe4 pseudo protein provided hydrophobic interaction with GA for efficient encapsulation of drug, while the HA component enabled the targeting delivery to CD44 positive tumor cells. In the presence of hyaluronidase, the release of GA from the nanocomplex was significantly accelerated, due to the enzymatic biodegradation of the carrier. The internalization of the nanocomplex in MDA-MB-435/MDR cells was mediated by both the overexpression of CD44 receptor, and clathrin-dependent pathway. GA-loaded nanocomplex exhibited significant cytotoxicity toward MDA-MB-435/MDR multidrug resistant melanoma cells, and induced enhanced level of apoptosis and mitochondrial depolarization, at low concentration of GA. Suppressed matrix metalloproteinase activity was also detected in MDA-MB-435/MDR melanoma cells treated by GA-loaded nanocomplex. The in vitro data suggested that GA-loaded HA(CD)-4Phe4 nanocomplex can provide the potential as a tumor-targeting delivery system to induce toxicity in CD44 positive tumor cells, and simultaneously inhibiting the tumor metastasis.

### *5.2 Introduction*

Cyclodextrin (CD), a family of macrocyclic oligosaccharides linked by α-1,4 glycosidic bonds, has been extensively studied in the field of drug delivery [1]. CD and their derivatives have been successfully employed to construct supramolecular functional materials, and the biomedical applications of CDs are attractive due to the low toxicity and low immunogenicity. β-cyclodextrin (β-CD), composed of 7 glucose units, is a truncated cone-shaped molecule with top and bottom diameters of 0.60 nm and 0.65 nm, respectively [2]. β-CD can form inclusion complex with various guest molecules based on complementary stereoelectronic arrangement of binding sites between host and guest [3]. The guest molecules include poly(propylene oxide) [4], poly(dimethylsiloxane)s [5], aliphatic polyesters [6], polyacrylate with adamantyl pendant group [7], and poly(β-benzyl L-aspartate) [8], etc. The wide range of guest molecules enables the versatile structural design for the supramolecular assembled nanostructure of β-CD, and can be developed as the nano-sized drug delivery vehicles. Zhang et al. [9] developed a nanostructure assembled form β-CD-grafted-polyethylene glycol and polyaspartatamide as the delivery vehicles for docetaxel. Fan et al. [10] developed a nano-assembly from β-CD grafted polyethyleneimine and adamantine-doxorubicin for the co-delivery of both doxorubicin and therapeutic gene pTRAIL.

Hyaluronic acid (HA) is a natural and biodegradable polysaccharide formed by D-glucuronic acid and N-acetyl-D-glucosamine repetitive units [11]. Identified as the ligand molecule for CD44 receptors, HA has attracted considerable research interests in the field of tumor-targeting delivery, due to the overexpression of CD44 receptors

on many types of tumor cells including breast tumors, colon cancers, and myeloma, etc [12]. HA-based nano-carriers exhibited enhanced selective binding and uptake by tumor cells, and have been developed to improve the potency of various therapeutic agents [13], such as chemotherapeutics, nucleic acids and proteins. HA has been studied as the nano-delivery vehicles for anti-cancer drug delivery [14]. However, very few literatures reported the inclusion complex from hyaluronic acid and other polymers via cyclodextrin functional groups. In the work by Kulkarni et al. [15], nanoparticles were prepared from the inclusion complex between PEI grafted with β-cyclodextrin and hyaluronic acid with adamantine groups, and developed as the delivery vehicles for plasmid DNA in HeLa cells.

Biodegradable amino acid based poly(ester amide)s (AA-PEAs), a new family of synthetic pseudo proteins, are synthesized from 3 building blocks: amino acids, dialcohol and diacids. The choice of different amino acids, and the hydrocarbons between the amide and ester groups, provides a versatile structural design of AA-PEAs and makes them tunable in hydrophilicity/hydrophobicity, charge density, and reactive sites for expanded properties and functionality. AA-PEAs have been studied for various biomedical applications and have also been hybridized with other polymers like polysaccharides and synthetic aliphatic polyesters to form unique hybrids with broadened properties and applications [16–18]. The current status of AA-PEAs have recently been reviewed [19,20].

Gambogic acid (GA), a natural compound from gamboge resin that produced by Garcinia hanburyi trees, has been reported [21–23] to exhibit significant cytotoxic activity against multiple tumor cells. Several mechanisms were proposed for

elucidating its anti-tumor effect [24,25], which include the inhibition of the expression of telomerase, telomerase reverse transcriptase mRNA and VEGF receptor signaling, downregulation of the Bcl-2,4 activating tumor necrosis factor (TNF)-induced cell death, etc. GA has been approved for the phase II clinical trial for cancer therapy by the Chinese Food and Drug Administration (CFDA) [26,27]. However, GA is still facing several challenges, such as low bioavailability due to its poor water solubility (< 1 μg/mL) and the lack of adequate tumor targeting due to the wide distribution of GA in normal tissues, which can limit its therapeutic efficacy. Nano-delivery vehicles can provide the advantage to solve the challenges associated with the direct administration of GA. Saxena et al. [28] developed poloxamers/TGPS mixed micelles to for the delivery of GA in MCF-7 breast carcinoma, resulting in 1.6-fold higher toxicity compared to free GA. Zhang et al. [29] developed lactoferrin based nanoparticles for the delivery of GA to S180 mice sarcoma, and they reported a significantly enhanced in vivo therapeutic effect. It is of particular interest to develop a tumor-specific nano-delivery system for GA, while simultaneously improve its water solubility and bioavailability.

The aim of this study was to develop a biodegradable nanocomplex from the inclusion complex between β-cyclodextrin and phenylalanine based poly(ester amide)s, and incorporate hyaluronic acid on the surface of the complex for the specific delivery of GA to CD44 positive tumor cells. The phenylalanine based poly(ester amide)s in the nanocomplex provided hydrophobic interaction with GA to improve its encapsulation capacity. MDA-MB-435/MDR multidrug resistant melanoma cells with overexpression of CD44 receptors were chosen for the in vitro examination of the GA

delivery system. In vitro characterization of the endocytosis and tumor cell inhibition by the GA-loaded nanocomplex was performed. Mitochondrial damage, cell death assay and the activity of matrix metalloproteinases were also investigated to further validate the potency of the GA-loaded nanocomplex.

## *5.3 Experimental*

### *5.3.1 Chemicals and cells*

Sodium hyaluronate (MW= 10 to 20 kDa) was purchased from Lifecore Biomedical (Chaska, MN). Tetrabutylammonium bromide, β-cyclodextrin (β-CD), 4-toluenesulfonyl chloride, succinic dihydrazide (SDH), N-hydroxysuccinimide (NHS), N-(3-dimethylaminopropyl)-N'-ethylcarbodiimide hydrochloride (EDC·HCl), 2-(N-morpholino)ethanesulfonic acid buffer (MES buffer, 0.5 M in water), hyaluronidase from bovine testes were from Sigma Aldrich (Milwaukee, WI). Amberlite IR-120 $H^+$ ion exchange resin was from Alfa Aesar (Ward Hill, MA). Gambogic acid (GA) was from BroadPharm (San Diego, CA). Lysotracker green was from Cell Signaling (Beverly, MA). Dimethyl sulfoxide (DMSO), methanol and other HPLC grade solvents were from JT Baker (Phillipsburg, NJ). JC-1 mitochondrial membrane potential assay kit was from Cayman Chemical (Ann Arbour, MI). Annexin V apoptosis detection kit was purchased from eBioscience (San Diego, CA). Snakeskin dialysis tubing (MWCO = 3.5 kDa or 10 kDa) and NHS-Rhodamine were from Pierce (Rockford, IL). Phenylalanine based poly(ester amide)s 4Phe4 was synthesized from our previous study [30].

MDA-MB-435/MDR multidrug resistant melanoma cells were donated by Dr. Robert Clarke (Georgetown University, Washington, D.C.) and MD Anderson Cancer Center (Houston, TX). MDA-MB-435/MDR cells were maintained at 37 ºC with 5% $CO_2$ in Minimum Essential Medium (Richter's modification) containing 2mM L-glutamine, phenol red, 10% fetal bovine serum, and 1% penicillin/streptomycin. NIH 3T3 fibroblasts were maintained in Dulbecco's Modified Eagle Medium (DMEM) supplemented with phenol red, 10% fetal bovine serum, and 1% penicillin/streptomycin.

### *5.3.2 Synthesis*

*Synthesis of 6-monotosyl β-cyclodextrin*. To introduce amine-reactive functional groups into β-cyclodextrin (β-CD), 6-monotosyl-β-CD was prepared from previously published study [31]. β-CD (17.22 g) was dissolved in 1% NaOH solution (200 mL). Toluene sulfonyl chloride (2.9 g) dissolved in acetonitrile (11 mL) was added dropwise. The reaction was stirred at room temperature for another 2 hrs. The pH of the filtered solution was adjusted to 2-3 with 0.1 M HCl solution and precipitated overnight at 4 °C. The white precipitate was filtered and re-crystalized twice in water to give purified 6-monotosyl β-CD.

*Synthesis of succinic acid dihydrazide grafted HA*. HA (300 mg) and succinic dihydrazide (SDH, 587 mg) were first dissolved in MES buffer (60 mL, 50 mM), and the pH was adjusted to 5.5 with 0.1 M hydrochloric acid. EDC·HCl (43 mg) and NHS (26 mg) were added and the reaction was stirred at room temperature overnight. The reaction mixture was dialyzed (MWCO = 3.5 kDa) against DI water for 48 hrs to give

the aqueous solution of HA grafted with succinic acid dihydrazide (HA-SDH). To improve the solubility of HA-SDH in organic solvents, HA-SDH was converted to its tetrabutylammonium salt (HA-SDH-TBA) via ion exchange method. Amberlite IR-120 $H^+$ resin was neutralized with NaOH, washed with deionized water and immersed in 0.25 M aqueous tetra-N-butylammonium bromide solution overnight. The resulting ion exchange resin was added to the dialyzed solution of HA-SDH and stirred overnight at room temperature. The resin was removed by filtration, and the aqueous solution was lyophilized to give HA-SDH-TBA.

*Synthesis of β-CD grafted HA*. HA functionalized with β-CD was prepared as indicated in Figure 5.1. HA-SDH-TBA (100 mg) was dissolved in DMSO with triethylamine (30 µL), 6-monotosyl β-CD (91 mg) was added and stirred for 24 hrs at 40 °C. The solution was dialyzed against DI water for 48 hrs, the pH of the solution was adjusted to 4.0 with 0.1 M HCl, kept at 4 °C overnight and filtered to remove unreacted 6-monotosyl β-CD. The filtered solution was converted to the TBA salt via ionic exchange method and lyophilized to give HA(CD)-TBA. The $^1$H-NMR was examined on a Varian Unity Inova 400 MHz spectrometer (Palo Alto, CA).

*Synthesis of rhodamine-labeled HA(CD)-TBA*. HA-SDH (100 mg) was dissolved in DI water (5 mL) and mixed with NHS-rhodamine (3 mg). The reaction was stirred overnight at room temperature, and dialyzed (MWCO=3.5 kDa) against DI water. The resulted rhodamine-labeled HA-SDH was converted to its TBA salt (rhodamine labeled HA-SDH-TBA) via ionic exchange method. The preparation of β-CD grafted HA-SDH-TBA labeled with rhodamine was the same as the preparation of HA(CD)-TBA.

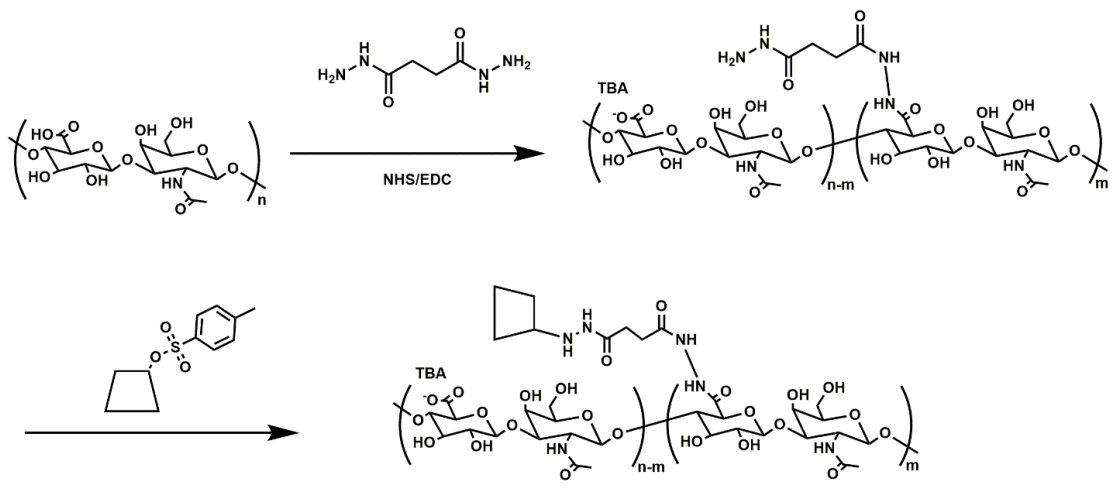


**Figure 5.1**. Synthesis scheme for tetrabutyl ammonium salt of β-CD grafted hyaluronic acid (HA(CD)-TBA).

### *5.3.3 Preparation of GA-loaded HA(CD)-4Phe4 nanocomplex*

Inclusion complex from HA(CD)-TBA and phenylalanine based poly(ester amide)s (4Phe4) was prepared via the host-guest interaction between β-CD and the phenyl groups of 4Phe4. 4Phe4 was synthesized based on published procedures [30], and had an average molecular weight of 20.6 kDa and PDI of 1.27.

To prepare GA-loaded HA(CD)-4Phe4 nanocomplex, HA(CD)-TBA (200 mg) was dissolved in DMSO (20 mL), DMSO solution of 4Phe4 (50 mg, 5 mL) was added and stirred overnight. Gambogic acid (GA, 25 mg) was then added and stirred for another 4 hrs. The resulting solution was dialyzed (MWCO = 3.5 kDa) against DI water for 48 hrs and filtered with 0.22 μm PVDF microfilter to remove unloaded drug or free 4Phe4. The filtered solution was lyophilized.

The GA loading content (LC) and encapsulation efficiency (EE) was determined by extracting GA from GA-loaded HA(CD)-4Phe4 nanocomplex in ethanol for 24 hrs at 40 °C [32] and the filtered with 0.22 μm PVDF microfilter. The GA-ethanol solution was dried in vacuo, and the resulting GA was re-dissolved in DMSO. The concentration of GA in DMSO was determined by the absorption at 360 nm on Lambda Bio40 spectrophotometer (Perkin-Elmer, Norwalk, CT), and calibrated with a standard GA curve.

The morphology of GA-loaded HA(CD)-4Phe4 nanocomplex was observed on a FEI Tecnai Spirit T12 TEM (FEI Co., Hillsboro, OR) at an operating voltage of 120 kV. Zeta potential and size of the nanocomplex were characterized at room temperature on a Zetasizer NanoZS system (Malvern, UK).

### *5.3.4 In vitro release profile of GA-loaded HA(CD)-4Phe4 nanocomplex*

GA-loaded HA(CD)-4Phe4 nanocomplex (10 mg) was dissolved in phosphate buffer (pH 7.4, 5mL) with or without the presence of 120 unit/mL hyaluronidase (Hyal). The solution was placed in dialysis tubing (MWCO = 10 kDa) and dialyzed against pH 7.4 phosphate buffer (30 mL) at 37 °C under shaking (100 rpm). At predetermined time intervals, 5 mL of the solution outside the dialysis tubing was retrieved and replaced by fresh media. The concentration of GA in each sample was determined by the absorption at 360 nm in UV-Vis spectra and calibrated against a standard curve of GA. The percentage of released GA was plotted vs. time. Each test was performed in triplicate.

### *5.3.5 Endocytosis and subcellular distribution of HA(CD)-4Phe4 nanocomplex*

To study the accumulated endocytosis of blank HA(CD)-4Phe4 nanocomplex, MDA-MB-435/MDR (CD44 positive) or NIH 3T3 cells (CD44 negative) were incubated with blank HA(CD)-4Phe4 nanocomplex labeled with rhodamine for 1, 2, 4, 8, 12 or 24 hrs. The cells were washed with PBS, harvested and the cellular fluorescence intensity was analyzed on FACSAria fusion fluorescence activated cell sorter (BD Biosciences, Franklin Lakes, NJ). $5 \times 10^4$ cells were analyzed for each sample, and the average fluorescence intensity was plotted vs. time.

Subcellular distribution of blank HA(CD)-4Phe4 nanocomplex was visualized on a Zeiss LSM710 confocal microscope (Carl Zeiss MicroImaging, Thornwood, NY). MDA-MB-435/MDR were incubated with blank HA(CD)-4Phe4 nanocomplex labeled with rhodamine (0.1 mg/mL) for 4 hrs. Cells were then stained with Lysotracker green as per manufacturer's instruction, washed with PBS and imaged alive by confocal microscopy.

To study the pathway of endocytosis, MDA-MB-435/MDR cells treated with inhibitors that block different endocytic pathways (nystatin, 50 μg/mL; chloropromazine, 30 μM; amiloride hydrochloride, 50 μM; methyl-β-cyclodextrin, 3 mg/mL or anti-CD44 antibody as per manufacturer's instruction) for 0.5 hr, before rhodamine labelled blank HA(CD)-4Phe4 nanocomplex was added and incubated for another 4 hrs. The cells were then washed with PBS, harvested and subjected to flow cytometry assay. The effect of low temperature (4°C) on endocytosis was also studied. Cells incubated with the blank nanocomplex at 37°C but not treated with any inhibitor were

tested as control. The mean fluorescence intensity for each sample was recorded and normalized to control. The tests were performed in triplicate.

### *5.3.6 Cytotoxicity of GA-loaded nanocomplex*

MDA-MB-435/MDR cells were incubated with blank nanocomplex, free GA or GA-loaded HA(CD)-4Phe4 nanocomplex (c(GA) =0.1 to 20 μM) for 24 hrs. The viability of cells were determined by MTT assay, and each experiment was run in six replicates. The absorbance at 570 nm was recorded and normalized to the results of the untreated cell control to give the percentage of cell survival. Each test was run in 6 replicates.

### *5.3.7 Mitochondrial membrane potential assay*

MDA-MB-435/MDR cells were incubated with blank nanocomplex, free GA or GA-loaded HA(CD)-4Phe4 nanocomplex (c(GA) =1 μM) for 24 hrs. The cells were stained with JC-1 probe as per manufacturer's instruction and analyzed by flow cytometry. The experiments were performed in triplicate. The percentage of cell population stained with higher degree of JC-1 monomer and lower degree of J-aggregates was recorded. 5 x $10^4$ cells were analyzed for each sample.

### *5.3.8 Apoptosis study*

MDA-MB-435/MDR cells were incubated with blank nanocomplex, free GA or GA-loaded HA(CD)-4Phe4 nanocomplex (c(GA) =1 μM) for 24 hrs. The cells were washed and harvested. For apoptosis assay, Annexin-V/PI double staining was

performed as per manufacturer's instruction. The percentage of dead/apoptotic cells were analysed by flow cytometry. 5 x $10^4$ cells were analyzed for each sample and each experiment was performed in triplicate. For the assay of caspase 3/7 activities, the cells were incubated with Apo-ONE Homogeneous Caspase-3/7 assay reagents (Promega, Madison, WI) as per manufacturer's instruction. The fluorescence intensity was recorded on a microplate reader ($\lambda$ex = 485 ± 20 nm/$\lambda$em = 528 ± 20 nm). The untreated cells were tested as control. The fluorescence for each sample was normalized to control to give the fold of caspase 3/7 activities. Each experiment was performed in triplicate.

### *5.3.9 Gelatin zymography*

MDA-MB-435/MDR cells were incubated in serum free medium with free GA, GA-loaded HA(CD)-4Phe4 nanocomplex or blank HA(CD)-4Phe4 nanocomplex (c(GA) =1 μM) for 24 hrs. The media were centrifuged (400 rcf, 5 min, 4 ºC), and gelatin zymography for the supernatant was performed as described previously [33]. In brief, SDS-PAGE gels were prepared containing 1% type B gelatin (w/v). After electrophoresis, the gels were washed with 2.5% Triton X-100 to remove SDS and incubated with developing buffer (50 mM Tris-HCl, 10 mM $CaCl_2$, 0.02% $NaN_3$, pH 7.6) at 37 °C for 16 hrs. The gels were stained with 0.25% Coomassie Brilliant Blue R-250 solution and destained with destaining solution (10% methanol, 5% acetic acid in DI water). Regions digested by matrix metalloproteinases (MMP) were observed as white bands against a dark background.

### 5.3.10 Statistical analysis

The data are presented as mean values with standard deviations (SD). All data were analyzed using one-way ANOVA, followed by Tukey's multiple comparison tests, and $p < 0.05$ was used for statistical significance.

## *5.4 Results and discussion*

### *5.4.1 The characterization of polymers*

β-Cyclodextrin-grafted HA (HA(CD)) was prepared from the reaction between 6-monotosyl-β-CD and succinic dihydrazide functionalized HA (HA-SDH). The tosyl groups in the 6-monotosyl-β-CD was reacted with the amine groups on HA-SDH to obtain HA(CD). As indicated in the $^{1}$H NMR spectra of HA(CD) in Figure 5.2, the typical peak for the methyl groups in HA was observed at 1.73 ppm, and the typical peak for the $^{1}$H proton from the glucose residue in β-CD was observed at 4.75 to 5.05 ppm. Based on the integral of these two peaks, the grafting ratio of β-CD onto HA, defined as the molar amount of β-CD divided by the total molar amount of HA repeating units, was calculated to be 13%. The $^{1}$H-NMR spectra suggested the effective grafting of β-CD onto HA, and the β-CD pendant groups provides available sites to form inclusion complex with the phenylalanine moiety of 4Phe4.

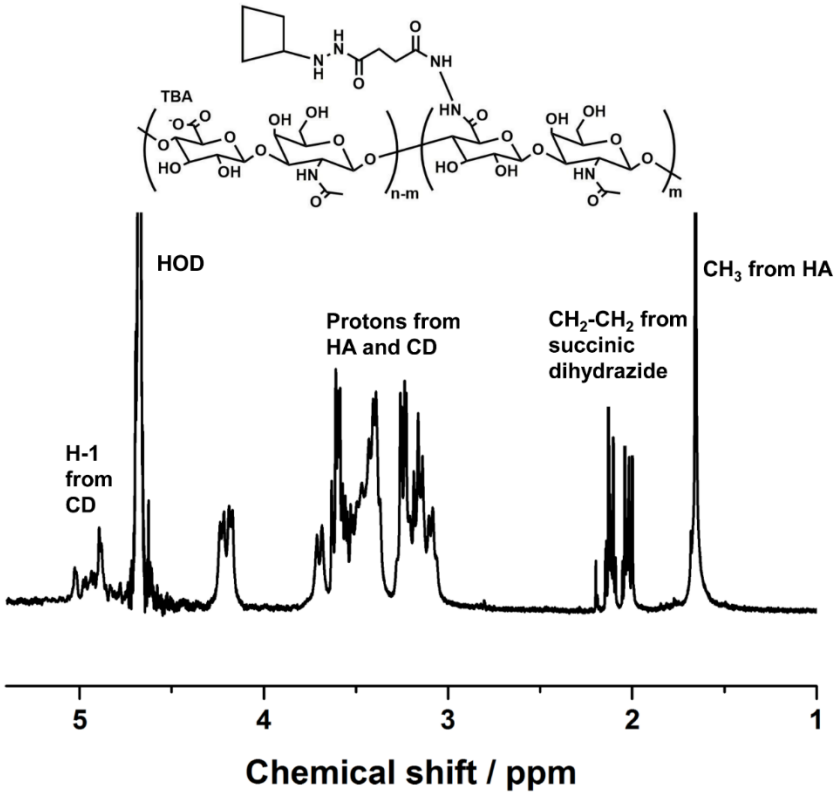


**Figure 5.2**. $^{1}$H NMR spectra of β-cyclodextrin-grafted HA (HA(CD)).

### *5.4.2 The characterization of GA-loaded HA(CD)-4Phe4 nanocomplex*

The scheme for the formation of HA(CD)-4Phe4 nanocomplex was illustrated in Figure 5.3. In aqueous environment, HA provided the hydrophilic component as the outer layer of the nanocomplex, and 4Phe4 provided the hydrophobic component in the interior. The hydrophobic and hydrophilic segments were held together via the host-guest interaction between β-CD side groups on HA(CD) and phenyl side groups on 4Phe4. The impact of the feed ratio between HA(CD) and 4Phe4 on the yield and size of the nanocomplex was shown in Table 1. When the weight ratio between HA(CD)/4Phe4 was 1:2, significant precipitate was obtained, which can be attributed

to the excessive amount of the hydrophobic 4Phe4 that didn't formed the inclusion complex with HA(CD), and the lack of stabilizing effect by the HA lead to the direct precipitation of 4Phe4. As the feed ratio between HA(CD)/4Phe4 increased, the HA(CD)-4Phe4 nanocomplex was effectively formed, and the average diameter of the nanocomplex decreased with an increase in the HA(CD) component, i.e. 732.63 ± 38.2 nm (yield 13.6%) for HA(CD)/4Phe4=1:1, and 148.5 ± 21.2 nm (yield 65.1%) for HA(CD)/4Phe4=2:1. When the HA(CD)/4Phe4 ratio increased further to 4:1, no significant change in diameter was detected, but the yield reduced to 27.5%, due to the fact that the excessive amount of HA(CD) which didn't form the nanocomplex was removed in the purification process. Negative zeta potential ranging from -19.5 ± 2.7 mV to -26.23 ± 3.2 mV was detected for the nanocomplex, which can be attributed to the presence of HA at the surface of the nanocomplex. Nano-carriers of smaller size (< 200 nm) were found to be more effective in drug delivery because they are less likely to be captured by reticuloendothelial system than larger particles during systemic circulation [34]. Based on the result of size and yield, the nanocomplex from HA(CD)/4Phe4=2:1 was selected for the following studies.

The hydrophobic interior of the HA(CD)/4Phe4 nanocomplex provided the loading capacity for GA due to the hydrophobic interaction. The loading content (LC) and encapsulation efficiency (EE) for GA in the nanocomplex were 12.5% and 88.6%, respectively. The loading of GA did not impact the size (diameter = 184.16 ± 16.3 nm, PDI = 0.169 ± 0.042) and surface charge (-20.2 ± 2.8 mV) of the HA(CD)-4Phe4 nanocomplex, when compared to the blank counterpart.

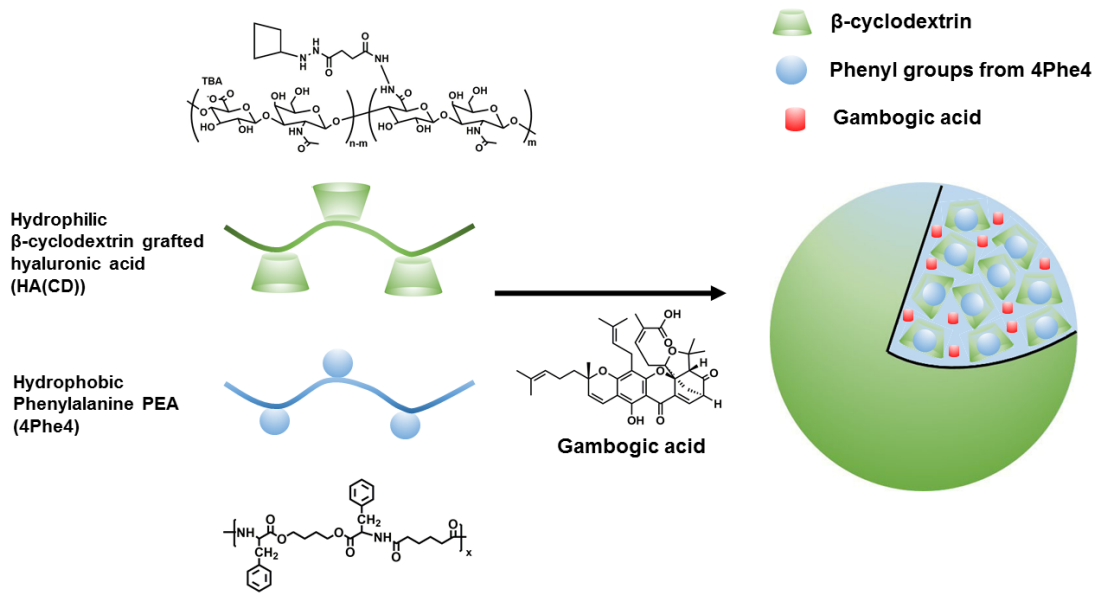


**Figure 5.3**. Chemical structures of β-cyclodextrin grafted HA (HA(CD)), phenylalanine based poly (ester amide)s (4Phe4), and gambogic acid (GA). HA(CD)-4Phe4 was formed from the inclusion complex between β-cyclodextrin moieties on HA(CD) and the phenyl groups from 4Phe4.

**Table 5.1**. Characterization of HA(CD)-4Phe4 nanocomplex with different HA(CD) to 4Phe4 ratios.

| HA(CD) to 4Phe4 / (w/w) in feed ratio | DLS diameter/nm | PDI | Zeta potential (mV) | Yield [a] |
|---|---|---|---|---|
| 1:2 | Precipitate [b] | NA | NA | NA |
| 1:1 | 732.63 ± 38.2 | 0.171 ± 0.061 | -26.23 ± 3.2 | 13.6% |
| 2:1 | 161.57 ± 11.2 | 0.176 ± 0.053 | -21.4 ± 1.7 | 65.1% |

| | | | | |
|---|---|---|---|---|
| 4:1 | 148.5 ± 21.2 | 0.181 ± 0.021 | -19.5 ± 2.7 | 27.5% |

a. Yield was calculated from the mass of purified nanocomplex divided by the total mass of HA(CD) and 4Phe4 in feed.

b. Formation of significant precipitate; the PDI, zeta potential and yield were non-detectable.

### *5.4.3 In vitro release of GA-loaded HA(CD)-4Phe4 nanocomplex*

The morphology of GA-loaded HA(CD)-4Phe4 nanocomplex was shown in Figure 5.4A. Spherical assembled structure was observed for GA-loaded HA(CD)-4Phe4 nanocomplex in aqueous dispersion. However, the assembled structure disappeared when a competing guest, 1-adamantane carbonyl acid (2 molar equivalent to cyclodextrin moieties), was added to the DMSO solution of HA(CD)-4Phe4 nanocomplex and dialyzed for 48 hrs. Significant precipitation was observed after dialysis, and no assembled structure was observed in the filtered solution, as suggested in Figure 5.4B. The replacement of phenyl groups from 4Phe4 with the competing guest lead to the dissociation of the nanocomplex, which further confirmed that the nanocomplex was formed form the host-guest inclusion complex between HA(CD) and 4Phe4.

After 48 hrs incubation with hyaluronidase, which is a specific enzyme that breaks down HA into oligosaccharide [35], the destabilization of the HA(CD)-4Phe4

nanocomplex was evidenced in Figure 5.4C, as no spherical assembled structure was observed.

The in vitro release profile of GA were shown in Figure 5.4D. At the end of 48 hrs, 61% cumulative GA was released in the presence of hyaluronidase (black curve), while only less than 20% cumulative release was detected in PBS (red curve). The release profiles of GA correlated directly with the morphological changes of HA(CD)-4Phe4 nanocomplex after incubation with hyaluronidase (Figure 5.4C), and the accelerated GA release can be attributed to the disintegration of the nanocomplex induced by enzymatic biodegradation.

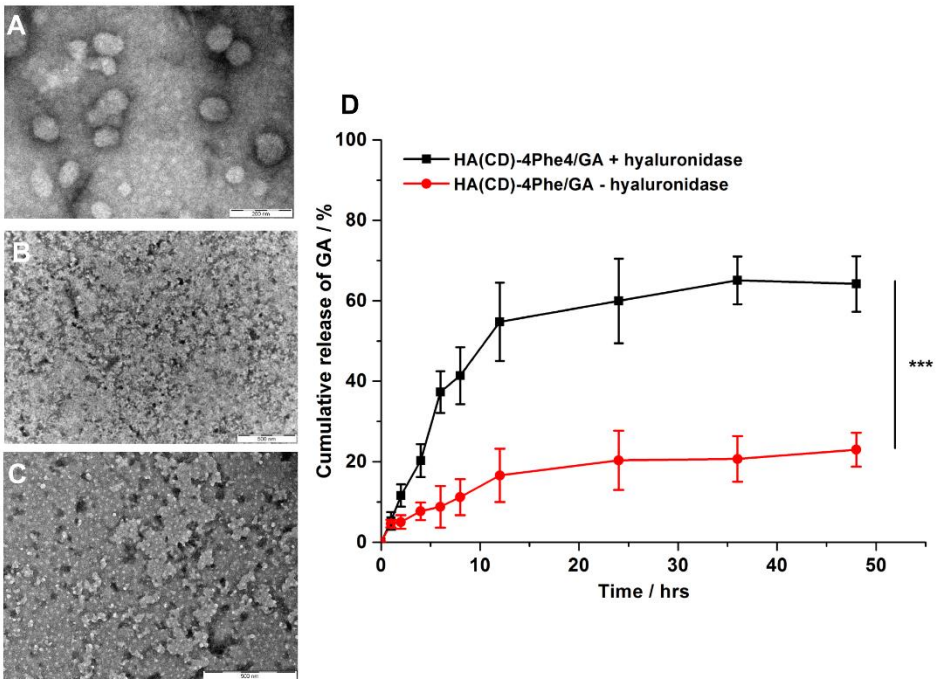


**Figure 5.4**. A) TEM image of GA-loaded HA(CD)-4Phe4 nanocomplex in aqueous dispersion (0.5 mg/mL). B) TEM image of GA-loaded HA(CD)-4Phe4 nanocomplex incubated with 1-adamantane carbonyl acid. C) TEM image of GA-loaded HA(CD)-

4Phe4 nanocomplex after 48 hrs incubation with 120 unit/mL hyaluronidase. D) Percentage of accumulated release of GA from HA(CD)-4Phe4 nanocomplex with or without the presence of 120 unit/mL hyaluronidase in phosphate buffer (pH = 7.4). Statistical significance: *** $p < 0.001$.

### *5.4.4 Endocytosis and subcellular distribution of blank HA(CD)-4Phe4 nanocomplex*

MDA-MB-435/MDR cell was selected as the in vitro model to study the endocytosis and subcellular distribution of the blank HA(CD)-4Phe4 nanocomplex, due to the overexpression of CD44 receptor [36]. 3T3 fibroblast, which is CD44 negative, was also included as the negative control. The endocytosis of the HA(CD)-4Phe4 nanocomplex as a function of time in both MDA-MB-435/MDR cell (CD44 positive) and 3T3 fibroblast (CD44 negative) were given in Figure 5.5. Significant difference in the intracellular level of the rhodamine-labelled nanocomplex between MDA-MB-435/MDR cells and 3T3 cells was observed throughout the 24 hrs incubation, as demonstrated in Figure 5.5B. HA(CD)-4Phe4 nanocomplex exhibited significantly enhanced endocytosis by CD44 overexpressed MDA-MB-435/MDR cells, and could be developed as the tumor-targeted delivery vehicles.

The subcellular distribution of the blank HA(CD)-4Phe4 nanocomplex after 4 hrs incubation was also studied and shown in Figure 5.5A. The red fluorescence from the rhodamine-labelled nanocomplex in 3T3 fibroblasts is weaker than in MDA-MB-435/MDR cells, which correlated well with the accumulated endocytosis results in Figure 5.5B. In MDA-MB-435/MDR cells, the red fluorescence of the rhodamine-

labelled HA(CD)-4Phe4 nanocomplex was identified to be co-localized with endolysosomes, as yellow pixels (combined from red nanocomplex with Lysotracker Green) were observed in the overlay images. The results suggested that HA(CD)-4Phe4 nanocomplex was entrapped inside endolysosomes which have a series of digestive enzymes to break down the nanocomplex and accelerate the release of GA, as indicated in Figure 5.4.

To identify the pathway for the entry of HA(CD)-4Phe4 nanocomplex into MDA-MB-435/MDR cells, inhibition study was performed and the results were shown in Figure 5.5C. The uptake of the HA(CD)-4Phe4 nanocomplex was decreased by 31% in MDA-MB-435/MDR cells pre-treated with anti-CD44 antibody, indicating that the entry of HA(CD)-4Phe4 nanocomplex was mediated by the CD44 receptor. Incubation of MDA-MB-435/MDR cells at 4 °C resulted in a reduction of 38% in the intracellular accumulation of the nanocomplex, indicating that the internalization of the nanocomplex is energy-dependent. Inhibition of clathrin-mediated pathway by chloropromazine resulted in 17% reduction in intracellular fluorescence, which suggested the endocytosis is also dependent on clathrin pathway. However, the inhibition of macropinocytosis, caveolae-mediated or lipid-raft mediated pathways by amiloride, nystatin or methyl-betaCD showed no significant reduction in the transmigration of HA(CD)-4Phe4 nanocomplex, which suggested that the internalization was independent of lipid raft, macropinocytosis or caveolae pathway. In general, the CD44-mediated endocytosis of the HA(CD)-4Phe4 nanocomplex in MDA-MB-435/MDR cells lead

to the selectivity between CD44 positive cells versus CD44 negative cells, which provide the rationale for the tumor-targeting delivery of GA.

Saxena et al. [28] reported the enhanced internalization rate of GA when loaded in Poloxamer 407/TPGS micelles compared to free GA. The internalization of free GA involved binding with transferrin receptor [37], and is less competent as the endocytosis of GA-loaded nano-delivery system. The HA(CD)-4Phe4 nanocomplex is expected to improve the intracellular availability of GA, and further impact its therapeutic efficiency.

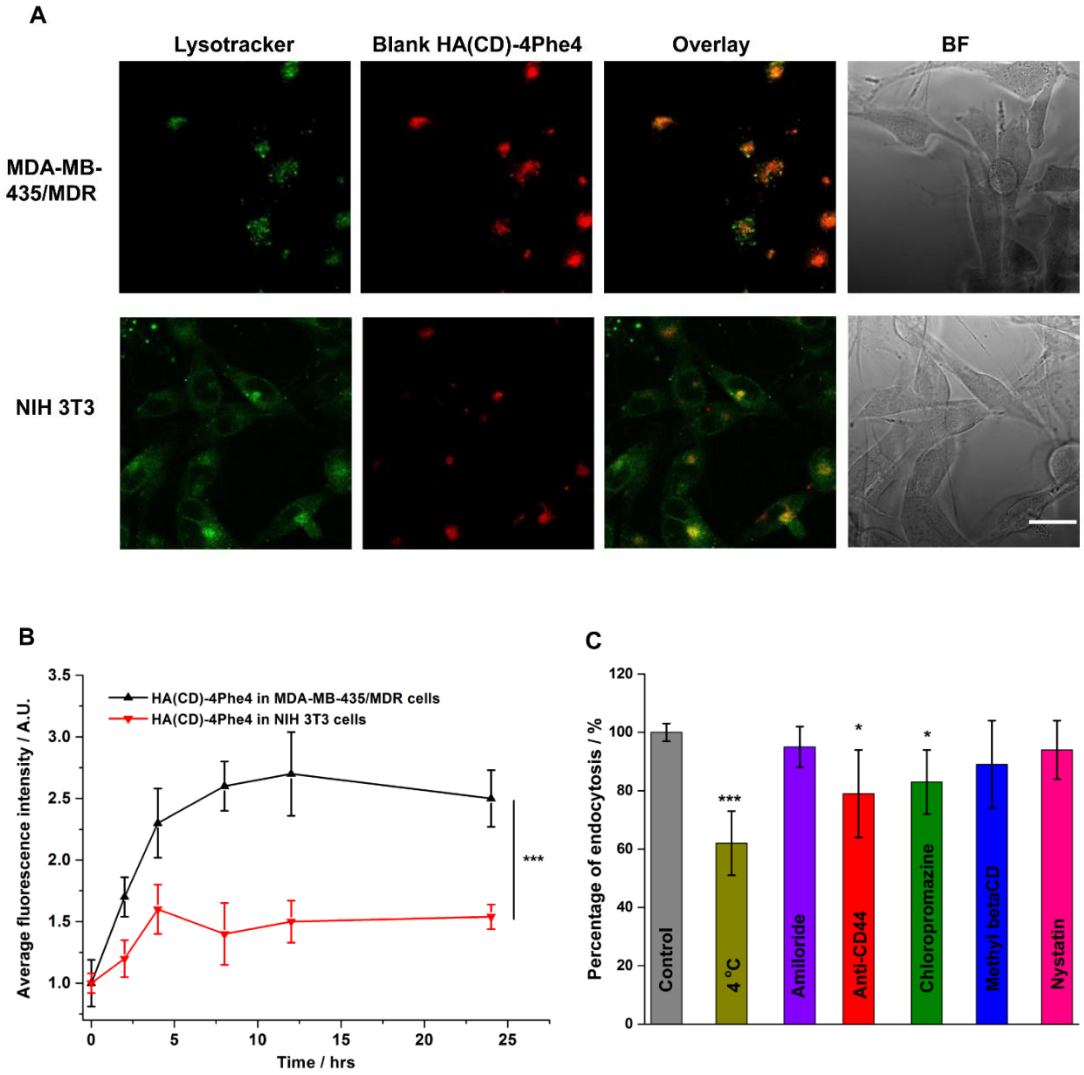

**Figure 5.5**. Endocytosis and subcellular distribution of blank HA(CD)-4Phe4 nanocomplex in MDA-MB-435/MDR cells (CD44 positive) or NIH 3T3 cells (CD44 negative). A) The confocal image of MDA-MB-435/MDR cells or NIH 3T3 fibroblasts incubated with blank HA(CD)-4Phe4 nanocomplex (0.1 mg/mL) for 4 hrs. Green (Lysotracker); red (rhodamine-labelled nanocomplex); the overlay of green and red pixels; and bright field (BF) image of the cells. Scale bar represented 20 μm. B) Accumulated endocytosis of blank HA(CD)-4Phe4 nanocomplex (0.1 mg/mL) in MDA-MB-435/MDR cells (CD44 positive) or NIH 3T3 cells (CD44 negative). The average cellular fluorescence from rhodamine-labelled nanocomplex was determined via flow cytometry. (n=3). Statistical significance: *** $p < 0.001$.

### *5.4.5 Cytotoxicity of GA-loaded HA(CD)-4Phe4 nanocomplex*

Cytotoxicity against MDA-MB-435/MDR cells after 24 hrs incubation with free GA, blank HA(CD)-4Phe4 and GA-loaded HA(CD)-4Phe4 nanocomplex was shown in Figure 5.6A. No significant cytotoxicity from the blank nanocomplex was observed at the concentration range from 1 to 100 μg/mL which correlated to equivalent GA concentration between 0.1 to 20 μM. Therefore, the cytotoxicity of GA-loaded HA(CD)-4Phe4 nanocomplex can be solely attributed to the loaded GA instead of the carrier.

Free GA and GA-loaded HA(CD)-4Phe4 nanocomplex exhibited concentration-dependent toxicity towards MDA-MB-435/MDR cells. Significantly higher toxicity from GA-loaded nanocomplex than free GA was detected at c(GA) =1 μM. However, GA-loaded nanocomplex exhibited similar cytotoxicity as free GA toward MDA-MB-

435/MDR cells at the rest of the tested GA concentrations. The $IC_{50}$ was calculated as 1.14 μM for GA-loaded nanocomplex, and 1.63 μM for free GA, respectively.

Cytotoxicity of free GA and GA-loaded HA(CD)-4Phe4 nanocomplex was also detected on MDA-MB-435/WT cells (without multidrug resistance) as shown in Figure 5.6B. After 24 hrs incubation, the $IC_{50}$ values of the wild type MDA-MB-435 cells were 0.45 μM for free GA and 0.37 μM for GA-loaded HA(CD)-4Phe4 nanocomplex. Comparing the $IC_{50}$ values between wild type vs. multidrug resistant phenotype, MDA-MB-435/MDR cells did not exhibit significant cross-resistance to GA treatment in the case of both free GA and GA-loaded HA(CD)-4Phe4 nanocomplex. As reported by Wang et al. [38], free GA showed good potency in the inhibition of docetaxel resistant BGC-823 gastric cancer cells, and could further reverse the drug resistance the presence of drug efflux pump on MDA-MB-435/MDR cells does not adversely affect the therapeutic performance of GA-loaded HA(CD)-4Phe4 nanocomplex, it may be the beneficial as a complementary treatment for multi-drug resistant tumors.

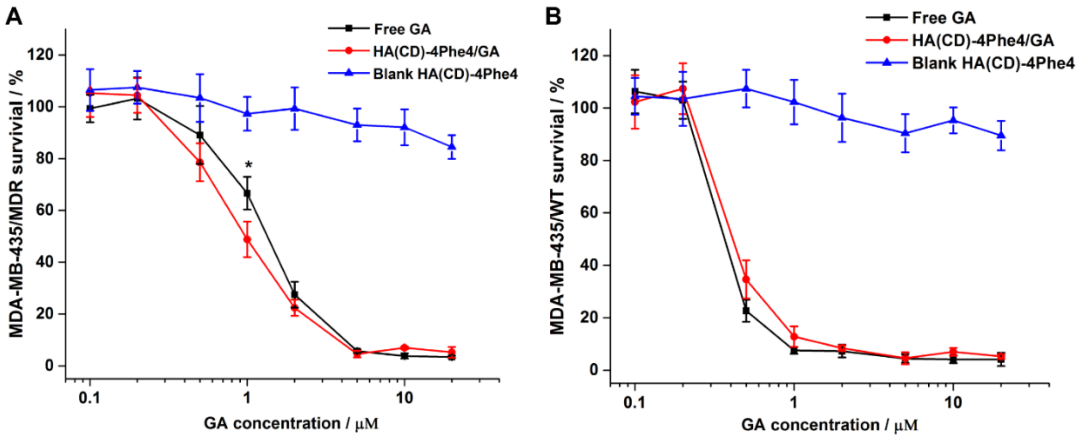

**Figure 5.6**. Viability of A) MDA-MB-435/MDR cells and B) MDA-MB-435/WT cells incubated with blank HA(CD)-4Phe4 nanocomplex, free GA or GA-loaded HA(CD)-4Phe4 nanocomplex with various GA concentrations for 24 hrs. Statistical significance was compared between free GA and GA-loaded nanocomplex treated groups: *, $p < 0.05$.

### *5.4.6 Mitochondrial depolarization*

The change in the mitochondrial membrane potential of MDA-MB-435/MDR cells was detected after treated by blank HA(CD)-4Phe4 nanocomplex, GA-loaded HA(CD)-4Phe4 nanocomplex or free GA (c(GA) = 1 μM) for 24 hrs. The percentage of cells with depolarized mitochondria can be identified as the population that stained with a higher level of green fluorescence (JC-1 monomer) and lower level of red fluorescence (J-aggregates), which is the population in quadrant 3 from flow cytometry results (Figure 5.7A). The quantitative results were also shown in Figure 5.7B.

In the case of blank HA(CD)-4Phe4 nanocomplex, only 3.91% of total cells were observed in quadrant 3 (with depolarized mitochondria), which was consistent with the untreated MDA-MB-435/MDR cells (i.e. 3.67% in quadrant 3). The result demonstrated the biosafety of the blank nanocomplex, which correlated directly with the low cytotoxicity of the blank HA(CD)-4Phe4 nanocomplex in Figure 5.6.

A significant loss of mitochondrial membrane potential was observed in MDA-MB-435/MDR cells treated by both free GA and GA-loaded HA(CD)-4Phe4 nanocomplex. At c(GA) =1 μM, GA-loaded HA(CD)-4Phe4 nanocomplex induced

greater level of mitochondrial depolarization, as 16.6% of cells were detected with depolarized mitochondria, compared to 10.3% of cells in quadrant 3 treated by free GA. The results suggested that the cytotoxicity induced by either free GA or GA-loaded HA(CD)-4Phe4 nanocomplex was related to mitochondria, and was also consistent with the study by Qiang et al. [39], in which 21% of Rat C6 glioma cells were detected with depolarized mitochondrial when treated by 1 μM free GA. The loss of mitochondrial membrane potential marks the dysfunction of mitochondria [40], and can be associated with the release of apoptogenic factors in the signaling of cell death. Further studies were performed to probe the cell death induced by GA-loaded HA(CD)-4Phe4 nanocomplex.

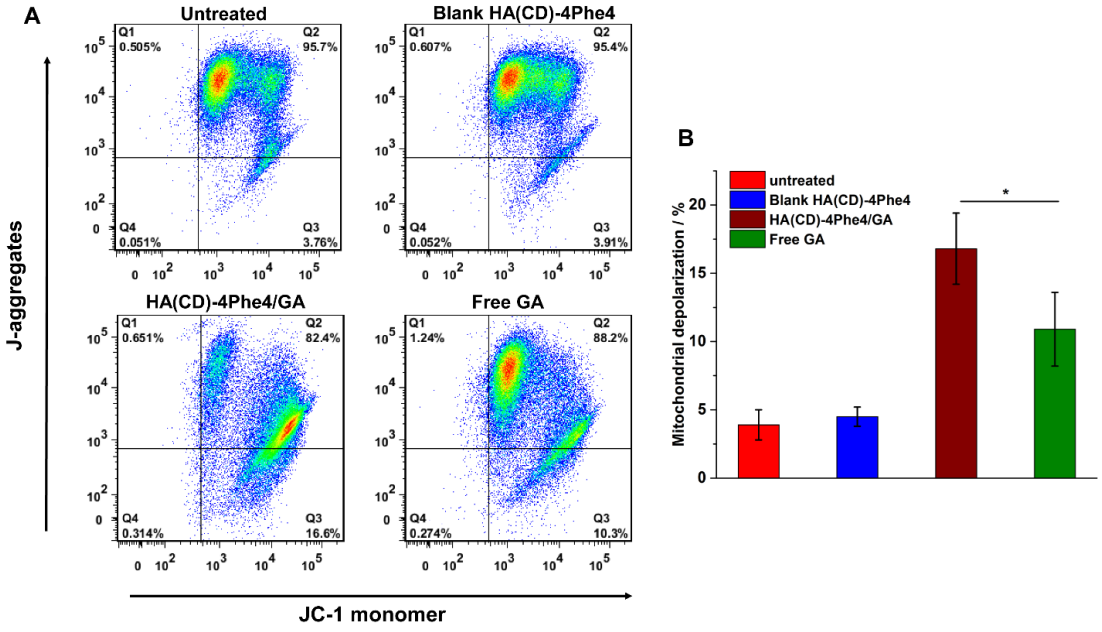


**Figure 5.7**. A) Mitochondrial membrane potential in MDA-MB-435/MDR cells incubated with blank HA(CD)-4Phe4 nanocomplex, free GA or GA-loaded HA(CD)-4Phe4 (c(GA) = 1 μM) for 24 hrs. B) The percentage of MDA-MB-435/MDR cells

with depolarized mitochondria (quadrant 3) in JC-1 assay were recorded. Statistical significance: *, $p < 0.05$.

### *5.4.7 Annexin-V and caspase 3/7 assay*

Flow cytometry results for the annexin V/PI assay were shown in Figures 5.8A and 5.8B. The percentages of cell population in each quadrant were obtained as: live cells ($PI^-$/annexin $V^-$, quadrant 4), dead cells ($PI^+$/annexin$^+$ and $PI^+$/annexin $V^-$, quadrant 1 and 2), and early apoptotic cells ($PI^-$/annexin $V^+$, quadrant 3). The blank HA(CD)-4Phe4 nanocomplex didn't induce significant cell death, as 81.5% of MDA-MB-435/MDR cells was alive. In both untreated group and blank nanocomplex treated group, minor cell population was detected as early apoptotic cells (6.73% and 6.76%, respectively). For MDA-MB-435/MDR cells treated by GA-loaded HA(CD)-4Phe4 nanocomplex (c(GA) = 1 μM), significantly higher population of dead cells was observed in quadrants 1 and 2, and only 51.0% of cells were identified as alive. The percentage of live cells treated by GA-loaded nanocomplex was also significantly lower than cells treated by free GA, in which 70.5% cells were detected alive. In addition, 33.2% of cells treated by GA-loaded HA(CD)-4Phe4 nanocomplex were subjected to early apoptosis, which was also significantly greater than cells treated by free GA (16.2%).

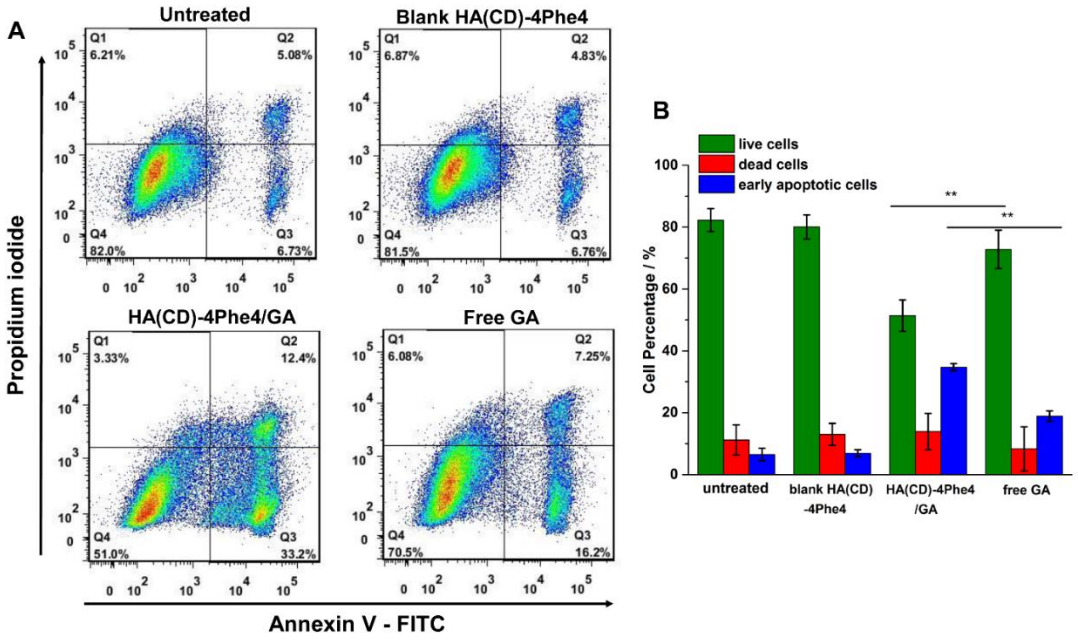


**Figure 5.8**. A) Annexin-V/PI staining of MDA-MB-435/MDR cells incubated with blank HA(CD)-4Phe4 nanocomplex, free GA or GA-loaded HA(CD)-4Phe4 nanocomplex (c(GA) = 1 μM) for 24 hrs. B) The percentage of live cells, early apoptotic cells and dead cells was recorded. Statistical significance: **, $p < 0.01$.

To further characterize apoptosis induced by GA-loaded nanocomplex, assay of caspase 3/7 activities were performed and the result was shown in Figure 5.9A. The activation of caspase marks the execution-phase of apoptosis, and subsequently result in the disassembly of cells. In MDA-MB-345/MDR cells treated by GA-loaded nanocomplex (c(GA) = 1 μM) for 24 hrs, significantly increased activities of caspase 3 and caspase 7 was observed, comparing to free GA. The detection of caspase activities was in line with the results from annexin V/PI assay in Figure 5.8A, which suggested that at relatively low GA concentration (1 μM), GA-loaded nanocomplex was more

potent in inducing apoptotic cell death to MDA-MB-435 melanoma cells, comparing to free GA.

Apoptotic death was reported in multiple cancer cells with drug resistance, such as doxorubicin resistant leukemia P388 cells [21], docetaxel-resistant gastric carcinoma BGC-823 cells [38], doxorubicin-resistant breast cancer cell line MCF-7/ADM [41], etc. In these researches, GA inhibited the growth of tumor cells which were resistant to common chemotherapeutics, and GA further provided the potential to reverse the chemo-resistance. GA-loaded HA(CD)-4Phe4 nanocomplex exhibited enhanced level of apoptosis and cytotoxicity in MDA-MB-435/MDR cells at lower concentration, which can be related to the effective endocytosis (Figure 5.5) and enzyme-accelerated release of GA (Figure 5.4). The GA-loaded nanocomplex could be developed as the complementary therapeutic treatment for tumor resistance.

### *5.4.8 Gelatin zymography*

Matrix metalloproteinases (MMPs) are a family of zinc-dependent endopeptidases that are involved in tumor invasion and metastasis. Due to the metastatic characteristics of MDA-MB-435 melanoma cells [42], it's of particular importance to address the impact of GA-loaded HA(CD)-4Phe4 nanocomplex on the MMP activities and further inhibiting the metastasis and invasion of tumor cells. Gelatin zymography was performed to examine the activities of MMP-2 and MMP-9 in MDA-MB-435/MDR cells treated by free GA or GA-loaded HA(CD)-4Phe4 nanocomplex (c(GA) = 1 μM).

As shown in Figure 5.9B, the zymography of either untreated cells or cells treated by the blank HA(CD)-4Phe4 nanocomplex showed broader bands digested by MMP, indicating a high level of MMP activity and that MDA-MB-435/MDR cells maintained strong tendency of metastasis. However, after being treated by free GA or GA-loaded HA(CD)-4Phe4 nanocomplex, smaller band area than the untreated control was observed, suggesting significantly suppressed MMP activities. No difference was observed between the free GA and GA-loaded HA(CD)-4Phe4 nanocomplex treated groups, and it can be concluded that the delivery of GA by HA(CD)-4Phe4 nanocomplex didn't hinder the pharmaceutical potency of GA in controlling tumor invasion.

In addition to exhibiting significant cytotoxicity, inducing mitochondrial depolarization and apoptotic cell death in MDA-MB-435/MDR melanoma cells, GA-loaded HA(CD)-4Phe4 nanocomplex also provide the potential to inhibit the invasion and metastasis of MDA-MB-435/MDR cells. As we demonstrated in vitro, the HA component of the HA(CD)-4Phe4 nano-carrier could introduce the tumor-targeting delivery property, which could further improve the therapeutic potency of this delivery system. To extend the current in vitro study to in vivo models, and further investigate the anti-tumor performance of GA-loaded HA(CD)-4Phe4 nanocomplex, would also be the focus of our future work.

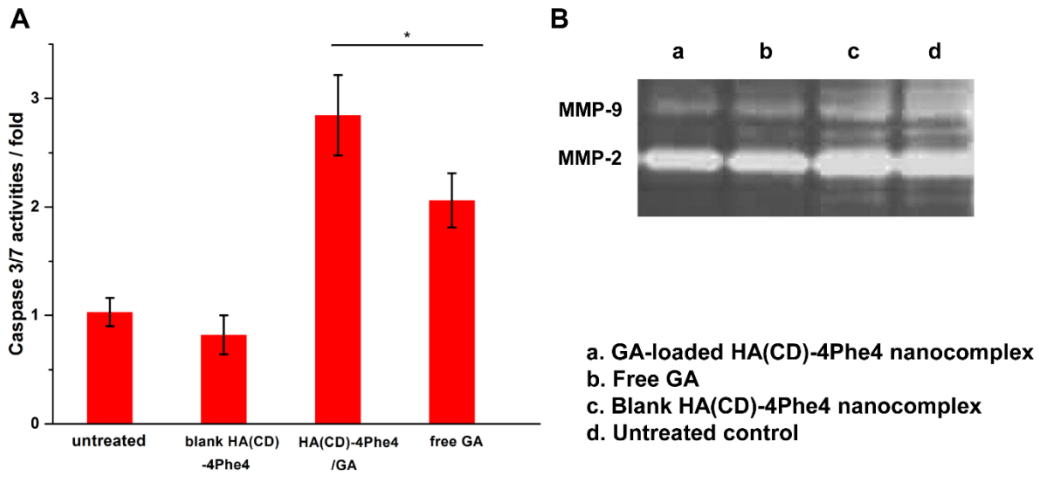


**Figure 5.9**. A) Caspase 3/7 activities of MDA-MB-435/MDR cells incubated with GA-loaded HA(CD)-4Phe4, free GA, or blank HA(CD)-4Phe4 nanocomplex for 24 hrs (c(GA) = 1 μM). Statistical significance: *, $p < 0.05$. B) Gelatin zymography of MDA-MB-435/MDR cells incubated with blank HA(CD)-4Phe4 nanocomplex, free GA or GA-loaded HA(CD)-4Phe4 (c(GA) = 1 μM) in serum-free media for 24 hrs. The area of bright band correlated to the activities of matrix metalloproteinases MMP-9 and MMP-2.

### *5.5 Conclusions*

In this study, biodegradable nano-delivery vehicles for GA was developed from the inclusion complex between cyclodextrin grafted HA and phenylalanine based pseudo protein. The 4Phe4 component provide hydrophobic interaction and loading capacity for GA, while the HA component of the nanocomplex targeted the overexpressed CD44 receptor on MDA-MB-435/MDR melanoma. The biodegradability of the HA(CD)-4Phe4 nanocomplex enabled an enzymatic-accelerated release of GA. The CD44-mediated internalization of GA-loaded

HA(CD)-4Phe4 nanocomplex significantly improved the selective endocytosis in the CD44 positive MDA-MB-435/MDR melanoma cells. Compared to free GA at 1 μM, GA-loaded HA(CD)-4Phe4 nanocomplex induced significantly enhanced mitochondrial depolarization and apoptotic cell death in MDA-MB-435/MDR cells, and effectively inhibited the MMP activity which is responsible for tumor metastasis. It is expected that the CD44-medicated tumor targeting from the HA component on the HA(CD)-4Phe4 nanocomplex could introduce more advantages in the in vivo performance in the future study Therefore, the HA(CD)-4Phe4 nanocomplex could hold a promising potential as the tumor-targeting delivery platform for gambogic acid or other hydrophobic drugs.

**Reference:**


[1] J. Zhang, P. X. Ma, *Adv. Drug Deliv. Rev.* **2013**, *65*, 1215.

[2] S. Li, W. C. Purdy, *Chem. Rev.* **1992**, *92*, 1457.

[3] J. Zhang, P. X. Ma, *Nano Today* **2010**, *5*, 337.

[4] A. Harada, M. Okada, J. Li, M. Kamachi, *Macromolecules* **1995**, *28*, 8406.

[5] H. Okumura, Y. Kawaguchi, A. Harada, *Macromolecules* **2001**, *34*, 6338.

[6] A. Harada, T. Nishiyama, Y. Kawaguchi, M. Okada, M. Kamachi, *Macromolecules* **1997**, *30*, 7115.

[7] J. Wang, M. Jiang, *J. Am. Chem. Soc.* **2006**, *128*, 3703.

[8] J. Zhang, P. X. Ma, *Polymer* **2011**, *52*, 4928.

[9] J. Zhang, K. Ellsworth, P. X. Ma, *J. Controlled Release* **2010**, *145*, 116.

[10] H. Fan, Q.-D. Hu, F.-J. Xu, W.-Q. Liang, G.-P. Tang, W.-T. Yang, *Biomaterials* **2012**, *33*, 1428.

[11] L. Schaefer, D. P. Reinhardt, *Adv. Drug Deliv. Rev.* **2016**, *97*, 1.

[12] K. Y. Choi, H. Chung, K. H. Min, H. Y. Yoon, K. Kim, J. H. Park, I. C. Kwon, S. Y. Jeong, *Biomaterials* **2010**, *31*, 106.

[13] F. Dosio, S. Arpicco, B. Stella, E. Fattal, *Adv. Drug Deliv. Rev.* **2016**, *97*, 204.

[14] G. Tripodo, A. Trapani, M. L. Torre, G. Giammona, G. Trapani, D. Mandracchia, *Eur. J. Pharm. Biopharm.* **2015**, *97*, 400.

[15] A. Kulkarni, R. VerHeul, K. DeFrees, C. J. Collins, R. A. Schuldt, A. Vlahu, D. H. Thompson, *Biomater. Sci.* **2013**, *1*, 1029.

[16] J. Wu, C.-C. Chu, *Acta Biomater.* **2012**, *8*, 4314.

[17] J. Wu, X. Zhao, D. Wu, C.-C. Chu, *J Mater Chem B* **2014**, *2*, 6660.

[18] D.-Q. Wu, J. Wu, C.-C. Chu, *Soft Matter* **2013**, *9*, 3965.

[19] C.-C. Chu, In *Biodegradable Polymers: New Biomaterial Advancement and Challenges*; Chu, C.-C., Ed.; Nova Science Publisher, 2015; Vol. 2.

[20] C.-C. Chu, In *Biomaterials – Principles and Practices*; Wong, J. Y.; Bronzino, J. D.; Peterson, D. R., Eds.; CRC Press, 2012.

[21] X. Li, S. Liu, H. Huang, N. Liu, C. Zhao, S. Liao, C. Yang, Y. Liu, C. Zhao, S. Li, X. Lu, C. Liu, L. Guan, K. Zhao, X. Shi, W. Song, P. Zhou, X. Dong, H. Guo, G. Wen, C. Zhang, L. Jiang, N. Ma, B. Li, S. Wang, H. Tan, X. Wang, Q. P. Dou, J. Liu, *Cell Rep.* **2013**, *3*, 211.

[22] Yan, *Oncol. Rep.* **2011**, *25*.

[23] R. Li, Y. Chen, L. Zeng, W. Shu, F. Zhao, L. Wen, Y. Liu, *Toxicology* **2009**, *262*, 98.

[24] X. Shi, X. Chen, X. Li, X. Lan, C. Zhao, S. Liu, H. Huang, N. Liu, S. Liao, W. Song, P. Zhou, S. Wang, L. Xu, X. Wang, Q. P. Dou, J. Liu, *Clin. Cancer Res.* **2014**, *20*, 151.

[25] N. Lu, Y. Yang, Q.-D. You, Y. Ling, Y. Gao, H.-Y. Gu, L. Zhao, X.-T. Wang, Q.-L. Guo, *Cancer Lett.* **2007**, *258*, 80.

[26] C. Wen, L. Huang, J. Chen, M. Lin, W. Li, B. Lu, Z. Rutnam, A. Iwamoto, Z. Wang, X. Yang, H. Liu, *Int. J. Oncol.* **2015**.

[27] Y. Chi, X. Zhan, H. Yu, G. Xie, Z. Wang, W. Xiao, Y. Wang, F. Xiong, J. Hu, L. Yang, C. Cui, J. Wang, *Chin. Med. J. (Engl.)* **2013**, *126*, 1642.

[28] M. D. Hussain, Saxena, *Int. J. Nanomedicine* **2012**, 713.

[29] Z.-H. Zhang, X.-P. Wang, W. Y. Ayman, W. L. L. Munyendo, H.-X. Lv, J.-P. Zhou, *Drug Deliv.* **2013**, *20*, 86.

[30] K. Guo, C. C. Chu, *J. Polym. Sci. Part Polym. Chem.* **2007**, *45*, 1595.

[31] I. Baussanne, H. Law, J. Defaye, J. M. Benito, C. O. Mellet, J. M. García Fernández, *Chem. Commun.* **2000**, 1489.

[32] M. He, L. Ro, J. Liu, C.-C. Chu, *J. Biomed. Mater. Res. A* **2016**.

[33] M. Toth, R. Fridman, In *Metastasis Research Protocols*; Humana Press: New Jersey, 2001; Vol. 57, pp. 163–174.

[34] S. A. Kulkarni, S.-S. Feng, *Pharm. Res.* **2013**, *30*, 2512.

[35] E . Menzel, C. Farr, *Cancer Lett.* **1998**, *131*, 3.

[36] X. Sun, P. Ma, X. Cao, L. Ning, Y. Tian, C. Ren, *Drug Deliv.* **2009**, *16*, 357.

[37] S. Kasibhatla, K. A. Jessen, S. Maliartchouk, J. Y. Wang, N. M. English, J. Drewe, L. Qiu, S. P. Archer, A. E. Ponce, N. Sirisoma, S. Jiang, H.-Z. Zhang, K. R. Gehlsen, S. X. Cai, D. R. Green, B. Tseng, *Proc. Natl. Acad. Sci.* **2005**, *102*, 12095.

[38] T. Wang, J. Wei, X. Qian, Y. Ding, L. Yu, B. Liu, *Cancer Lett.* **2008**, *262*, 214.

[39] L. Qiang, Y. Yang, Q.-D. You, Y.-J. Ma, L. Yang, F.-F. Nie, H.-Y. Gu, L. Zhao, N. Lu, Q. Qi, W. Liu, X.-T. Wang, Q.-L. Guo, *Biochem. Pharmacol.* **2008**, *75*, 1083.

[40] D. B. Zorov, M. Juhaszova, S. J. Sollott, *Biochim. Biophys. Acta BBA - Bioenerg.* **2006**, *1757*, 509.

[41] X. Wang, R. Deng, Y. Lu, Q. Xu, M. Yan, D. Ye, W. Chen, *Basic Clin. Pharmacol. Toxicol.* **2013**, *112*, 25.

[42] J. M. Rae, C. J. Creighton, J. M. Meck, B. R. Haddad, M. D. Johnson, *Breast Cancer Res. Treat.* **2007**, *104*, 13.

# CHAPTER 6

# LIGHT-FACILITATED DELIVERY OF OVALBUMIN WITH BIODEGRADABLE POLY(ESTER AMIDE)S NANOPARTICLES FOR MHC-I ANTIGEN PRESENTATION IN VITRO

### *6.1 Abstract*

The generation of CD8 T cells is crucial in the adaptive immunity against cancer and many infectious diseases. Vaccine aimed to stimulate CD8 T cell response typically became ineffective because the antigens are primarily subject to sequestration by endocytic compartment, instead of being delivered cytosolically for MHC-I processing and presentation to elicit CD8 T cell responses. In this study, a biodegradable nano-carrier for ovalbumin (OVA) was developed from arginine and phenylalanine based poly(ester amide)s, and formed electrostatic complex with photosensitizer AlPcS2a (Arg-Phe-PEA(AP) nanoparticles). The enzymatic biodegradability of the nano-carrier enabled enzyme-accelerated release of OVA, and significantly enhanced the internalization rate by dendritic cells, compared to free OVA. The photochemical interruption of endocytic compartments by the AlPcS2a in the Arg-Phe-PEA(AP) nanocarrier enabled the light-facilitated endosomal escape of the OVA-loaded nanoparticles into cytosol, and hence to facilitate the process of MHC-I presentation of CD8 T cell response. The MHC-I response by OVA-loaded Arg-Phe-PEA(AP) nanoparticles was dependent on the light dose, as well as the concentration of the photosensitizer. The proper dose of both photosensitizer and light was determined in vitro for optimized level of MHC-I response.

### *6.2 Introduction*

Cytotoxic T lymphocyte (CD8 T lymphocytes)-mediated immunity is believed to be critical for the full protection from diseases, such as HIV, malaria, and cancer [1].

Therefore, many research efforts have been directed to guide antigen into major histocompatibility complex (MHC)-I processing pathways of antigen presenting cells, which is critical for the generation of CD8 T cell responses. Dendritic cells, the most potent antigen presenting cells, endocytose, process, and load antigens onto MHC class I or II molecules for the presentation to naive CD8 or naive CD4 T cells, respectively. Cytosolic processing of exogenous antigen proteins such as vaccines can be achieved by MHC-I pathway, and further potentiate CD8 T cell response. The MHC-I presentation of vaccines [2] involves the endocytosis of the antigen, transmigration of the antigen into cytosol, degradation of the antigen in proteasome, the display of immune complex from the degraded antigenic peptide on the surface of antigen presenting cells, and the communication with CD8 T cells.

Several challenges are associated with the direct vaccination of free antigen [3], which include inherent instability of soluble antigens, low internalization efficiency of antigens, and the lack of manipulation over a phenotype of immune response, etc. Nanoparticle-based vaccine delivery system [4] has been developed for the hope to overcome these limitations by providing protection against premature degradation of antigen, and enabling targeted delivery and sustained release of payloads, effective interaction with antigen presenting cells, and multivalent presentation, etc. Poly (γ-glutamic acid) (PGA), N-trimethyl chitosan (TMC), poly(lactide-co-glycolide) (PLGA) are the most extensively studied polymers [5] as either nanogels or nano-micelles for the delivery of ovalbumin to dendritic cells and other immune cells.

It is reported [6–8] that antigens of conventional vaccines typically end up in the MHC-II pathway after being localized in phagosomes and lysosomes, and elicit CD4

T cell response instead of CD8 T cell response. For CD8 T cell-inducing vaccination, functionally intact antigen must be transported across barriers to reach intracellular sites of action. The sequestration of antigens in endocytic compartments can impede the cytosolic MHC-I processing and subsequent presentation [9].

Among the current strategies to overcome the endocytic sequestration of cargos, photochemical internalization (PCI), developed by Berg and colleagues [10], is a highly efficient technology which takes advantage of photochemical rupture of endocytic vesicles which enables the cytosolic release of therapeutic payloads. PCI-capable photosensitizers include a series of phthalocyanine and porphyrin derivatives which contain hydrophobic fused aromatic rings and hydrophilic sulfonate groups. The amphiphilic nature of PCI-capable photosensitizers exhibits specific affinity with the membrane of endocytic vesicles, where PCI-capable photosensitizers generate reactive oxygen species (ROS) upon a light irradiation [11], and are responsible for the oxidative rupture of endolysosomal membrane [12], followed by the subsequent release of cargos from endolysosomal compartment into cytosol. The most commonly studied PCI-capable photosensitizers include aluminum phthalocyanine disulfonate (AlPcS2a, excited at 660-670 nm light) [13] and the chemical structure of AlPcS2a is shown in Figure 6.1A. Other PCI-capable photosensitizers such as meso-tetraphenylporphine disulfonate (TPPS2a) and Amphinex were also studied, both of these two photosensitizers are excited at 435 nm light [14]. PCI-capable photosensitizers are non-toxic in the absence of light, and has been demonstrated to enhance the efficacy of various therapeutic agents, such as macromolecular chemotherapeutics, proteins, genes, etc, in more than 80 cell lines and animal models

[10]. Håkerud et al. [15] studied the intradermal delivery of free photosensitizer TPCS2a and ovalbumin to mice, and the PCI effect increased the stimulation of CD8 T-cell responses as measured by antigen-specific proliferation and secretion of pro-inflammatory cytokines. Additionally, photosensitizer (TPCS2a) was also reported to facilitate the cytosolic delivery of ovalbumin-loaded liposomes [16] or ovalbumin-loaded PLGA (poly(lactic-co-glycolic acid)) nanoparticles [17].

In the published studies of the PCI-facilitated vaccine delivery, photosensitizers and the antigens were administered separately, and there are no published studies that co-delivery both photosensitizers and OVA simultaneously. The discrepancy in their endocytosis rate by antigen presenting cells and circulation profiles in body fluid can impact the efficiency of PCI-facilitated vaccination. Therefore, it is of great importance to develop a complex system for the co-delivery of PCI-capable photosensitizers and antigen-loaded delivery vehicles simultaneously, and to elicit cytosolic delivery of antigens with subsequent MHC-I presentation and activation of CD8 T cell response. In this study, we proposed a co-delivery of both AlPcS2a photosensitizer and OVA simultaneously via a new amino acid-based synthetic biodegradable biomaterial.

Synthetic amino acid based poly (ester amide)s (AA-PEA) is a new family of biodegradable polymers synthesized from 3 building blocks: amino acids, dialcohol, diacids. AA-PEAs have been engineered into electrospun nanofibrous membranes, melt-spun fibers, microspheres, nanospheres, micelles, 3D microporous hydrogels and films for multiple biomedical applications, such as coating as drug eluting stents including the latest biodegradable magnesium

alloy-based [18–23], treatment of burn wounds [24], non-viral gene vectors [25–27], coating of sutures for reducing suture-induced inflammatory response [28], and delivery vehicles for mast cell stabilizers to treat diabetic retinopathy [29], and other synthetic or protein-based drugs [30,31]. The current status of AA-PEAs and their distance relative, amino acid-based poly(ester urea urethane) (AA-PEUU) have recently been reviewed [32–35].

Among the amino acids for AA-PEA synthesis, arginine (Arg) is the most unique as it can retain cationic charge over a wide range of pH due to its high pI value (10.76) of its pendant guanidine group. Arg-based PEAs are cationic at a physiological pH, suitable to form electrostatic complex with other negatively charged materials or payloads [36]. Chu et al. have demonstrated that Arg-based PEAs facilitated the penetration through cell membrane with an excellent cell biocompatibility, and worked as effective delivery systems for therapeutic agents including genes [37].

In this study, we aimed to develop a biodegradable cationic Arg-based poly(ester amide)s nano-carrier in complex with anionic PCI-photosensitizer, AlPcS2a, as the delivery vehicles for ovalbumin (OVA). As the most typically studied antigen, OVA can be cytosolically degraded into residues 257–264 (SIINFEKL) peptide, and presented with the murine Kb MHC-I molecule on the surface of dendritic cells to further potentiate CD8 T cell response. The Arg-based PEA nanoparticles f are expected to form an electrostatic complex with anionic AlPcS2a, and provides an efficient encapsulation of OVA which exhibits anionic charge in aqueous environment. The delivery performance of the Arg-based PEA nanoparticles was examined in

dendritic cells, and the light-facilitated rupture of endocytic compartments in dendritic cells was studied. The MHC-I presentation of OVA-loaded nanoparticles in dendritic cells was also validated in vitro.

### *6.3. Experimental*

#### *6.3.1 Chemicals and cells*

SIINFEKL peptide (OVA254-267), chlorophenol red-β-D-galactopyranoside (CPRG), fluorescein isothiocyanate (FITC), 4-nonylphenyl-polyethylene glycol (NP-40), methyl-β-cyclodextrin, α-chymotrypsin from bovine pancreas and QuantiPro BCA assay kit were from Sigma Aldrich (Milwaukee, WI). Aluminum phthalocyanine disulfonate (AlPcS2a) was from Frontier Scientific (Logan, UT). Ovalbumin (OVA) was from Hyglos GmbH (Regensburg, Germany). Lysotracker green DND and Hoechst 33342 were from Cell Signaling Technology (Beverly, MA). Nystatin, chloropromazine, amiloride hydrochloride were from Cayman Chemical (Ann Arbor, MI). Snakeskin dialysis tubing (MWCO = 10 kDa) were from Pierce (Rockford, IL). Fluorescein isothiocyanante labeled ovalbumin (FITC-OVA) was from Molecular Probes (Eugene, OR). The monomer Arg-4 (tetra-p-toluenesulfonic acid salt of bis-L-arginine butane-1, 4-diester), Phe-4 (tetra-p-toluenesulfonic acid salt of bis-L-phenylalanine butane-1, 4-diester) and NA (di-p-nitrophenyl adipate) were synthesized according to our previously studies [38,39].

DC2.4 cells were generously donated by Dr. Kenneth Rock (University of Massachusetts Medical Center) and were maintained in RPMI 1640 media supplemented with 10% fetal bovine serum, 2 mM glutamine, 10 mM MEM Non-

Essential Amino Acids, 0.055 mM 2-mercaptoethanol, 100 U/mL penicillin, 100 μg/mL streptomycin, and 10 mM HEPES buffer. B3Z T cell hybridoma were generously donated by Dr. John Frelinger (University of Rochester Medical Center) and were maintained in RPMI 1640 supplemented with 10% FBS, 2mM glutamine, 1 mM sodium pyruvate, 100 U/mL penicillin, 100 μg/mL streptomycin, 0.055 mM 2-mercaptoethanol and 10 mM HEPES buffer. Cells were incubated in water-jacketed incubator at 37 °C in 5% $CO_2$.

### *6.3.2 Synthesis of Arg-Phe-PEA polymer*

The amphiphilic copolymer, arginine (Arg) and phenylalanine (Phe) based poly(ester amide)s (Arg-Phe-PEA) were synthesized according to our prior published study [40]. Briefly, monomer NA (1.0 mmol), Arg-4 (0.5 mmol) and Phe-4 (0.5 mmol) in 1.5 mL of dry DMSO were mixed well by vortexing. The solution was heated to 70 °C with stirring to obtain a uniform mixture. Triethylamine (0.31 mL, 2.2 mmol) was added dropwise to the mixture at 70 °C under vigorous stirring until a complete dissolution of the monomers. The reaction vial was then kept for 24 hrs at 70 °C. The resulting polymer was precipitated in cold ethyl acetate, filtered, and purified by a Soxhlet extractor with ethyl acetate for 24 hrs. The purified Arg-Phe-PEA polymer was dried in vacuo at room temperature.

### *6.3.3 Preparation of OVA-loaded Arg-Phe-PEA(AP) nanoparticles*

*Preparation of Blank Arg-Phe-PEA nanoparticles*. Blank Arg-Phe-PEA nanoparticles were prepared via a single-step nanoprecipitation method as previously

described [40]. Briefly, the Arg-Phe-PEA polymer was dissolved in DMSO (20 mg/mL). The resulting Arg-Phe-PEA solution was then added into 1% poly(vinyl alcohol) (PVA) aqueous solution dropwise under stirring at room temperature. The residual organic solvent and free molecules were removed by repeated washing the nanoparticle solution with Amicon Ultra-4 centrifugal filter (MWCO=100 kDa).

*Preparation of OVA-loaded Arg-Phe-PEA nanoparticles.* To prepare ovalbumin (OVA) loaded Arg-Phe-PEA nanoparticles, the Arg-Phe-PEA polymer was dissolved in DMSO and mixed with the same volume of OVA solution in PBS on ice. The final concentration of Arg-Phe-PEA and OVA in the mixture was 20 mg/mL and 2 mg/mL, respectively. The mixture solution was added into 1% poly(vinyl alcohol) (PVA) aqueous solution dropwise under stirring on ice, and repeated washed with DI water in Amicon Ultra-4 centrifugal filter (MWCO=100 kDa). In addition, fluorescein labeled ovalbumin (FITIC-OVA) was also loaded in Arg-Phe-PEA nanoparticles in exactly the same procedure.

To determine the loading content (LC) and encapsulation efficiency (EE) of OVA in the Arg-Phe-PEA nanoparticles, the filtered solution which contained the un-encapsulated FITC-OVA was collected from the collector tube of the Amicon centrifugal filter. The fluorescence intensity was quantified ($\lambda$ex=488 nm, $\lambda$em=520 nm) on a PTI spectrofluorometer (Photon Technology International, South Brunswick, NJ), and calibrated against a standard curve of FITC-OVA.

*Preparation of Arg-Phe-PEA(AP) nanoparticles.* To prepare the electrostatic complex between anionic photosensitizer AlPcS2a and cationic OVA-loaded Arg-Phe-PEA nanoparticles (OVA-loaded Arg-Phe-PEA(AP)), an aqueous solution of OVA-

loaded Arg-Phe-PEA nanoparticles (10 mg/mL) was mixed with AlPcS2a in a final concentration of 10, 50 or 250 μg/mL. The mixture solution was stirred in dark at room temperature for 2 hrs and repeated washed with DI water in Amicon Ultra-4 centrifugal filter (MWCO=100 kDa) to remove free AlPcS2a. The concentration of AlPcS2a in the OVA-loaded nanoparticles was determined by inductively coupled plasma mass spectrometry (ICP-MS) according to the published procedure [41]. The complex of AlPcS2a and blank Arg-Phe-PEA nanoparticles was also prepared in the same method.

The morphology of the nanoparticles was observed on a FEI Tecnai Spirit T12 TEM (FEI Co., Hillsboro, OR) at an operating voltage of 120 kV. Zeta potential and size of the nanoparticles were characterized at room temperature on a Zetasizer NanoZS system (Malvern, UK).

### *6.3.4 Relative oxygen concentration in blank Arg-Phe-PEA(AP) solutions with irradiation*

To probe the oxygen consumption rate, the relative concentration of oxygen was determined as a function of irradiation time in aqueous solution of blank Arg-Phe-PEA(AP) nanoparticles. Clark-type oxygen electrode (Hansatech Instruments Ltd, UK) was used as previously described [42] to directly measure the partial pressure of oxygen, was inserted into the PBS solution of free AlPcS2a or blank Arg-Phe-PEA(AP) nanoparticles with an equivalent AlPcS2a concentration. 10% FBS was also present in each testing condition as the receptor for reactive oxygen species. Irradiation by LED arrays (660 nm, 25 mW/cm$^2$, Elixa Ltd, Albuquerque, NM) was used for all the

following test including in vitro cell work. Before each measurement, the system was calibrated in PBS bubbled with air. Relative oxygen concentration was acquired by normalizing the measured partial pressure of oxygen in each sample to that of untreated PBS bubbled with air, and the results were plotted as a function of irradiation time. Relative oxygen concentration correlated with the oxygen consumption, and further reflected the efficiency of ROS generation. Relative oxygen concentration of non-irradiated solution of free AlPcS2a or blank Arg-Phe-PEA(AP) were also tested as the controls.

### *6.3.5 In vitro release of OVA from Arg-Phe-PEA(AP) nanoparticles*

In vitro release profiles of OVA from the Arg-Phe-PEA(AP) nanoparticles were examined in 10 mM phosphate buffer (pH 7.4) with or without the presence of α-chymotrypsin (0.2 mg/mL). The release profiles were determined according to the previously published studies by Lee et al. [43]. FITC-OVA loaded Arg-Phe-PEA nanoparticles (1 mg/mL) were dispersed in PBS containing 0.02% sodium azide and 0.2 mg/mL α-chymotrypsin. The suspension was then aliquoted to 1 mL/microfuge tube, and the microfuge tubes were kept at 37 °C. At 1, 2, 4, 8, 12, 24, 48 hrs, the microfuge tubes were centrifuged at 15,000 rcf for 10 min, and the supernatants were filtered through 0.22 μm syringe filter. The concentration of the released FITC-OVA in the supernatants was determined by a spectrofluorometer (λex=488 nm, λem=520 nm) and calibrated against a standard curve of FITC-OVA. In the case of OVA release upon light irradiation treatment (at 660 nm, 1.5 J/cm$^2$, 1 min), the release data were collected right after irradiation. Except the light irradiation treatment, the rest of the

experiments were performed in dark to minimize the photo-bleaching of the fluorophore. The percentages of the released FITC-OVA were plotted vs. time. Each test was performed in triplicate.

### *6.3.6 Endocytosis of blank Arg-Phe-PEA(AP) nanoparticles*

*Endocytosis inhibition assay.* DC2.4 cells were seeded in a 6-well plate (1 x $10^6$ cells per well) and pre-incubated for 4 hrs. The cells were treated with inhibitors that block different endocytic pathways [44,45] (nystatin, 50 μg/mL; chloropromazine, 30 μM; amiloride hydrochloride, 50 μM; methyl-β-cyclodextrin, 3 mg/mL) for 0.5 hr before blank Arg-Phe-PEA (AP) nanoparticles were added and incubated for another 4 hrs. The cells were then washed with PBS, harvested and subjected to flow cytometry assay on FACSAria fusion fluorescence activated cell sorter (BD Biosciences, Franklin Lakes, NJ). The effect of low temperature (4°C) on endocytosis was also studied. Cells incubated with Arg-Phe-PEA(AP) nanoparticles at 37°C but not treated with any inhibitor were tested as the control. The mean fluorescence intensity for each sample was recorded on a FACSAria fusion fluorescence activated cell sorter (BD Biosciences, Franklin Lakes, NJ) and normalized to control. The tests were performed in triplicate.

*Accumulated endocytosis study*. To monitor the accumulated endocytosis of the blank Arg-Phe-PEA(AP) nanoparticles as a function of time, DC2.4 cells were seeded at 1 x $10^6$ cells per well in a 6-well plate and pre-incubated for 4 hrs. DC2.4 cells were then incubated with blank Arg-Phe-PEA(AP) nanoparticles or free AlPcS2a with an equivalent concentration for 1, 2, 4, 8, 12, 24hrs. The cells were washed and harvested,

and the mean cellular fluorescence intensity was then examined by flow cytometry. Each test was run in 3 replicates.

### *6.3.7 Light-facilitated cytosolic delivery of blank Arg-Phe-PEA(AP) nanoparticles*

DC2.4 cells were seeded in a 35 mm glass-bottomed-dish (1 x $10^6$ cells/well, MaTek, Ashland, MA) and incubated for 4 hrs. Blank Arg-Phe-PEA(AP) nanoparticles were added and incubated for 4 hrs. The cells were washed and labeled with Lysotracker green (50 nM) as per manufacturer's instruction, and imaged alive by confocal microscopy (Zeiss LSM710, Carl Zeiss MicroImaging, Thornwood, NY). Light irradiation was then applied by LED arrays (120 arrays, 25 mW/cm$^2$, Elixa Ltd, Albuquerque, NM) at 660 nm with light dosages of 0.5, 1.5 or 3 J/cm$^2$. The Pearson's coefficient for co-localization between Arg-Phe-PEA(AP) nanoparticles and Lysotracker before and after irradiation was determined with Fiji software (National Institutes of Health), 30 images were analyzed for each group.

### *6.3.8 Endocytosis of OVA loaded in Arg-Phe-PEA(AP) nanoparticles*

DC2.4 cells were seeded at 1 x $10^6$ cells per well in a 6-well plate and pre-incubated for 4 hrs. DC2.4 cells were then incubated with FITC-OVA-loaded Arg-Phe-PEA(AP) nanoparticles or free FITC-OVA with an equivalent OVA concentration of 5 μg/mL for 4 hrs. The cells were washed and light irradiation was applied at 660 nm by LED arrays (1.5 J/cm$^2$). The cells were further incubated for another 4 hrs and then harvested, and the mean cellular fluorescence intensity was then examined by flow cytometry. Each test was run in 3 replicates.

### *6.3.9 Cytotoxicity of OVA-loaded Arg-Phe-PEA(AP) nanoparticles*

DC2.4 cells were seeded at $1x10^4$ cells per well in a 96-well plate and pre-incubated for 4 hrs. The cells were incubated with the OVA-loaded Arg-Phe-PEA(AP) nanoparticles with various concentrations of AlPcS2a, free OVA or blank Arg-Phe-PEA nanoparticles 4 hrs. The cells were washed and incubated for another 20 hrs before light irradiation was applied at 660 nm by LED arrays (0.5. 1.5 or 3 J/cm$^2$). The viability of DC2.4 cells was determined 24 hrs post irradiation with MTT assay. The absorbance at 570 nm was recorded and normalized to the results of the untreated cell control to give the percentage of cell survival. Cells incubated the above treatments but without light irradiation was also determined. Each experiment was run in six replicates.

### *6.3.10 In vitro MHC-I cross presentation*

DC 2.4 dendritic cells were seeded at $4 \times 10^4$ /well in round-bottomed 96-well plates and incubated for 4 hrs until cells were completely anchored. Free OVA, OVA-loaded Arg-Phe-PEA(AP) nanoparticles with different concentrations of AlPcS2a were incubated with DC2.4 cells with an equivalent concentration of ovalbumin at 5 μg/mL. DC2.4 cells were then washed with PBS twice, chased for another 20 hrs, before light irradiation was applied at 660 nm for 0.5, 1.5 or 3 J/cm$^2$. B3Z cells were then added at $1 \times 10^5$ /well and co-cultured for 16 hrs [46]. For the positive control, SIINFEKL peptide (1 nM) was added simultaneously with B3Z cells. The medium was then replaced by 100 μL of CPRG lysis buffer (0.15 mM CPRG, 0.5% NP-40 in

PBS). The plates were kept in dark at room temperature for 72 hrs, and the absorbance at 570 nm was read on a Synergy HT microplate reader (BioTek, Winooski, VT).

### *6.3.11 Statistical analysis*

The data are presented as mean values with standard deviations (SD). All data were analyzed using one-way ANOVA, followed by Tukey's multiple comparison tests, and $p < 0.05$ was used for statistical significance.

## *6.4. Results and discussions*

### *6.4.1 Characterization of OVA-loaded Arg-Phe-PEA(AP) nanoparticles*

The synthesis of arginine(Arg) and phenylalanine (Phe) based poly(ester amide)s (Arg-Phe-PEA) was based on our prior published studies [40], and the ratio between Arg and Phe moieties in the polymers was 1:1, as shown in Figure 6.1A. The average molecular weight of the Arg-Phe-PEA polymer was detected as $1.93 \times 10^4$ Da, with a PDI of 1.27. The Arg-Phe-PEA polymer was reported [40] to form self-assembled structure in aqueous solution due to the hydrophilicity of Arg moieties that stayed on the outer layer of the nano-assembly, and the hydrophobicity of Phe moieties that stayed in the interior of the nano-assembly. Cationic charge was detected on blank Arg-Phe-PEA nanoparticles in aqueous solution, as shown in Table 6.1. The zeta-potential for blank Arg-Phe-PEA nanoparticles was 26.2 ± 3.1 mV, with an average dimeter of 170.2 ± 8.9 nm.

The hydrophobic interior provided loading capacity for the relatively less hydrophilic protein such as bovine serum albumin (BSA) [40] and ovalbumin (OVA)

[47], and the scheme for the formation of OVA-loaded Arg-Phe-PEA nanoparticles was also shown in Figure 6.1A. The characterization of OVA-loaded nanoparticles was listed in Table 6.1 and Figure 6.2. Spherical structure was observed for OVA-loaded Arg-Phe-PEA nanoparticles was observed in aqueous dispersion. A slightly increased diameter was detected as 210.4 ± 9.2 nm compared to the blank nanoparticles, and the zeta-potential of the OVA-loaded Arg-Phe-PEA nanoparticles was 15.6 ± 6.5 mV. The loading content (LC) and encapsulation efficiency of OVA in Arg-Phe-PEA nanoparticles was detected as 6.2 % and 67.5% respectively. The Arg-Phe-PEA nanoparticles provided effective loading of OVA, and the loading efficiency was comparable to that of PLGA nanoparticles (45% to 70%) [47–49], which was extensively investigated as the delivery carriers for OVA-based vaccine.

The cationic charge on the surface of OVA-loaded Arg-Phe-PEA nanoparticles provided capability to form electrostatic complex with other anionic molecules. The two adjacent sulfonate groups on the photosensitizer AlPcS2a rendered it anionic charge in aqueous solution. And by mixing the cationic OVA-loaded nanoparticles and AlPcS2a, the electrostatic complex was formed and denoted as OVA-loaded Arg-Phe-PEA(AP) nanoparticles. As shown in Figure 6.2, spherical structure was maintained in OVA-loaded Arg-Phe-PEA(AP) nanoparticles and we further studied the effect of the AlPcS2a concentration in feed on the size and zeta-potential of the complex structure. With the concentration of OVA-loaded Arg-Phe-PEA (10 mg/mL) and AlPcS2a (50 μg/mL) in feed, the resulting nanoparticles was denoted as OVA-loaded Arg-Phe-PEA (AP 0.5), and we also studied the nanoparticles with higher ratio of AlPcS2a (OVA-loaded Arg-Phe-PEA (AP 2.5)), as well as the ones with lower ratio

of AlPcS2a (OVA-loaded Arg-Phe-PEA (AP 0.1)). As indicated in Table 6.1, the formation of electrostatic complex with AlPcS2a resulted in a decrease on the zeta-potential of the nanoparticles, and OVA-loaded Arg-Phe-PEA(AP) exhibited a slightly cationic charge (4.3 to 6.3 mV) with various concentration of AlPcS2a, compared to 15.6 mV for the nanoparticles with the absence of AlPcS2a. The AlPcS2a content in the nanoparticles didn't introduce significant change in the diameter, as the nanoparticles exhibited DLS diameter ranging from 201.5 nm to 235. 2 nm.

To induce effective photochemical rupture of endolysosomes, AlPcS2a should be localized specifically in the lipid bilayer in the endolysosomes [50], instead of other subcellular compartments. The binding of AlPcS2a on the surface of the nanoparticles enabled the close contact between AlPcS2a and endolysosomal membrane. The scheme for photosensitizer induced cytosolic delivery of OVA, as well as the subsequent MHC-I processing and presentation, were illustrated in Figure 6.1B.

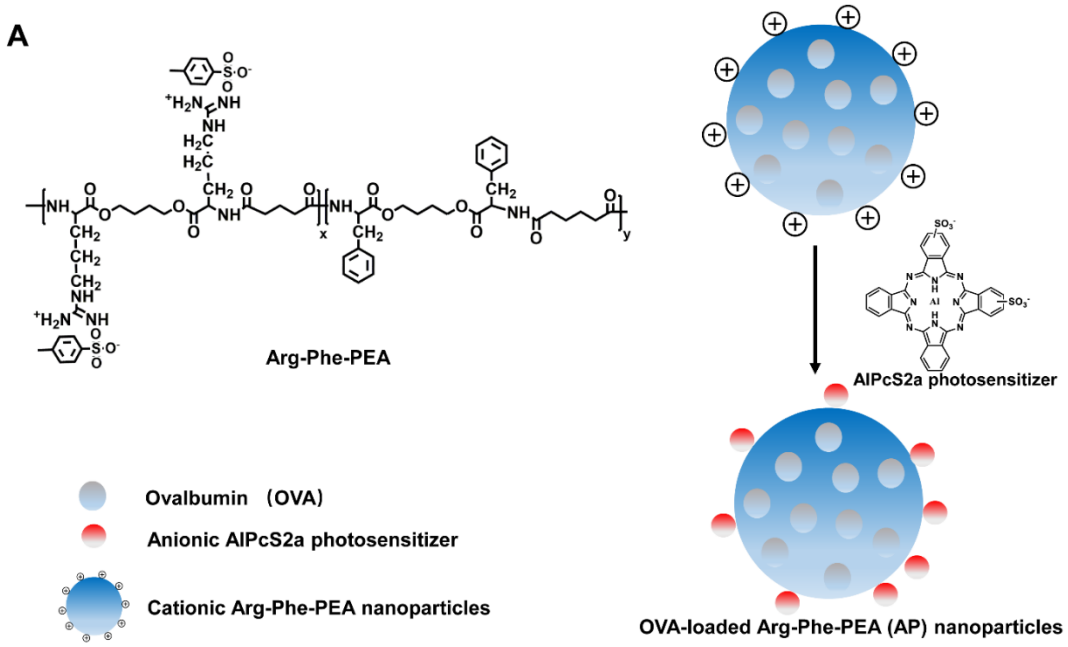

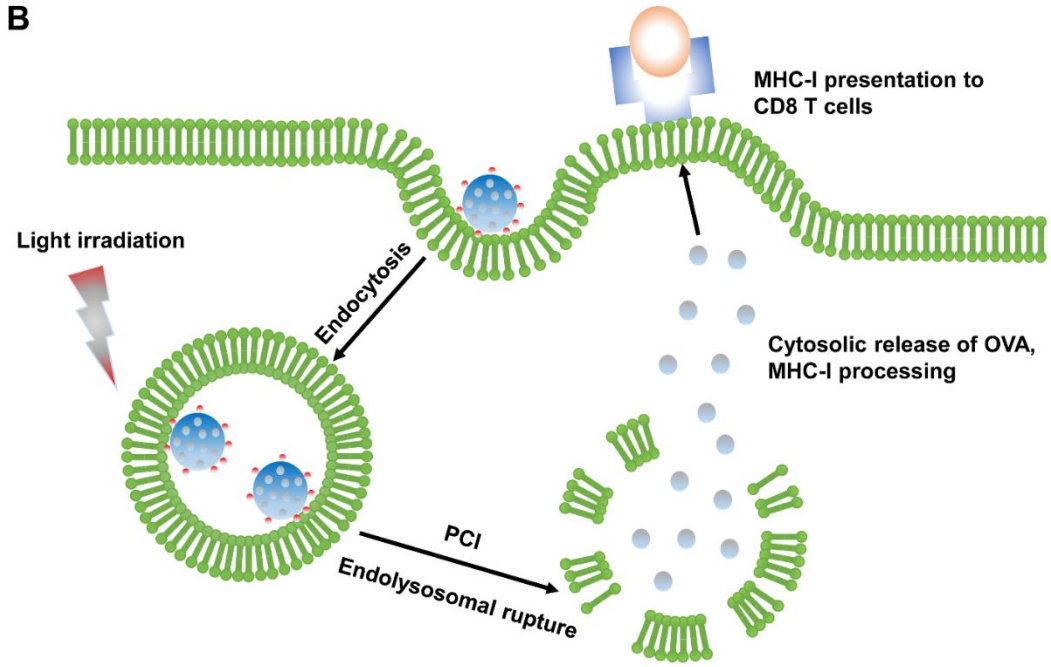


**Figure 6.1**. A) Chemical structure of Arg-Phe-PEA polymers. The scheme for the formation of OVA-loaded Arg-Phe-PEA nanoparticles, and the electrostatic complex between anionic photosensitizer AlPcS2a with cationic OVA-loaded Arg-Phe-PEA nanoparticles (OVA-loaded Arg-Phe-PEA(AP)). B) Illustration of the light-facilitated cytosolic delivery of OVA by Arg-Phe-PEA(AP) nanoparticles in dendritic cells, and the subsequent MHC-I presentation to CD8 T cells.

**Table 6.1**. Characterization of OVA-loaded Arg-Phe-PEA(AP) nanoparticles.

| | DLS diameter/ | Zeta potential | LC (OVA) | EE (OVA) | Content of AlPcS2a / |
|---|---|---|---|---|---|

| | nm | /mV | /% | /% | wt% |
|---|---|---|---|---|---|
| Blank Arg-Phe-PEA | 170.2 ± 8.9 | 26.2 ± 3.1 | NA | NA | NA |
| OVA-loaded Arg-Phe-PEA | 210.4 ± 9.2 | 15.6 ± 6.5 | | | NA |
| OVA-loaded Arg-Phe-PEA (AP 0.1) | 201.5 ± 11.2 | 6.3 ± 1.2 | 6.2 % | 67.5% | 0.15 % |
| OVA-loaded Arg-Phe-PEA (AP 0.5) | 228.7 ± 7.5 | 4.3 ± 1.4 | | | 0.36 % |
| OVA-loaded Arg-Phe-PEA (AP 2.5) | 235.2 ± 11.2 | 5.1 ± 2.2 | | | 1.9 % |

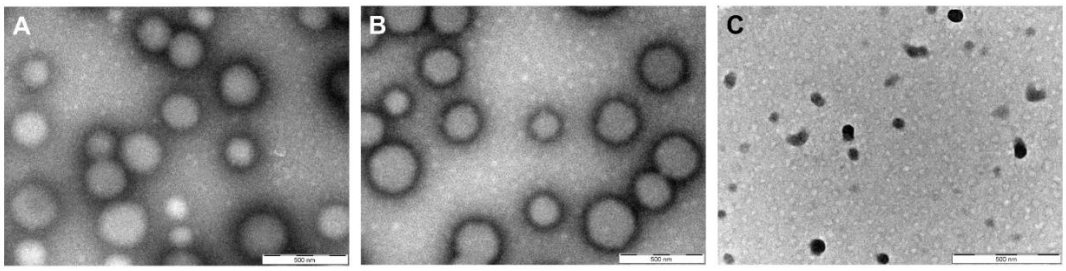


**Figure 6.2**. TEM images of A) OVA-loaded Arg-Phe-PEA nanoparticles in PBS. B) OVA-loaded Arg-Phe-PEA(AP) nanoparticles in PBS. C) OVA-loaded Arg-Phe-PEA(AP) nanoparticles after 48 hrs incubation with α-chymotrypsin (0.2 mg/mL).

### *6.4.2 Relative oxygen concentration in blank Arg-Phe-PEA(AP) solution with irradiation*

As the photosensitizing effect of AlPcS2a involves the photo-induced generation of free radical, and further interact with oxygen molecules to form reactive oxygen species (ROS). The relative oxygen concentration correlates with the consumption of oxygen, which reflected the efficiency of ROS generation by Arg-Phe-PEA nanoparticles. As shown in Figure 6.3A, significantly reduced relative oxygen concentration was observed when light irradiation was applied to the Arg-Phe-PEA(AP) nanoparticles, when comparing to the counterpart in dark. The relative oxygen concentration treated by Arg-Phe-PEA(AP) nanoparticles decreased with irradiation time, which was 0.97 (with light dose of 0.5 J/cm$^2$), 0.91 (1.5 J/cm$^2$), and 0.77 (3 J/cm$^2$), respectively. In addition, relative oxygen concentration profile for Arg-Phe-PEA(AP) nanoparticles was almost identical to that of free AlPcS2a, especially at the first 180 sec of irradiation at 660 nm (25 mW/cm$^2$). The results suggested that AlPcS2a-loaded Arg-Phe-PEA(AP) nanoparticles was as competent as free AlPcS2a in ROS generation, and could provide an equivalent potential to initiate PCI.

### *6.4.3 In vitro release of OVA from Arg-Phe-PEA(AP) nanoparticles*

The lack of effective intracellular trigger [51] for the release of loaded antigen can be a challenge that reduced the delivery efficiency. Due to the enzymatic biodegradability of the Arg-Phe-PEA(AP) carriers [40], the release of OVA could be accelerated by enzymatic degradation. And we further investigated the release profile of OVA from nanoparticles incubated with α-

chymotrypsin, an enzyme which preferentially attacks the hydrophobic amino acids such as phenylalanine, and cleaves the amide bonds. The release profile of OVA was shown in Figure 6.3B. In the testing groups without light irradiation, at the end of 48 hrs, 65% cumulative OVA was released from Arg-Phe-PEA(AP) in the presence of α-chymotrypsin (red curve), while only 23 % cumulative was achieved without any enzyme (black curve), indicating that OVA release was effectively accelerated by enzymatic degradation of the carrier. The results correlated well with the TEM morphology of OVA-loaded Arg-Phe-PEA nanoparticles in Figure 6.2B and 6.2C, in which the spherical nano-structure disappeared after 48 hrs incubation with α-chymotrypsin.

When light irradiation was applied at 660 nm (25 mW/cm$^2$, 1.5 J/cm$^2$, 1 min) right before the release test, the release of OVA from the light-irradiated Arg-Phe-PEA(AP) nanoparticles didn't exhibit any significant difference from the corresponding groups in dark. For example, without the presence of α-chymotrypsin, 22% of total OVA was released from Arg-Phe-PEA(AP) in dark (black curve), vs. 18% released from Arg-Phe-PEA(AP) with 1.5 J/cm$^2$ irradiation, which exhibited no significant difference between irradiated vs. non-irradiation group. In addition, 60% of OVA was released from Arg-Phe-PEA(AP) nanoparticles when 1.5 J/cm$^2$ irradiation was applied (green curve), which exhibited no difference from the OVA released from Arg-Phe-PEA(AP) in dark (red cure). The resulted suggested that 1.5 J/cm$^2$ irradiation didn't impact the release of OVA, and enzymatic biodegradation played a key role in the accelerated OVA release profile observed in Figure 6.3B.

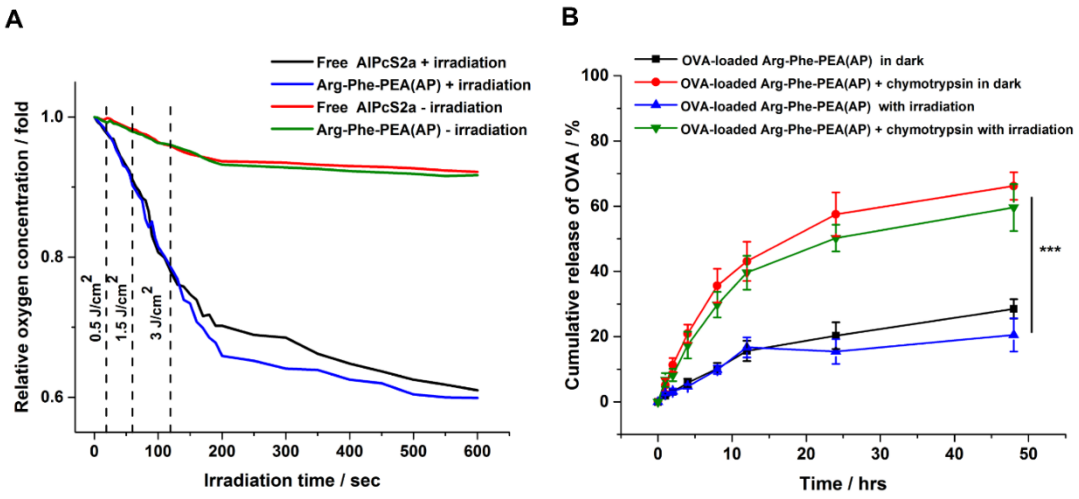


**Figure 6.3**. A) Relative oxygen concentration vs. irradiation time for Arg-Phe-PEA(AP) nanocomplex or free AlPcS2a in PBS containing 10% FBS under irradiation (660 nm, 25 mW/cm$^2$), the relative oxygen concentration was obtained by normalizing the oxygen partial pressure of samples to that of untreated PBS, probed by Clark-type micro electrode. Irradiation time that resulted in light dosages of 0.5, 1.5 or 3 J/cm$^2$ were marked as dotted lines on the time scale. B) In vitro release profile of FITC-OVA from the Arg-Phe-PEA(AP) nanoparticles in PBS with or without the presence of α-chymotrypsin (0.2 mg/mL). In the case of OVA release with light irradiation, irradiation at 660 nm (1.5 J/cm$^2$) was applied for 1 min, and the release profile was collected right after irradiation. Except when light irradiation was applied, the rest of the experiments were performed in dark. Values represent the average ± SD (n=3). Statistical significance: ***, $p < 0.001$.

### *6.4.4 Endocytosis of blank Arg-Phe-PEA(AP) nanoparticles*

Inhibition study was performed to explore the endocytosis pathway of blank Arg-Phe-PEA(AP) nanoparticles, and the data was shown in Figure 6.4A. Incubation of DC2.4 cells with Arg-Phe-PEA(AP) nanoparticles at 4 °C for 4 hrs resulted in a 43% decrease in the intracellular fluorescence. Similarly, inhibition of macropinocytosis (by amiloride) and the clathrin-mediated pathway (by chloropromazine) also resulted in a significant inhibition of transmigration of the nanoparticles. On the other hand, inhibition of caveolae (by nystatin) and lipid raft mediated endocytosis (by methyl-β-cyclodextrin), resulted in no significant difference in intracellular level of the blank nanoparticles compared to control. We therefore conclude that the translocation of blank Arg-Phe-PEA(AP) nanoparticles in DC2.4 cells was energy-dependent and involved both macropinocytosis and clathrin-mediated endocytosis.

We further studied the accumulative endocytosis of blank Arg-Phe-PEA(AP) nanoparticles in DC2.4 cells as a function of time. As illustrated in Figure 6.4B, a distinct difference in intracellular AlPcS2a fluorescence was observed between Arg-Phe-PEA(AP) nanoparticles and free AlPcS2a at the first 8 hrs, and the fluorescence intensity from the nanoparticle-treated DC2.4 cells was 2.5-fold higher than the free AlPcS2a at 4 hrs. The fluorescence signals from the free AlPcS2a, however, gradually increased with time until the difference in intracellular fluorescence between the two treatments narrowed at 12-20 hrs. Due to the low pKa of sulfonated groups in free AlPcS2a, the free AlPcS2a exhibits negative charge in biological environment [50], resulting in a slower rate of internalization due to the anionic nature of the cellular membrane. The incorporation of AlPcS2a in Arg-Phe-PEA(AP) nanoparticles

significantly enhanced the internalization efficiency of AlPcS2a at a relatively short incubation time (4 hrs). Hence 4 hrs were chosen in the following study as the incubation time between OVA-loaded nanoparticles and DC2.4 cells.

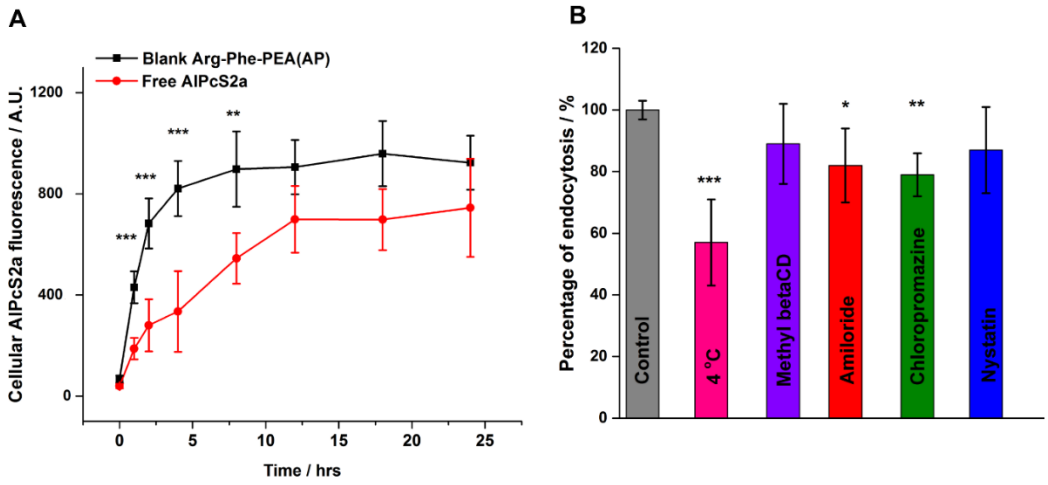


**Figure 6.4.** A) Mean fluorescence of free AlPcS2a and blank Arg-Phe-PEA(AP) nanoparticles (c(AlPcS2a) = 0.5 μg/mL) in DC2.4 cells as a function of incubation time. B) Endocytosis inhibition studies. DC2.4 cells pre-treated with various endocytosis inhibitors or low temperature were incubated with blank Arg-Phe-PEA(AP) nanoparticles for 4 hrs. Mean cellular fluorescence was recorded by flow cytometry and normalized to the control (cells incubated with nanoparticles but not treated by any inhibitor). Values represent the average ± SD (n=3). Statistical significance was compared with control. *, $p < 0.05$; **, $p < 0.01$, ***, $p < 0.001$.

### *6.4.5 Light facilitated cytosolic delivery of blank Arg-Phe-PEA(AP) nanoparticles*

The effect of AlPcS2a photosensitizer to induce cytosolic transmigration of Arg-Phe-PEA(AP) nanoparticles was then evaluated by confocal microscopy and shown in Figure 6.5A. Before light irradiation was applied, the red pixels of Arg-Phe-PEA(AP)

nanoparticles co-localized with the green pixels of endolysosomes (merging into yellow pixels), and Pearson's coefficient was determined as 0.67, indicating the endolysosomal sequestration of the nanoparticles. After 0.5 hr further incubation in dark, no significant change in Pearson's coefficient were observed in the absence of irradiation. These results demonstrated that the blank Arg-Phe-PEA(AP) nanoparticles were largely entrapped inside endolysosomes. However, when 660 nm irradiation at 1.5 J/cm$^2$ was applied for 1 min, the transmigration the nanoparticles from endolysosomes into cytosol was observed, as a lower level of yellow pixels was observed, and red pixels from Arg-Phe-PEA(AP) nanoparticles was observed and diffused into cytosol. Significant difference in Pearson's coefficient was also observed before and after irradiation, which further confirmed the endolysosomal escape upon 660 nm irradiation. The reduction of green fluorescence from Lysotracker after 660 nm irradiation indicated the disruption of endolysosomes. Lysotracker is a pH-specific probe for acidic endocytic compartments, it can only label the intact endolysosomes, instead of the ruptured one, in which the endolysosomal membrane was disintegrated and the acidic pH character was no longer maintained.

The effect of light dose on the cytosolic delivery of in the Arg-Phe-PEA(AP) nanoparticles was also investigated, as shown in Figure 6.5B. At a lower light dose (0.5 J/cm$^2$), the difference in Pearson's coefficient before and after irradiation was not statistically significant, which suggested that 0.5 J/cm$^2$ was not sufficient to result in effective endosomal escape of the blank nanoparticles. However, at higher light doses of 1.5 J/cm$^2$ and 3 J/cm$^2$, significant difference in Pearson's coefficient was observed, indicating effective endolysosomal escape of the blank nanoparticles.

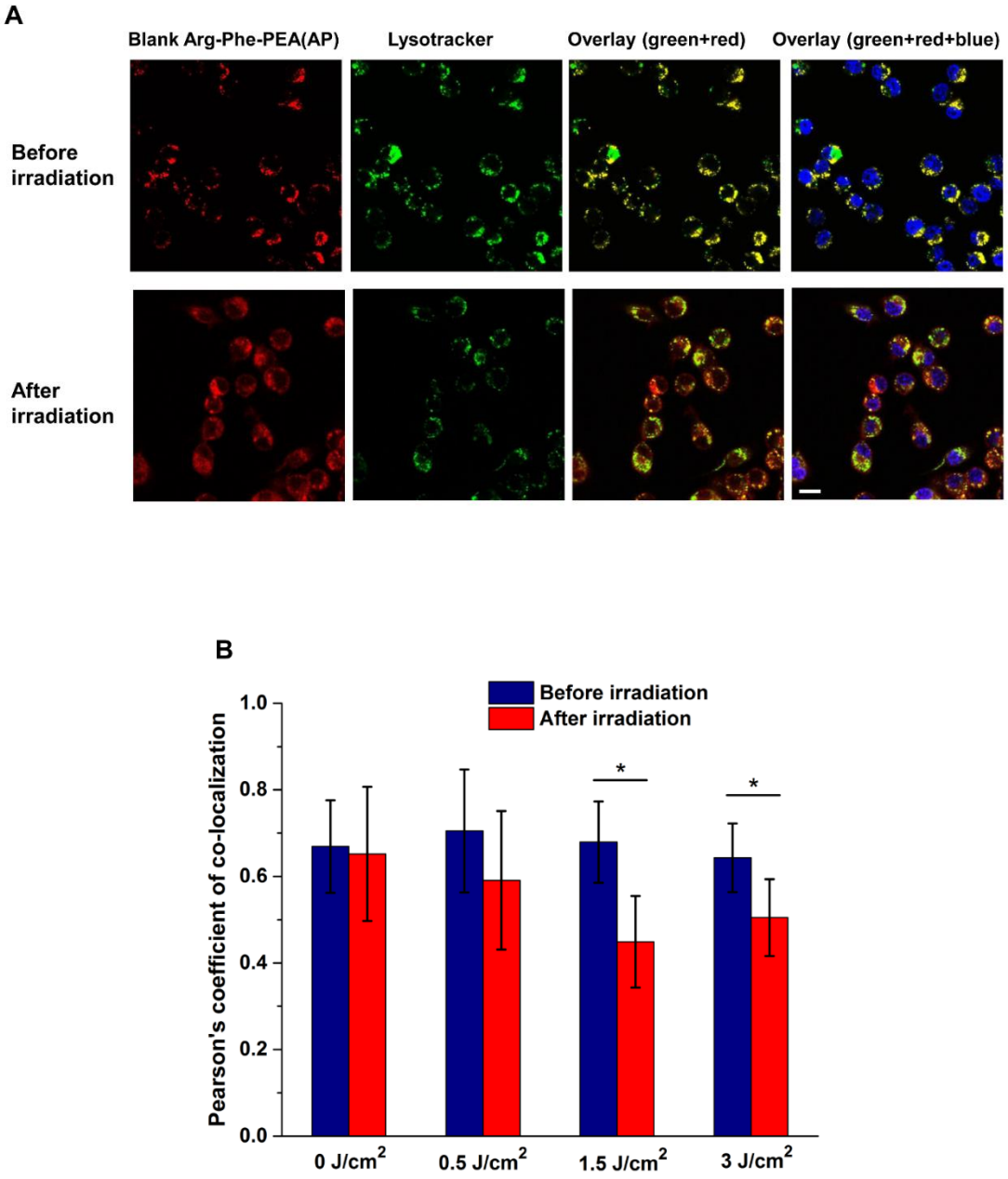


**Figure 6.5**. DC2.4 cells incubated with blank Arg-Phe-PEA(AP) nanoparticles for 4 hrs. A) Intracellular fluorescence of Lysotracker (green), blank Arg-Phe-PEA(AP) nanoparticles (red), and nuclei (blue) was recorded before irradiation and 0.5 hr post irradiation (660 nm,1.5 J/cm$^2$). B) Pearson's coefficient for co-localization degree between blank Arg-Phe-PEA(AP) nanoparticles and Lysotracker before and 0.5 hr

after irradiation was applied at various light dose (660 nm, 0. 0.5, 1.5 or 3 J/cm$^2$). Values represent the average ± SD (n=30). Statistical significance: *, $p < 0.05$.

### *6.4.6 Endocytosis of OVA loaded in Arg-Phe-PEA(AP) nanoparticles*

To demonstrate that Arg-Phe-PEA(AP) carrier can promote the uptake of OVA, flow cytometry was performed to investigate the endocytosis of FITC-OVA in DC2.4 cells, and the results were shown in Figure 6.6. Comparing with the internalized free FITC-OVA, the mean cellular fluorescence from OVA loaded in Arg-Phe-PEA(AP) was enhanced by 5.1-fold (without irradiation) and 5.6-fold (with irradiation) respectively. However, the uptake of OVA-loaded nanoparticles was not affected by irradiation, as no significant difference in mean cellular fluorescence was observed before and after irradiation. Several nano-delivery vehicles were reported to increase the rate of uptake of OVA-based antigens including liposomes [52], PLGA nanoparticles [47] or chitosan nanogels [53]. Consistent with the published studies, the result suggested that OVA loaded in Arg-Phe-PEA(AP) was more efficient in cellular uptake than free OVA. As effective antigen presentation positively correlated with the level of internalized antigen in antigen presenting cells, enhanced intracellular level of OVA loaded in nano-carriers is expected to elicit increased antigen-specific immune response.

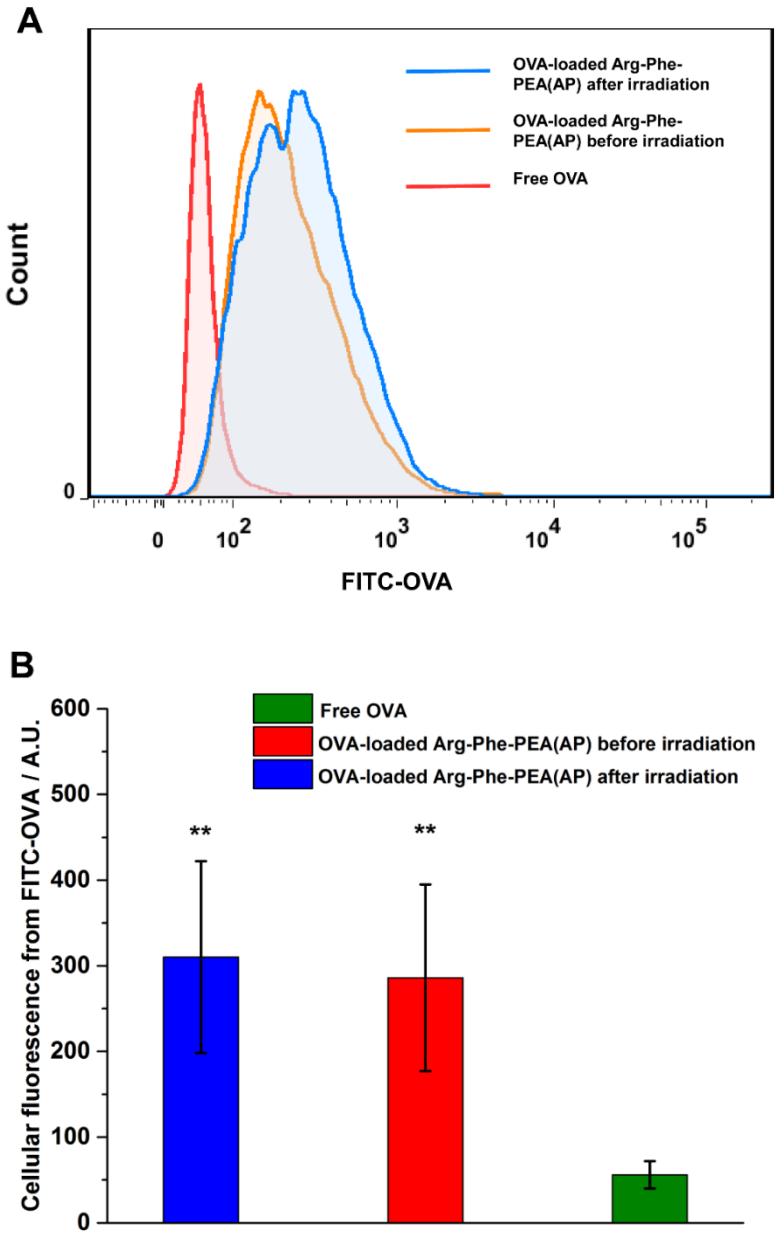


**Figure 6.6**. Uptake of FITC-OVA loaded in Arg-Phe-PEA(AP) nanoparticles or free FITC-OVA in DC2.4 cells. Light irradiation at 660 nm (1.5 J/cm$^2$) was applied 4 hrs after incubation and cellular fluorescence was measured by flow cytometry. A) The histogram of FITC-OVA in DC2.4 cells. B) The mean cellular fluorescence from FITC-OVA in DC2.4 cells. Values represent the average ± SD (n=3). Statistical

significance was compared between FITC-OVA loaded nanoparticles and free FITC-OVA. **, $p < 0.01$.

### *6.4.7 Cytotoxicity of OVA-loaded Arg-Phe-PEA(AP) nanoparticles with irradiation*

Figure 6.5 demonstrated the PCI effect of Arg-Phe-PEA(AP) nanoparticles. PCI techniques highlighted the light-facilitated rupture of endocytic compartments and the subsequent release of cargos in cytosol. However, overdose of light or photosensitizers may lead to cell death, and suppression of antigen presenting cells by excessive photosensitizing effect should be avoided in antigen delivery. In light of this, we investigated the toxicity of OVA-loaded Arg-Phe-PEA(AP) nanoparticles with different dose of light irradiation and the results were shown in Figure 6.7.

Firstly, blank Arg-Phe-PEA nanoparticles, free OVA or OVA-loaded Arg-Phe-PEA without photosensitizer (Arg-Phe-PEA(AP0)) didn't exhibit any significant toxicity at all testing conditions, which suggested the biosafety of the blank nanoparticles, as well as the antigen. Any cytotoxicity should be attributed to the photosensitizer AlPcS2a and its photosensitizing effect. Secondly, without light irradiation (0 J/cm$^2$), no cytotoxicity was observed for OVA-loaded Arg-Phe-PEA(AP) with all the three AlPcS2a concentrations (AP0.1, 0.1 μg/mL; AP0.5, 0.5 μg/mL; AP2.5, 2.5 μg/mL). The results suggested the biocompatibility of AlPcS2a-containing nanoparticles in dark, and any toxicity from these nanoparticles should be related to the photosensitizing effect. Thirdly, significant toxicity (<50% survival of DC2.4 cells) was evident for OVA-loaded Arg-Phe-PEA(AP2.5) at 1.5 J/cm$^2$ and 3 J/cm$^2$, indicating that higher concentration of AlPcS2a in combination with higher light dose

was not good for antigen delivery to DC2.4 cells. However, slight toxicity was observed for OVA-loaded Arg-Phe-PEA(AP0.5) irradiated at 1.5 J/cm$^2$, or OVA-loaded Arg-Phe-PEA(AP0.1) at 3 J/cm$^2$, it's reasonable to expect that DC2.4 cells would maintain viable and proper biological functional at these treatment conditions. Photosensitizer (TPCS2a) facilitated delivery of ovalbumin by liposomes was reported by Hjálmsdóttir et al. [16] and photosensitizer (TPCS2a) facilitated delivery of ovalbumin by PLGA nanoparticles was reported by Bruno et al. [17]. However, the in vitro screening for optimized concentration of photosensitizer as well as the light dose, were absent in the reported studies. Waeckerle-Men et al. [54] studied the free photosensitizer Amphinex facilitated vaccination of free OVA, in which a declined IFN- γ secretion was observed at higher concentration of photosensitizer (0.05 μg/mL) due to excessive death of antigen presenting cells, and the in vitro MHC-I immune response was dependent on both light dose and the concentration of photosensitizer.

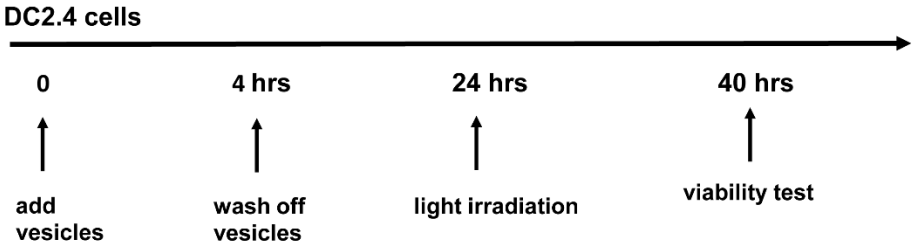

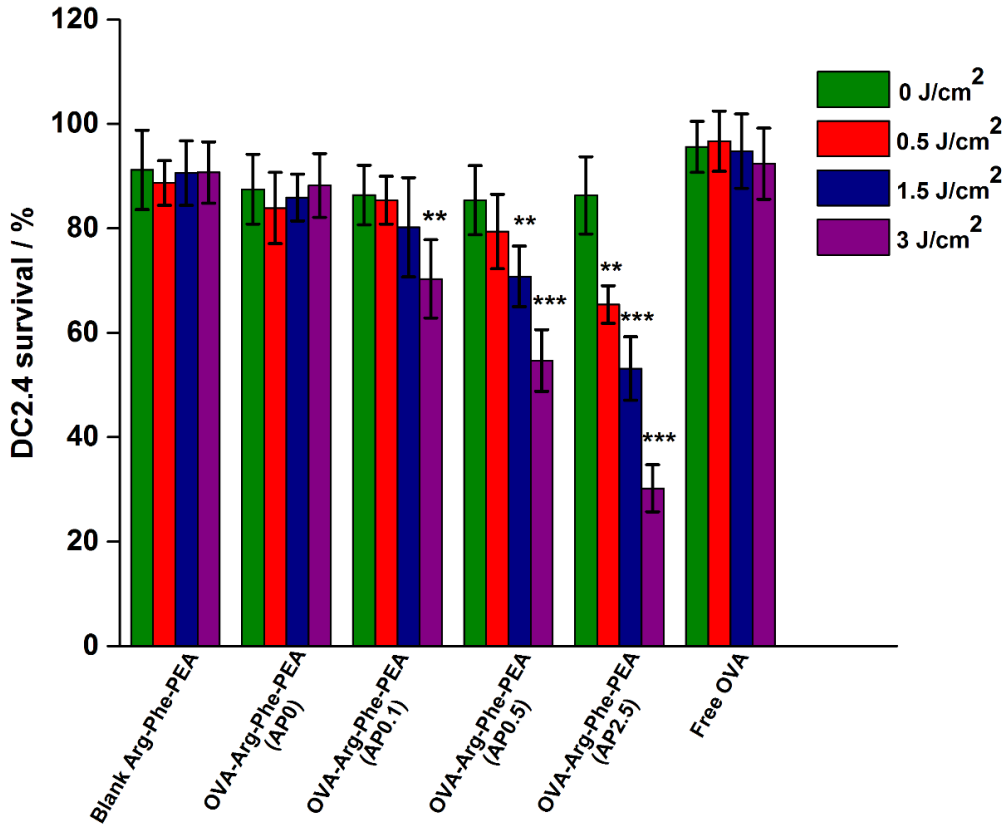


**Figure 6.7.** Survival of DC2.4 cells after incubation with OVA-loaded Arg-Phe-PEA(AP0) with no AlPcS2a, OVA-loaded Arg-Phe-PEA(AP0.1) with 0.1 μ/mL AlPcS2a, OVA-loaded Arg-Phe-PEA(AP0.5) with 0.5 μ/mL AlPcS2a, OVA-loaded Arg-Phe-PEA(AP2.5) with 2.5 μ/mL AlPcS2a, blank Arg-Phe-PEA, free OVA, and the equivalent concentration of OVA in all the samples were 5 μg/mL. Light irradiation was applied at 660nm with light dose of 0, 0.5, 1.5 or 3 J/cm$^2$. Values represent the average ± SD (n=6). Statistical significance was compared between non-irradiated group with the groups that received different light dose. **, $p < 0.01$, ***, $p < 0.001$.

### *6.4.8 Light-facilitated MHC-I presentation of OVA-loaded Arg-Phe-PEA(AP) nanoparticles*

To further investigate the interaction between light-facilitate delivery of OVA-loaded Arg-Phe-PEA nanoparticles and DC2.4 cells, in vitro B3Z assay of MHC-I presentation was performed. B3Z [55] is a CD8 T-cell hybridoma that specifically recognizes ovalbumin residues 257–264 (SIINFEKL) presented on the murine Kb MHC-I molecule containing the LacZ reporter gene driven by transcriptional control of the nuclear factor of activated T cells (NFAT) element. The presentation of the SIINFEKL epitope to B3Z cells activates NFAT and results in the induction of β-galactosidase synthesis by B3Z. The amount of β-galactosidase produced can be measured by the hydrolysis of the chromogenic substrate CPRG (chlorophenol red-β-D-galactopyranoside) and is an indication of the amount of MHC-I immune-complexes presented on the surface of antigen presenting cells.

As suggested in Figure 6.8, firstly, blank Arg-Phe-PEA nanoparticles didn't elicit any MHC-I response. Secondly, all non-irradiated particulate formulations of OVA enhanced MHC I antigen presentation compared to free OVA, which can be correlated to the enhanced endocytosis of OVA in Figure 6.6. Thirdly, when light irradiation was applied, OVA-loaded Arg-Phe-PEA(AP0.5) with 1.5 J/cm$^2$ irradiation resulted in 5-fold increase in MHC-I response compared to free OVA, and 2-fold increase compared to its non-irradiated counterpart. Additionally, OVA-loaded Arg-Phe-PEA(AP0.5) with 3 J/cm$^2$ irradiation, and OVA-loaded Arg-Phe-PEA(AP2.5) with 0.5 J/cm$^2$ irradiation, induced significantly enhanced MHC-I response than the non-

irradiated ones, as well as free OVA. The result is positively correlated with the PCI effect in Figure 6.5. The PCI effect by Arg-Phe-PEA(AP) induced effective rupture of endolysosomes, and the leaky endocytic compartments release antigen to the cytosol, where the proteasomes can digest OVA to MHC-I binding peptides that consequently can be presented to CD8 T cells.

However, OVA-loaded Arg-Phe-PEA(AP2.5) with higher light dose (1.5 and 3 J/cm$^2$) exhibited reduced MHC-I presentation compared to both non-irradiated ones, and it could be dependent on the viability result (Figure 6.7), in which higher dose of photosensitizers/higher light dose induced significant cytotoxicity.

In general, the Arg-Phe-PEA(AP) nanoparticles proved enhanced and cytosolic delivery of OVA, and elicit enhanced level of MHC-I antigen presentation when facilitated with light. The stimulated MHC-I response was dependent on the concentration of photosensitizer and light dose. The level of MHC-I presentation correlates with the activation of cytotoxic CD8 T cells and the adaptive immunity against tumors, and the light-facilitated Arg-Phe-PEA(AP) delivery systems could hold the potential to be developed as the platform for tumor vaccine delivery.

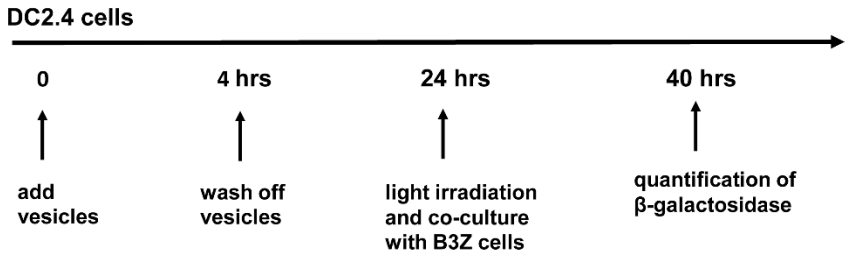

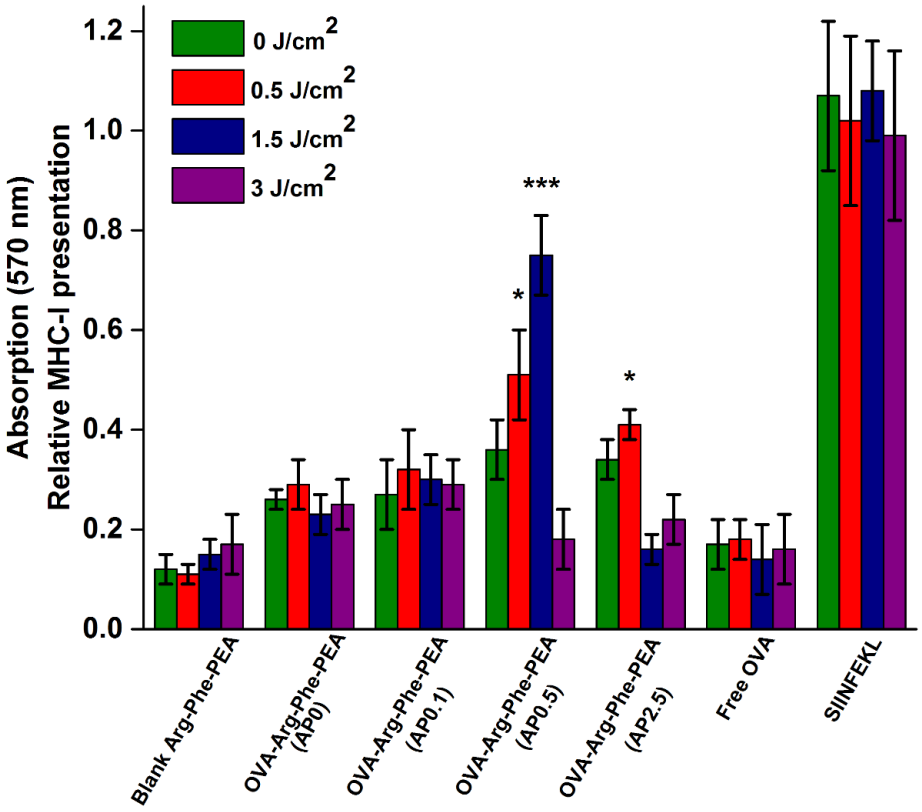


**Figure 6.8.** MHC-I antigen presentation (B3Z assay) by DC 2.4 cells. DC2.4 cells were incubated with the OVA-loaded Arg-Phe-PEA(AP0) with no AlPcS2a, OVA-loaded Arg-Phe-PEA(AP0.1) with 0.1 μ/mL AlPcS2a, OVA-loaded Arg-Phe-PEA(AP0.5) with 0.5 μ/mL AlPcS2a, OVA-loaded Arg-Phe-PEA(AP2.5) with 2.5 μ/mL AlPcS2a, blank Arg-Phe-PEA, free OVA, and the equivalent concentration of OVA in all the samples were 5 μg/mL. Cells incubated with SIINFEKL peptide was also tested as positive control. Light irradiation was applied at 660nm with light dose of 0, 0.5, 1.5 or 3 J/cm$^2$. The β-galactosidase in B3Z cells after MHC-I presentation was quantified calorimetrically by the absorption at 570 nm, which reflected the level of MHC-I presentation. Values represent the average ± SD (n=3). Statistical

significance was compared between non-irradiated group with the groups that received different light dose. *, $p < 0.05$; **, $p < 0.01$, ***, $p < 0.001$.

### *6.5 Conclusions*

A biodegradable arginine and phenylalanine based poly(ester amide)s nanoparticles in complex with PCI-photosensitizer AlPcS2a, were developed for the light-facilitated cytosolic delivery of ovalbumin. The OVA-loaded Arg-Phe-PEA(AP) nanoparticles exhibited slightly cationic charge, and the average diameter was between 200 – 240 nm, with the OVA loading content of 6.2% and encapsulation efficiency of 67.5%, respectively. The enzymatic biodegradability of the Arg-Phe-PEA(AP) enabled enzyme-accelerated release of OVA, and significantly enhanced the internalization rate by dendritic cells, compared to free OVA. In vitro PCI effect by Arg-Phe-PEA(AP) nanoparticles was validated in dendritic cells, and enabled the cytosolic transmigration of the OVA-loaded nanoparticles to further potentiate MHC-I immune response. The MHC-I response by OVA-loaded Arg-Phe-PEA(AP) nanoparticles was dependent on the light dose, as well as the concentration of the photosensitizer. Medium level of both light dose and AlPcS2a concentration lead to significant MHC-I presentation, while excessive photosensitizing effect introduced cytotoxicity to dendritic cells, and further adversely impacted the efficiency of MHC-I presentation. The Arg-Phe-PEA(AP) delivery systems achieved the simultaneous delivery of both photosensitizer and antigens, and the light-facilitated PCI-effect enhanced the access of antigens into cytosol for subsequent MHC-I processing and presentation. The biodegradable and light-facilitated poly(ester amide)s nanoparticles

have the promising potential to be developed as the platform for vaccine delivery, to elicit CD8 T cell immunity against multiple diseases including cancer.

**Reference:**


[1] N. P. Restifo, M. E. Dudley, S. A. Rosenberg, *Nat. Rev. Immunol.* **2012**, *12*, 269.

[2] G. T. Belz, F. R. Carbone, W. R. Heath, *Crit. Rev. Immunol.* **2002**, *22*, 439.

[3] D. Shae, A. Postma, J. T. Wilson, *Ther. Deliv.* **2016**, *7*, 193.

[4] A. E. Gregory, R. Titball, D. Williamson, *Front. Cell. Infect. Microbiol.* **2013**, *3*.

[5] S. A. Ferreira, F. M. Gama, M. Vilanova, *Nanomedicine Nanotechnol. Biol. Med.* **2013**, *9*, 159.

[6] J. W. Yewdell, E. Reits, J. Neefjes, *Nat. Rev. Immunol.* **2003**, *3*, 952.

[7] M. F. Princiotta, D. Finzi, S.-B. Qian, J. Gibbs, S. Schuchmann, F. Buttgereit, J. R. Bennink, J. W. Yewdell, *Immunity* **2003**, *18*, 343.

[8] P. J. Lehner, P. Cresswell, *Curr. Opin. Immunol.* **2004**, *16*, 82.

[9] E. Mathew, G. E. Hardee, C. F. Bennett, K.-D. Lee, *Gene Ther.* **2003**, *10*, 1105.

[10] P. K. Selbo, A. Weyergang, A. Høgset, O.-J. Norum, M. B. Berstad, M. Vikdal, K. Berg, *J. Controlled Release* **2010**, *148*, 2.

[11] A. P. Castano, T. N. Demidova, M. R. Hamblin, *Photodiagnosis Photodyn. Ther.* **2004**, *1*, 279.

[12] P. K. Selbo, A. Weyergang, A. Høgset, O.-J. Norum, M. B. Berstad, M. Vikdal, K. Berg, *J. Controlled Release* **2010**, *148*, 2.

[13] K. Berg, M. Folini, L. Prasmickaite, P. Selbo, A. Bonsted, B. Engesaeter, N. Zaffaroni, A. Weyergang, A. Dietzea, G. Maelandsmo, E. Wagner, O.-J. Norum, A. Hogset, *Curr. Pharm. Biotechnol.* **2007**, *8*, 362.

[14] K. Berg, P. K. Selbo, L. Prasmickaite, T. E. Tjelle, K. Sandvig, J. Moan, G. Gaudernack, O. Fodstad, S. Kjølsrud, H. Anholt, G. H. Rodal, S. K. Rodal, A. Høgset, *Cancer Res.* **1999**, *59*, 1180.

[15] M. Håkerud, Y. Waeckerle-Men, P. K. Selbo, T. M. Kündig, A. Høgset, P. Johansen, *J. Controlled Release* **2014**, *174*, 143.

[16] Á. Hjálmsdóttir, C. Bühler, V. Vonwil, M. Roveri, M. Håkerud, Y. Wäckerle-Men, B. Gander, P. Johansen, *Mol. Pharm.* **2016**, *13*, 320.

[17] C. Bruno, Y. Waeckerle-Men, M. Håkerud, T. M. Kündig, B. Gander, P. Johansen, *J. Immunol.* **2015**, *195*, 166.

[18] S. H. Lee, I. Szinai, K. Carpenter, R. Katsarava, G. Jokhadze, C.-C. Chu, Y. Huang, E. Verbeken, O. Bramwell, I. De Scheerder, M. K. Hong, *Coron. Artery Dis.* **2002**, *13*, 237.

[19] Costantini, C.R., Londero, H., DeScheeder, I., Tarbine, S.G., Costantini, C.O., Cabrera, M.J., *Am. J. Cardiol* **2005**.

[20] Y. Huang, L. Wang, S. Li, X. Liu, K. Lee, E. Verbeken, F. van de Werf, I. de Scheerder, *Acute Card. Care* **2006**, *8*, 210.

[21] Chu, C.C., Fischell, D.R., Pomerantz, M., *9th World Biomaterial Congress, Cheng-Du, China,* **2012**.

[22] M. Webster, S. Harding, D. McClean, W. Jaffe, J. Ormiston, A. Aitken, T. Watson, *EuroIntervention* **2013**, *9*, 46.

[23] H. Song, C. C. Chu, *J. Appl. Polym. Sci.* **2012**, *124*, 3840.

[24] Schwartz, S, Demars, S., Chu, C.C., White, J., Cooper, A., Rothrock, M., Adelman, M., Yurt, R., *3rd World Union of Wound Healing Societies* **2008**.

[25] D. Yamanouchi, J. Wu, A. N. Lazar, K. C. Kent, C.-C. Chu, B. Liu, *Biomaterials* **2008**, *29*, 3269.

[26] J. Wu, D. Yamanouchi, B. Liu, C.-C. Chu, *J. Mater. Chem.* **2012**, *22*, 18983.

[27] J. Liu, X. L. Liu, T. F. Xi, C. C. Chu, *J Mater Chem B* **2015**, *3*, 878.

[28] K. A. Hernandez, R. C. Hooper, T. Boyko, A. R. Golas, M. van Harten, D. Q. Wu, A. Weinstein, C. C. Chu, J. A. Spector, *J. Biomed. Mater. Res. B Appl. Biomater.* **2015**, *103*, 457.

[29] Knecht Daniel, C.C.Chu, In *Biodegradable Polymers, Volume 1: Advancement in Biodegradation Study and Applications*; Nova Science Publisher: New York, 2015.

[30] K. Guo, C. C. Chu, *J. Biomed. Mater. Res. B Appl. Biomater.* **2009**, *89B*, 491.

[31] L. Li, C.-C. Chu, *J. Biomater. Sci. Polym. Ed.* **2009**, *20*, 341.

[32] C.-C. Chu, In *Biodegradable Polymers: New Biomaterial Advancement and Challenges*; Chu, C.-C., Ed.; Nova Science Publisher, 2015; Vol. 2.

[33] C.-C. Chu, In *Biomaterials – Principles and Practices*; Wong, J. Y.; Bronzino, J. D.; Peterson, D. R., Eds.; CRC Press, 2012.

[34] C. C. Chu, *J. Fiber Bioeng. Inform.* **2012**, *5*, 1.

[35] C.C.Chu, In *L-Arginine: Structure, Dietary Sources and beneficial Effects*; Nova Science Publisher: New York, 2016.

[36] C.C.Chu, In *L-Arginine – Structure, Dietary Sources and Beneficial Effects*; Nova Science Publisher: New York, In Press.

[37] J. Wu, D. Yamanouchi, B. Liu, C.-C. Chu, *J. Mater. Chem.* **2012**, *22*, 18983.

[38] J. Wu, C.-C. Chu, *Acta Biomater.* **2012**, *8*, 4314.

[39] H. Song, C. C. Chu, *J. Appl. Polym. Sci.* **2012**, *124*, 3840.

[40] J. Wu, C.-C. Chu, *J Mater Chem B* **2013**, *1*, 353.

[41] S. G. Kimani, T. A. Shmigol, S. Hammond, J. B. Phillips, J. I. Bruce, A. J. MacRobert, M. V. Malakhov, J. P. Golding, *Photochem. Photobiol.* **2013**, *89*, 139.

[42] W.-D. Jang, Y. Nakagishi, N. Nishiyama, S. Kawauchi, Y. Morimoto, M. Kikuchi, K. Kataoka, *J. Controlled Release* **2006**, *113*, 73.

[43] Y.-R. Lee, Y.-H. Lee, S.-A. Im, K. Kim, C.-K. Lee, *Immune Netw.* **2011**, *11*, 163.

[44] H. Silva, F. Frézard, E. J. Peterson, P. Kabolizadeh, J. J. Ryan, N. P. Farrell, *Mol. Pharm.* **2012**, *9*, 1795.

[45] D. Colin, E. Limagne, S. Jeanningros, A. Jacquel, G. Lizard, A. Athias, P. Gambert, A. Hichami, N. Latruffe, E. Solary, D. Delmas, *Cancer Prev. Res. (Phila. Pa.)* **2011**, *4*, 1095.

[46] L. Cui, J. A. Cohen, K. E. Broaders, T. T. Beaudette, J. M. J. Fréchet, *Bioconjug. Chem.* **2011**, *22*, 949.

[47] M. Garinot, V. Fiévez, V. Pourcelle, F. Stoffelbach, A. des Rieux, L. Plapied, I. Theate, H. Freichels, C. Jérôme, J. Marchand-Brynaert, Y.-J. Schneider, V. Préat, *J. Controlled Release* **2007**, *120*, 195.

[48] C. S. W. Chong, M. Cao, W. W. Wong, K. P. Fischer, W. R. Addison, G. S. Kwon, D. L. Tyrrell, J. Samuel, *J. Controlled Release* **2005**, *102*, 85.

[49] K. Newman, J. Samuel, G. Kwon, *J. Controlled Release* **1998**, *54*, 49.

[50] K. Berg, A. Weyergang, L. Prasmickaite, A. Bonsted, A. Høgset, M.-T. R. Strand, E. Wagner, P. K. Selbo, In *Photodynamic Therapy*; Gomer, C. J., Ed.; Humana Press: Totowa, NJ, 2010; Vol. 635, pp. 133–145.

[51] E. Fleige, M. A. Quadir, R. Haag, *Adv. Drug Deliv. Rev.* **2012**, *64*, 866.

[52] M. J. Copland, M. A. Baird, T. Rades, J. L. McKenzie, B. Becker, F. Reck, P. C. Tyler, N. M. Davies, *Vaccine* **2003**, *21*, 883.

[53] S. Yu, J. Hu, X. Pan, P. Yao, M. Jiang, *Langmuir* **2006**, *22*, 2754.

[54] Y. Waeckerle-Men, A. Mauracher, M. Håkerud, D. Mohanan, T. M. Kündig, A. Høgset, P. Johansen, *Eur. J. Pharm. Biopharm.* **2013**, *85*, 34.

[55] J. E. de Vries, H. Spits, *J. Immunol. Baltim. Md 1950* **1984**, *132*, 510.

# Appendix

## *Appendix I. JC-1 mitochondrial membrane potential assay*

JC-1 cationic dye exhibits potential-dependent accumulation in mitochondria, indicated by a fluorescence emission shift between green (JC-1 monomers, λem = 525 nm) and red (J-aggregates, λem = 590 nm). Consequently, mitochondrial depolarization is indicated by a decrease in the red/green fluorescence intensity ratio. The potential-sensitive color shift is due to concentration-dependent formation of red fluorescent J-aggregates. JC-1 can be used as an indicator of mitochondrial potential in a variety of cell types.

1. HCT116 cells or MDA-MB-435/MDR cells were seeded in 6 well plate ($0.3 \times 10^6$ cells/well) and pre-incubated for 24 hrs. Vehicles or free drug were then added and incubated for predetermined time. Cells were then washed twice with PBS (phosphate buffer saline, pH 7.4), harvested by incubation with 1 mL of accutase per well for 3-5 min, and pelleted by centrifugation (200 rcf, 5 min).

2. JC-1 stock (2.5 mg/mL in dimethyl sulfoxide) was equilibrated to room temperature, and diluted to 10 μg/mL in PBS by vigorous agitation to avoid the formation of any precipitation or flakes. Cells were re-suspended in JC-1/PBS solution in the concentration of $1 \times 10^6$ cells/mL, returned to the incubator, and incubated at 37 °C for 15-30 min for labelling. Untreated cells stained with JC-1 was used as negative control, and cells treated with CCCP (carbonyl cyanide 3-chlorophenylhydrazone, 5 μM) simultaneously with JC-1 staining, was used as positive control. CCCP is the typical mitochondrial membrane potential disrupter.

3. After sufficient incubation with JC-1 dyes, each sample was washed once with 2 mL of PBS and resuspended in 0.5 mL PBS by gentle flicking the tube.

4. Flow cytometry was performed immediately after staining, on a flow cytometer with 488 nm excitation using emission filters appropriate for Alexa Fluor 488 dye and R-phycoerythrin. Gate on the cells, excluding debris. CCCP-treated sample was used to perform standard compensation.

5. The percentage of cell population stained with higher level of green fluorescence and lower level of red fluorescence was recorded for each sample, which indicated the percentage of cells with depolarized mitochondrial. As suggested in Figure A1, the population that fell in quadrant 3 represented cells with mitochondrial depolarization. Each test was performed in 3 replicates.

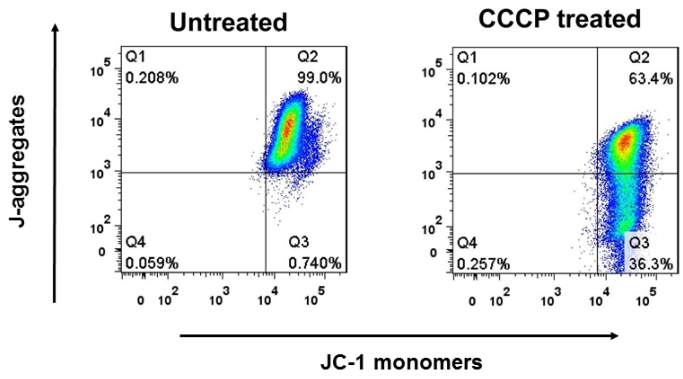


**Figure A1**. JC-1 assay of HCT116 cells treated with CCCP (carbonyl cyanide 3-chlorophenylhydrazone, 5 μM) for 30 min. Flow cytometry detection of cellular fluorescence from J aggregates or JC-1 monomers were recorded. 50,000 cells were analyzed for each sample.

***Appendix II. Annexin V apoptosis assay***

The appearance of phosphatidylserine (PS) residues (normally hidden within the plasma membrane) on the surface of the cell is an early event in apoptosis, and can be used to detect and measure apoptosis. During apoptosis, PS is translocated from the cytoplasmic face of the plasma membrane to the cell surface. Annexin V has a strong, $Ca^{2+}$ dependent affinity for PS and therefore can be used as a probe for detecting apoptosis.

1. HCT116 cells or MDA-MB-435/MDR cells were seeded in 6 well plate ($0.3 \times 10^6$ cells/well) and pre-incubated for 24 hrs. Vehicles or free drug were then added and incubated for predetermined time. Cells were then washed twice with PBS (phosphate buffer saline, pH 7.4), harvested by incubation with 1 mL of accutase per well for 3-5 min, and pelleted by centrifugation (200 rcf, 5 min).

2. Annexin V binding buffer was prepared: 0.01 M HEPES, pH 7.4; 0.14 M NaCl; 2.5 mM $CaCl_2$

3. Wash cells once annexin V binding buffer, and resuspend cells in binding buffer at 1-5 $\times 10^6$ cells/mL.

5. Add 5 μL of FITC-conjugated annexin V staining solution (eBioscience 88-8007) to 100 μL of the cell suspension. Incubate 10-15 minutes at room temperature, protected from light.

7. Wash cells with 2 mL binding buffer and resuspend in 200 μL binding buffer.

8. Add 5 μL of propidium iodide staining solution (eBioscience 88-8007).

9. Analyze by flow cytometry immediately after staining, on a flow cytometer with 488 nm excitation using emission filters appropriate for Alexa Fluor 488 dye and R-

phycoerythrin. Gate on the cells, excluding debris. Percentage of early apoptotic cells were identified with higher level of green fluorescence (stained with annexin V FITC) and lower level of red fluorescence (stained with propidium iodide). As suggested in Figure A2, cell populations that fell in quadrant 3 represent early apoptotic cells, cells in quadrant 1 are live cells and cells in quadrant 1 and 2 are late apoptotic cells or dead cells.

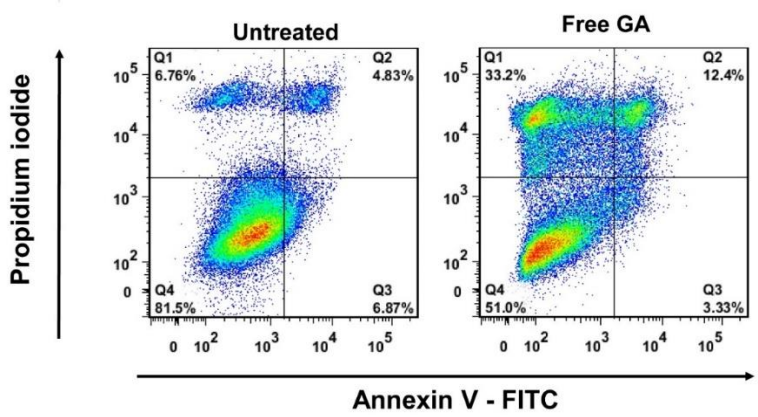


**Figure A2**. Annexin V assay of MDA-MB-435 cells treated with free Gambogic acid (1 µM) for 24 hrs. Flow cytometry detection of cellular fluorescence from annexin V-FITC or propidium iodide were recorded. 50,000 cells were analyzed for each sample.

***Appendix III. Western blot assay for cleaved caspase-3***

Western blot assay enables the separation and specific detection of individual protein in a complex sample. Proteins are separated. Proteins are commonly separated using polyacrylamide gel electrophoresis (PAGE) according to physical properties as they are forced through a gel by an electrical current. Electrophoretic transfer of proteins involves placing a protein-containing polyacrylamide gel in direct contact

with a piece of protein-binding membrane and sandwiching between two electrodes submerged in a conducting solution. When an electric field is applied, the proteins move out of the polyacrylamide gel and onto the surface of the membrane, where the proteins become tightly attached. The result is a membrane with a copy of the protein pattern that was originally in the polyacrylamide gel. Immunostaining was then performed on the blotted membrane, and the specificity of the antibody-antigen interaction enables a target protein to be identified in the midst of a complex protein mixture. Western blotting can produce qualitative and semiquantitative analysis for the target protein.

1. HCT116 cells were cultured in T75 flask and grew to 80-90% confluency. Vehicles or free drugs were added and incubated for predetermined time. Cells were then washed twice with ice cold PBS.

2. 500 μL of RIPA (radioimmunoprecipitation) lysis buffer was added to each flask, cells were immediately scraped off and transfer to a microcentrifuge tube on ice. Probe sonication was performed to cell lysate three times for 10-15 seconds to complete cell lysis and shear DNA.

3. Total protein amount in each sample was determined by BCA (bicinchoninic acid) assay and stored at -20° C.

7. Immediately prior to protein electrophoresis, diluted samples with SDS sample buffer containing DTT (Cell Signaling) so that the final total protein concentration in each sample was 1 mg/mL and heated the diluted samples to 95–100 °C for 5 min. Samples were then microcentrifuged at 10000 rcf for 5 min and stored on ice.

8. Protein electrophoresis was performed with 4-20% Tris-glycine mini wedge-well

gel (Novex), rinsed in running buffer (25 mM Tris base, 190 mM glycine, 0.1% SDS). 35 μL samples were loaded in each lane and electrophoresis was performed at 225V for 45-60 min.

9. Protein band was then transferred to PVDF membrane in transfer stack rinsed in transfer buffer (25 mM Tris base, 190 mM glycine, 20% methanol).

10. The transferred membrane was blocked at room temperature for 1 hr in blocking buffer (5% bovine serum albumin in TBST buffer (Tris-buffered saline containing 0.1% Tween 20)), then washed three times for 5 min each with TBST buffer.

11. The membrane was incubated with primary antibody cleaved caspase-3 (Asp175) rabbit mAb (Cell Signaling, 1:1000 dilution in blocking buffer) at 4°C overnight, and washed three times for 5 min each with TBST buffer.

12. The membrane was incubated with anti-rabbit IgG, HRP-conjugated secondary antibody (Cell Signaling, 1:2000 dilution in blocking buffer) for 1 hr at room temperature, and washed three times for 5 min each with TBST buffer.

13. The membrane was incubated with LumiGLO (Cell Signaling) developing solution with gentle agitation for 1 min at room temperature. The membrane was drained, wrapped in plastic wrap and exposed to X-ray film for 1.5 min to develop western blot image.

***Appendix IV. 3D multicellular spheroid culture and viability assay***

Evaluations of anti-tumor delivery system are usually completed in 2D cell culture systems, in which cells were grown in monolayer on a hard and flat surface.

Oftentimes, successful nanoparticle delivery observed in 2D cell culture studies does not translate to similar results in vivo. The extracellular matrix from 2D culture was less dense in monolayer apical side compared to cells in 3D environment, and limitations in monolayer cultures were observed that failed to account for extracellular barriers that are present in vivo. 3D culture systems that more closely mimic in vivo tumor tissues in terms of functionality and morphological, provide a more predictive platform for assessing in vivo efficiencies of delivery vehicles. Such systems can serve to bridge the considerable gap between traditional 2D monolayer experiments and in vivo studies.

1. Monolayer of MDA-MB-231 breast carcinoma were maintained in Dulbecco's modified Eagle medium (DMEM) supplemented with 10% fetal bovine serum, 2 mM L-glutamine, 100 unit/mL penicillin, and 100 μg/mL streptomycin.

2. At 80-90% of confluency, cells were harvested by incubation with accutase, resuspended in complete DMEM medium supplemented with 2.5% Matrigel (BD Bioscience), and seeded in ultra-low-attachment 96-well plate (CellCarrier, Perkin Elmer) at $0.5 \times 10^4$ cells/well.

3. The plate was centrifuged at 1000 rcf for 10 min, before it was returned to incubator and cultured for 3 days to obtain multicellular spheroids with average diameter of 400-500 μm.

4. Vehicles or free drug was incubated with spheroids for predetermined time and washed with culture medium twice. 10 μL of WST-1 assay reagent (Sigma Aldrich) was added to each well, returned to the incubator and incubated for 4 hrs.

5. The contents in the ultra-low-attachment 96 well plate was transferred to regular

flat-bottom 96 well plate and mixed well on orbital shaker. The absorbance in each well was measured on microplate reader at 450 nm. Untreated spheroids were analyzed as control and the viability of spheroids was normalized to control. 10 replicates were measured for each treatment.

***Appendix V. DNA ladder assay for apoptosis detection***

Apoptosis is a programmed physiological mechanism for cell death. Fragmentation of chromatin DNA at the nucleosomal level (around185 bp) is one of the hallmarks of apoptosis. The DNA fragmentation can be detected as laddering using gel electrophoresis.

1. MDA-MB-435/MDR cells were seeded in 6 well plate ($0.3 \times 10^6$ cells/well) and pre-incubated for 24 hrs. Vehicles or free drug were then added and incubated for predetermined time. Cells were then washed twice with PBS (phosphate buffer saline, pH 7.4), harvested by incubation with 1 mL of accutase per well for 3-5 min, and pelleted by centrifugation (200 rcf, 5 min).

2. Resuspend the pellet thoroughly in 200 µL of Resuspension Solution (GenElute Mammalian Genomic DNA Miniprep Kit, Sigma Aldrich). All the following reagents were from the same DNA miniprep kit.

3. Add 20 µL of the Proteinase K solution to the sample, followed by 200 µL of Lysis Solution C. Vortex thoroughly, and incubate at 70 °C for 10 minutes.

4. Add 500 µL of the Column Preparation Solution to each pre-assembled GenElute

Miniprep Binding Column and centrifuge at 12,000 rcf for 1 minute. Discard flow-through liquid.

5. Add 200 µL of ethanol (95–100%) to the lysate; mix thoroughly by vortexing 5–10 seconds.

6. Transfer the entire contents of the tube into the treated binding column. Use a wide bore pipette tip to reduce shearing the DNA when transferring contents into the binding column. Centrifuge at 6500 rcf for 1 minute. Discard the collection tube containing the flow-through liquid and place the binding column in a new 2 mL collection tube.

7. Add 500 µL of Wash Solution to the binding column and centrifuge for 1 minute at 6,500 rcf. Discard the collection tube containing the flow-through liquid and place the binding column in a new 2 mL collection tube.

8. Add another 500 µL of Wash Solution to the binding column; centrifuge for 3 minutes at maximum speed (12,000-16,000 rcf) to dry the binding column. Centrifuge the column for one additional minute at maximum speed if residual ethanol is seen. Discard the collection tube containing the flow-through liquid and place the binding column in a new 2 mL collection tube.

9. Pipette 200 µL of the Elution Solution directly into the center of the binding column; centrifuge for 1 minute at 6,500 rcf to elute the DNA. To increase the elution efficiency, incubate for 5 minutes at room temperature after adding the Elution Solution, then centrifuge.

10. DNG gel electrophoresis was performed in Flashgel system (Lonza). As prepared DNA samples were diluted with Flashgel loading dye (1:5 v/v) and loaded onto 1.2%

FlashGel DNA Cassette at 5 µL per lane. The electrophoresis was performed at 275 V for 5 min and the DNA bands were visualized on the FlashGel Dock.

***Appendix VI. Gelatin zymography***

The invasion and metastasis of tumor cells has been shown to require proteolytic activity in order to degrade components of the extracellular matrix (ECM). A major group of proteases that has been directly associated with tumor metastasis is the matrix metalloproteinases (MMP). The gelatinases MMP-2 and MMP-9 are two members of the MMP family that have been extensively studied owing to their consistent association with tumor invasion and metastasis. Gelatin zymography identifies gelatinolytic activity of MMP using sodium dodecyl sulfate (SDS)-polyacrylamide gels impregnated with gelatin, after protein electrophoresis, the non-denatured MMP can degrade the gelatin, leaving a cleared zone that can be detected by Coomassie blue staining. The gelatinolytic results correlate directly with the activation status of MMP.

1. $3\times 10^5$ MDA-MB-435/MDR cells per well were seeded in a 6-well plate pre-incubated for 24 hrs.

2. Cell were then treated with vesicles in serum-free DMEM for 24 hrs.

3. The media were collected and centrifuged (400 rcf, 5 min, 4 ºC). The supernatant (75 µL) was mixed with 25 µL sample buffer (250 mM Tris-HCl, pH 6.8; 40% glycerol; 8% SDS; and 0.01% bromophenol blue). The mixture was vortexed and kept at room temperature for 10 – 15 min.

4. The gels were provided with 1% type B gelatin (w/v). Gently pull the comb out from the stacking gel and peel off the tape from the bottom of the cassette. Place the cassette into the gel apparatus and fill the buffer chambers with running buffer (0.1% SDS, 25 m*M* Tris base and 190 m*M* glycine, pH 8.3).

5. Load the samples (as prepared from step 3) and run the gel at constant voltage (125 V, starting current should be approximately 30–40 mA/gel) until the bromophenol blue tracking dye reaches the bottom of the gel (approximately 90 min).

6. Carefully remove the gel from the cassette and place it in plastic tray containing 100 mL of renaturing solution (2.5% v/v Triton X-100 in DI water). Incubate the gel for 30 min at room temperature with gentle agitation.

7. Decant the solution and rinse the gel at least once with 300 mL of DI water. Incubate the gel at room temperature for an additional 30 min in 100 mL of developing buffer (50 mM Tris-HCl buffer containing 10 mM of $CaCl_2$, 0.02% $NaN_3$, pH 7.6) with gentle agitation.

8. Decant the developing buffer and replace it with 100 mL of fresh developing buffer. Incubate the gel at 37°C for approximately 16 hrs in a closed container.

9. Decant the developing buffer and stain the gel in staining solution (0.5% Coomassie blue R-250, 5% methanol, and 10% acetic acid in DI water.) until the gel is uniformly dark blue.

10. Destain the gel with destaining solution (10% methanol, 5% acetic acid in DI water) until areas of gelatinolytic activity appear as clear bands over the background.